Structure and Properties of Nanostructures from Polyelectrolytes and Porphyrins: Self-Assembly in Aqueous Solution

Dissertation
zur Erlangung des Grades
„Doktor der Naturwissenschaften”
im Promotionsfach Chemie

am Fachbereich Chemie, Pharmazie und Geowissenschaften
der Johannes Gutenberg-Universität
in Mainz

Christian Ruthard

geboren in Mainz

Mainz, 2010

Für Annika

ABSTRACT

In this work self-assembling model systems in aqueous solution were studied. The systems contained charged polymers, polyelectrolytes, that were combined with oppositely charged counterions to build up supramolecular structures. With imaging, scattering and spectroscopic techniques it was investigated how the structure of building units influences the structure of their assemblies. Polyelectrolytes with different chemical structure, molecular weight and morphology were investigated. In addition to linear polyelectrolytes, semi-flexible cylindrical bottle-brush polymers that possess a defined cross-section and a relatively high persistence along the backbone were studied. The polyelectrolytes were combined with structural organic counterions having charge numbers one to four. Especially the self-assembly of polyelectrolytes with different tetravalent water-soluble porphyrins was studied. Porphyrins have a rigid aromatic structure that has a structural effect on their self-assembly behavior and through which porphyrins are capable of self-aggregation via π-π interaction. The main focus of the thesis is the self-assembly of cylindrical bottle-brush polyelectrolytes with tetravalent porphyrins. It was shown that the addition of porphyrins to oppositely charged brush molecules induces a hierarchical formation of stable nanoscale brush-porphyrin networks. The networks can be disconnected by addition of salt and single porphyrin-decorated cylindrical brush polymers are obtained. These two new morphologies, brush-porphyrin networks and porphyrin-decorated brush polymers, may have potential as functional materials with interesting mechanical and optical properties.

ZUSAMMENFASSUNG

In dieser Arbeit wurden selbst-organisierende Modellsysteme in wässriger Lösung untersucht. Geladene Polymere, sogenannte Polyelektrolyte, wurden mit entgegengesetzt geladenen Ionen in Verbindung gebracht, um supramolekulare Strukturen aufzubauen. Mit abbildenden Methoden, Spektroskopie und Streumethoden wurde untersucht, inwiefern die Struktur der Bausteine die Struktur der selbstorganisierten Systeme beeinflusst. Hierbei wurden Polyelektrolyte mit unterschiedlicher chemischer Struktur, Molekulargewicht und Architektur verwendet. Zusätzlich zu linearen Polyelektrolyten wurden semiflexible zylindrische Bürstenpolymere mit definiertem Durchmesser und relativ hoher Hauptkettenpersistenz untersucht. Den Polyelektrolyten wurden strukturelle organische Gegenionen mit der Ladungszahl eins bis vier zugegeben. Insbesondere die Selbstorganisation von Polyelektrolyten mit verschiedenen tetravalenten und wasserlöslichen Porphyrinen wurde untersucht. Porphyrine haben eine steife aromatische Struktur, die einen strukturellen Effekt auf ihr Verhalten bei der Selbstorganisation hat und durch diese Porphyrine die Möglichkeit besitzen durch π-π Wechselwirkungen zu aggregieren. Der Hauptfokus dieser Arbeit liegt in der Selbstorganisation von zylindrischen Bürstenpolyelektrolyten mit tetravalenten Porphyrinen. Es konnte gezeigt werden, dass die Zugabe von Porphyrinen zu entgegengesetzt geladenen Bürstenpolymeren zu einem hierarchischen Aufbau von stabilen, nanoskaligen Bürsten-Porphyrin Netzwerken führt. Die Netzwerkverbindungen können durch Zugabe von Salz gelöst werden und einzelne Porphyrin-beladene, zylindrische Bürstenpolymere werden erhalten. Diese beiden neuen Strukturen, Bürsten-Porphyrin Netzwerke und Porphyrin-beladene Bürstenpolymere, haben Potential als funktionelle Materialien mit interessanten mechanischen und optischen Eigenschaften.

TABLE OF CONTENTS

Page

CHAPTER

APPENDICES

CHAPTER 1

1 INTRODUCTION

Sometimes the views of people seem to be quite different: an artist that paints landscape motifs will see the beauty in the big picture; maybe he will be especially attracted by a nice combination of green trees at a blue lake surrounded by an astonishing mountain view. However, in the microscope view of a scientist a single living cell can be really beautiful as well. Many researchers admire the shear complexity and functionality of biological systems at the molecular level. Not even closely arrived by laboratory experiments the processes steering life on small length scales have been optimized by an unimaginable number of cycles in the course of billions of years.

One example for a process used ubiquitously by nature is called “self-assembly”: “The Science of Things That Put Themselves Together” – as it was quite properly stated in the title of a recent book [1]. Many functional and complex biological systems like DNA-protein complexes and lipid bilayer membranes are built up from smaller units that self-assemble directed by secondary intermolecular interaction forces. The question of just how nature is able to create these complicated systems is a valuable field of research. One goal of this research is to use the rich knowledge of biological systems to build up functional synthetic materials by a facile self-assembly approach. However, natural systems are usually relatively complicated and thus working with self-assembling model systems can be quite useful to get valuable insights into the self-assembly field.

It is necessary to understand how the properties of building units direct the later structure of their supramolecular assemblies. Important factors are chemical structure, molecular shape and the ability to interact via secondary forces [2]. Secondary interactions are crucial in the formation of supramolecular structures. Systems that have been intensively studied involved amphiphilic association (e.g. surfactants) [3-7], hydrogen bonding [3-6], metal coordination [7], and ionic interaction [8-11].

The polymers of nature like DNA and proteins are water-soluble due to charged units and these charged polymers, polyelectrolytes, are important building units in biological self-assembly processes. In aqueous synthetic model systems therefore the self-assembly of polyelectrolytes to supramolecular structures has been extensively studied [12-18]. Naturally, here ionic interactions play a dominant role.

However, self-assembly processes usually involve a combination of several secondary interactions. A very interesting approach is the formation of supramolecular assemblies by polyelectrolyte complexation with water-soluble organic dyes. Here, ionic interactions of charged dye groups with polyelectrolyte charges are combined with inter-dye π-π interactions. It has been shown that due to their rigid structure with well defined geometry, aromatic dyes represent a suitable building block to study self-assembly processes [19-27]. In addition, the spectroscopic properties of dyes provide an extra method to study inter-dye interaction that is not available e.g. for surfactants or simple salt ions. This thesis is intended to expand the knowledge of polyelectrolyte-dye assembly in aqueous solution.

In particular, this study focuses on polyelectrolyte complexation with water-soluble porphyrin molecules. Porphyrins are dyes with an extended aromatic system that are capable of extensive self-aggregation via π-π stacking. Porphyrin stacks have potential applications as antennae in photosynthetic model systems [28-31] and photosensitizers for photodynamic therapy of cancer diseases [32-34]. For both the mentioned applications porphyrin self-aggregation on polyelectrolyte templates is of large interest. In antennae, templates may direct porphyrin aggregation to more defined and controlled states. In photodynamic therapy, interaction of porphyrin molecules with charged biopolymers is actually taking place in the target tissue. Thus, a more fundamental understanding of polyelectrolyte-porphyrin interaction is naturally important here.

Porphyrins can be easily manipulated by pH equilibria and metal insertion and thus this enables additional options in studying their assembly behavior. In this thesis the influence of porphyrin molecular structure, pH and central metal on polyelectrolyte complexation was studied.

In addition to the influence of porphyrin structure, this thesis also focuses on the influence of polyelectrolyte chemical structure, architecture and size. Specifically, polyelectrolyte building blocks in the shape of semi-flexible cylinders, polyelectrolyte bottle brushes, were investigated in comparison to linear and flexible polyelectrolytes. The cylindrical shape is expected to influence the structure of supramolecular assemblies.

CHAPTER 2

2 THEORY & METHODS

2.1 Methods to Study Polyelectrolyte Complexation

2.1.1 Light Scattering

Light scattering is a powerful characterization method that can reveal information of size, mass and shape of particles. The information of interest is encoded in the light scattered from a diluted sample solution. The usual setup is depicted in Figure 2.1: an optical system focuses a laser beam on the sample solution and a detection system on a goniometer arm measures the scattered light at different angles. The method is noninvasive and in contrast to many imaging techniques truly detects the solution properties of a sample. This section will give a short and practical overview of the light scattering method, for details of theory and further applications the reader is referred to the respective text books [35-38].

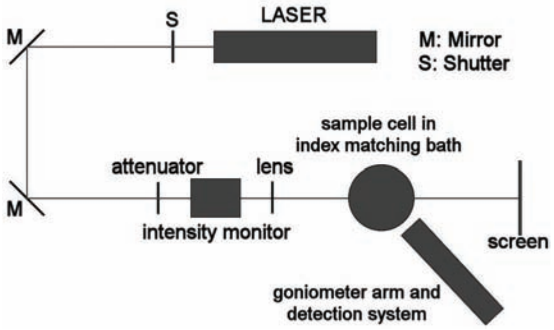

Figure 2.1: Scheme of light scattering setup.

Light scattering is operated in two modes: in static light scattering (SLS) the average scattering intensity of the sample (sample scattering minus solvent) is measured, whereas in dynamic light scattering (DLS) the time fluctuations of scattered light are evaluated. In SLS angle dependent data is analyzed and the extracted variables are: weight average molecular mass M_w, second virial coefficient of osmotic pressure A_2 and radius of gyration R_g. In DLS the diffusion coefficient of a particle and thus its hydrodynamic radius R_h can be determined.

Static Light Scattering

Equation 2.1 is central to SLS measurements. Here R(q) represents the Rayleigh ratio that is used as a measure for the normalized intensity of scattered light.

$$R(q) = \frac{(I_s(q) - I_{sol}(q))r^2}{I_0} = \frac{(I_s(q) - I_{sol}(q))}{I_{tol}(q)} I_{tol,abs} \qquad (2.1)$$

The Rayleigh ratio is computed by first subtracting solvent scattering $I_{sol}(q)$ from sample scattering $I_s(q)$ to obtain the scattering intensity of the particles in solution. Then it is normalized with the distance r from sample to detector and incident laser intensity I_0 so that R(q) becomes independent on the actual instrumentation. Since the accurate measurement of r is problematic, the instrumentation is usually calibrated with a toluene standard instead. As shown in eq. 2.1 the measured scattering intensity of toluene $I_{tol}(q)$ is used in combination with a literature value for toluene scattering $I_{tol,abs}$. The letter q in eq. 2.1 denotes the scattering vector of the measurement. The scattering vector is defined by the difference between wave vectors of scattered (**k**) and incident light ($\mathbf{k_0}$) and is directly related to the scattering angle θ as given in eq. 2.2.

$$|\mathbf{q}| = |\mathbf{k} - \mathbf{k_0}| = \frac{4\pi n}{\lambda_0} \sin\left(\frac{\theta}{2}\right) \qquad (2.2)$$

The Rayleigh ratio can be derived from fluctuation theory and thermodynamics as given in eq. 2.3. The equation includes the partial derivative of refractive index n with respect to concentration c since contrast of scattered light is given by concentration fluctuations of the refractive index.

$$R(q) = \frac{4\pi^2 n_0^2}{\lambda_0^4 N_A} \left(\frac{\partial n}{\partial c}\right)^2 cRT \left(\frac{\partial c}{\partial \Pi}\right) S(q) \qquad (2.3)$$

The osmotic pressure Π in eq. 2.3 can be expanded to a virial equation for diluted solutions as given in eq. 2.4 where M is the molecular weight of the polymer and A_2 and A_3 are the virial coefficients that contain information about the quality of the solvent.

$$\Pi = RT\left(\frac{c}{M} + A_2 c^2 + A_3 c^3 + \ldots\right) \qquad (2.4)$$

Eq. 2.3 also contains the structure factor S(q) of the investigated sample that contains information about the spatial distribution of a sample polymer and the angle dependent interference effects thereof (eq. 2.5). The structure factor S(q) can be partitioned in an intermolecular part $S_{inter}(q)$ that describes the distribution of independent macromolecules in solution and an intramolecular part P(q) (eq. 2.5) that describes the distribution of the polymer segments within the macromolecule. In dilute solution and for isotropically distributed molecules intermolecular contributions are negligible and thus the intermolecular structure factor $S_{inter}(q)$ approaches unity. Thus, S(q) in eq. 2.3 may be approximated by the form factor P(q) that contains information of the shape and size of the investigated macromolecule encoded in interference effects that are resolvable by detecting light scattered at multiple angles. An extrapolation to small angles and thus small q allows for a series expansion of P(q) as given in eq. 2.6.

$$S(q) = \sum_i \sum_j \left\langle \exp(iqr_{ij}) \right\rangle = S_{\text{inter}}(q)P(q) \qquad (2.5)$$

$$P(q) = 1 - \frac{1}{3} q^2 < R_g^2 > \qquad (2.6)$$

Assuming A_3 of eq. 2.4 is zero, the combination of equations 2.3, 2.4 and 2.6 results in the well-known Zimm equation (eq. 2.7) where K is the optical constant defined by eq. 2.8. In a Zimm-plot SLS data is plotted both versus scattering vector q and concentration c and thus R_g and A_2 can be extracted from the slopes as well as the weight average of molecular mass M_w from the intercept.

$$\frac{Kc}{R(q)} = \frac{1}{M_w}(1 + \frac{1}{3} < R_g^2 >_z q^2) + 2A_2 c \qquad (2.7)$$

$$K = \frac{4\pi^2 n_0^2}{\lambda_0^4 N_A} \left(\frac{\partial n}{\partial c} \right)^2 \qquad (2.8)$$

Dynamic Light Scattering

In static light scattering it is assumed that the scattered light has the same frequency than the incident beam (elastic scattering). However, the frequency spectrum of scattered light besides its elastic average shows a broadening in comparison to the sharp spectrum of incident light. This broadening can be described as a Doppler effect due to the Brownian movement of scattering particles. The line width depends on the speed of sample molecules which in turn depends on temperature and molecule size. Instead of directly measuring the frequency shift with an interferometer it is easier to correlate time dependent fluctuations of the scattered light with DLS. The time autocorrelation function $g_2(\tau)$ of scattering intensity (eq. 2.9; τ is the relaxation time in the autocorrelation function) is the Fourier transform of the frequency spectrum and thus contains information of the speed of sample particles.

$$g_2(\tau) = \langle I(0)I(\tau) \rangle \qquad (2.9)$$

Via Siegert relation the measured intensity autocorrelation function is converted to $g_1(\tau)$: the field correlation function (eq. 2.10; A: base line of $g_2(\tau)$). The field autocorrelation function shows an exponential decay and is directly related to the diffusion coefficient D of the macromolecule (eq. 2.11, eq. 2.12; Γ is the relaxation rate of the autocorrelation function; B is the signal-to-noise ratio). The larger a particle and thus the lower its diffusion coefficient D is, the more $g_1(\tau)$ will be shifted to longer relaxation times.

$$g_1(\tau) = \sqrt{\frac{g_2(\tau) - A}{A}} \qquad (2.10)$$

$$g_1(\tau) = B \exp(-\Gamma \tau) \qquad (2.11)$$

$$\Gamma = \frac{1}{\tau} = q^2 D \qquad (2.12)$$

The expression in eq. 2.11 describes a monoexponential decay function which is only valid if the sample particles show only one uniform diffusion coefficient. However, especially synthetic polymers usually exhibit a polydisperse size distribution. Thus, for such samples an average of many exponentials is obtained. It can be shown that the measured function is a z-average as given in eq. 2.13 (m_i, M_i: mass and molecular weight of indexed particle). and thus also the z-average of the diffusion coefficient is measured.

$$g_1(\tau) = B \frac{\sum m_i M_i \exp(-q^2 D_i \tau)}{\sum m_i M_i} \qquad (2.13)$$

The extracted diffusion coefficient D_z is both dependent on angle and concentration and has to be extrapolated to the self-diffusion coefficient $D_{z,0}$ for zero angle and concentration. Via Stokes-Einstein relationship the hydrodynamic radius R_h can then be calculated as in eq. 2.14 (for a given size of a particle the diffusion coefficient is both dependent on temperature T and viscosity η).

$$R_h = \left\langle \frac{1}{R_h} \right\rangle_z^{-1} = \frac{k_B T}{6\pi\eta D_{z,0}} \qquad (2.14)$$

There are several methods to analyze field correlation functions. Presumably the most basic method is the so-called cumulant expansion. Here the natural logarithm of $g_1(\tau)$ is plotted versus time. Evidently, for a monoexponential function as in eq. 2.11 this would give a straight line with slope Γ. If due to polydispersity several exponential functions contribute to $g_1(\tau)$ the plot deviates from linearity and gets bended upwards. The function then can be fitted by a polynomial with least adequate degree; often a polynomial of second order yields satisfactory fitting quality. In the cumulant method a Taylor expansion of $\ln(g_1(\tau))$ is conducted. As can be seen in eq. 2.15 the linear coefficient of the series, the so-called first cumulant is equal to the relaxation rate Γ (Γ, μ_2, μ_3: first, second and third cumulant). Thus, the diffusion coefficient can be calculated from the linear coefficient of the polynomial fit.

$$\ln(g_1(\tau)) = -\Gamma\tau + \frac{\mu_2}{2}\tau^2 - \frac{\mu_3}{6}\tau^3 + \ldots \qquad (2.15)$$

The ratio of the second-order to the first-order coefficient for a polynomial fit will reveal the degree of upward-bending and thus will give a measure of polydispersity of the sample. Thus, PDI_{cum} as defined in eq. 2.16 can be used to compare polydispersities of different samples.

$$PDI_{cum} = \frac{\mu_2}{(\Gamma)^2} \qquad (2.16)$$

Dynamic Light Scattering of Polyelectrolytes

Polyelectrolytes are charged polymers that are soluble in aqueous solution. Generally, polymer analysis methods for the characterization of polyelectrolytes are carried out in aqueous salt solution with similar ease as with uncharged polymers. However, in aqueous solutions with low or no salt unusual effects for several measurement techniques have been observed that are summed up by the term “polyelectrolyte effects”. For example, it was shown that in salt-free solution the viscosity of polyelectrolytes can actually rise for low concentrations. For an overview and details of the solution properties of polyelectrolytes the reader is referred to the literature [39-40]. Here a short introduction to the behavior of polyelectrolytes in dynamic light scattering is given.

DLS investigations in literature of quaternized poly(vinyl pyridine) (PVP) in salt-free aqueous solutions yielded two-step correlation functions as shown in Figure 2.2. However, if salt is added to the same sample, the two modes fuse into a single decay.

Figure 2.3 summarizes several experiments from the same investigations where the salt concentration is varied. For high salt concentrations a single diffusion coefficient was observed as it would be also the case for the unquaternized and thus uncharged PVP precursor in an organic solvent. If the salt concentration is lowered, a new mode with substantially lower diffusion coefficient as in Figure 2.2 is detected. This new mode is called “slow-mode” and often explained by domains of polyelectrolytes that are formed due to the long-range electrostatic interaction potential in the absence of salt.

Very interestingly, the mode with the higher diffusion coefficient, the “fast-mode”, is also changed by lowering the salt concentration. Evidently from Figure 2.3, the diffusion coefficient increases for lower salt content. The investigated polyelectrolyte molecule thus moves faster in salt-free conditions. This is due to the coupled motion of polyelectrolytes and counterions [39]. While at high salt concentrations the measured diffusion coefficient describes pure self-diffusion due to Brownian motion, there is an additional self-accelerating component present at low salt concentration. In consequence, eq. 2.14 is only applicable if no slow-mode is present and in addition the fast-mode is not accelerated.

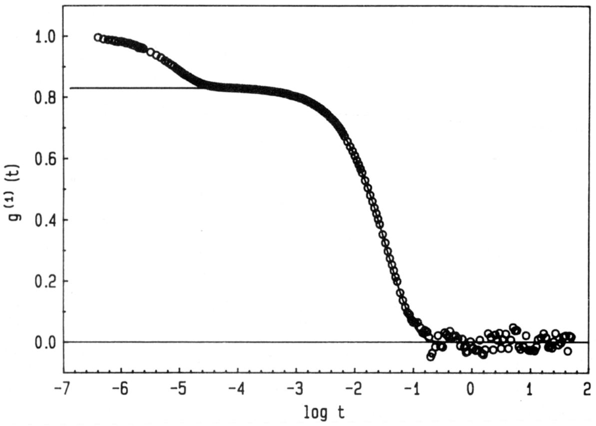

Figure 2.2: Correlation function of quaternized PVP in salt-free water as reported in [40].

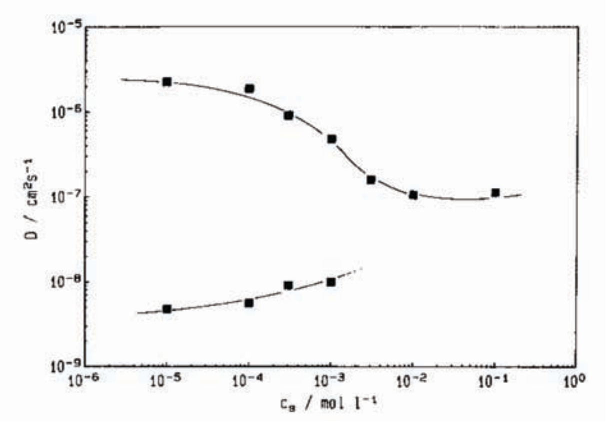

Figure 2.3: Diffusion coefficients for PVP in aqueous solution extrapolated to zero angle, lower branch: slow mode, upper branch: fast mode, as reported in [40].

2.1.2 Atomic Force Microscopy

Atomic force microscopy (AFM) is an imaging method with possible resolution below 10 nm. In contrast to microscopy methods, the surface is not imaged with the help of optical systems but by mechanically scanning the surface with a tip. The principal setup is shown in Figure 2.4: a cantilever containing a very sharp tip (tip radius < 10 nm) is scanned over a surface by a Piezo element. According to the topography of the surface the cantilever will be bended up and down during scanning. In order to measure the deflection of the cantilever a laser is focused on its backside and on the center of a four-segment diode. From the measured deflection of the cantilever the topographic information of scanned lines can be computed to a three-dimensional height image of the surface.

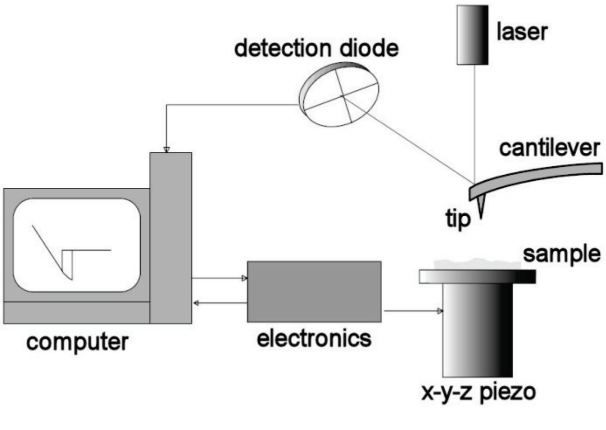

Figure 2.4: Schematic representation of AFM setup.

There are two main operating modes in AFM: in contact mode the tip is always close to the surface and scanning proceeds in just the same way one would intuitively scan his or her palm with a finger. In this mode highest resolution can be obtained, however, the tip can easily damage soft surfaces. Thus, this mode often is used for metals. For soft biological or polymeric material another less damaging mode is more suitable: in tapping mode the cantilever is oscillated close to its resonance frequency and thus gets in direct contact to the surface once per oscillation cycle. This mode still gives topological height information but due to the reduced direct contact is less destructive. Interestingly, this oscillational mode provides the so-called phase image in addition to a height image. Here changes in the phase of the oscillating cantilever occur due to the stickiness of the material for the cantilever. Thus, phase images contain information about material properties in addition to a height profile.

2.2 Porphyrins

2.2.1 The Absorption Spectrum of Porphyrins

The family of porphyrins and similar molecules is relatively versatile. There are prominent examples in nature as well as extensively studied synthetic porphyrin molecules. The two most famous natural porphyrin representatives presumably are hemoglobin that is responsible for oxygen transport in our blood as well as for its red color and chlorophyll that is the green pigment of plants responsible for catching the sun light and thus for the biological uptake of our predominant energy source.

So why is blood red and grass green? The reason lies in the sensitivity of light absorption spectra of porphyrins and their derivatives on their molecular structure. In this particular case chlorophyll lacks one double bond in its porphyrin ring if compared to hemoglobin (and thus is called a chlorin) and it is possible to explain the different colors by different electron delocalization pathways. Since the present text is not intended to give an extensive review of porphyrin spectra but rather focuses on a small part of the large spectrum of porphyrins the reader is referred to excellent literature overviews [41-42].

A porphyrin ring is a planar aromatic system with 22 π–electrons. However, it has been shown that only 18 electrons are conjugated (see Figure 2.5) and thus the number is according to Hückels famous 4n+2 rule for aromatic systems.

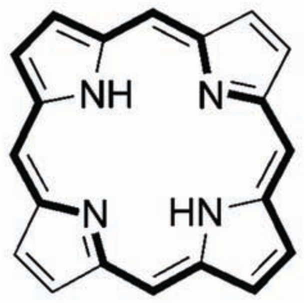

Figure 2.5: Molecular structure and π-electron conjugation of a porphyrin ring.

In this thesis the focus is set on synthetic water-soluble and meso-substituted porphyrins, where “meso” indicates the positions of the ring that bridge the four pyrrol rings. The solubility in water is achieved by charged groups that are attached to phenyl groups at the porphyrin meso positions. One example is the porphyrin TAPP that is depicted in Figure 2.6 and that is investigated in detail within this text. The porphyrin has four charged trimethylammonium groups attached to its tetraphenylporphyrin basic structure. Generally, free porphyrin molecules can act as a chelating ligand to most metal ions. Thus, it has to be differentiated between metal-free porphyrins and metalloporphyrins. One example of a metalloporphyrin is ZnTAPP: a TAPP derivative where Zn^{2+} was incorporated. Figure 2.6 gives the molecular structures of both TAPP and ZnTAPP. Evidently, the symmetry is changed upon metal addition. Whereas TAPP can be described by point group D_{2h}, ZnTAPP has higher symmetry: D_{4h}. In addition, measured UV-vis spectra of both ZnTAPP and TAPP are given in Figure 2.6 and the exhibited pattern is well documented in literature: D_{4h} porphyrins show less bands than D_{2h}. For a systematic approach first the spectrum of more symmetric ZnTAPP will be discussed. Two domains are visible: an extremely strong band at around 400-430 nm, usually referred to as “B-band” or “Soret-band” and weaker signals in the visible region (~500-650 nm) called the “Q-band”. Here the Q-signals are attributed to π-π* transitions of $S_o \rightarrow S_1$ whereas the B-band results from much more intense $S_o \rightarrow S_2$ transitions [41,43]. In well resolved metalloporphyrin spectra both for the Q-band and the B-band two vibrational modes can be seen (right spectrum in Figure 2.6).

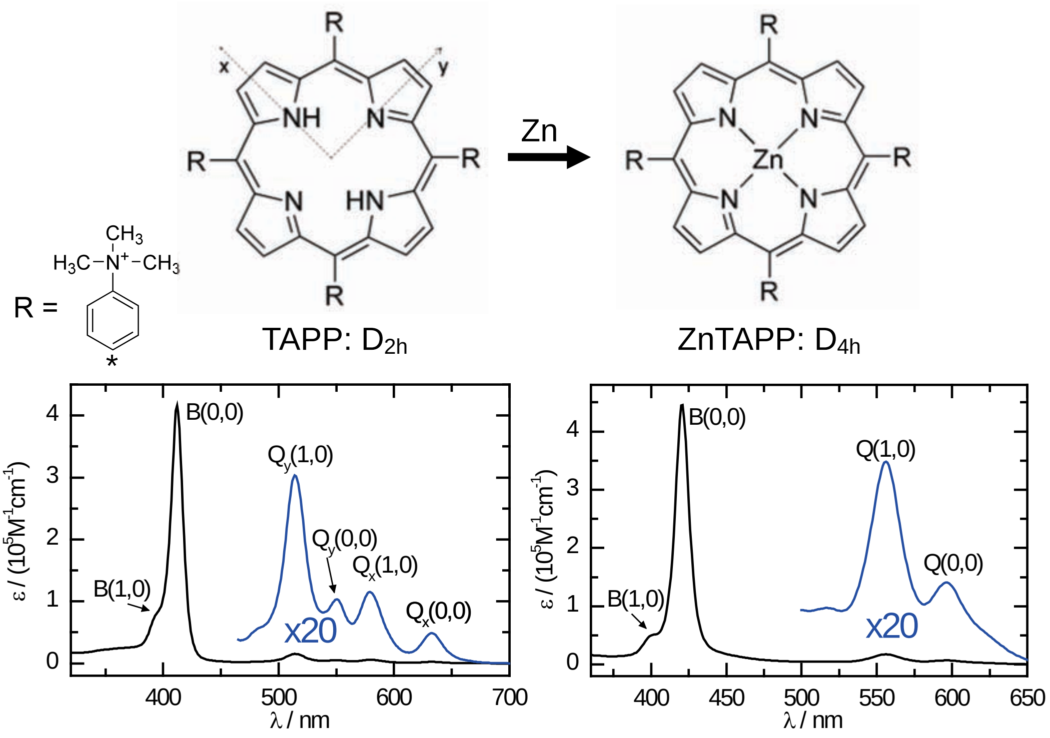

Figure 2.6: Molecular structure and UV-vis absorption spectrum in aqueous solution of porphyrins TAPP and ZnTAPP.

For metal-free porphyrins the two axes depicted in Figure 2.6 are not same as it is the case for metalloporphyrins. It has been shown that therefore the Q-bands split in Q_x and Q_y transitions and that for the B-band the B_x and B_y components are degenerate [43]. Thus, metal-free porphyrin TAPP shows its characteristic 4-band Q-spectrum.

Structure analysis of tetraphenylporphyrins revealed that the phenyl rings are orthogonal to the inner porphyrin ring (see Figure 2.7-a) in the free base porphyrin. However, if by addition of acids the two inner nitrogen bases are protonated, the resulting porphyrin dication exhibits a strongly distorted structure: parts of porphyrin pyrrol rings twist out of the porphyrin plane as well as the meso-substituted phenyl groups rotate closer to planarity with the porphyrin ring [42]. It has been shown that still porphyrin dications exhibit S_4 geometry and thus show similar spectra than the correspondent D_{4h} metalloporphyrins with two Q-bands. However, whereas upon metal addition the B-band of porphyrins is usually not much affected, porphyrin dications regularly show a red shift in the B-band due to the ring distortions [43].

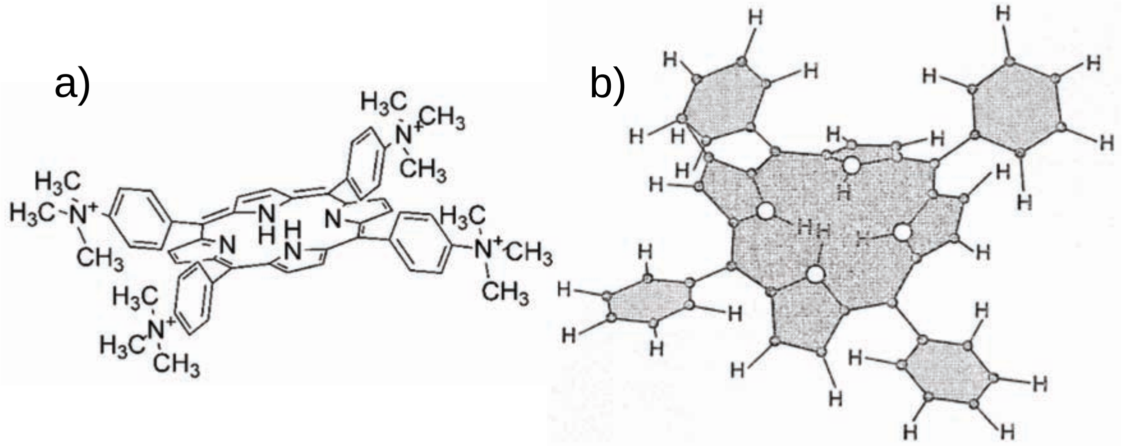

Figure 2.7: Conformation of a) TAPP in neutral state and b) tetraphenylporphyrin as protonated porphyrin dication; b) from [42].

2.2.2 Porphyrin Aggregation

It is well reported in literature that the Soret signal of porphyrins is very sensitive to perturbations of their electronic structure and thus can indicate self-aggregation of the chromophores [44-49]. Several external influences may promote self-aggregation of water-soluble porphyrin molecules. The thorough understanding of these influences is crucial for the characterization of porphyrin-polyelectrolyte interactions and thus is the of the macrocycle π-systems. For water-soluble porphyrins charge repulsion is the most influential factor for preventing self-aggregation since this repulsion force counteracts the attractive π-π interaction. Therefore, especially such factors that control the state and effective strength of porphyrin charge will affect aggregation behavior. In particular, the main factors are pH of the solution, porphyrin concentration and ionic strength.

It is well reported in literature that divalent porphyrin ions have a much stronger self-aggregation tendency than their tetravalent counterparts since the former porphyrin species exhibits less charge self-repulsion [50]. In this context, it is necessary to consider protonation/deprotonation equilibria of porphyrins dependent on the solution pH. In order to simplify such investigations of acid/base processes, the following experiments will focus on porphyrin molecules with four peripheral charge centers that have a fixed charge state independent of pH. Considering the chemical structure of charge sites, quaternary ammonium salts for positive and sulfonic acid groups for negative charges are employed. Typical examples such as *meso*-tetrakis(4-(trimethyl-ammonium)phenyl)-porphyrin (TAPP) and *meso*-tetrakis(4-sulfonatophenyl)porphyrin

(TPPS) are depicted in Figure 2.8.

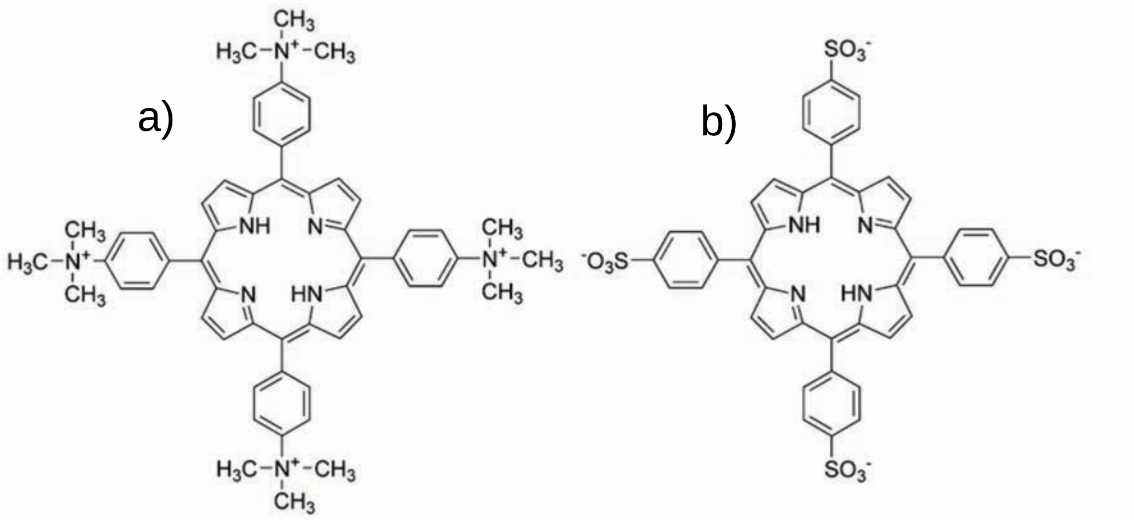

Figure 2.8: Molecular structure of TAPP (a) and TPPS (b).

Even though the peripheral charges of the employed porphyrins are pH independent, there are possible acid/base equilibria in the porphyrin center as it is schematically illustrated in Figure 2.9.

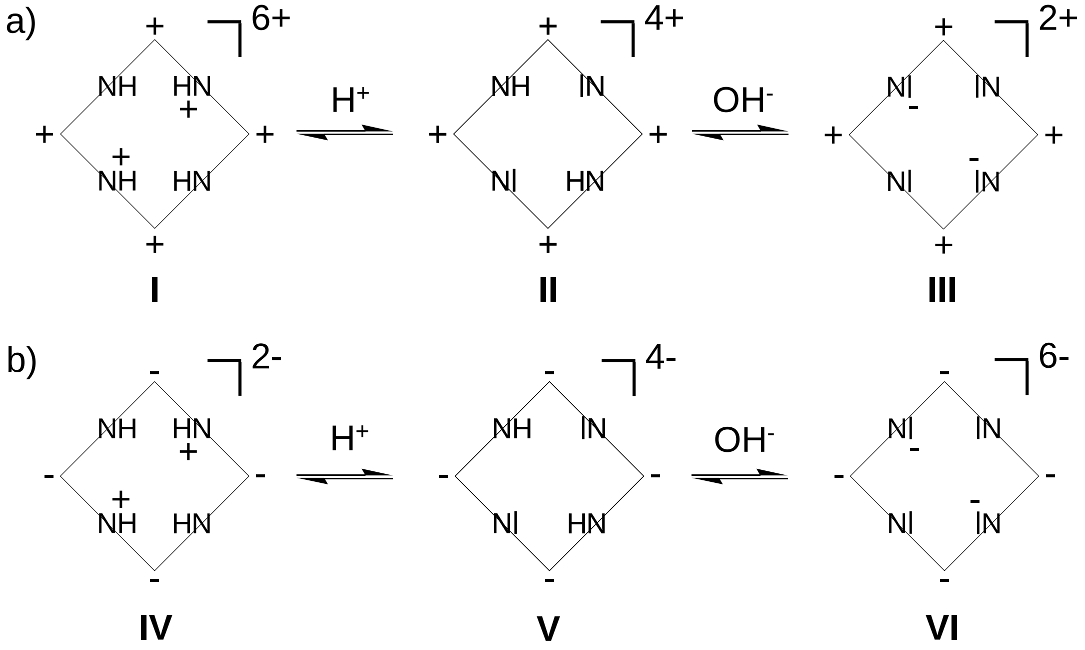

Figure 2.9 Charge states of tetravalent porphyrins at different pH.

In neutral conditions (pH ~7) - where most of the studies within this research are conducted - tetravalent species **II** and **V** in Figure 2.9 are the prevalent states of positive TAPP and negative TPPS, respectively. The crucial point to notice in Figure 2.9 is that the porphyrin total charge can be tuned by the protonation state of the inner nitrogen centers. Of primary interest within the present investigations are charge manipulations that “switch” between valencies four and two. That is because in charge mediated aggregation processes there is a strong difference of the behavior of building blocks being divalent to such entities with a multivalent functionality. Multivalent counterions, for example, are reported to induce DNA condensation [51-52], whereas divalent counterions do not exhibit a pronounced activity in aggregating DNA at stoichiometric conditions but are effective only at high excess [53].

It is relatively simple to protonate the inner two nitrogen bases of a porphyrin cycle, and species **I** or **IV** will be present at strong acidic conditions (e.g. pH ~2). Thus, the tetravalent and negatively charged TPPS encounters an overall valency decrease from four to two in acidic medium (**IV**, Figure 2.9b). Species **IV** is an extensively studied porphyrin and its self-assembly behavior to porphyrin J-aggregates at $pH \leq 2$ is well reported in literature [45-46,54-55]. The aggregates show extensive electronic communication of a large number of porphyrin centers and exhibit rodlike morphology as revealed by imaging methods. It is concluded that besides the factor of reduced charge valency the zwitterionic character of **IV** mainly influences this aggregation behavior. Here the positively charged porphyrin center of one molecule may interact with the negative sulfonic acid group of another entity and thus this intermolecular charge interaction promotes aggregation.

In addition to the effect this charge reduction may have on TPPS self-aggregation, it is quite interesting to note that it will also be important for the behavior of the porphyrin as a linker agent in the presence of polyelectrolytes. The molecule is “switched” from a multivalent to a divalent state and thus should have a lower capability of interconnecting polyelectrolyte molecules. This will be addressed in chapter 7.

As illustrated in Figure 2.9, there is also another theoretically feasible path of influencing total porphyrin charge by deprotonating the R_2NH groups. For water-soluble porphyrins this is a much more difficult task than the previously discussed protonation of the nitrogen bases. The corresponding base of R_2NH (that is R_2N^-) is considerably stronger than OH^- und thus in common aqueous bases like sodium hydroxide the R_2NH function will clearly dominate [56-57]. There is to the best knowledge of the author no report of the deprotonation of porphyrin TAPP (Figure 2.8) in aqueous solutions in literature. Accordingly, also no proof of its deprotonation in strong basic and aqueous conditions could be found as will be reported below. Nevertheless, it is of general interest here that the deprotonation of the R_2NH groups of a positively charged tetravalent porphyrin ion may lead to a charge switch from four to two (**II** → **III**) in analogy to the previously described protonation of a negatively charged porphyrin and this idea will be addressed in section 5.3.

CHAPTER 3

3 COMPLEXATION OF PSS BRUSHES WITH NONAROMATIC STRUCTURAL COUNTERIONS

In several parts of this thesis the complexation of cylindrical polyelectrolytes brushes with different counterions is studied. Polyelectrolyte brushes consist of charged polymeric side chains connected to a polymer backbone that force this backbone to adopt a more elongated conformation than in an usual polymer coil, resulting in semi-flexible cylindrical molecules (Figure 3.1) [58-69].

In literature it is reported that the elongated conformation of cylindrical polymer brushes can be affected by different stimuli. Conformational changes of worm-like polyelectrolyte brushes have been observed for example for poly(L-lysine) bottle brushes upon addition of the surfactant sodium dodecylsulfate (SDS): semi-flexible cylindrical molecules in the absence of SDS transform to helical structures at intermediate brush-to-surfactant ratios and collapse in access of surfactant conditions [70-71]. A further report shows the transition from cylindrical to globular shape for brush molecules having poly-N-isopropylacrylamide (PNIPAM) side chains when the temperature is raised above the lower critical solution temperature (LCST) of PNIPAM [72]. A rodlike to globular transition for cylindrical brush molecules deposited on mica surfaces was also observed driven by a combination of solvent and surface effects [73-74]. For cylindrical brush polymers with copolymeric molecular structure consisting of both PVP and PMMA side chains, solvent induced shape variations from elongated cylinders to strongly curved “horseshoe” and “meander like” structures were reported [75].

The effect of external salt stimuli on the conformation of cylindrical polyelectrolyte brushes is directly related to the effect of the respective stimulus on the brush side chains [65,76]. If the extended side chains of a cylindrical polymer brush collapse, the elongated state of the brush will collapse as well. It is known from literature that the extension of charged polymeric chains within a brush layer can be both affected by the grafting density of the chains within the layer as well as on salt effects on charged chains [65,77-79]. However, it was reported for cylindrical polyelectrolyte brushes with very high grafting densities that side chain extension and thus overall brush size is mostly unaffected by the charge state of the side chains [65]. The brush molecules described therein were prepared via the polymerization of macromonomers (“grafting through”) and thus each main chain monomer carries a polymeric side chain. For such cylindrical brushes with high grafting densities that are also used in the experimental studies of this thesis (e.g. from PVP or PSS) no significant dimensional variations are detected upon charging the side chains and upon addition of monovalent salt [65].

Differently from this observation, it was recently reported that poly((2-(methacryloyloxy)ethyl) trimethylammonium iodide) (PMETAI) cylindrical polyelectrolyte brushes evidently collapse upon addition of relatively high monovalent salt concentrations (~0.5 M) [80]. The different observations may presumably be explained by the lower grafting density of the described material. Here only 50% of the main chain monomers are functionalized by side chains (the brush molecules were synthesized by the grafting from approach) and thus sterical crowding of side chains is less pronounced allowing for a stronger effect of salt on their swelling. Addition of divalent and trivalent salt to the same PMETAI brush molecules was reported to induce a collapse at much lower salt concentrations (at around stoichiometric conditions) [81]. At pre-stoichiometric salt concentrations formation of helices were observed [81], similarly to the observations in [70].

In this chapter the interaction of counterions of different valency with highly grafted polyelectrolyte brushes is studied. Poly(styrene sulfonate) bottle brushes investigated in this chapter are described in appendix A.1. The light scattering analysis of the brushes in salt-free water is also given in the appendix and yielded radii of $R_g = 50.0$ and $R_h = 37.8$. It is one goal of the present text to investigate how structural counterions may be able to interconnect brush molecules to supramolecular aggregates. Therefore, it is certainly interesting to both investigate the influence of the molecular structure of counterions as well as of their charge valency on the aggregation process.

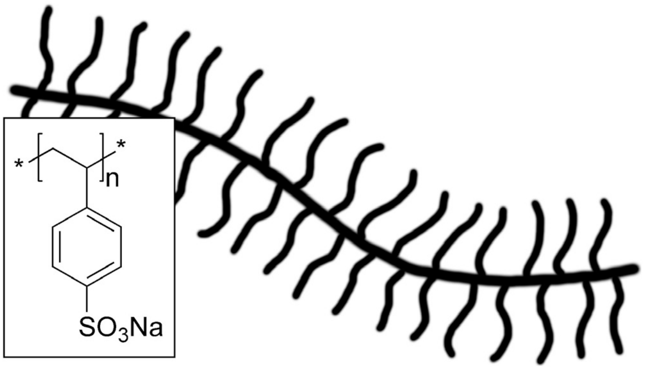

Figure 3.1: Schematic presentation of negatively charged PSS bottle brush.

In studies of the author preceding the present thesis PSS brush was combined with two model counterions of valency one and two (Figure 3.2): (a) trimethylphenylammonium chloride and (b) *p*-phenylene bis(trimethylammonium tosylate) [82].

They both have positive charges that are independent of pH and the chemical structure of their charge centers was chosen to be very similar to the later studied porphyrin TAPP (Figure 2.8). For both counterions a combination with PSS brush resulted in no size changes in light scattering at charge stoichiometry and even at tenfold counterion excess [23,82]. It was concluded that the counterions are not able to interconnect the brush molecules to supramolecular aggregates at the chosen concentration. Presumably, for the supramolecular assembly of brush polyelectrolytes counterions with valency larger than two are needed and thus such multivalent counterions will be the focus of further studies described here.

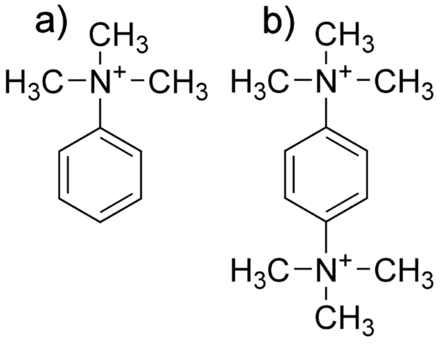

Figure 3.2: Molecular structure of counterions: (a) trimethylphenylammonium chloride and (b) *p*-phenylene bis(trimethylammonium tosylate).

In further experiments the ratio of added counterion to polyelectrolyte plays an important role and thus will be defined here. To compare counterions of different valency the molar concentration of charges will be used in computing the counterion to polyelectrolyte ratio (for the polyelectrolyte generally molar monomer charge concentrations are used, by definition not taking into account a possibly smaller effective charge concentration due to counterion condensation). This charge ratio *l* is defined as:

$$l = \frac{c_{charge}(counterion)}{c_{charge}(polyelectrolyte)} \tag{3.1}$$

For example for the positively charged divalent counterion *p*-phenylene bis(trimethylammonium tosylate) (Figure 3.2) in combination with NaPSS polyelectrolyte the charge ratio is computed by taking the molar charge concentration of the counterion (that is twice the concentration of the divalent counterion) and dividing it by the molar concentration of monovalent styrene sulfonate monomer.

In an extension to the experiments with the counterions depicted in Figure 3.2, the tetravalent counterion C6T^{4+} (4,4′-(hexane-1,6-diyl)bis(1-ethyl-1,4-diazoniabicyclo [2.2.2]octane) was studied (Figure 3.3) [22]. In contrast to tetravalent porphyrins that were introduced in section 2.2, C6T^{4+} does not contain aromatic units. It is of general interest in this thesis whether a) C6T^{4+} acts differently than a divalent counterion due to its higher charge number and b) if for the tetravalent case it makes a difference if the counterion is aromatic or not.

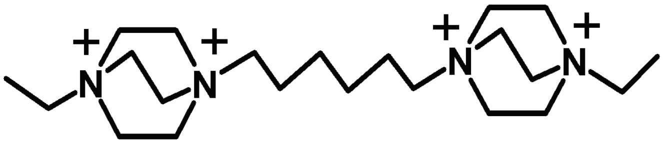

Figure 3.3: Molecular structure of C6T^{4+}.

The addition of counterion C6T^{4+} in charge ratios where there is an excess of PSS brush ($l < 1$) leads to size changes in light scattering. This is in strong contrast to the behavior of mono- and divalent counterions discussed above where addition of counterion does not affect brush size at the chosen relative concentrations. As can be seen from Figure 3.4, already at a charge ratio $l = 0.2$ different radii were measured with light scattering. When the brush concentration was fixed (c = 50 mg/L) and the counterion was added at different charge ratios an intriguing result was obtained. At stoichiometric charge ratios of counterion to brush (*l* = 1) there is a pronounced size reduction from R_g = 50 nm to R_g = 22.9 nm.

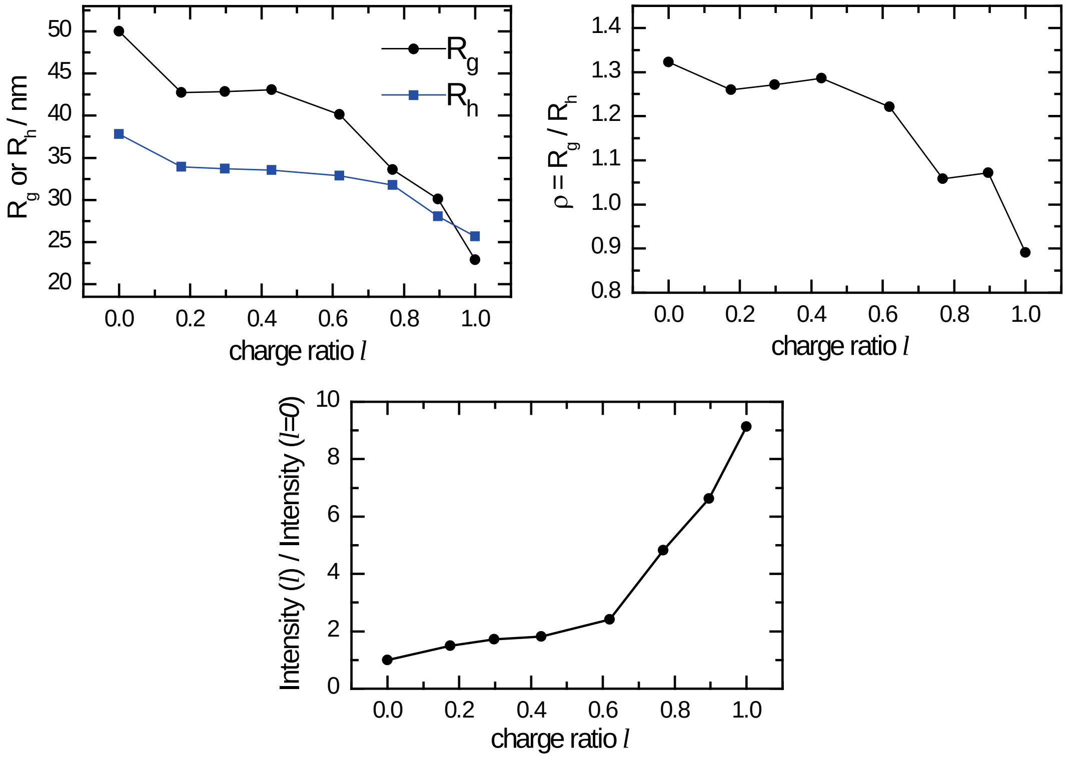

Figure 3.4: Light scattering results for samples with fixed NaPSS brush and different C6T^{4+} content. The charge ratio *l* is 0 for pure PSS brush and *1* for a 1:1 mixture (laser wavelength λ = 632.8 nm).

The reduction of R_h is less severe than the one of R_g and the characteristic ratio $\rho = R_g/R_h$ is strongly affected by counterion addition. It starts at a relatively high value of ρ = 1.3 for the pure brush. This value is considerably higher than the literature value for spheres (ρ = 0.778) due the worm-like appearance of the bottle brush (for an AFM image of PSS brush see Figure A.5; another contribution to the ratio will be the polydispersity of brush molecules due to their length distribution, polydispersity generally increases the ratio ρ). At a charge ratio of *l* = 1 the ratio of the two radii decreases to ρ = 0.89 indicating a more compact morphology of the polyelectrolyte brush.

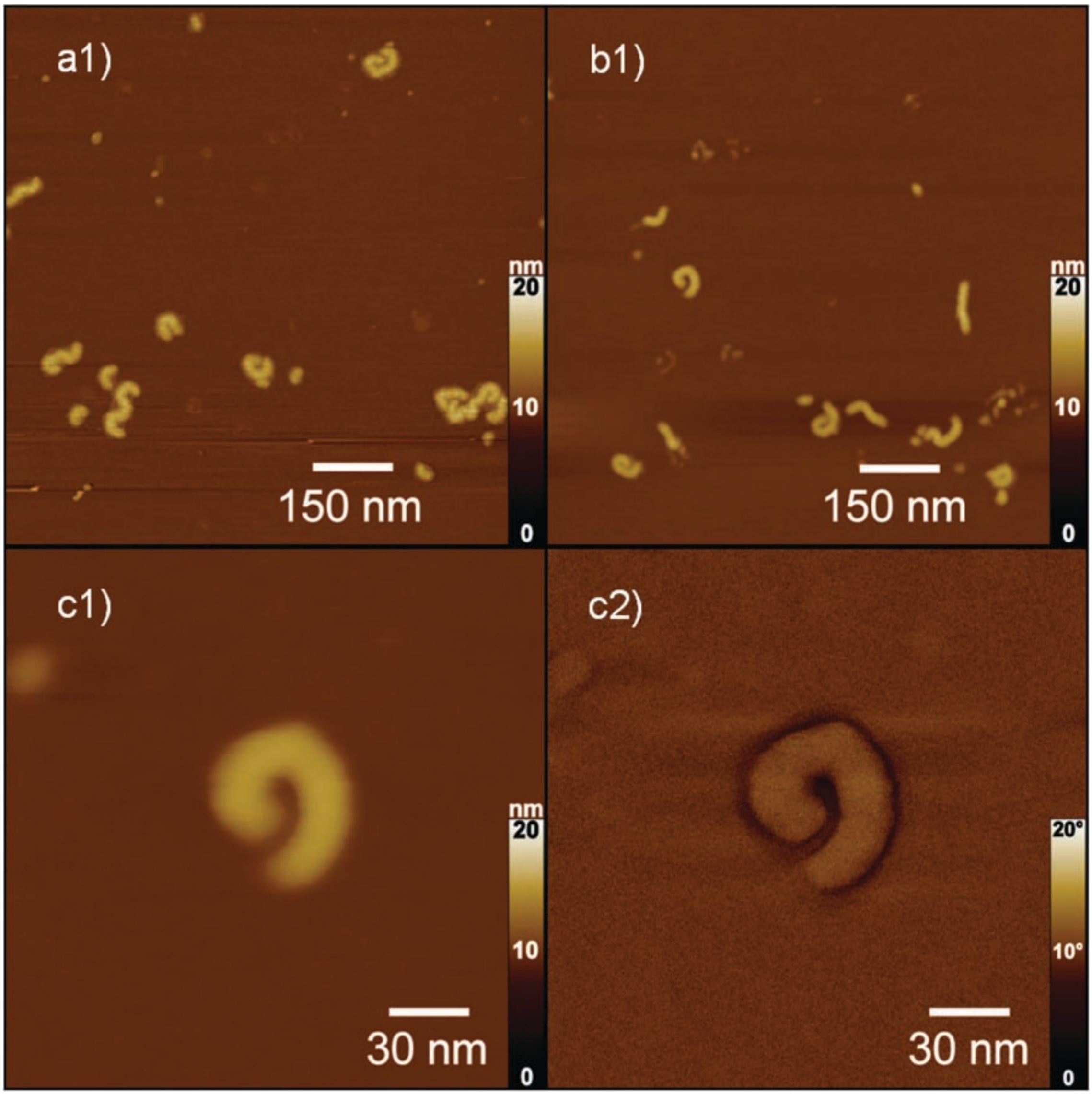

Figure 3.5: AFM height (1) and phase (2) images of PSS brush-C6T^{4+} samples at *l* = 1.

Upon size reduction to R_g = 22.9 nm, the light scattering intensity of the sample increases by a factor of nine. This is an indication that counterions C6T^{4+} bind to the brush molecule (the light scattering intensity of the pure counterion in water at same concentration is close to pure water scattering intensity. This is much lower than brush and complex scattering).

In order to get a better picture of the reasons for the observed radius reduction, the sample at *l* = 1 was imaged by AFM (Figure 3.5). Brush molecules that are predominantly curled are seen in the images. This is in strong contrast for the result of pure PSS brush where much more stretched conformations are seen (Figure A.5). The observation of brush molecules that transfer to a curled state upon C_6T^{4+} addition fits well to the light scattering results in Figure 3.4. Brush molecules that are in curled formation will show a reduced radius of gyration if compared to its extended counterpart. In addition, the reduction of the ratio $\rho = R_g/R_h$ can be well explained by the observed structural change to a more compact structure.

In contrast to literature reports for less highly grafted polyelectrolyte brushes described in the outline of this section [80-81] no collapsed brush structures were observed for the interaction of PSS with C6T^{4+} but rather curled cylinders were observed for the cases with minimal hydrodynamic size. This can be explained by the fact that due to the high side chain density the chains may not collapse due to salt effects. Also the absence of helical structures may be presumably explained by the lower grafting density since the crowding of side chains potentially prohibits the conformational changes needed for helix formation. Actually, it can be seen that the diameter of the brush molecules is not significantly changed but rather the bending of the main chain is increased. Explaining the observed effects, it would be a reasonable conclusion that the tetravalent counterion induces intramolecular linkages in between side chains within the brush molecules that lead to the overall bending of the brush.

Very interestingly, no such curled brush conformations that are observed in this section are seen throughout chapter 5 where PSS brush molecules are combined with the tetravalent porphyrin TAPP (for the molecular structure see Figure 2.8). Besides the observed phenomenon of PSS brush forming supramolecular structures with the porphyrin TAPP that will be discussed in chapter 5, AFM images of brush-porphyrin assemblies generally show extended worm-like conformations very similar to the pure brush (cf. Figure A.5, Figure 5.15 and Figure 5.34). This difference in behavior of the two counterions presumably results from the different molecular structure. Whereas in C6T^{4+} the two DABCO (1,4-Diazabicyclo[2.2.2]octane) cage structures mostly fix the distance of the two charged nitrogen atoms to each other, the distance between the two DABCO units is not fixed due to the flexible hexamethylene bridge (see Figure 3.3). This relative flexibility of charge center positions is in contrast to the situation in porphyrin TAPP where the rigid aromatic porphyrin ring fixes the distance of all charge centers to each other. Another difference of theses two molecules is given by the delocalized π-electrons in the aromatic porphyrin that may lead to electronic interaction with the σ-system of another porphyrin molecule [83] (this interaction is usually, but not accurately, named π-π interaction). Thus, a mechanism exists that provides inter-counterion attraction that will certainly affect brush-counterion complexation. Apparently, these two main differences in the structural geometry between counterions $C6T^{4+}$ and TAPP are likely to induce the observed difference between a collapsed and a stretched brush-counterion complex.

Apart from intramolecular binding no indications for the supramolecular interaction of several brush molecules for the brush-$C6T^{4+}$ system investigated in the present section can be seen. This is in strong contrast to the studies in chapter 5 where PSS brush is combined with the porphyrin TAPP. There it was found that finite-size aggregates at polyelectrolyte excess (that is at $l < 1$) show hydrodynamic radii larger than the brush size and also in AFM images supramolecular brush-porphyrin aggregates can be seen. Given the results and conclusions discussed in chapter 5 it may be a reasonable explanation for this difference that the porphyrin TAPP is binding cooperatively to the brush polyelectrolyte. That is porphyrin TAPP preferably binds next to an already polyelectrolyte-bound porphyrin due to the mutual π-π interaction between the porphyrins. This cooperative binding apparently promotes the formation of brush-porphyrin assemblies of network structure and finite-size due to local accumulation and charge inversion as will be discussed in chapter 5. The $C6T^{4+}$ counterion on the contrary is not expected to exhibit such preferential binding adjacent to further counterions and gets essentially equally distributed throughout the brush binding sites. The lack of this cooperativity effect may give a reasonable explanation for not observing supramolecular aggregates here.

Upon further addition of $C6T^{4+}$ to NaPSS brush at a counterion excess for $l > 1.3$ spontaneous phase separation and precipitation of a white solid material was found (all samples of Figure 3.4 were clear). Likely, neutralization by counterion binding reduces the charge of the polyelectrolyte to an extent that it is not soluble any more in aqueous solution. This behavior was also observed at porphyrin excess for the brush-TAPP case.

It is interesting to explore the situation in the transition regime $1 < l < 1.2$ where no precipitation occurs upon mixing. Here radii larger than the brush size were found that indicate the buildup of supramolecular aggregates. Directly after combining brush and counterion at this slight counterion excess, clear solutions with increased radii are obtained. However, radii increased over time and reached a constant value after about 10 days (thereafter the radii were time-stable). At this final value the samples at charge ratios $1 < l < 1.2$ were slightly turbid but no extensive sedimentation of a solid material was observed. Thus, it is interesting to compare this sizing behavior with the brush-porphyrin results in chapter 5 where radii larger than brush size were obtained that did not depend on time. Light scattering results of the final values (10 days after sample preparation) are given in Figure 3.6.

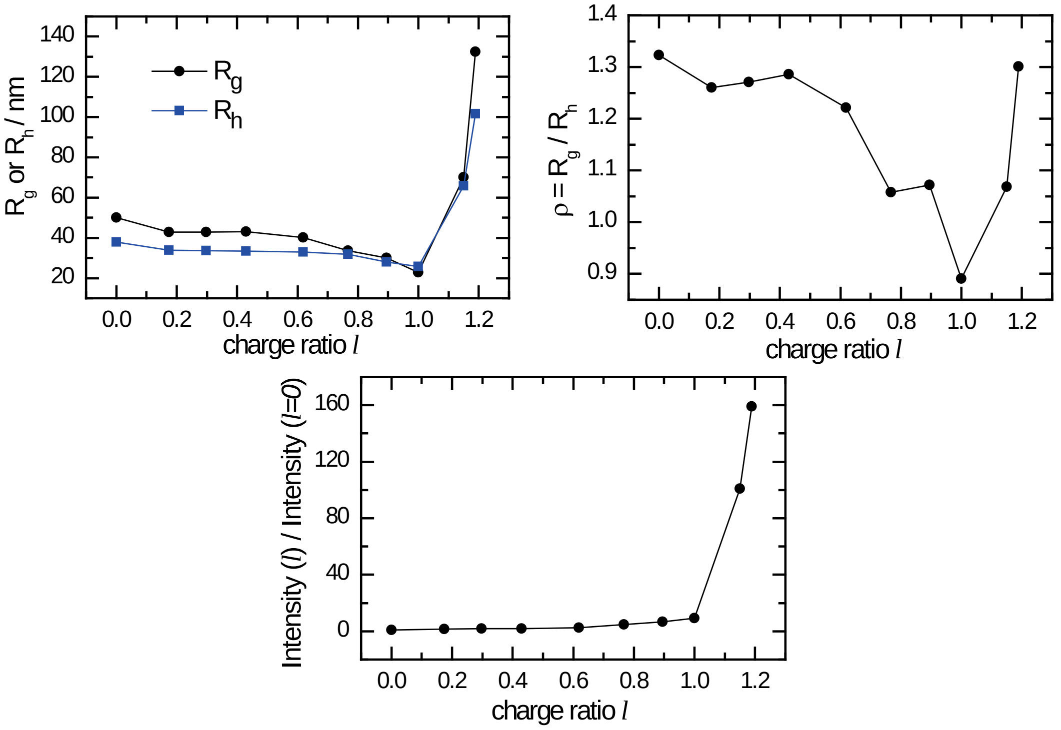

Figure 3.6: Light scattering results for samples with fixed NaPSS brush and different C6T^{4+} content. Reproduction of Figure 3.4 including samples with $l > 1$ (laser wavelength $\lambda = 632.8$ nm).

To get a better picture of the situation at $1 < l < 1.2$ an AFM image at $l = 1.2$ (after the incubation period of 10 days) is given in Figure 3.7. A larger structure of several brush molecules can be seen. Apparently, the brush molecules within this aggregate are still in a curled conformation as was the case for $l < 1$. Comparing this aggregate with brush-TAPP network structures seen in chapter 5 (see Figure 5.15), there are no gaps in between brush molecules but they rather lie adjacent to each other at the surface. The brush molecules are more or less bundled without showing meshes like they do with TAPP. This result strongly indicates that the mutual π-π interaction of TAPP is crucial for directing the brush TAPP aggregate structure towards networks as will be discussed in chapter 5.

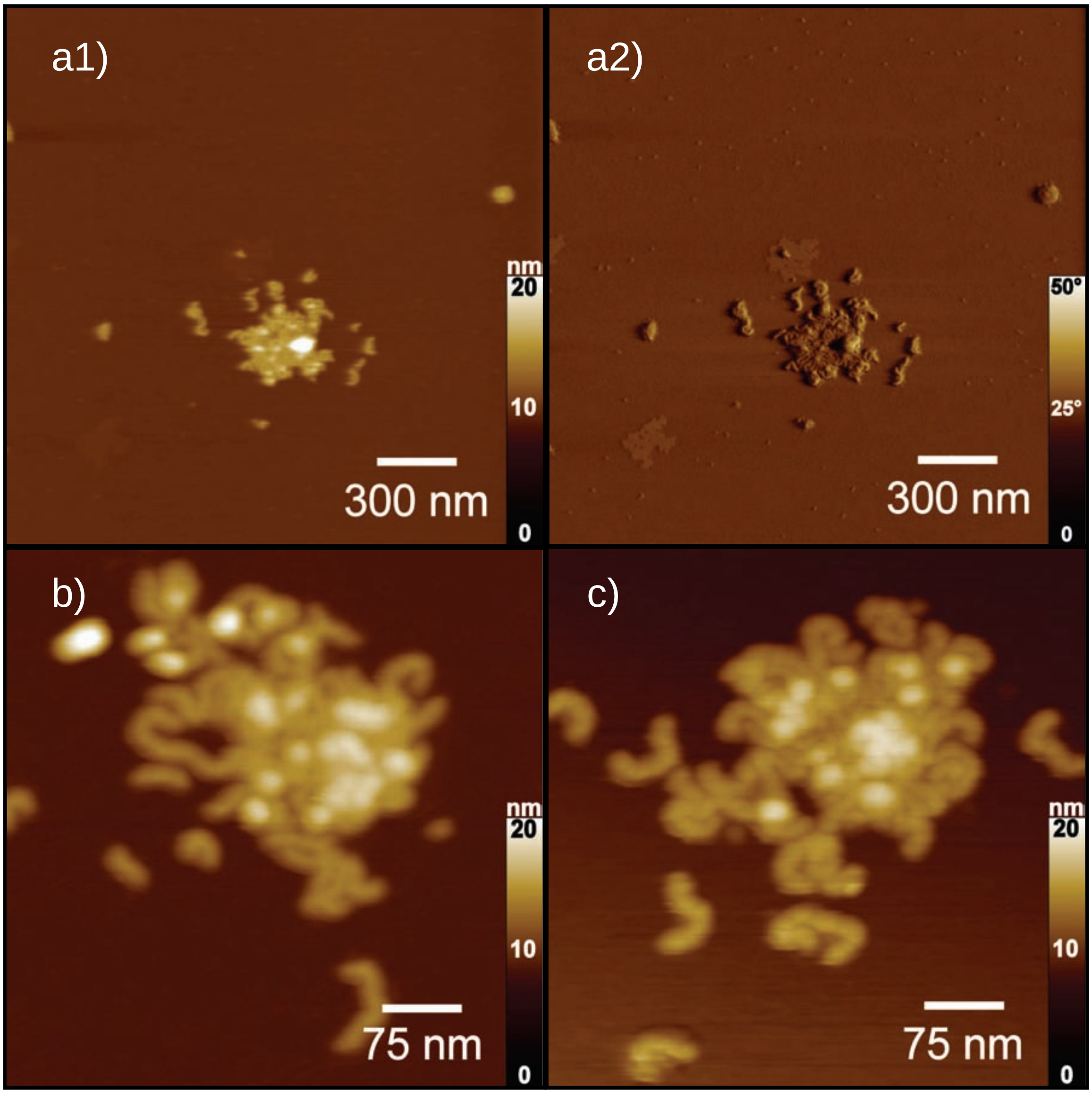

Figure 3.7: AFM height (1) and phase (2) images of a PSS brush-C6T^{4+} sample at l = 1.2.

CHAPTER 4

4 SELF-AGGREGATION OF WATER-SOLUBLE PORPHYRINS

4.1 Cationic Porphyrin: TAPP

As pointed out in section 2.2, three main parameters control the self-aggregation of charged porphyrins in water. These are pH, porphyrin concentration and ionic strength. In this section the self-association behavior of the tetravalent and positively charged porphyrin TAPP (Figure 2.8) at pH = 7 is investigated. Because of the high sensitivity of the Soret-band to porphyrin self-interaction, absorption spectroscopy is used for this investigation.

Porphyrin Concentration

There is a natural upper concentration limit for the usefulness of UV-vis spectroscopy in studying porphyrin aggregation because of the very high extinction coefficients of these molecules at the B-band and the lower practical threshold of 1 mm for the optical length of the measurement cells. For the example of TAPP with an extinction coefficient of 4.16×10^5 M^{-1} cm^{-1} [84] and the assumption that the maximum tolerable absorption is A = 3 the upper concentration limits gives c(TAPP) = 70 μM.

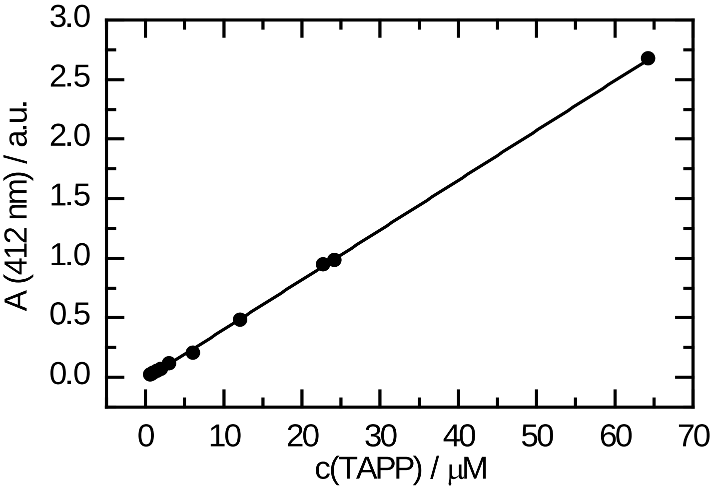

Figure 4.1: Lambert-Beer Plot for Porphyrin TAPP in water, l = 1 mm.

According to literature, there is no evidence for TAPP self-association in water up to c(TAPP) = 200 µM, and in agreement with this reports a linear dependence of TAPP B-band absorption on porphyrin concentration until c(TAPP) = 65 µM could be found at pH = 7 (Figure 4.1) [47,85].

Kano et al. in [47] reported ^{1}H NMR data that indicate that TAPP is fully self-associated at c = 10 mM and exhibits initiation of aggregation at around 4-6 mM. However, this concentration range is quite different from the usual concentrations of TAPP that are used in the present investigations (2-30 µM), and thus it can be concluded that TAPP exists as single molecule in water if there are no other influences like e.g. electrolyte concentration acting on it.

Ionic Strength

Since the main aim of the presented investigations is the characterization of porphyrin-polyelectrolyte interactions, it is of interest how simple monovalent electrolytes influence porphyrin behavior. It will be shown in later chapters that the Soret band of TAPP is strongly influenced by the presence of equimolar concentrations of negatively charged polyelectrolytes. However, for monovalent electrolytes the porphyrin absorption spectrum remains unaltered even for 1000-fold salt excess. Adding sodium chloride up to c(NaCl) = 0.13 M to a TAPP solution with c(TAPP) = 3.6 µM does not change the porphyrin spectrum. Therefore, it can be concluded that TAPP is still present as single molecule unaffected by other porphyrin molecules (Figure 4.2).

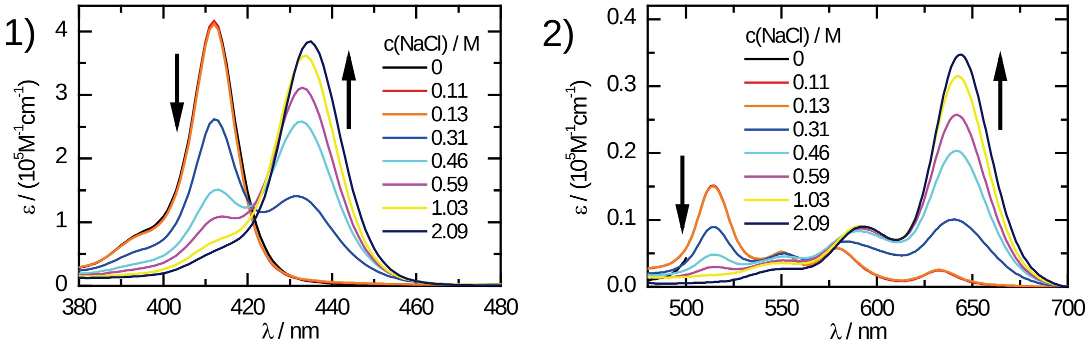

Figure 4.2: Titration of sodium chloride to a constant porphyrin concentration of c(TAPP) = 3.6 µM.

For c(NaCl) = 0.13 M there is an excess of NaCl chloride ions to TAPP charges of around 9000. As can be seen in Figure 4.2, the porphyrin spectrum reacts on the salt stimulus at c(NaCl) = 0.31 M where the ratio of salt to porphyrin charge has increased to 24000. With further addition of sodium chloride systematic variations of the B and Q-bands can be observed.

First the spectral shifts at the B-band are analyzed (right part of Figure 4.2). Here a clear isosbestic point at 422 nm indicates the presence of two porphyrin species in solution, and hence a continuous transition from the unaffected TAPP monomer at 412 nm to a different species at 435 nm takes place which is nearly complete at c(NaCl) = 2 M. Without further experimental data it would be quite reasonable to assume porphyrin aggregation as being the course of this bathochromic spectral deviation. The increase in ionic strength will decrease porphyrin charge-charge repulsion due to screening by salt ions, and thus the π-systems of two macrocycles may be more prone to intermolecular interaction. Therefore, the band at 435 nm would be assigned using the principle of parsimony to the TAPP dimer. Additionally, there is no evidence of a third species that would e.g. be higher aggregates in Figure 4.2 which is also highly supported by the observation of an isosbestic point.

To the knowledge of the author, there are three reports in literature by Kano [47], Dixon [86] and Huang [87] of spectral investigations on the impact of NaCl on TAPP that will be revisited here.

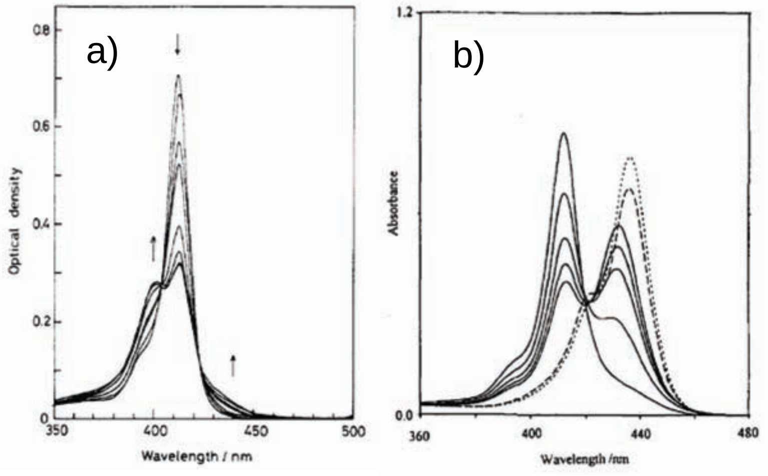

Figure 4.3: Literature spectra of TAPP Soret band upon NaCl addition. Left [47]: c(TAPP) = 20 µM, c(NaCl) = 0, 0.5, .., 3.5 M, pH = 7; Right [87]: c(TAPP) = 2.5 µM, c(NaCl) = 0, 0,05, .., 0.2 M, pH = 3.8, solid lines - dashed lines are unrelated to present discussion.

The findings of Kano et al. (Figure 4.3, left spectrum) and Dixon et al. (not shown) are quite similar. Kano describes the formation of a new band at 404 nm and a shoulder band at 435 nm with concomitant hypochromicity at 412 nm upon salt addition. Dixon reports the buildup of a band at 402 nm but no shoulder band around 435 nm for similar conditions. Both authors assign the blue shifted band to the TAPP dimer due to salt induced porphyrin aggregation, and Kano assigns the reported 435 nm band to higher porphyrin aggregates.

In strong contrast to these reports, no blue shift of the 412 nm band in the present salt titration but a strong red shift to 435 nm was observed. It remains unclear if there is an analogy to the 435 nm shoulder band presented by Kano, but the differences in band shape and intensity suggests to better reject this hypothesis. However, the new evolving band observed here shows strong resemblance to the spectrum of TAPP at low pH as presented in Figure 4.4. At pH = 2 the free base porphyrin H_2TAPP^{4+} is protonated to H_4TAPP^{6+} (Figure 2.9: **II** → **I**).

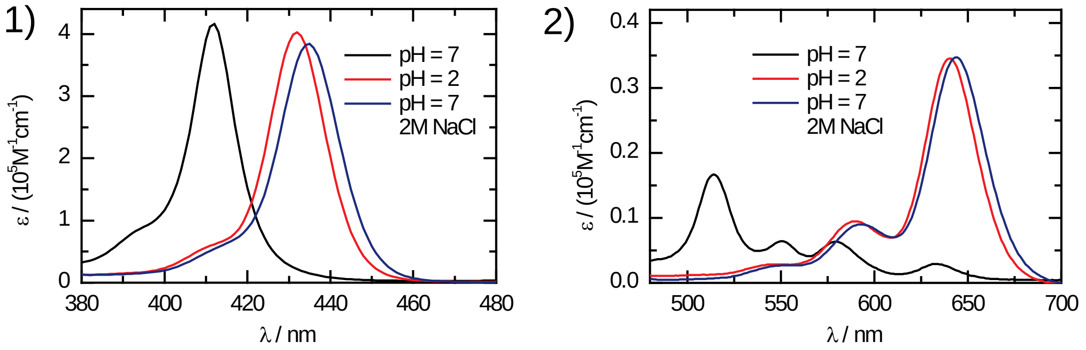

Figure 4.4: Effect of pH and salt on TAPP spectrum. TAPP in pH = 7 and pH = 2 buffer, 2 μM (from [82]) and TAPP in water at 2 M NaCl (from Figure 4.2).

Band height width and position (432 nm) of the Soret signal of TAPP in protonated state is remarkably similar to the TAPP spectrum in 2 M NaCl. Even more so, the results for the Q-bands not yet discussed indicate a strong familiarity of these two spectra. In analogy to the effect at the Soret band, there is a continuous shift of the Q-bands upon salt addition to the spectrum of the new species exhibiting an isosbestic point at 576 nm (Figure 4.2). The Q-band "fingerprint" here transforms from the D_{2h} tetramodal TAPP spectrum two a two-band signal which is characteristic for the D_{4h} spectrum of protonated TAPP. Additionally, the very strong similarity of the TAPP at pH = 2 in Figure 4.4 with the spectrum in 2 M salt strongly suggests that indeed TAPP in aqueous salt solution at this concentration is present in the protonated state. It should be noted that the Q-band fingerprint here provides a very significant proof for this conclusion. Spectra of aggregated TAPP as shown in later chapters usually show shifts in the Q-band too, but the four-band signature here generally remains (see for example Figure 5.4).

Assuming the conclusion of TAPP being protonated in salt is correct, the question arises why this is the case. The pK_a of TAPP is reported to be 3.0 [48] and significant spectral deviation in salt-free water sets in at around pH = 3.3 [87]. Since the pH value of the purified water used here is around pH = 7, and because the addition of salt will not affect pH, protonation of TAPP appears implausible. However, Huang et al. [87] presented data of an interesting experiment where the authors added sodium chloride to a 2.5 μM TAPP solution at pH = 3.8 (Figure 4.3, right spectrum). Here the solid lines represent the B-band of TAPP with subsequent rise of NaCl concentration from 0 to 0.2 M. There is a bathochromic shift to 435 nm with an isosbestic point at 422 nm indicating a spectral behavior very similar to the present result. The authors explain this observation by the influence of the shielding salt ions to the proton transfer to TAPP. Thus, following these results the addition of salt may facilitate the protonation of TAPP, and this may give a partial explanation to the effects in Figure 4.2. However, the present experiment was unlike the one by Huang et al. set up at a pH very distant to the protonation threshold of TAPP, and although the spectral deviations in the present case set in at a higher salt concentration than in [87], it is questionable if the same reasoning can be applied to the observations presented here. In addition, the deviations of spectral shifts in the present study from the results in [47,86] remain unexplained.

In the past section the spectral deviations of TAPP upon salt addition have been examined in a relatively detailed way since the explanation for the observed effect is of general interest. However, the shifts here apply at relatively high ionic strength and these salt concentrations are much higher than the maximum electrolyte concentration that will be used in the following investigations. For example, the salt concentration that will be used in section 5.2 to disassemble polyelectrolyte-porphyrin complexes is in maximum c(NaCl) = 10 mM. Also the charge concentration of added polyelectrolyte will never be higher than this value. Therefore, it can be concluded from the results in this section and the previous discussion about porphyrin concentration that TAPP will be present as a monomolecular and unprotonated molecule in solution if only simple salts are present. It will later be shown that the transition from small electrolytes to charged polymers will change this picture dramatically.

4.2 Anionic Porphyrin: TPPS

TPPS (Figure 2.8) is comparable to TAPP in that sense that both porphyrins have charge centers located at the periphery of the porphyrin ring. In each case the charge is electronically isolated from the porphyrin π-system and thus may not delocalize into the inner ring. However, as was already discussed in chapter 2 the marked difference is that upon protonation of its nitrogen bases TPPS transfers into a zwitterionic molecule in acidic conditions. This feature gave a strong motivation for many research groups to study its aggregation behavior in the zwitterionic state, where charge interactions of the outer negative charge sites of one porphyrin molecule with the positive core of another molecule may lead to interesting structures. The groups of Fleischer and Pasternack have first reported the time dependent appearance of sharp and intense new peaks in absorption spectroscopy at around 490 nm and 706 nm that appear when TPPS solutions are acidified to pH = 1-3 [44,88-89]. The observed spectral influence of pH on TPPS was later explained by the formation of TPPS J-aggregates by the groups of Ohno, Akins and Ribo [45,90-91]. They also reported that the extent of J-aggregation is increased with porphyrin and proton concentration. Choosing adequate combinations of porphyrin concentration and pH is reported to yield protonated but unaggregated TPPS molecules whereas at either higher porphyrin concentration or lower pH strong J-aggregation was observed [90-91]. Further investigations by scattering techniques provided evidence that these J-aggregates have rodlike morphology and that each porphyrin cylinder has an aggregation number in the order of $\sim 10^5$ [54,92-95]. More recent reports support the previous findings of TPPS nanorod formation by several imaging techniques (AFM, TEM, STM) [55,96-99]. Interestingly, TPPS nanorods were found to be photoconductive [100] and their formation by aggregation may lead to spontaneous chiral symmetry breaking [101-102].

Within the scope of the present dissertation it is of interest to investigate the self-aggregation behavior of TPPS to better understand its interaction with polyelectrolytes that will be reported in chapter 7. The characteristic features of the TPPS absorption spectrum are essentially identical to that of TAPP in neutral and salt-free aqueous solution (see Figure 7.2). In analogy to TAPP (see Figure 4.1), TPPS does not self-aggregate in neutral salt-free solution at the concentration range investigated here. This conclusion can be derived from the spectral features of TPPS that are constant with increasing concentration and additionally from investigations reported in literature [88]. Also in full analogy to TAPP, it is not expected that there is salt-induced aggregation of TPPS at neutral pH for the relatively low salt concentration employed within the present investigation. In addition, it is reported that TPPS stays in its monomolecular state at least up to a salt concentration of 0.4 M NaCl [103]. It can be concluded that in neutral solution TPPS behaves very similar to TAPP and thus complexation experiments of TPPS with positively charged polyelectrolytes should be comparable to experiments of TAPP with negatively charged polyelectrolytes.

As was already mentioned above, TPPS behaves very differently to TAPP at a pH lower than the pK_a of the porphyrin that is where the porphyrin diacid is dominant. The pK_a of TAPP is $pK_a = 3$ [48] whereas pK_a (TPPS) = 4.8 [88]. This difference can be explained by the opposite sign of the respective peripheral charges. The sulfonic acid groups of TPPS are capable of stabilizing the positive charge in the porphyrin center which is formed upon its protonation. In contrast, the positive charges in TAPP will destabilize the protonated center. Therefore, TPPS needs a smaller proton concentration to transform into the diacid state. Nevertheless, it is clear that both porphyrins are protonated at pH = 2 and thus it is of interest to compare their behavior at this proton concentration.

The spectrum of the diacid form of TAPP is given in Figure 4.4. Protonation yields a strong red shift of the Soret band to 435 nm. Additionally, in the Q-band there is a transformation to a 2-band spectrum (592 nm und 644 nm) that is characteristic for the porphyrin transition to D_{4h} symmetry. These observations are entirely time stable and can be very well explained by a diacid porphyrin molecule that is not aggregated. It can be concluded that TAPP does not self-aggregate at pH = 2.

On the contrary, TPPS exhibits a rather complicated spectral behavior at pH = 2. In addition to the signals that can be assigned to the diacid as was done for TAPP, it is reported that there are two new signals at 489 nm and 708 nm (see above) [88] which evolve with time. From literature it is evident that these two signals can be assigned to the time dependent formation of J-aggregates that exhibit the structural feature of nanorods. The conclusion for a J-aggregate is strongly supported by a very narrow and red shifted Soret signal at 489 nm. It is well known that extensive electronic communication leads to spectral narrowing and J-aggregate formation to red-shifted spectra. Within the present investigation J-aggregate signals at 492 nm and 708 nm at pH = 2 are observed (Figure 4.5).

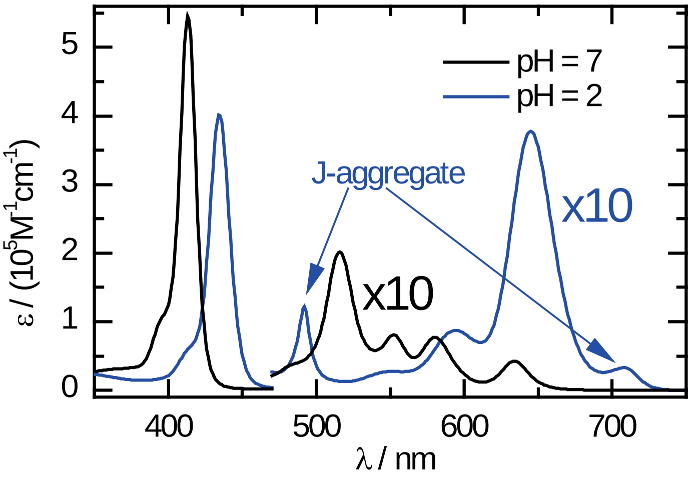

Figure 4.5: Absorption spectrum of TPPS (c = 25μM) at pH = 7 and pH = 2.1.

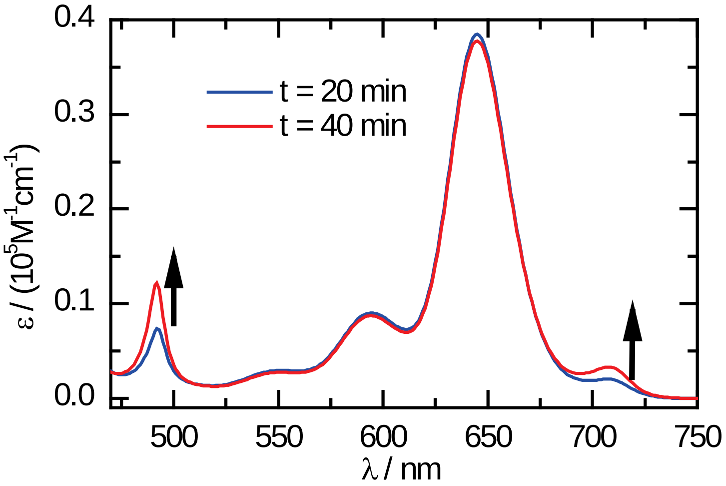

Figure 4.6: Time dependent evolution of J-aggregates, TPPS pH = 2, t: time after changing pH from pH = 7 to pH = 2. Further rise of J-signal not shown.

In accordance to literature, these signals exhibit a time-dependent evolution (Figure 4.6) [44-45,88,90-91]. In addition to its time-dependent character, the extent of J-aggregation is apparently also dependent on porphyrin concentration [95]. As can be seen from Figure 4.7, J-aggregation is strongly enhanced for higher concentrations.

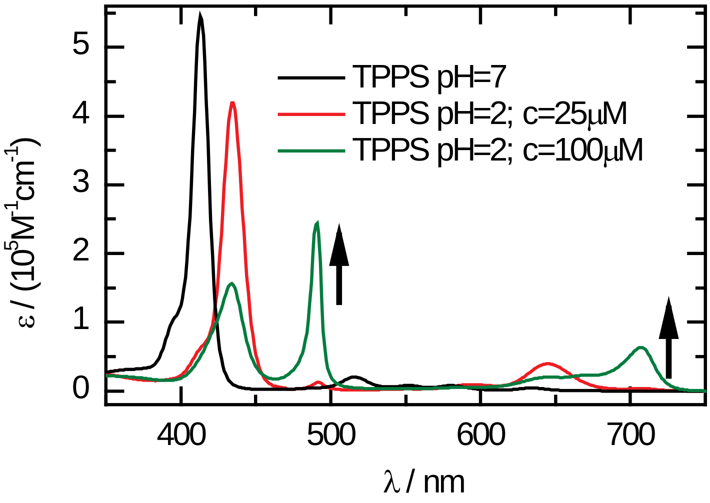

Figure 4.7: J aggregates from TPPS, TPPS pH = 7: no J-aggregates; TPPS pH = 2, c = 25 µM; TPPS pH = 1.6, c = 100 µM.

The residual signals at 434 nm, 594 nm and 645 nm can be assigned to the monomeric type of porphyrin diacid. The shift to a two-band Q-spectrum for this species results from the $D_{2h} \rightarrow D_{4h}$ transition as described before and reflects full conversion to porphyrin diacid. Figure 4.8 demonstrates the spectral shifts of Q-band that occur upon protonation of porphyrin.

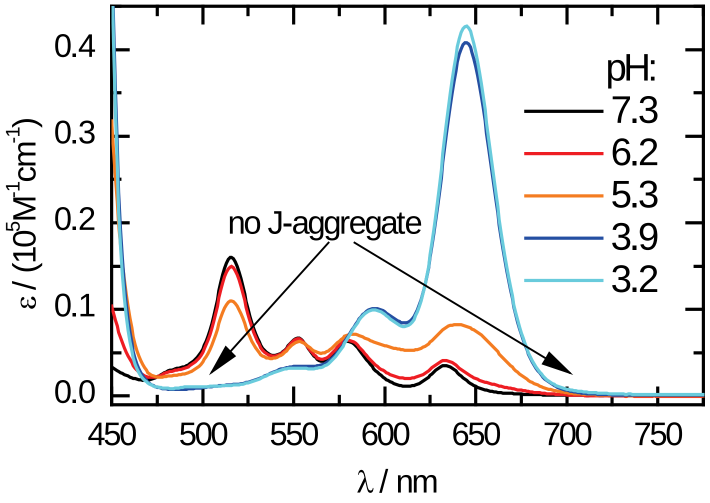

Figure 4.8: Absorption spectrum of TPPS (c = 25 µM) at different pH.

In accordance to the above mentioned pK_a of TPPS, the conversion to porphyrin diacid is complete at pH = 3.9. Interestingly, there is no sign of porphyrin diacid J-aggregation in this pH range (3.2 - 3.9) at the chosen concentration. This is not surprising since J-aggregate formation is both dependent on pH and absolute concentration (see above) and thus the given pH range represents the regime of unaggregated by protonated TPPS at the given porphyrin concentration. The observation is very useful for the current studies, since it enables to conduct complexation experiments of TPPS at three different states: a) tetravalent and monomeric porphyrin at pH = 7, b) divalent and monomeric porphyrin diacid at pH = 3.2 - 3.9, c) J-aggregates of porphyrin diacid at pH = 2.

In order to confirm the literature observation that the TPPS J-aggregates in strongly acidic condition show a cylindrical structure in the present system, the J-aggregates were deposited by spin-coating on mica and imaged via Atomic Force Microscopy (Figure 4.9). Rodlike TPPS aggregates with remarkable persistence lengths of up to several micrometers have been observed. In addition to the nanorods, the mica surface is covered with two further species. First the surface is fully covered with more or less spherical particles that are present in the free space between the rodlike objects as well as directly adjacent to the porphyrin rods. Second, there are spherical and larger objects with heights comparable to the nanorods that are distributed over the surface with an observable tendency to attach to the porphyrin rods.

There are two possible explanations for such additional objects present on the surface after drying. First, apparently (from spectral evidence) there are TPPS molecules present in the sample that have not aggregated to J-aggregates but rather are in the monomolecular diacid state. Second, in order to lower the pH HCl was introduced with significantly higher concentration than TPPS itself - c(HCl) = 14 mM compared to c(TPPS) = 25 μM. Since HCl was not removed prior sample deposition but rather the intact sample was spin-coated on mica the introduced ions are still present.

Figure 4.10 gives cross-sectional profiles of TPPS nanorods. From the profiles two main conclusions may be drawn. First, the rods seem to have a quite regular shape that can be seen in the close resemblance of four sectional profiles. Second, it can be seen that the rods have a profile of a flattened circular or oval shape that is wider than high probably due to surface interaction (this phenomenon will be described for cylindrical brush molecules in section 5.1.2 below).

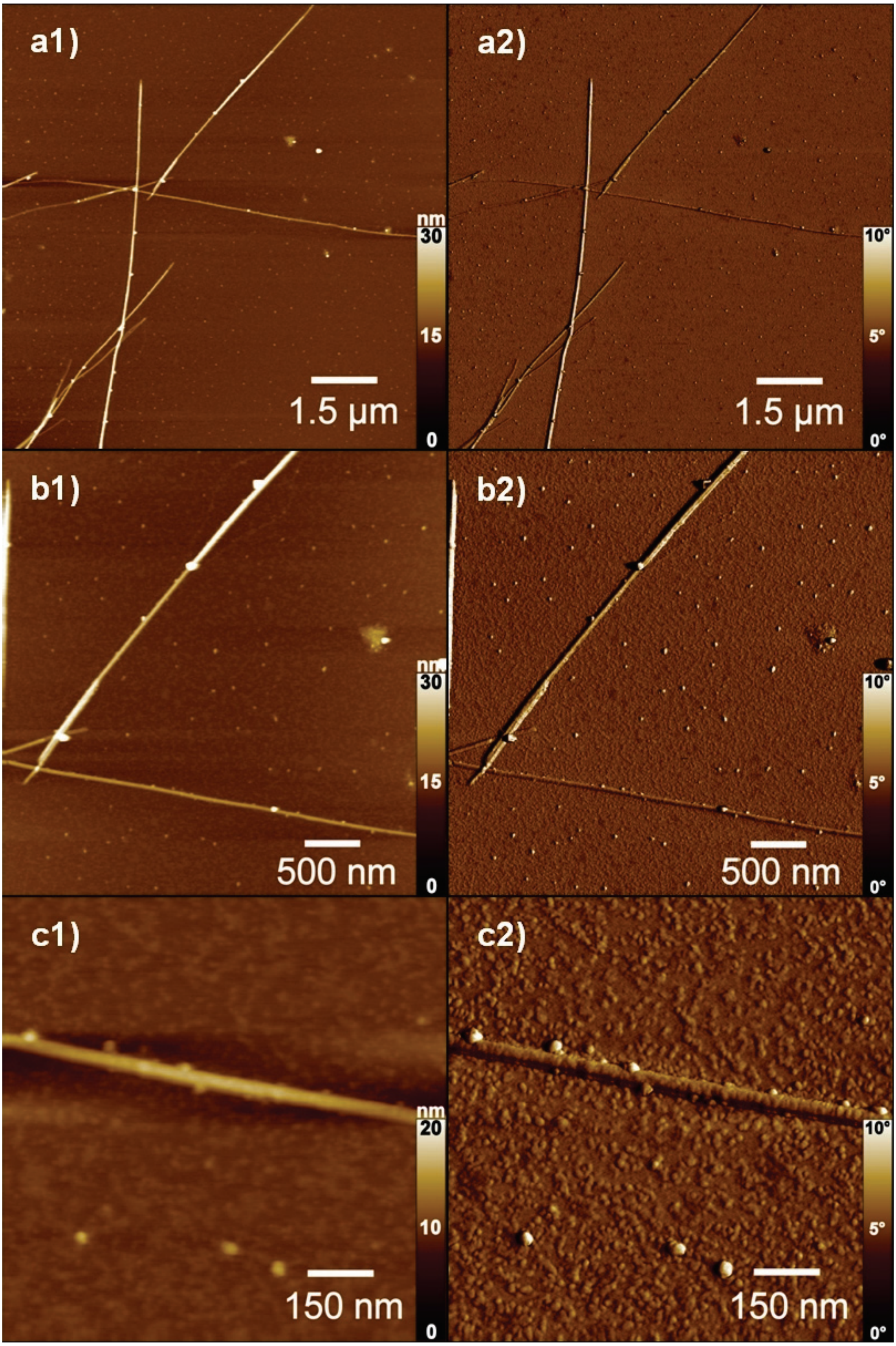

Figure 4.9: AFM images of TPPS nanorods 30 µM at pH = 2 (left: height, right: phase).

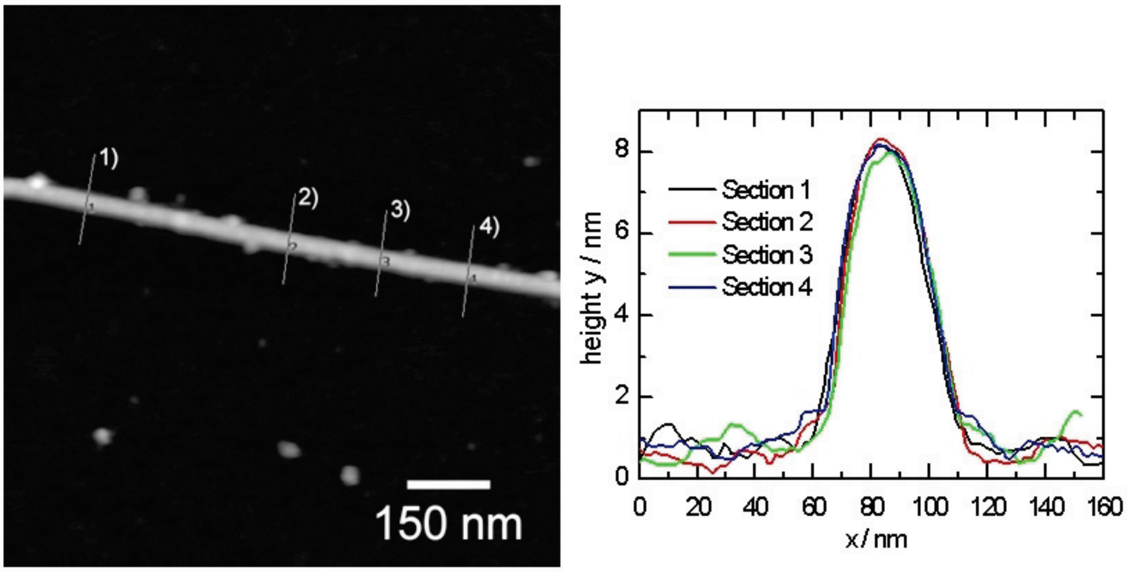

Figure 4.10: Cross-sectional profiles of TPPS nanorods from Figure 4.9-c1.

It is of interest to additionally investigate the J-aggregate formation of TPPS at pH = 2 by infrared light scattering. Measuring dynamic light scattering of a TPPS solution with c = 100 µM at 90° at pH = 7, the solution exhibits roughly twice the light scattering intensity of pure water and no build-up of a clear correlation function. Adding HCl resulting in pH = 4 does not change the scattering behavior. The count rate remains same and still no decay in the correlation function is measured. However, if the pH is adjusted to pH = 2 drastic changes of scattering behavior are observed. The count rate increases by a factor of 700 and a clear decay in the correlation function is observed (Figure 4.11). Second order cumulant evaluation results in a hydrodynamic radius of 78.5 nm (Table 4.1). Thus, the appearance of TPPS nanorods is visible by light scattering detection as well. Since time dependent spectral evolution of J-aggregate signals was monitored with UV-vis spectroscopy, it should also be interesting to investigate the time dependency of nanorod size. Surprisingly no such time dependency was observed. Due to handling issues light scattering measurement was started about 20 minutes after addition of HCl to pH = 2 (the sample to which HCl was added to did not show strong scattering prior to HCl addition as was discussed above). Already the first measurement showed the 700-fold increase in light scattering intensity and the reported hydrodynamic radius. Intensity and radius thereafter stayed nearly constant for at least 16 hours as it is shown in Figure 4.11. Presumably, at the length scale visible by light scattering the evolution of TPPS nanorods is completed after 20 min at the relatively high concentration of c(TPPS) = 100 μM. Nevertheless, rearrangements corresponding to spectral changes may still take place even though the nanostructure remains of same size.

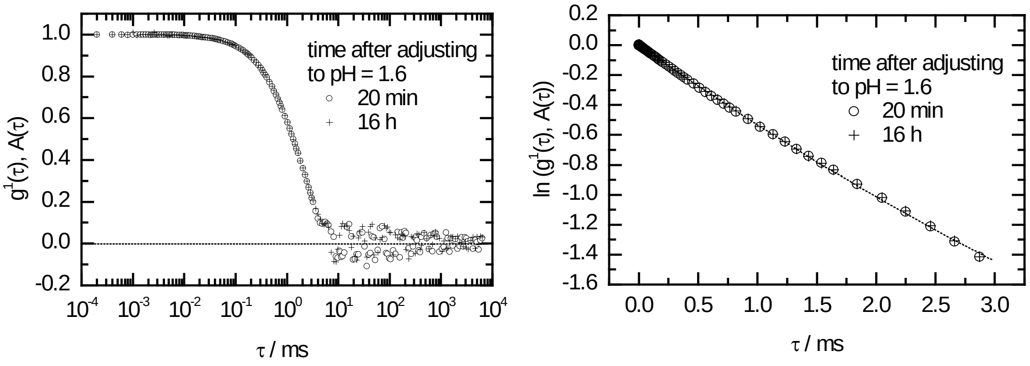

Figure 4.11: Dynamic light scattering results of TPPS c = 100 μM at 90° (λ = 831.5 nm) shortly after adjusting to pH = 2 and after 16 h.

Table 4.1: Results of second order cumulant expansion of correlation function in Figure 4.11, I/I_{water}: scattering intensity as multiple of water scattering intensity.

R_h/nm	**$\mu_2/(\Gamma)^2$**	**I/I_{water}**
78.5	0.152	1360

CHAPTER 5

5 SELF-ASSEMBLY OF PSS BRUSHES WITH THE CATIONIC PORPHYRIN TAPP

5.1 Brush-TAPP Complexes in Salt-Free Water

In this chapter it will be investigated how the porphyrin TAPP interacts with polyelectrolytes [23]. Since TAPP is positively charged its interaction with negatively charged polymers that provide TAPP with adequate binding sites will be studied. It is expected that the porphyrin will bind to a negative polyelectrolyte via its quaternary ammonium groups. The polyelectrolyte of choice within this investigation will be the sodium salt of polystyrene sulfonate (PSS). The focus will be on the interaction of TAPP with a cylindrical NaPSS brush that was described and characterized in section 3.1.

The interaction of positively charged and water soluble synthetic porphyrins with polyelectrolytes was first studied for porphyrin complexation with nucleic acids, in particular with DNA [50,87,104-127]. The focus of most of these studies was set on the binding mode of porphyrins on DNA (e.g. base pair intercalation, groove binding or external aggregation). For porphyrins that aggregate on DNA very similar correlations of stacking tendency with structural porphyrin parameters were observed than it was previously found for porphyrin aggregation in the absence of polyelectrolytes: metal porphyrins show similar stacking tendency trends dependent on the metal atom and porphyrins that carry less charges per molecule generally tend to show higher aggregation numbers (for porphyrin aggregation in general see chapter 2) [44,106-107,109,111,128-129]. Positively charged porphyrins were also studied in the combination with other biological or biosimilar polymers. The complexation of porphyrins with polypeptides and proteins has been demonstrated with spectroscopic techniques [110,130-138]. In these studies the general trends of porphyrin self-aggregation dependent on porphyrin structure described above were shown to be valid for polypeptide templates as well. The number of association studies for positively charged porphyrins with synthetic polymers is less pronounced. Studies are reported with oligomeric amino-terminated poly(propylene oxide) [139], cyclodextrins [140-

141] and carboxyl-terminated poly(amidoamine) (PAMAM) dendrimers [139,142]. Besides these studies systematic investigations of water-soluble and positively charged synthetic porphyrins with synthetic polyelectrolytes are mostly lacking [143]. Thus, the next three chapters were motivated by the need to evaluate synthetic polyelectrolyte-porphyrin systems for possible material applications adding to the existing polyelectrolyte-porphyrin literature that is focused predominantly on biological and biomedical applications. Whereas chapter 5 and 6 cover the association of positively charged porphyrins with synthetic polyelectrolytes, chapter 7 investigates negatively charged porphyrins.

5.1.1 Spectroscopic Properties of Complexes from NaPSS Brush and TAPP

Light absorption spectroscopy is a powerful tool to analyze not only porphyrin self-aggregation but also its interaction with polyelectrolytes as well as porphyrin self-interaction induced by the polymer template. Combining the porphyrin TAPP with the PSS brush results in a color shift that is already visible by eye as it is shown in Figure 5.1. While TAPP in aqueous solution shows a violet color (right), combination with the colorless brush solution (left) results in a light-brown solution (middle). As it was pointed out in section 4.1, TAPP exists as single unperturbed molecule in aqueous salt-free solution within the concentration regime investigated here, and thus the violet solution represents the single porphyrin. Because of the substantial spectral shift to light-brown, it is obvious that the addition of polyelectrolyte brush strongly perturbs the π-system of TAPP. This perturbation may be explained by two mechanisms or a combination of both.

One explanation is self-interaction of porphyrin molecules induced by the polyelectrolyte and mutual perturbation of two or more porphyrin π-systems. It is well known from literature that dye π-π interaction in general and porphyrin π-π interaction in particular may lead to strong color shifts, a phenomenon usually referred to as "metachromasia" [44-48,129,144-146]. Besides by the self-interaction of porphyrin π-systems, spectral shifts may also be explained by the interaction of the porphyrin with the polyelectrolyte template. Here such factors as the different microenvironment, sterical constraints that distort porphyrin geometry and especially direct π-π interactions with the polyelectrolyte (if it contains aromatic groups) may play crucial roles.

Figure 5.1: Photograph demonstrating color shifts in water. Left: NaPSS brush (c(NaPSS) = 240 μM), center: NaPSS brush with TAPP (c(NaPSS) = 240 μM, c(TAPP) = 25 μM, *l* = 0.4) , right: TAPP (c(TAPP) = 25 μM).

In general, the first explanation that strong spectral shifts are due to porphyrin self-aggregation should in context of the literature on polyelectrolyte-dye interaction be considered as the more likely reason. The observed spectral shifts will be quantitatively evaluated with absorption spectroscopy and it will be clear that the system is best described by a combination of both explanations.

In order to differentiate between porphyrin-polyelectrolyte and self-porphyrin interaction it is reasonable to set up an experiment where the polyelectrolyte is present in relatively large excess to the porphyrin (e.g. 9000-fold excess). Here the idea is that the large number of free binding sites per given porphyrin molecule could lead to independently bound porphyrins on the polyelectrolyte surface, and thus porphyrin-porphyrin interactions should not perturb the spectra. Figure 5.2 gives the time dependent absorption spectrum of porphyrin TAPP in the presence of a 9200-fold excess (*l* = 1/9200) of the polyelectrolyte NaPSS. The concentration of styrene sulfonate units here (c = 0.125 M) is close to the range of salt concentrations that can induce TAPP self-aggregation (Figure 4.2). However, it was shown in chapter 4 that at this ionic strength the salt does not induce porphyrin aggregation in pure TAPP solution and thus no complication effects of TAPP aggregation by simple charge shielding is expected.

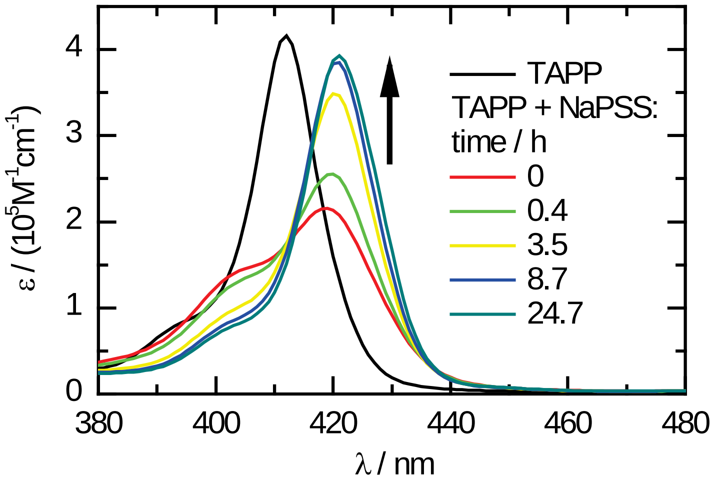

Figure 5.2: Addition of NaPSS (0.125 M) to porphyrin TAPP (3.4 μM), charge ratio polyelectrolyte to porphyrin = 9200 (*l* = 1/9200). Time after preparation in hours.

In Figure 5.2 the porphyrin Soret spectrum is strongly perturbed directly after addition of PSS to TAPP. Apparently, the band formerly at 412 nm is split into two signals at 403 nm and 419 nm (red line). With time the signal at 403 nm weakens in expense of the signal at 419 nm and the red shifted signal further shifts to 421 nm. There is an isosbestic point present at 412 nm. After around 10 h a time stable spectrum is observed. Due to the large excess of PSS here it is reasonable that this final spectrum represents the signal of porphyrin TAPP that is bound to the polyelectrolyte but does not interact with further porphyrins. Thus, it can be concluded that the band shifts in Figure 5.2 from initial to final state are due to the binding of a single porphyrin to the polyelectrolyte template. As was pointed out above, this shift can be explained by the different microenvironment at the polyelectrolyte or e.g. by π-π interactions with the aromatic PSS polyelectrolyte. Band shape, proportions and height of porphyrin TAPP bound to the PSS polyelectrolyte are besides slight hypochromicity quite similar to free TAPP. Presumably, this is an indication that the electronic state of TAPP does not change to a large extent upon binding to PSS. Thus, both a geometrical distortion of the porphyrin ring and a strong electronic perturbation by direct interaction of the aromatic π-electrons with PSS π-electrons would not be expected by this observation. A possible conclusion is here that the porphyrin simply binds to PSS via its peripheral charges without distortions of its planar geometry and without the mentioned π-π interaction with aromatic PSS. This conclusion is supported by the strong tendency of TAPP to self-aggregate on PSS. Specific aromatic-aromatic dye-polyelectrolyte interaction in contrast is reported to lead to relatively low aggregation tendencies due to a competition of interaction patterns [147-148].

In Figure 5.2 the isosbestic point at 412 nm is not crossed by the pure TAPP spectrum but by all subsequent spectra. In combination with the large excess of PSS it is clear that there is no free monomeric TAPP present in the equilibrium indicated by the isosbestic point from t = 0 h on. Since the final situation was already identified as a single TAPP bound to the polyelectrolyte, the equilibrium seen here is between this species and a new to be identified TAPP form. The conclusion is that the intermediate spectral signals are induced by TAPP porphyrins self-interacting on the polyelectrolyte (the other option of TAPP self-interacting freely apart from the polyelectrolyte is canceled out by the fact that the salt concentration here is lower than the threshold concentration for simple salt induced porphyrin interaction identified in Figure 4.2).

Thus, porphyrin self-interaction is observed although the ratio of polyelectrolyte binding sites to porphyrin molecules is 2300 (9200 divided by 4). Even given this large choice of binding sites the porphyrin preferably binds to the polyelectrolyte adjacent to another TAPP. The time dependent spectral changes can than be explained by a reorganization process of the bound molecules that distribute more homogenously over the binding sites due to the large excess.

To better understand spectral shifts in Figure 5.2 and for further quantitative investigations, the signals of pure TAPP and polyelectrolyte-bound TAPP were deconvoluted by Gaussian fits as it is demonstrated in Figure 5.3. Each spectrum was fitted by three Gaussian functions. This minimal number was needed to adequately fit the signals of the porphyrin Soret peaks and the fitted single TAPP spectrum will be of use below.

A further experiment for studying TAPP self-interaction on PSS is adding PSS to TAPP in ratios where neither of the components is present in large excess. The experiment was carried out as a titration: PSS brush concentration was gradually increased while the concentration of porphyrin was kept fixed (Figure 5.4).

The first observation seen in the titration results is a strong intensity weakening (hypochromicity; weakening to about 25 % of original value) upon moving from the pure porphyrin to charge stoichiometry (l = 1). In addition the band at l = 1.01 is much broader than the signal for the pure porphyrin. Apparently, there is an isosbestic point at

423 nm that is crossed by pure TAPP as well as by all samples with $l \geq 1$, but is not crossed anymore by subsequent samples with PSS excess ($l \leq 1$). In a first step only the part of the titration with $\underline{l \geq 1}$ will be discussed.

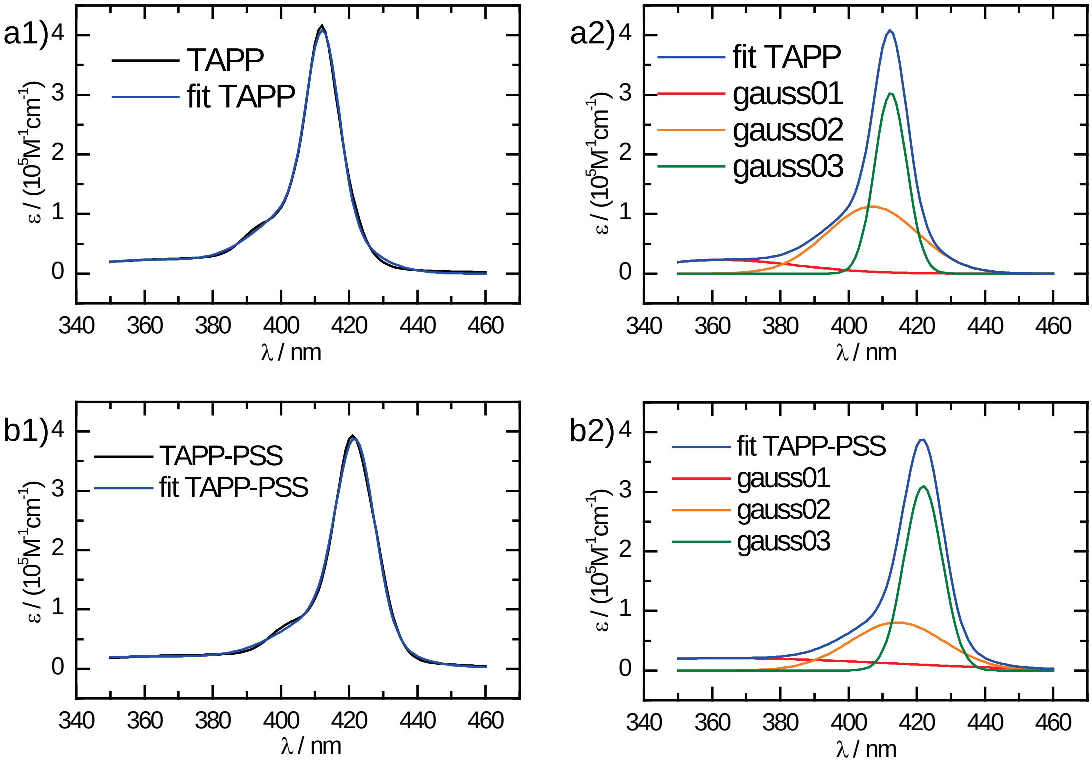

Figure 5.3: Empirical fitting procedure by three Gaussian functions of (a) a pure TAPP sample and of (b) TAPP bound as isolated molecule to PSS.

Due to the isosbestic point that is also crossed by free TAPP it is clear that there is an equilibrium between free porphyrin and another species. The presence of monomeric TAPP is not surprising since at $l \geq 1$ there are simply not enough polyelectrolyte binding sites available for the porphyrin. From the results in Figure 5.2 it is quite clear that the band broadening and the hypochromicity results from porphyrin molecules that both are bound to the polyelectrolyte and also self-interact with further porphyrin molecules. It is unclear whether the observed TAPP self-aggregates represent dimers or aggregates with larger numbers of porphyrins. But it is clear that there is an equilibrium between monomeric TAPP and only one further spectral species. However, this could be explained either by only one type of aggregate (that potentially would be chosen to be the dimer by the principal of parsimony) or also by the potential fact that the absorption spectrum does not change for self-interacting TAPP upon moving from a dimer to an oligomer.

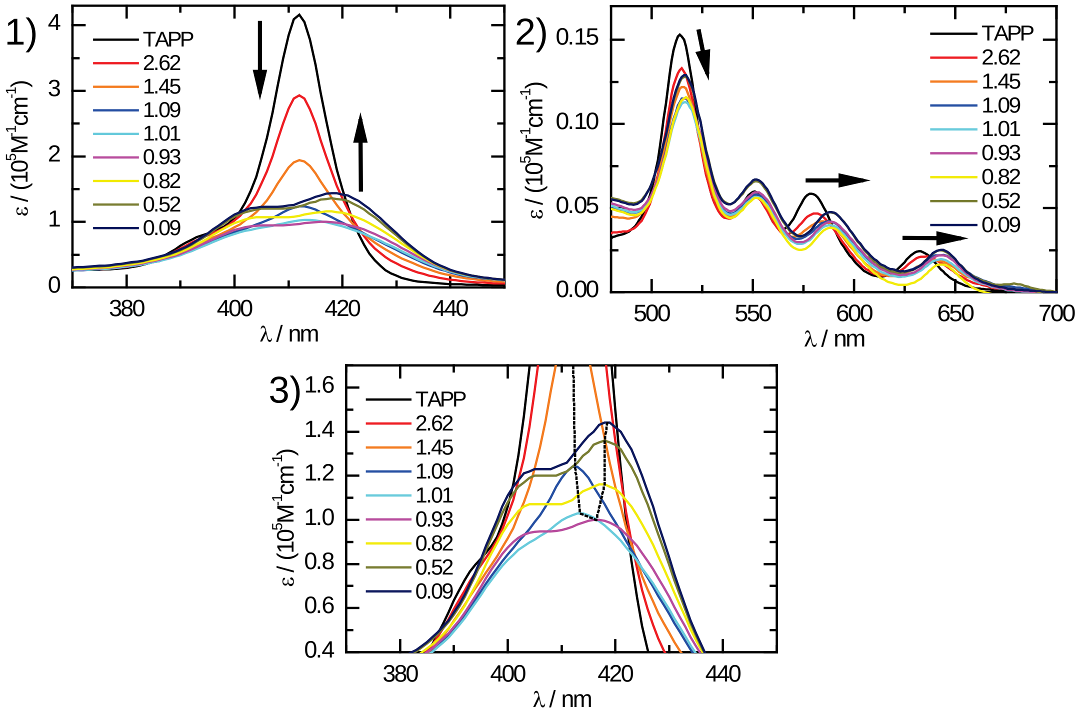

Figure 5.4: Spectral changes of TAPP absorption spectra upon addition of polyelectrolyte brush c(TAPP) = 2.85 μM: (1) Soret bands, (2) Q-bands; (3): expansion of (1); legend: charge ratio *l* = [TAPP]/[PSS].

Table 5.1: Wavelengths and extinction coefficients of signals in Figure 5.4, s shoulder.

	B-bands: λ/nm (ε/10^4 M^{-1} cm^{-1})	**Q-bands: λ/nm (ε/10^4 M^{-1} cm^{-1})**
TAPP	412 (41.6), 391s (6.83)	514 (1.53), 551 (0.60) 579 (0.59), 634 (0.42)
TAPP+PSS *l* = 0.93	403 (9.32), 417 (10.0)	517 (1.15), 552 (0.59) 589 (0.42), 643 (0.22)

In addition to the results for the Soret band in Figure 5.4 the spectral shifts for the Q-bands in Figure 5.4-2 may reveal some structural information about the stacked porphyrin TAPP. There are red spectral shifts for the Q-band but the overall band shape does not change and thus the self-aggregated TAPP spectrum also shows a 4-band Q-spectrum. From this observation it can be concluded that TAPP is not protonated in the inner porphyrin core but rather is present as the tetravalent porphyrin in the TAPP stacks.

In the Soret spectrum, for l = 0.93 a band shape of similar width than for l = 1.01 is obtained, but now clearly two bands can be differentiated at 403 nm and 417 nm (Table 5.1). The broadening observed at $l \geq 1$ is due to the coexistence of free porphyrin maximum at 412 nm and these two new bands. In a first approximation it can be assumed that there is no further contribution of free monomeric TAPP to the spectrum at l = 0.93 since there is no local maximum visible any more at 412 nm. Thus, the spectrum at l = 0.93 represents the signal of TAPP molecules that are both bound to PSS and undergo self-interaction. It is assumed that both bands at 403 nm and 417 nm belong to the self-aggregated and bound TAPP species. The presence of a third species here is unlikely due to the sharp isosbestic point.

Band splitting of dye signals upon self-interaction can be explained by exciton theory [149-151]. Also several publications cover the description of spectral shifts of porphyrins with exciton theory (see [152-154] and references therein). Dimerization generally leads to a splitting of excited states into two levels of higher and lower energy. Exciton theory in principal can explain by a semi-classical vector model whether transitions to one of the two new levels are forbidden. Thus, experimental observations of shifts in absorption spectra may be related to inter-dye orientation. The exciton splitting energy (the separation of the exciton levels) is given by eq. 5.1 where **M** is the transition moment of monomer and R is the center-to-center distance of the dyes. There is a proportional relation of the strength of monomer transition moment to the splitting energy and an inverse relation between exciton splitting and the distance of dipoles. In most experimental cases it is a reasonable approximation to assume that two dye molecules interact in a coplanar orientation. Thus, interdipole orientation can be defined by two angles: the twist angle α between the two polarization axes of the coupling dyes and the angle θ between the dye center connection line and their dipole (see Figure 5.5). Eq. 5.1 also provides a relation of these angles to the splitting energy.

$$\Delta E = \frac{2|\boldsymbol{M}|^2}{R^3}(cos\alpha + 3cos^2\theta) \qquad (5.1)$$

For the case with twist angle α = 0, exciton energy levels are given in Figure 5.6-1 and Figure 5.6-2. Here either the dipoles are oriented side-by-side ($\theta = 90^\circ$) or head-to-tail ($\theta = 0^\circ$).

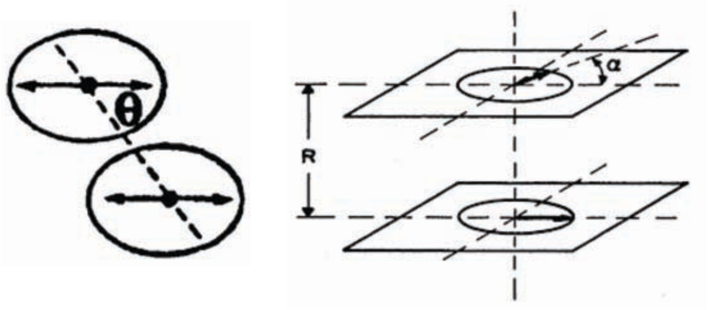

$(\alpha = 0^\circ)$ $(\theta = 90^\circ)$

Figure 5.5: Definition of angles between interaction transition dipole moments; from [149,155].

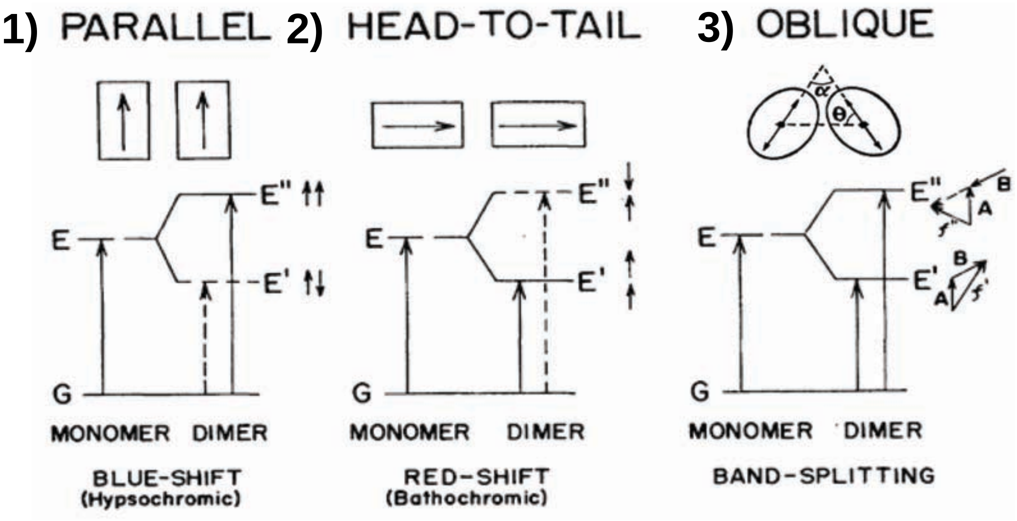

$(\alpha = 0^\circ, \theta = 90^\circ)$ $(\alpha = 0^\circ, \theta = 0^\circ)$

Figure 5.6: Relation of observable spectral shifts to coupling dipole geometry; from [151].

In the framework of exciton theory it can be shown that a side-by-side arrangement of dipoles as in Figure 5.6-1 will lead to an allowed transition of higher energy than the monomer spectrum and thus a blue-shifted signal in absorption spectrum will be observed that is referred to as “H-band“ (see Figure 5.6). For the head-to-tail stacking type a red shifted signal is expected (J-band). For geometries that do not fit in either of the two cases ($0^\circ < \alpha,\theta < 90^\circ$) it can be shown that both transitions are partially allowed and thus the band will split into two signals, one is blue-shifted, the other red-shifted in respect to the original signal. Thus, the observation of band-splitting of the porphyrin TAPP signal upon coupling with another porphyrin indicates a stacking geometry that is neither parallel, nor head-to-tail but more or less oblique. The extent of exciton splitting observed here is given in Table 5.2.

Table 5.2: Positions (wave number) of TAPP monomer and H- and J-bands of TAPP-brush aggregate.

$\tilde{\nu}_{mon}$/cm^{-1}	$\tilde{\nu}_{H}$/cm^{-1}	$\tilde{\nu}_{J}$/cm^{-1}	$\Delta\tilde{\nu}$/cm^{-1}
24272	24814	23981	833

The Soret signal of the stacked TAPP at *l* = 0.93 was fitted in a way similar as in Figure 5.3 and the result is given in Figure 5.7. Clearly the contributions from H-band and J-band after exciton splitting can be seen in the deconvolution. As it is seen in Figure 5.7 the fitting procedure results in a very good fit to the aggregate spectrum.

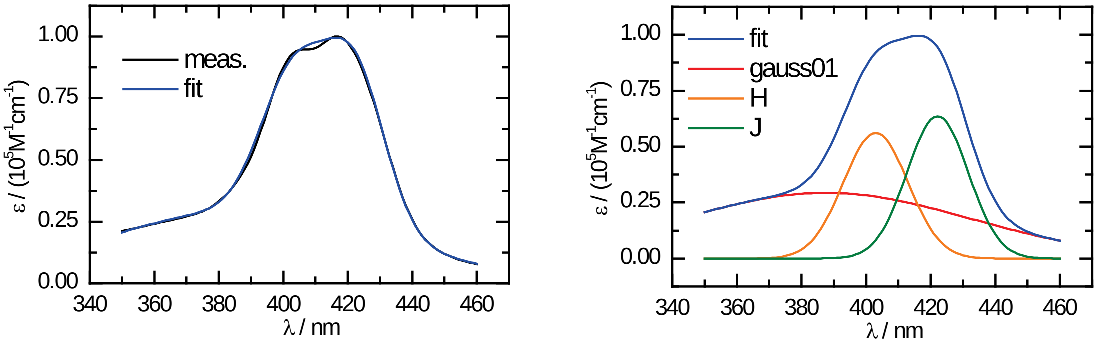

Figure 5.7: Empirical fitting procedure with three Gaussian functions of a TAPP-PSS sample at *l* = 0.93 (spectrum reproduced from Figure 5.4).

After having identified the Soret spectrum of TAPP as it is bound under self-aggregation to PSS, it now should be possible to quantitatively evaluate the equilibrium found for *l* ≥ 1: the transition from free TAPP to bound self-aggregates. The fitting procedure is demonstrated in Figure 5.8: the spectra were fitted as a weighted sum of the respective overall fit (the sum of the three Gaussians) of free TAPP and self-aggregated porphyrin. As it can be seen, this procedure provides an excellent fit to the spectrum.

The application of the described fitting procedure to the data in Figure 5.9-1 results in a linear correlation of free monomer concentration to polyelectrolyte concentration (inverse charge ratio at fixed porphyrin concentration). There is a direct conversion of free TAPP to bound porphyrin electronically coupled to another porphyrin. Thus, within the chosen approximations TAPP is solely binding in a cooperative process here.

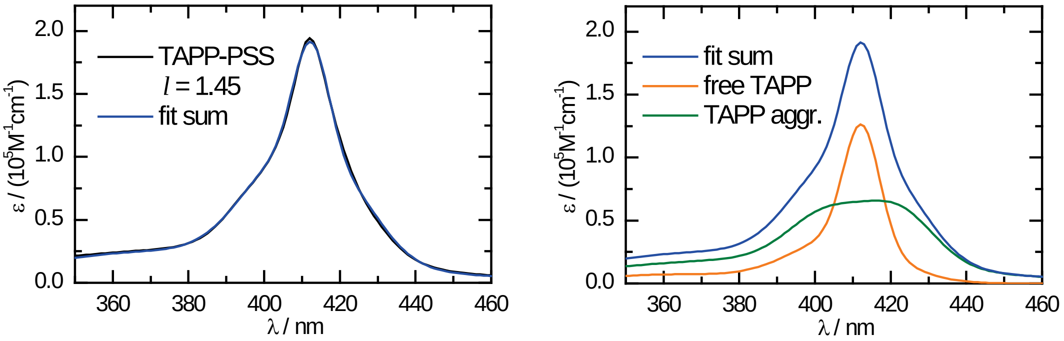

Figure 5.8: Fitting of TAPP-PSS sample with l = 1.45 (Figure 5.4) as the weighted sum of free TAPP and TAPP self-aggregate spectrum.

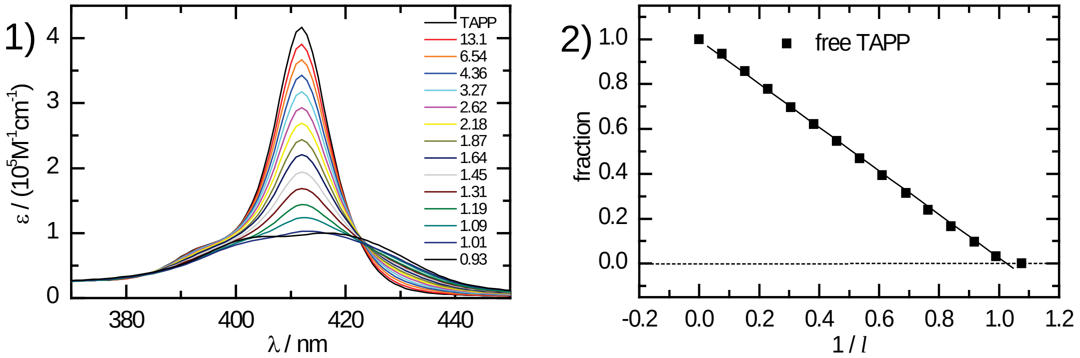

Figure 5.9: Fitting results for UV-vis titration at $l \geq 1$: (1) titration measurement; numbers in label are charge ratios l; (2) fraction of free TAPP as a function of inverse charge ratio $1/l$; fitting procedure according to Figure 5.8.

As was mentioned above, the isosbestic point at 423 nm is not crossed for samples with charge ratio $l \leq 1$ (that is with excess PSS). This can be clearly seen in Figure 5.10: upon further addition of PSS the band intensity gradually increases (the extent of hypochromicity weakens) but the band shape stays quite similar.

On a first glance the observed effect can be best described by a band that gradually shifts up without changing its shape and without passing any isosbestic point. For all spectra no local maxima can be observed at the free monomeric TAPP wavelength of 412 nm. Thus, there is obviously no free TAPP porphyrin present here which is reasonable due to PSS excess. It is questionable whether separately bound porphyrin (as in Figure 5.2) contributes to the spectra in Figure 5.10. A superposition of the spectrum of coupled TAPP with isolatedly bound TAPP would lead to a different ratio of the intensities for the two bands with a higher intensity for the 417 nm band. In addition, such a transition to isolatedly bound TAPP would have to include the presence of an isosbestic point as was the case in Figure 5.2. It should be a reasonable assumption that there is no considerable extent of isolated TAPP present here, in particular since the experiment in Figure 5.2 has shown that even a much larger excess of PSS the system only reluctantly breaks up inter-porphyrin bonds.

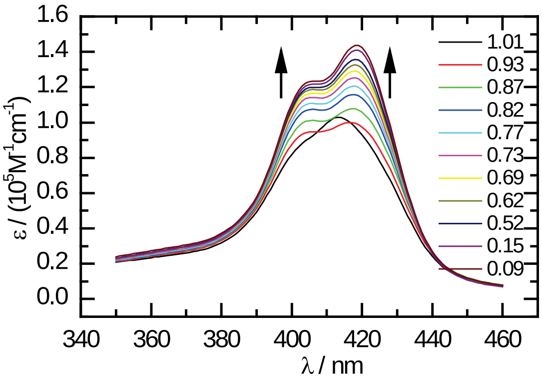

Figure 5.10: UV-vis titration results for TAPP-PSS brush for charge ratio.

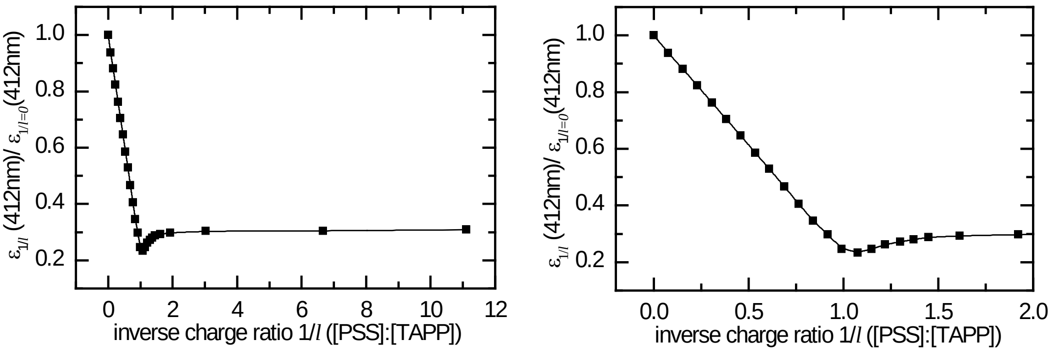

Figure 5.11: Normalized extinction coefficient of TAPP at 412 nm vs. inverse charge ratio (increasing PSS concentration from left to right).

In a plot of extinction coefficient at monomer band (412 nm) vs. inverse charge ratio $1/l$ (Figure 5.11) clearly the minimum at $l = 1$ can be seen. It was already described that intensity rises again after passing the minimum due to the weakening of hypochroism occurring at brush excess. The actual plot here in addition reveals that the extent of hypochroism decreases for excess PSS but levels off (intensity reduction to 23% of monomer level at *l* = 1; 30% for 1/*l* > 2.

If the spectral changes in Figure 5.10 are looked at more closely, there is a slight red shift of the two bands to 406 nm and 418.5 nm. Also, relative intensity of the bands slightly changes from 1:1.06 to 1:1.16. As was pointed out, it is not expected that this change results from the change of TAPP aggregate concentration in the system, but rather the explanation is given by a structural change of the porphyrin stacks themselves. Apparently, further addition of polyelectrolyte induces slight changes in the average stacking geometry that lead to red shift and the different intensity ratio of H- and J-band. Effects of hypochromism are not explained within exciton theory. Nevertheless, since the extent of hypochromism is usually related to the strength of interdipole interaction, the weakening of the effect at 1/*l* > 1 may be explained by a weakening of TAPP aggregation due to the increasing number of polyelectrolyte binding sites. Interestingly, this weakening effect levels off for a two-fold excess of PSS as was shown in Figure 5.11 and thus for 1/*l* > 2 the addition of PSS up to at least ten-fold excess does not affect the existing TAPP self-aggregates. It again should be stressed that TAPP shows a cooperative effect here in that sense that although further polyelectrolyte binding sites are added the porphyrin is not homogenously distributed but rather prefers to stay adjacent to other porphyrin molecules.

Spectroscopic properties of TAPP-PVS aggregates

It was discussed above that PSS contains aromatic groups and in principal may undergo π-π interactions with the porphyrin. Although the interpretation of results in the previous section indicated that such interactions do not significantly influence observed band shapes, it would be interesting to design a clear experiment where no such π-π interaction will take place.

Therefore, TAPP was combined with the nonaromatic but negatively charged polyelectrolyte polyvinyl sulfuric acid potassium salt (PVS) with a molecular weight of around 175.000 g/mol (as stated by the supplier Acros). An UV-vis titration in analogy to the experiments above was carried out and the results are given in Figure 5.13.

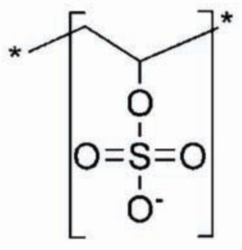

Figure 5.12: Molecular structure of polyvinyl sulfuric acid, here used as the potassium salt.

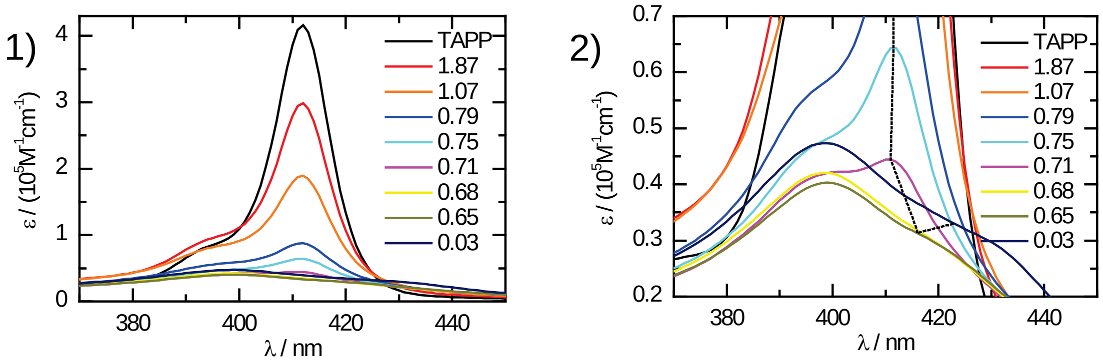

Figure 5.13: UV-vis titration of TAPP (c = 3.9 μM) with PVS; (3): expansion of (1); legend: charge ratio *l* = [TAPP]/[PVS].

The general trend in Figure 5.13 is quite similar to the results for the TAPP-PSS case. Upon PVS addition the signal of monomeric TAPP weakens and splits into a red- and blue-shifted signal (H- and J-band) and the intensity increases again after passing a minimum at a certain threshold value for the charge ratio. In addition, an isosbestic point is seen at around 427 nm. Wave numbers of H- and J-band as well as the exciton splitting is given in Table 5.3.

Table 5.3: Positions (wave number) of TAPP monomer and H- and J-bands of TAPP-PVS aggregate.

$\tilde{\nu}_{mon}$/cm^{-1}	$\tilde{\nu}_H$/cm^{-1}	$\tilde{\nu}_J$/cm^{-1}	$\Delta\tilde{\nu}$/cm^{-1}
24272	25063	24038	1025

Apparently, exciton splitting is somewhat higher as for the brush-porphyrin case. The H-band lies at 399 nm and the J-band at 416 nm. In contrast to the experiment of TAPP-PSS the minimum intensity at monomer wavelength is observed at around 1.5-fold PVS excess (l = 0.65) and a larger hypochromicity of about 8% of original value is seen (Figure 5.14).

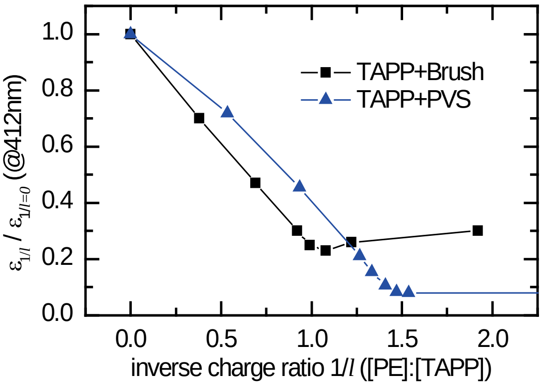

Figure 5.14: Normalized extinction coefficient of TAPP upon addition of PSS brush and PVS at 412 nm vs. the inverse charge ratio 1/l ([polyelectrolyte]/[TAPP]).

In addition, there is a significant difference of band shape for TAPP molecules aggregated on PVS polyelectrolyte if compared to the situation on PSS brush. Here the H-band shows higher intensity than the J-band with a ratio of 1.47:1 whereas TAPP on PSS splits into two levels of equal intensity. Obviously interacting TAPP dipoles are oriented differently on PVS than on PSS. The high complexity of porphyrin spectra prohibits a straightforward quantitative determination of inter-dipole orientation from the band-splitting observed here (e.g. transitions B_x and B_y are degenerate in single porphyrin but not in porphyrin aggregates, see [152] and references therein). However, the main conclusion from experiments combining TAPP with the nonaromatic PVS is that similar results are obtained as for the aromatic PSS. Thus, these results support the conclusion from above that TAPP attaches to the polyelectrolyte mainly by its peripheral charges and π-π interactions to an aromatic backbone do not considerably affect the porphyrin aggregation process. Strong differences of dye-polyelectrolyte interaction between systems with aromatic and non-aromatic polyelectrolyte templates that were reported before could not be detected in the present study [147-148,156-162]. Apparently, self-aggregation tendency of TAPP on the template dominates its binding characteristics and thus π-π TAPP-polyelectrolyte interactions do not significantly contribute here. The small differences in stacking orientation can be explained by the different chemical environment at the polyelectrolyte and this will be shown again for a different nonaromatic polyelectrolyte in chapter 8 (polysaccharide chondroitin sulfate groups of aggrecan).

5.1.2 Imaging of Complexes from NaPSS Brush and TAPP

Imaging of PSS brush - TAPP complexes

The imaging of PSS brush molecules on a mica surface by AFM is described in detail in appendix A.1. Upon addition of TAPP to the NaPSS brush there is a dramatic change of structural features, as can be seen in Figure 5.15 and Figure 5.17. Network-like structures of several 100 nm size are found, in which the previously isolated brush molecules are interconnected in a non-parallel fashion.

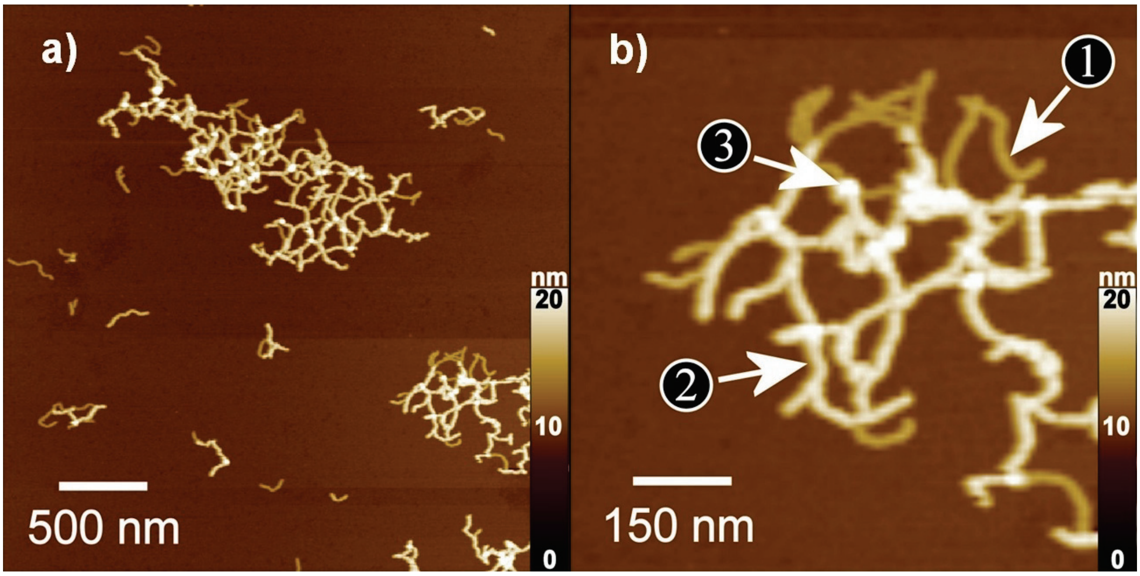

Figure 5.15: AFM height images of NaPSS brush-TAPP networks spin-coated on bare mica, (b) represents a magnified image of parts of (a); charge ratio *l* = 0.4.

A closer analysis of the network structure at the surface reveals two distinct cylindrical species of different height, as can be easily seen in Figure 5.15-b. The lower species - (1) in Figure 5.15 - has a measured height of 4.1 nm, which is close to the height of pure brushes. The second species (2) exhibits a larger height of 6.0 (see Table 5.4). Also it should be noted that species (2) is in addition wider than species (1) (see Figure 5.16). The observed networks mainly consist of the species with larger height. Additionally, in the AFM image there are several sites exhibiting much larger heights (~15 nm, (3)). These are predominantly located at network joints, but there are also network joints without this observation. The presence of species (3) can have two reasonable explanations. One simple reason for such larger heights clearly stems from three dimensional networks collapsed on the surface.

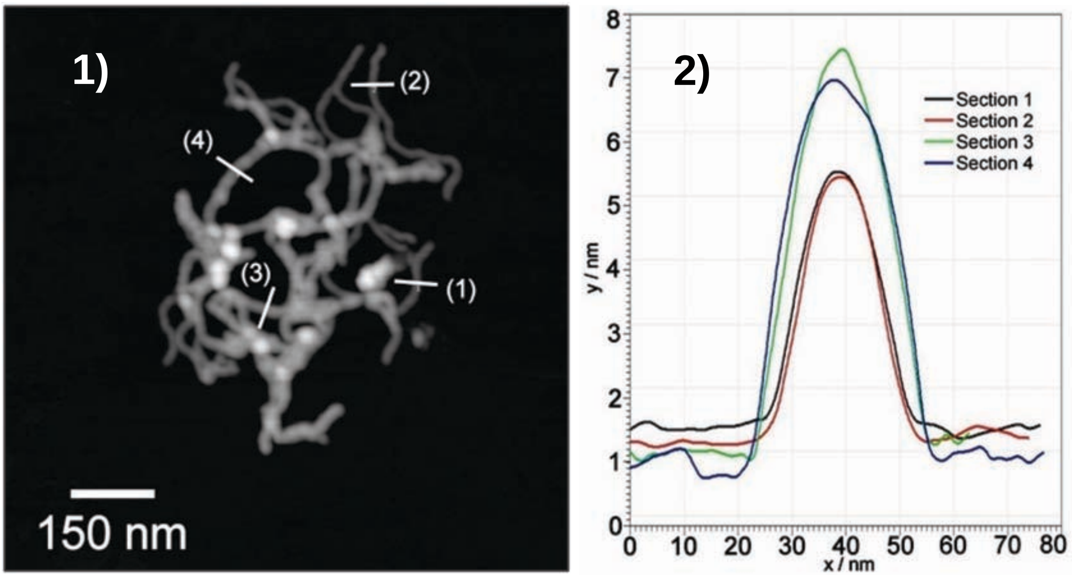

Figure 5.16: AFM height image of PSSbrush-TAPP complexes (1) and four sectional profiles (2).

Table 5.4: Measurements for heights and widths of brush species as taken from sectional profiles extracted from Figure 5.15 data; the width was taken as the full width at half maximum (see appendix B.2).

brush species	height/nm	width/nm
“low”	4.1 ± 0.2	17.9 ± 3.0
“high”	6.0 ± 0.7	24.3 ± 2.4

This effect can be well observed in particular in Figure 5.17-b1. Here obviously several network entities are packed onto each other on the surface. The white spots of collapsed network structure are well recognizable. The same phenomenon is also well resolved in the large network seen in the lower part of Figure 5.17-a1. However, also some isolated white spots of “species 3” can be found in the figures here. They also can be explained by two brush layers on top of each other but also larger clusters of porphyrin TAPP could play a role here.

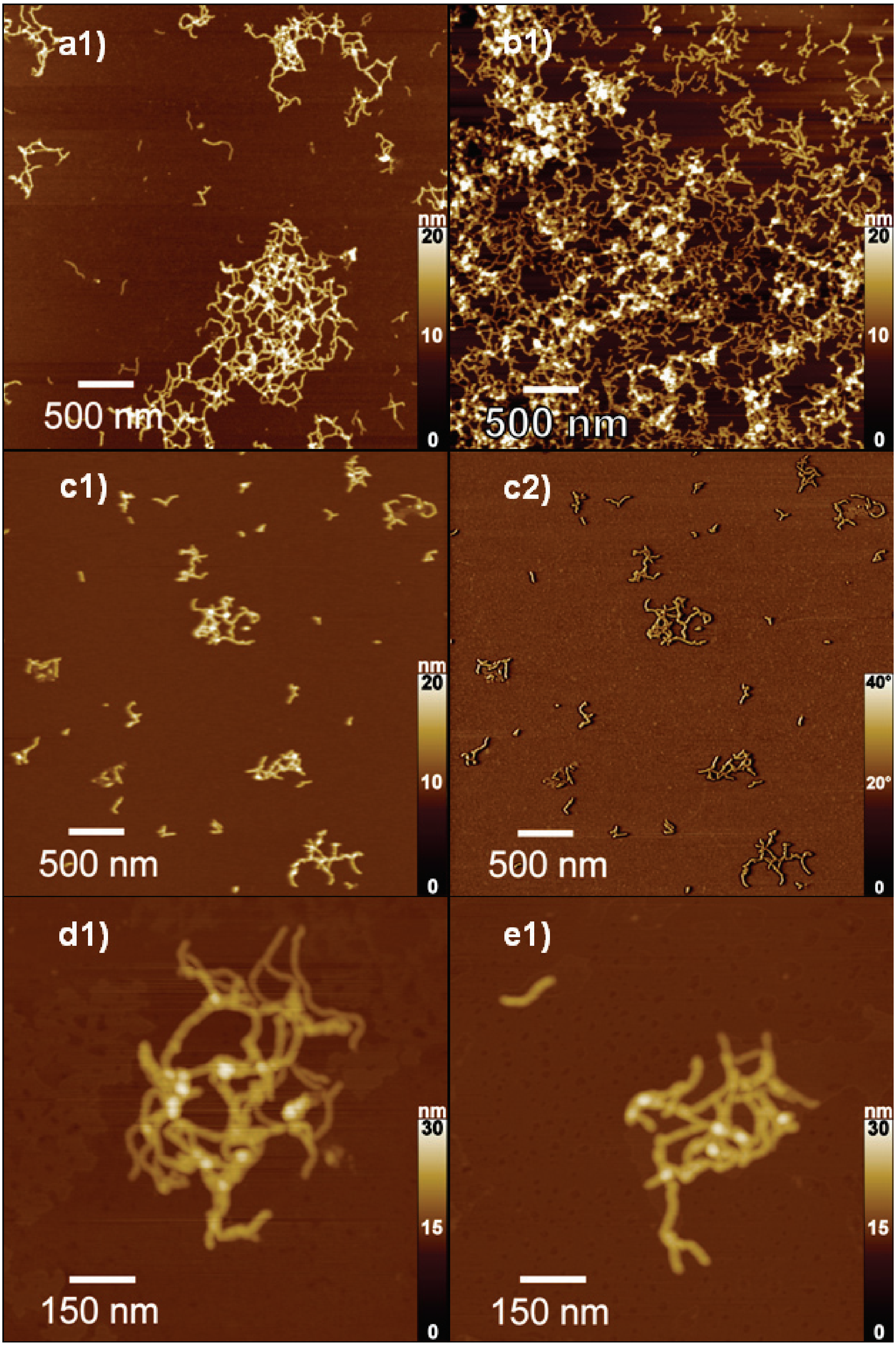

Figure 5.17: AFM height (1) and phase (2) images of NaPSS brush-TAPP networks.

It should be noted that the size distribution of the networks is quite broad, from individual brush molecules to networks of 800 nm in diameter (surface coverage in Figure 5.17-b1 presumably results from an overlay of several networks and does not represent a single very large network).

The formation of these networks may be a hierarchical process. The first step of hexarchy is the complexation of porphyrin molecules to the brush template and these brush-porphyrin complexes than assemble into networks (see scheme in Figure 5.18)

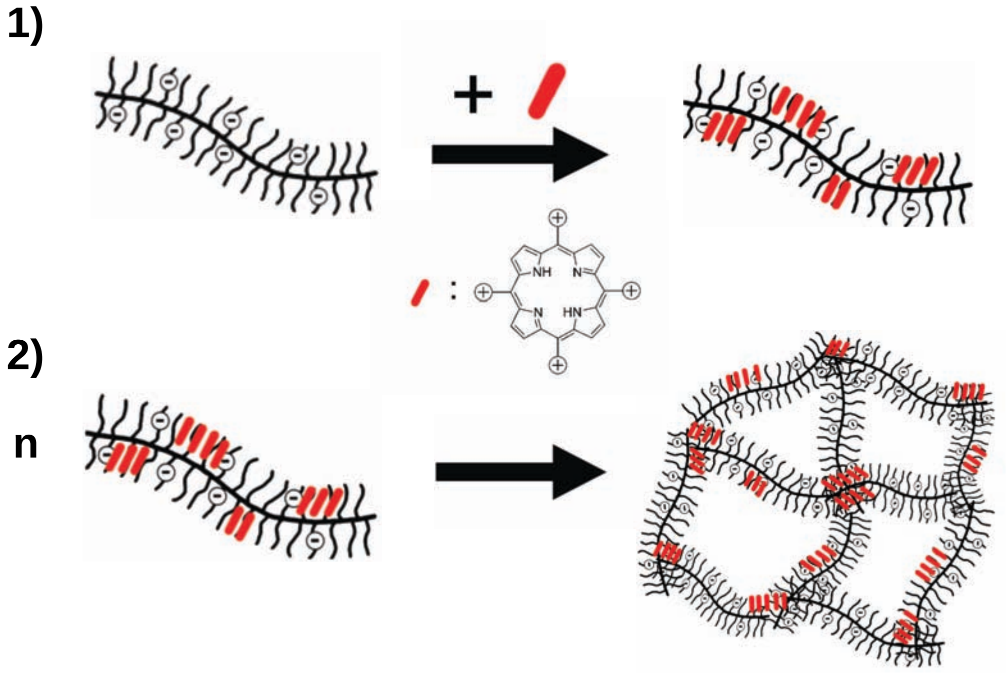

Figure 5.18: Schematic representation of hierarchical brush-porphyrin network formation. Drawing is not to scale: diameter brush: 10 nm, side-to-side distance in porphyrin: 2 nm.

The lower height species present here most likely represent brush molecules that are not loaded with porphyrin counterions whereas the higher cylindrical parts likely represent brush-porphyrin complexes. This coexistence is consistent with the excess of brush in comparison to porphyrin present in this sample. The fact that porphyrin-loaded brush and unloaded brush entities are found indicates that porphyrin counterions preferably bind in an accumulated way within the same region, leaving other brushes or brush parts empty rather than distribute uniformly. This is in accordance with a cooperative binding process as postulated based on the UV-vis results and as known for the binding of dyes to linear polyelectrolytes [144-145]. The observation of network formation is in accordance with experimental and simulation studies described in the literature in that self-assembly of rigid objects often leads to network-like objects, and stiffness likely is a prerequisite for network formation [163]. In addition, comparable experiments with combining linear flexible PSS with porphyrins yield collapsed structures rather than networks (see chapter 6).

In order to check for the possible influence of drying effects on results it was tried to immobilize and image the brush-porphyrin networks in aqueous solution on an APTES-modified surface rather than to dry in air (see Figure 5.19). In the resulting image larger structures can be seen in coexistence with single brush molecules (cf. Figure A.5). Whereas the brush molecules can be imaged quite successfully the larger structures show very bad resolution. The reason for this observation is most likely given by the fact that brush-porphyrin networks possess a smaller charge density than pure brushes because of partial charge neutralization upon network formation. Because of the lesser net charge this supramolecular objects are less strongly bound to the surface and thus will be moved by the AFM probe. Nevertheless, the network structures are apparently bound to the surface and can be seen in the images (the control experiment using non-modified negatively charged mica reveals a flat surface, thus no takes place in this case). After longer equilibration time and at higher resolution it was possible to image smaller network structures as can be seen in Figure 5.19-b. Thus, network structures can be observed in solution as well and thus do not simply represent drying artifacts. However, as pointed out before, surface-sample interaction still can be influential on sample structure and thus an imaging technique in solution without surface contact will be needed to verify the solution structure of the brush-porphyrin aggregates.

Cryo-TEM allows for the imaging of samples in their near natural state. Imaging of PSS brushes was successful at a PSS concentration that was higher than the one for AFM investigation by a factor of 10 (c_{NaPSS} = 0.5 g/L). A resulting image is given in Figure 5.20-a. The semi-flexible cylinder morphology is well resolved and the measured cross-sectional diameter of the brush molecules is 10.3 ± 1.3 nm (compare to cross-sectional dimensions on surface as determined by AFM; here the brush molecule has in contrast to the situation on surface a circular cross-sectional profile).

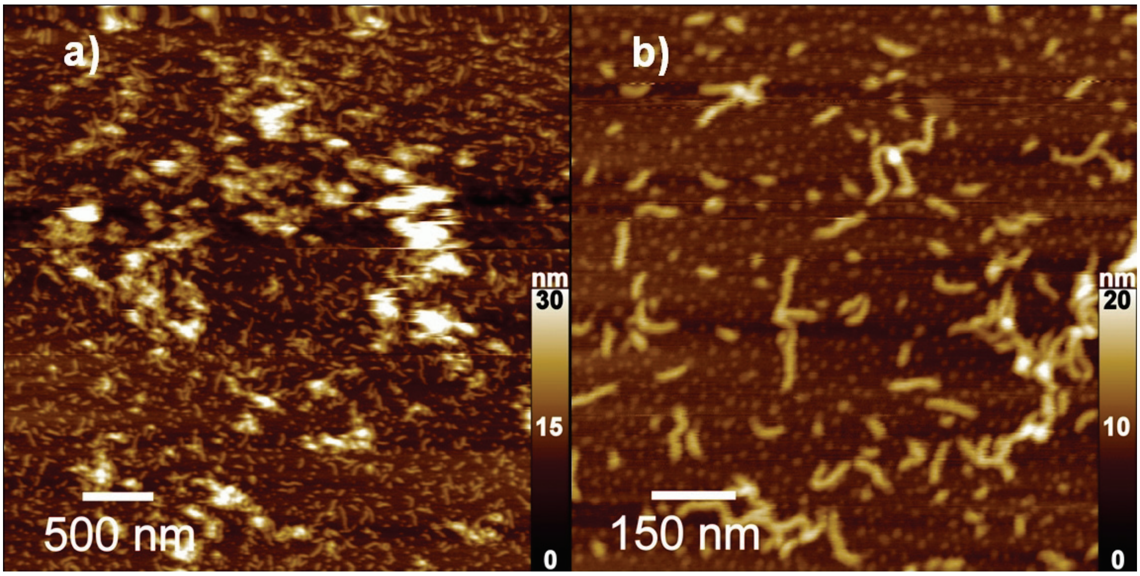

Figure 5.19: AFM height images measured in water of PSSbrush-TAPP aggregates partially immobilized on an APTES-modified mica surface.

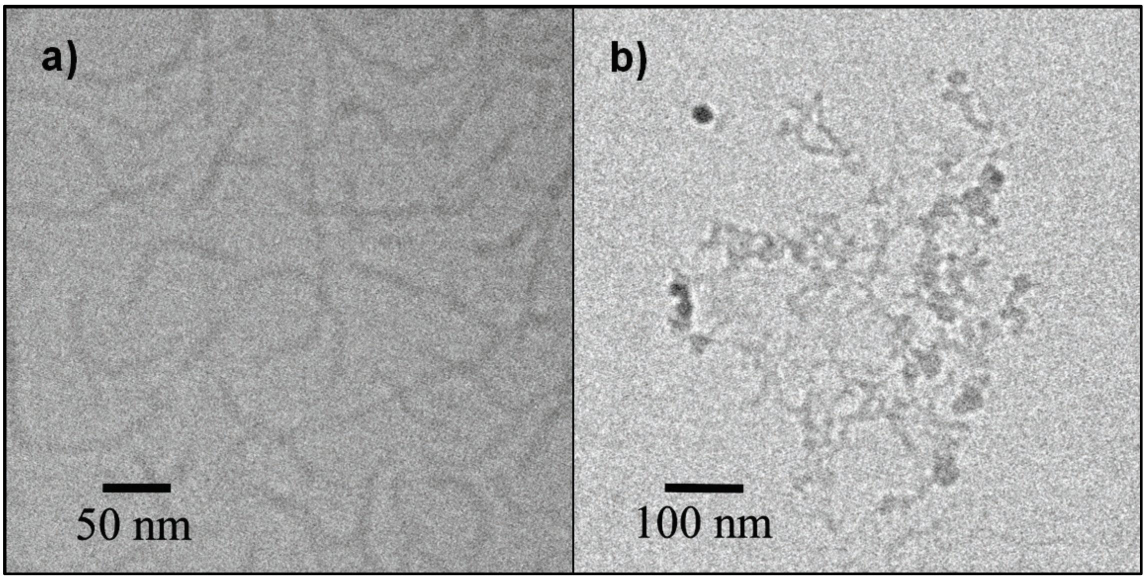

Figure 5.20: Cryo-TEM image of NaPSS brush (a) and brush-TAPP complex (b).

If TAPP is added to PSS brush the same qualitative picture in cryo-TEM was obtained as with AFM before. The aggregated object in Figure 5.20-b closely resembles network structures found on mica surface by AFM. Thus, it can be safely concluded that the network structure of PSS-TAPP complexes is not an artifact of sample-surface interaction, drying or sample deposition. The network structure is present in solution as well. However, Figure 5.20-b also shows poor resolution of structural features and in addition measurement or preparation artifacts are present.

A strongly increased imaging contrast is obtained by intrinsically staining the porphyrin dye with relatively heavy Cu. Instead of the free base porphyrin TAPP, the derivative CuTAPP with a Cu atom incorporated into the porphyrin center was used for further cryo-TEM investigations (Figure 5.21). Naturally, transforming TAPP to its copper derivative is not only enhancing contrast but also changing the properties of the porphyrin. In the next paragraphs it will be shown that the structural features of brush-porphyrin networks from TAPP and CuTAPP are fully comparable and thus for imaging investigations using CuTAPP is assumed to be comparable to using TAPP. Nevertheless, at the smaller length scales investigated by UV-vis spectroscopy differences in the stacking behavior of TAPP and CuTAPP on PSS are found and addressed in chapter 6.

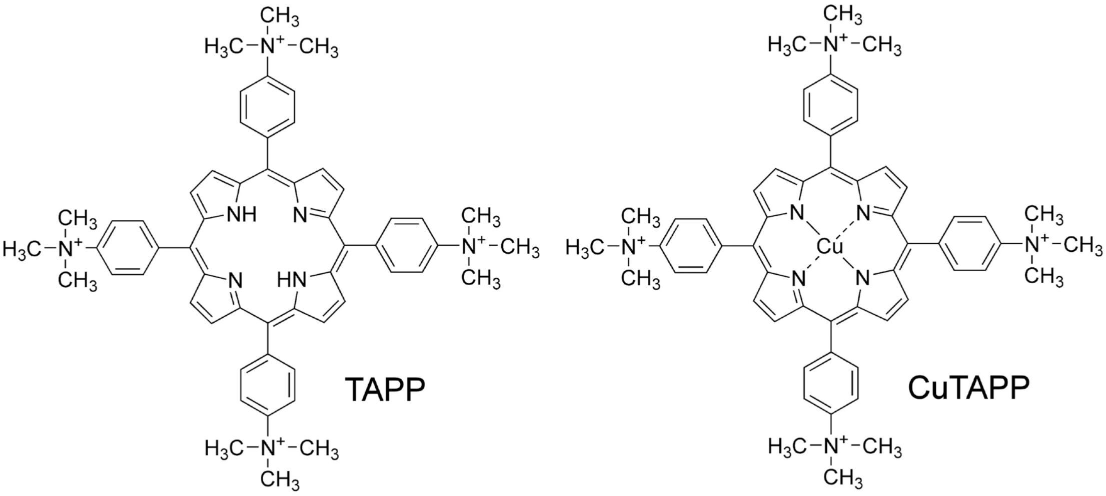

Figure 5.21: Chemical structures of porphyrin TAPP and CuTAPP; counterions of TAPP: tosylate, CuTAPP: chloride.

Apparently, the imaging of brush-CuTAPP aggregates was successful as shown in Figure 5.22. The scattering contrast of Cu allowed for detailed imaging of brush-CuTAPP assemblies. As can be seen in the images, brush-CuTAPP aggregates clearly show network structure in solution. Figure 5.22-1 exhibits very close similarity to the AFM images of PSS-TAPP networks in Figure 5.15. From the results of TAPP-brush AFM images and cryo-TEM results for TAPP-brush and CuTAPP-brush system it can be concluded that the two systems both have network structure in solution where no surface effects are present.

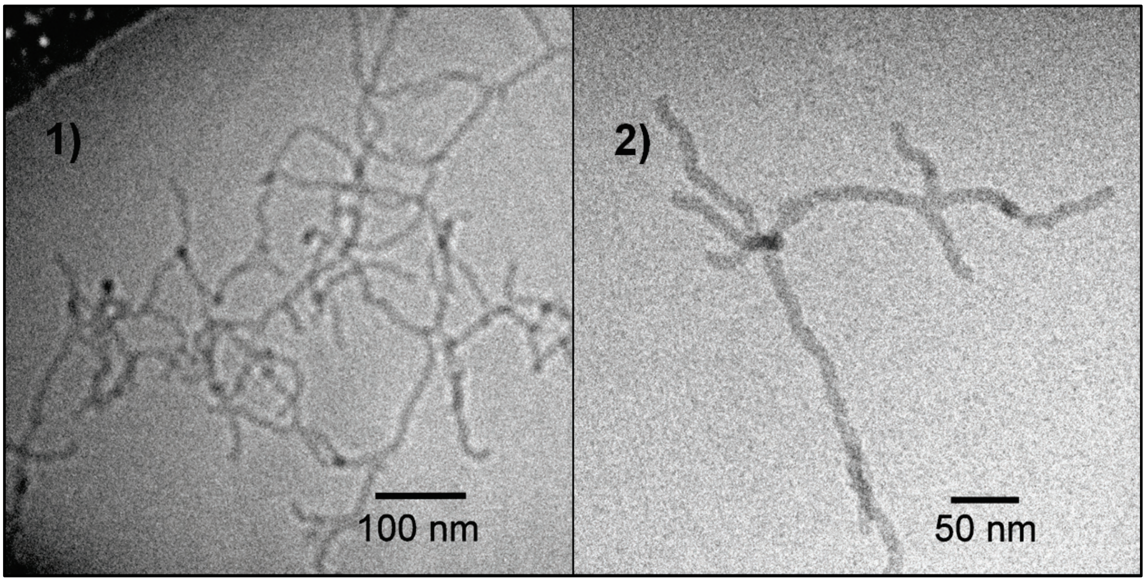

Figure 5.22: Cryo-TEM images of PSS brush – CuTAPP complexes.

The high resolution quality of Figure 5.22 enables a closer analysis of brush-porphyrin network structure. Reproducing the results from AFM images, it can be seen that the networks are not regular but show a high variety of mesh sizes. In addition, darker points can be seen in the solution picture. For the AFM images it was concluded that higher spots may result from two brush molecules of one network lying on top of each other because of the network collapse upon drying on the surface. Here (in solution) darker spots may result from two brush molecules that are on top of each other in respect to the electron beam but not necessarily touching each other. This effect may be a good explanation for the left hand dark spot in Figure 5.22-2. Nevertheless, this reasoning does not seem to explain the dark spot on the right side of Figure 5.22-2. Here an isolated region of higher intensity on one single brush structure is seen. The presence of this spot may be explained by cluster formation of porphyrin molecules on the brush template.

The TEM image in Figure 5.22-2 is taken in-focus and thus allows for a measurement of brush diameter. Very surprisingly, the diameter is with d = 10.1 ± 1.2 nm very close to the diameter of pure brush given above (10.3 ± 1.3 nm). This is in contrast to the AFM results described above but in accordance with SANS measurements, as will be presented in the next section.

5.1.3 Small-Angle Neutron Scattering of Brush-Porphyrin Aggregates

To analyze the structure of brush-porphyrin aggregates in solution on a smaller size scale, small-angle neutron scattering (SANS) was performed. Results are shown in Figure 5.23. Figure 5.23-1 shows scattering curves for the NaPSS brush in D_2O, 0.01 M NaCl, and a brush-porphyrin aggregate in D_2O. All scattering curves show the shape typical of wormlike chains [69,164]. This is to be expected as the overall network size is not covered in this experiment where the q range approximately covers a size range of up to 185 nm. The scaling in the linear part is -1.40 ± 0.05. SANS is of particular interest to resolve the cross-sectional dimension. Cross-section Guinier plots are shown in Figure 5.23-2. The linear dependence proves the rodlike structure. Quantitatively, resulting cross-sectional radii of gyration $R_{g,c}$ are $R_{g,c} = 4.9 \pm 0.1$ nm for the brush in salt-free solution, $R_{g,c} = 4.6 \pm 0.1$ nm for the brush in NaCl solution, and $R_{g,c} = 4.6 \pm 0.1$ nm for the brush-porphyrin network. Thus, the brush in salt solution shows a slightly smaller $R_{g,c}$ than in salt-free aqueous solution while the porphyrin-brush complex again shows the same $R_{g,c}$ as the brush in salt solution.

In front of the AFM results, this may be a surprising result. Evidently, in solution the porphyrin counterions associate with the polyelectrolyte brush in such a way that its cross-sectional radius of gyration is not changed. Thus, the two different heights of the brush and brush-porphyrin parts are only caused by surface interactions when preparing the AFM samples. This is in accordance with the cryo-TEM observation that brush-CuTAPP complexes show the same diameter as pure brushes (see above). Figure 5.23-3 shows cross-sectional pair distance distribution functions $P_c(r)$ that are obtained from the scattering curve by indirect Fourier transformation [165-168]. The $P_c(r)$ gives the number of distances within the diameter as a function of distance and is thus typical of the radial density profile. It allows to analyze the form factor oscillations at high q while assuming cylindrical geometry (as deduced from the cross-section Guinier plots). Again, it can be seen that all three samples are quite similar. The total diameter is between 17 and 18 nm. The $R_{g,c}$ values corresponding to these $P_c(r)$ functions are in good agreement with the ones from Guinier analysis. The slight decrease in brush diameter upon salt addition is again visible, while the complex more resembles the brush in salt solution rather than in salt-free solution.

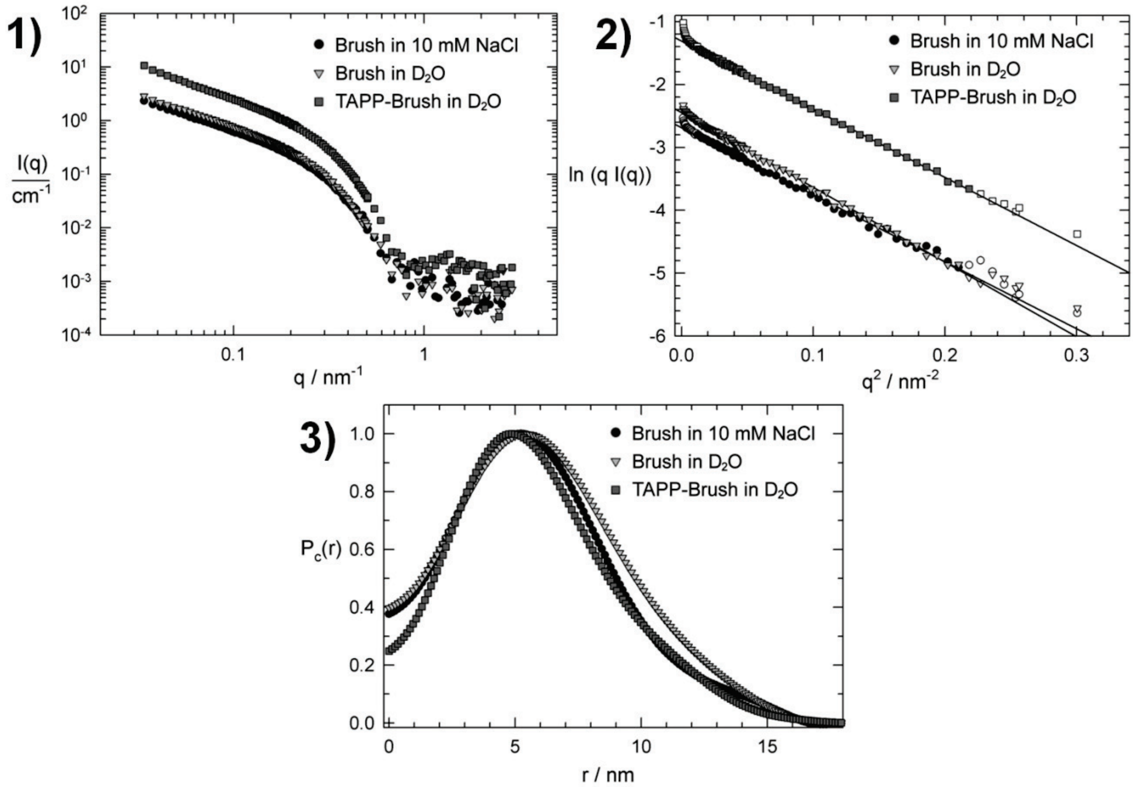

Figure 5.23: Small-angle neutron scattering of cylindrical NaPSS brush in 10 mM NaCl solution, in salt-free solution, and TAPP-brush complex (l = 0.4) in salt-free solution: (1) scattering curves $I(q)$, (2) cross-section Guinier plot (filled symbols were included in the Guinier extrapolation), (3) normalized cross-sectional pair distance distribution functions $P_c(r)$, c(NaPSS) = 1 g/L (4.8 mM).

This may be understood by the fact that binding of porphyrin decreases the brush net charge. The density distribution is very similar to the brush in NaCl. However, as compared to the brush in NaCl, the maximum is slightly shifted to the inside, and $P_c(r)$ is less expressed at larger r, indicating a slight shift of the main density contribution toward the interior. (The fact that $P_c(r)$ does not decrease to 0 at $P_c(0)$ is due to resolution problems; determined by q_{max}. The difference in this region thus has no physical meaning. The finite intercept is also the reason why deconvolution into a density profile is not possible; compare also [167]).

It is important to note that if two different species are present as was concluded from AFM results, pure brush and brush-porphyrin cylindrical parts, the $P_c(r)$ represents an overlay of the two $P_c(r)$ functions. However, a clearly altered density profile or thickness change in 50% of the cylindrical species would be clearly visible also in the averaged $P_c(r)$. Thus, SANS clearly shows that no significant thickness change of the brush upon binding of porphyrin is observed in solution. While the normalized scattering curves of brush and complex almost exactly overlay (not shown) and thus structural parameters including persistence length are very similar, there is a clear difference in absolute scattering intensity (Figure 5.23-1).

The difference in scattering intensity on an absolute scale (differential scattering cross section in cm^{-1}) can be translated into an estimate for the number of porphyrin molecules per brush unit, assuming in a first approximation that the partial specific volume at infinite dilution is constant, which represents a common approach for diluted polymer solutions [36]. The result is consistent with the added porphyrin at $l = 0.4$ being completely bound to the brush. The amount can be determined more exactly by analytical ultracentrifugation, which showed that no excess porphyrin stays in solution when the complex sediments, that is, the porphyrin is completely (> 98%) bound to the brush.

5.1.4 Size of Brush-Porphyrin Aggregates by Light Scattering

Whereas neutron scattering analysis provides information about size-ranges in the order of the brush diameter, light scattering enables determination of brush and network size. Light scattering experiments of NaPSS brush in salt-free aqueous solution are described in appendix A. From these results it was concluded that the PSS brush may well be characterized in the absence of added salt and that extracted diffusion coefficients may be converted to hydrodynamic radii. Because of the presence of red light absorbing porphyrins present in the samples of study here, the experiments were carried out using an infrared laser light source ($\lambda = 831.5$ nm) as described in appendix A. The studied porphyrin does not absorb infrared light and thus the presented results are not affected by this possible experimental complication.

In addition to the structural characterization of brush-porphyrin aggregates given above it is of interest to investigate the size of networks in solution and which parameters control that size. Figure 5.24 demonstrates the changes in scattering behavior that occur upon complexation and aggregation of PSS brush with TAPP. As can be seen, TAPP addition shifts the correlation function to higher relaxation times τ due to a size increase from single brush molecules to brush-porphyrin networks (Figure 5.15).

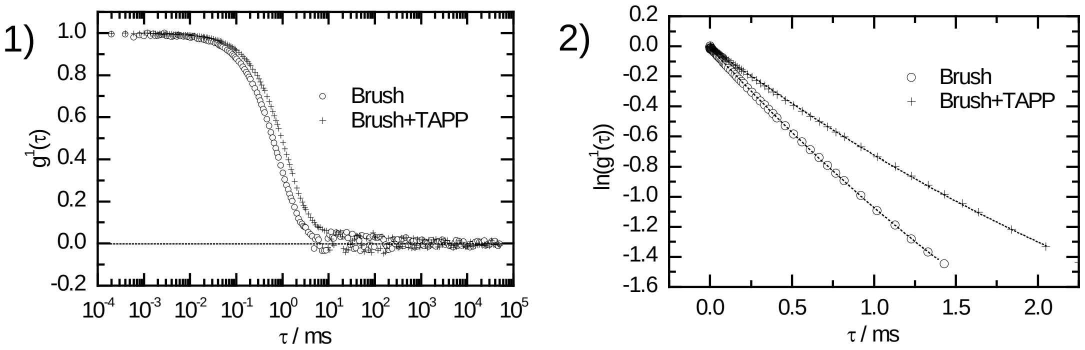

Figure 5.24: Dynamic light scattering results for pure PSS brush and PSS-TAPP (*l* = 0.4) aggregates at 90° (IR laser); 1) electric field autocorrelation function; 2) second order cumulant evaluation of 1.

Since obviously porphyrin molecules act as linker molecules that interconnect brush molecules, it is expected that adding more porphyrin linkers should generally increase network size. In order to test the impact of this influential parameter and if network size can be controlled by adjusting it, the porphyrin concentration was varied at constant brush concentration. To quantify the ratio of porphyrin to brush the charge ratio *l* was used, as it was introduced above. The ratio *l* is the concentration of positive charges introduced to the system by the porphyrin TAPP divided by the concentration of negative charges from PSS brush molecules. A ratio of *l* = 1 indicates charge stoichiometry, that is each binding site of PSS brush may theoretically be occupied by a porphyrin charge. In general, at this charge ratio precipitation of aggregated material was obtained, that is the formed aggregates are not colloidally stabilized. It is a reasonable conclusion that the stabilization of water-soluble aggregates that were found for the experiment in Figure 5.24 is at least partially explained by the charged nature of the aggregates. The rest charge is deriving from the fact that there is an excess of brush charge centers (l = 0.4, so in theory up to 40% of PSS charge sites may be occupied) and thus upon complexation PSS charge is only partially neutralized. All experiments described in this section are carried out at polyelectrolyte excess, since the interest lies in the characterization of polyelectrolyte-dye aggregates formed and stabilized in aqueous solution. Naturally, charge excess conditions may as well be realized with excess of porphyrin to PSS brush. Nevertheless, this condition of counterion TAPP excess (*l* > 1) is not desired here since the porphyrin molecule (in contrast to the polyelectrolyte) is too small to efficiently measure its hydrodynamic radius at the chosen low concentration. Thus, it is not possible to measure the size of pure component before addition of the second one. Additionally, it may be expected that the local excess of porphyrin charge upon addition of few brush molecules may induce the build-up of few large networks that may be rather widely distributed in size and thus may prevent clean characterization of aggregate build-up. In short, here only brush charge excess conditions were studied.

Starting from pure brush molecules (l = 0), a series of samples with increasing porphyrin but constant brush concentration was prepared and measured with infrared dynamic light scattering. The angle dependent plots of extracted diffusion coefficient (correlation function analysis by second order cumulant expansion) for some selected samples are given in Figure 5.25. Clearly, diffusion coefficients decrease upon further addition and complexation with TAPP. Apparently, the idea of TAPP acting as linker molecule describes this behavior very well. Linear extrapolation of the plots in Figure 5.25 to zero scattering angle and converting the diffusion coefficients to hydrodynamic radii results in Figure 5.26. From the plot of size of brush-porphyrin aggregates it is evident that aggregate size correlates very well with the TAPP to porphyrin ratio in a linear regime from l = 0 to l = 0.6 (black measurement points in Figure 5.26). The apparent hydrodynamic radius increases from 36 nm to 84 nm within the linear regime. In Figure 5.27 the relative scattering intensities at angles $\theta = 50°$ and $\theta = 90°$ reported as a multiple of pure brush scattering are shown. The relative intensity rises from 1 to 70 at $\theta = 50°$ and from 1 to 33 at $\theta = 90°$ when the charge ratio is lifted from l = 0 to l = 0.6. The scattering intensity exhibits a very similar linear dependence on charge ratio as was reported for the hydrodynamic radius. All sample represented in Figure 5.26 are clear solutions that contain the water soluble aggregate. Remarkably, aggregate size and intensity of the samples are well reproducible and remain constant for at least 4 weeks (for some selected sample even after 4 months no change was observed).

For aggregates with ratios larger than l = 0.7 (not appearing in Figure 5.26) spontaneous percolation and precipitation of solid red aggregate material is obtained and thus light scattering characterization for l > 0.7 is not feasible. The aggregates here are not colloidally stabilized due to the high extent of charge neutralization as was discussed above.

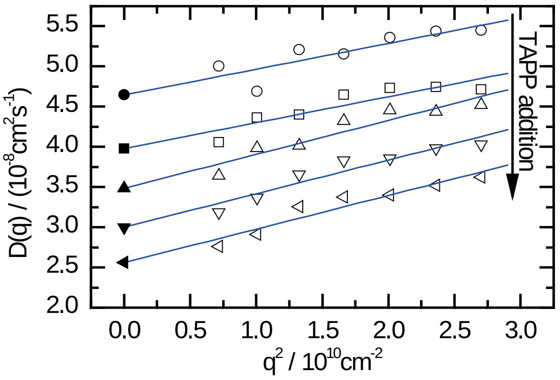

Figure 5.25: Angular dependent presentation of light scattering results from PSS-TAPP aggregates as taken from cumulant analysis. Increasing TAPP content from top to bottom: charge ratio *l* = 0.11; 0.23; 0.31; 0.47; 0.66.

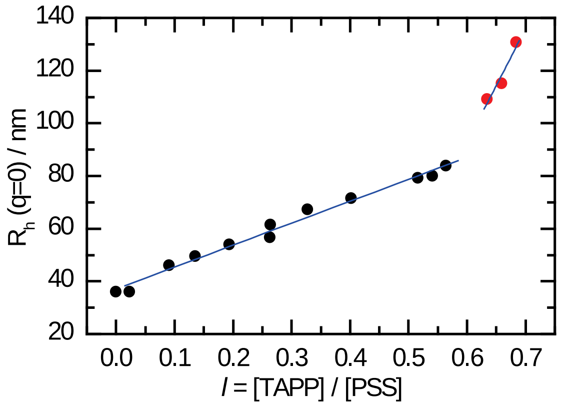

Figure 5.26: Hydrodynamic radii R$_h$ (extrapolated to zero angle) of brush-porphyrin aggregates versus the charge ratio of porphyrin to brush.

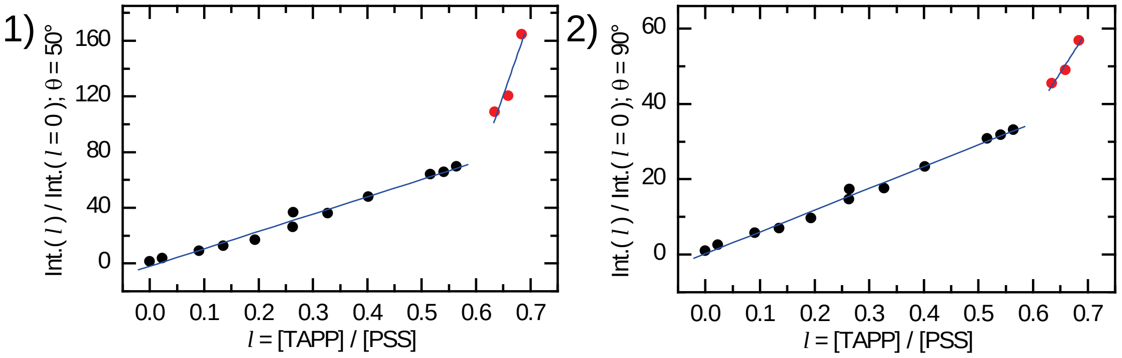

Figure 5.27: Scattering intensity at angle θ = 50° (1) and θ = 90° (2) as a multiple of pure brush scattering intensity (*l* = 0).

In the transition regime with $0.6 < l < 0.7$ (red measurement points in Figure 5.26 and Figure 5.27) brush-porphyrin aggregates with much larger radii and scattering intensity are obtained than would be expected from an expansion of the linear regime at $l < 0.6$. Presumably, the onset of percolation is seen here.

In addition to the average values of R_h and intensity given here, it is of interest to investigate the size distribution of brush-porphyrin networks. AFM (see e.g. Figure 5.15) indicated a quite broad distribution of network size. Nevertheless, AFM imaging only gives poor statistics since only a small fraction of the sample is imaged. In this respect, light scattering is more powerful since it averages over the very large number of molecules in the scattering volume.

A cumulant expansion for pure brush light scattering in Figure 5.24-2 shows deviations from linearity. That is because the PSS brush molecules have a distribution of brush lengths given by the synthetic route chosen for their preparation (see appendix A.1). This distribution is manifested in the ratio of molecular weights $M_w/M_n = 1.5$ (appendix A.1). Thus, cumulant expansion gives a number of $PDI_{cum} = 0.18$ for the pure brush (Figure 5.28). Apparently, the polydispersity of samples increases upon network formation due to TAPP addition. Already at very low TAPP-to-brush ratios PDI_{cum} is distinctively larger. Upon further addition of TAPP a trend of increasing polydispersity can be seen in Figure 5.28. PDI_{cum} reaches 0.28 at $l = 0.7$. Thus, the result from AFM that networks of different sizes are formed during the self-assembly process is reproduced by light scattering.

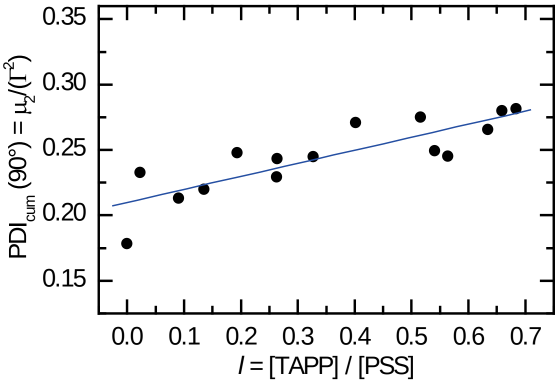

Figure 5.28: Polydispersity index PDI_{cum} from cumulant expansion at 90° for the samples of Figure 5.26.

5.1.5 Influence of Sample Preparation Protocol

When investigating self-assembly processes, it is of interest whether the resulting structures depend on the preparation procedure, i.e., are kinetically frozen, or represent equilibrium structures, which usually means the same structures can be obtained via different preparation routes. While complexes of two oppositely charged polyelectrolytes usually represent kinetically trapped structures due to the high number of charges [169-170], recently described assemblies of ionic dendrimers with divalent dye counterions were shown to be equilibrium structures [19-21]. On the basis of charge numbers, the system investigated here may be considered as “in between”, and thus the influence of sample preparation is highly interesting. The samples presented above were prepared by adding porphyrin to brush, since in then it is assured that during sample preparation there is always excess of brush. This may be important since complexes may precipitate in excess of porphyrin. So if during preparation the regime of the “phase diagram” where the sample usually precipitates is crossed, it may be that the precipitate formed is not redissolved because of kinetic trapping. A clear solution as final thermodynamic state may not be reached. Adding porphyrin to brush to reach a final brush concentration of c(NaPSS) = 240 μM and charge ratio l = 0.4 gives a clear solution. Dynamic light scattering yielded different results depending on the way of preparation: lower radii (R_h = 71-76 nm) which are well reproducible if the samples were stirred during drop wise addition of porphyrin and higher radii (R_h = 147-183 nm) with lower definition in size if TAPP was added to a still solution and the sample was mixed after the addition of each drop (Figure 5.29, Table 5.5).

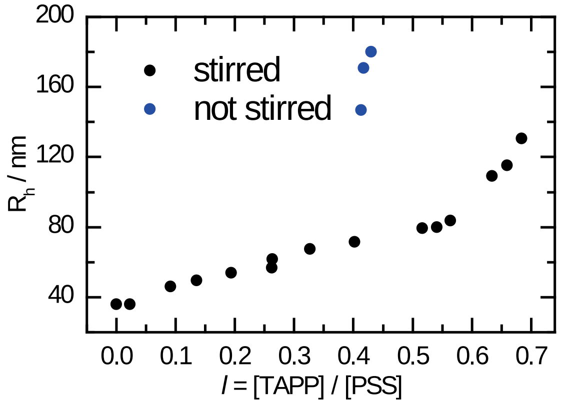

Figure 5.29: Hydrodynamic radii R_h (extrapolated to zero angle) of brush-porphyrin aggregates for stirred and not-stirred samples; results for stirred samples are reproduced

from Figure 5.26.

Table 5.5: Light scattering results for TAPP-brush samples obtained by different preparation methods, c(NaPSS) = 240 μM (50 mg/L), *l* = 0.4.

	TAPP to brush	**Brush to TAPP**
no stirring	final solution: clear R_h = 147-183 nm	final solution: clear R_h = 193-290 nm intermediate turbidity at *l* = 2.8
stirring	final solution: clear R_h = 71-76 nm	final solution: turbid intermediate turbidity at *l* = 2.8

The origin of this observation may lie in the temporary distribution of TAPP molecules throughout the sample. When one drop of porphyrin is added to a still brush solution locally, a small volume with higher TAPP concentration and thus excess of TAPP relative to brush molecules is created. Some very large aggregates may form locally that do not redissolve later, and thus a larger ensemble-averaged hydrodynamic radius results. Hence, structures resulting from preparation without stirring may be considered kinetically controlled. In contrast, if the porphyrin is added to a turbulent brush solution, TAPP will be immediately distributed throughout the total sample volume and local porphyrin excess can be avoided. Therefore, it was decided to focus on the preparation via addition of porphyrin to brush under stirring and all samples discussed in this text (apart from the current section) were prepared via this route. Both for stirring and no stirring, the resulting network sizes stayed constant for several months.

To further investigate the influence of sample preparation on network size, also the opposite procedure was applied, that is, adding the brush solution to a porphyrin solution. Upon addition of the third drop of brush solution (*l* = 2.8) turbidity was observed (for both stirring and not). Distinguishing “clear” and “turbid” thereby is most obvious by looking at a screen showing the transmitted laser beam pattern (Figure 5.30).

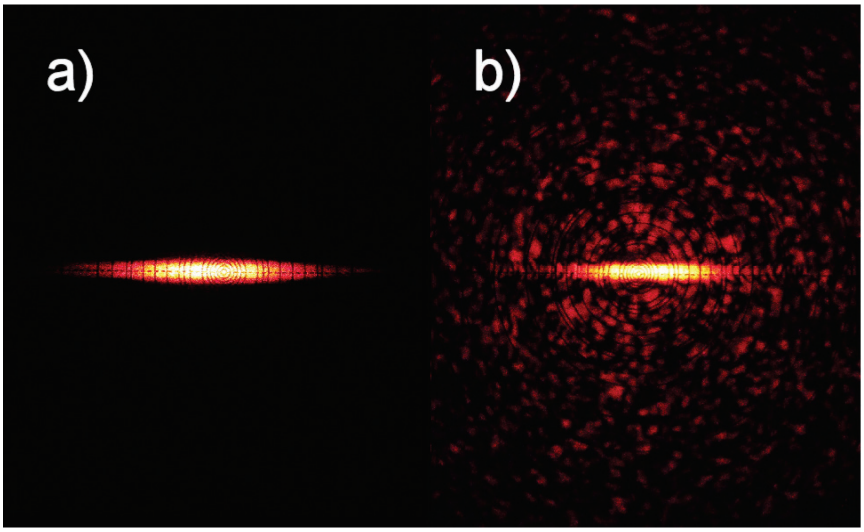

Figure 5.30: He-Ne laser pattern in transmission geometry on a screen during the process of drop wise sample preparation: a) c(NaPSS) = 43 μM, l = 4 (clear sample), b) c(NaPSS) = 60 μM, l = 2.8 (turbid sample, multiple scattering).

Addition of further drops to reach c(NaPSS) = 240 μM and l = 0.4 under stirring caused the sample to remain turbid. In contrast, without stirring the solution went back to clear. The explanation may again be related to the distribution of components (here the NaPSS brush) during addition. Thus, in combination it may be concluded that, in particular under stirring, results strongly depend on the sequence of component addition. However, this does not necessarily mean that by the preparation method chosen in the main part of this study (addition of porphyrin to brush under stirring) the aggregates were kinetically trapped. The reason for the influence of preparation technique may rather be within the phase regimes that are crossed during sample preparation in case of intermediate precipitation (or intermediate formation of larger aggregates) in porphyrin excess. Therefore, as mentioned above, the chosen preparation method avoids crossing this regime. Results of this section show the importance of investigating variations in the preparation procedure for the self-assembly of strongly interacting building blocks.

5.2 Brush-TAPP Complexes in Salt Solution

As the self-assembled structures investigated within the scope of this thesis are based on ionic interaction, addition of low-molecular-mass salt such as NaCl should influence the structure formation due to screening of electrostatics. Therefore, NaCl solution was added to a stable brush-TAPP sample with $l = 0.4$ that was previously prepared in salt-free solution. Time-dependent light scattering experiments show a decrease of the hydrodynamic radius from $R_h = 71.5$ nm to $R_h = 32$ nm within 1-2 days when the salt-free sample was prepared by stirring and from $R_h = 183$ nm to $R_h = 28$ nm within 8 h when there was no stirring during sample preparation. The final hydrodynamic radius represents the size of the NaPSS brush only; that is, networks are disconnected upon salt addition and individual brush molecules remain (see Figure 5.31). The time dependent decay of scattering intensity of an unstirred sample due to network disconnection is shown in Figure 5.32.

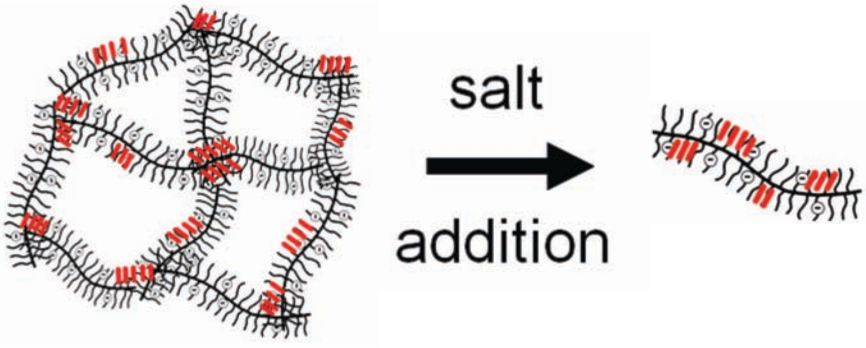

Figure 5.31: Scheme of network disconnection by salt. The red bars represent TAPP porphyrin molecules.

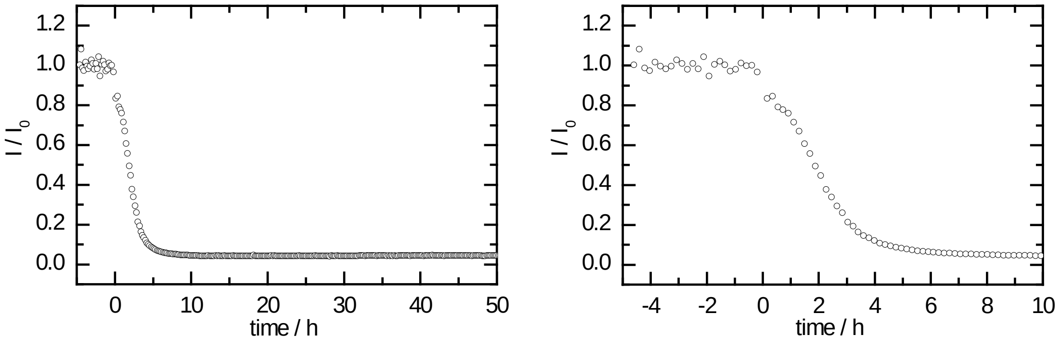

Figure 5.32: Time dependent decay of scattering intensity at 30°. Addition of 10 mM NaCl at t = 0. Right figure is enlargement of left figure.

Figure 5.33 shows UV-vis spectra of the resulting brush samples. The spectrum is the one typical of the porphyrin-NaPSS complexes with stacked porphyrins in difference to the spectrum of the noninteracting porphyrins. Thus, the network is dissolved but the porphyrin molecules stay connected with the brush.

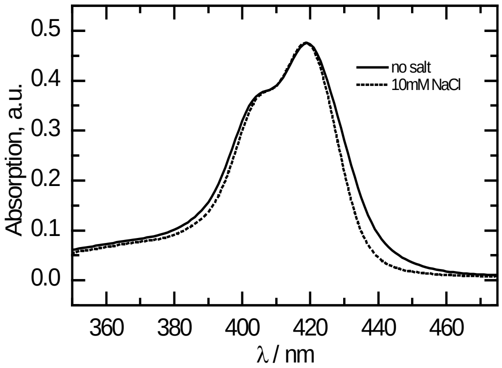

Figure 5.33: UV-vis Soret band before and after addition of 10 mM NaCl for a TAPP-brush aggregate at *l* = 0.4.

This is confirmed by the AFM images in Figure 5.34 that show individual brushes with larger height than the pure brush (see Table 5.6) , in accordance with brush-porphyrin complexes present in the networks.

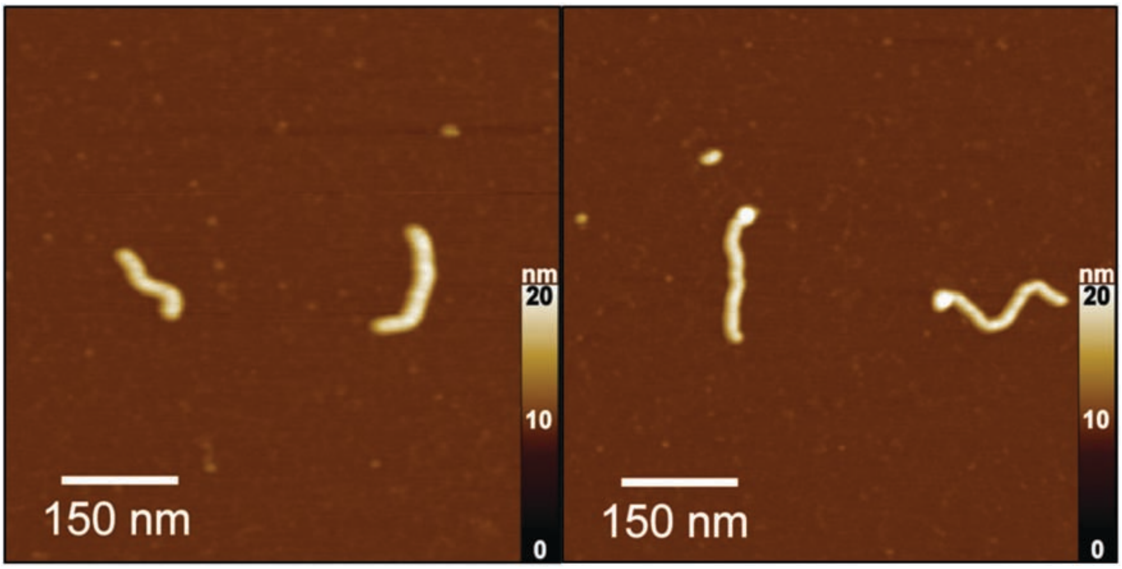

Figure 5.34: AFM height images of cylindrical brush-porphyrin complexes after network disconnection with 10 mM NaCl.

Table 5.6: Cross-sectional dimensions of brush-porphyrin complexes in salt, sectional profiles taken from Figure 5.34.

height/nm	width/nm
8.6 ± 0.3	24.5 ± 1.5

Because of the added salt an AFM sample preparation was chosen that does not rely on sample deposition by drying in contrast to Figure 5.15. Freshly cleaved mica was exposed to the sample solution for 5 min and extensively rinsed with water afterwards The possibility to immobilize the brush-porphyrin complexes on the negatively charged mica surface indicates that the brush-porphyrin complex is positively charged; that is, there is charge inversion of the polyelectrolyte upon complexation of NaPSS with TAPP. For comparison, negatively charged (pure) NaPSS brushes cannot be immobilized on a mica surface by the same method.

Figure 5.35 shows SANS results of samples in salt solution as cross-section Guinier representation. Again scattering curves (not shown) differ in intensity but almost not in shape. Thus, no substantial change of brush thickness, density profile, and persistence length of the brush-porphyrin complex as compared to the brush is observed in solution. Cross-section Guinier plots reveal a radius of gyration of $R_{g,c}$ = 4.6 ± 0.1 nm that does not differ whether TAPP or CuTAPP is used, even though the band shifts in UV-vis spectroscopy (see above) indicate a different stacking behavior of TAPP and CuTAPP on the brush template.

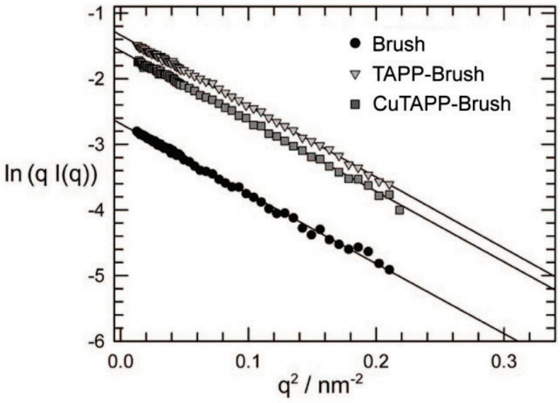

Figure 5.35: SANS of NaPSS brush in 10 mM NaCl solution, TAPP-brush complex (l = 0.4) in 10 mM NaCl and CuTAPP-brush complex (l = 0.4) in 10 mM NaCl: cross-section Guinier plot (filled symbols were included in the Guinier extrapolation).

Likewise, the cross-section pair distance distribution $P_c(r)$ function (not shown) again indicates almost no change in the cross-sectional dimensions. The fact that the structural features stay unchanged upon porphyrin binding is of particular interest because brush-surfactant complexes in organic solvent in contrast show an increase in diameter and a decrease in persistence length [164]. These results again demonstrate the hierarchical structure formation of networks investigated in this study, where the higher-level networks are dissolved upon salt addition. This finding proves that this level is based on electrostatic interactions. The first level of organization remains intact even in a salt solution of 10 mM NaCl. This is reasonable as electrostatics is strong here with tetravalent TAPP counterions as opposed to monovalent screening ions and particularly since additional π-π interactions are possible. Thus, by addition of salt single PSS brushes decorated with porphyrins can be obtained. These may be interesting as functional molecular assemblies. Porphyrin stacks are of interest for many reasons, molecular electronics, and photoconductivity being only examples. The polymer template here may provide a much more stable and size controlled assembly than porphyrin stacks investigated by other authors. Thus, this structure could provide an important model system, but also mechanical stability and processability may make it more appropriate for applications. On the other hand, the brush-porphyrin networks may combine special optical and mechanical properties. In addition, the possibility to disconnect the network by facile salt addition may also be interesting for potential applications that rely on the network properties responding to added salt or otherwise caused changes in the environmental ionic strength.

5.3 Brush-TAPP Complexes in the Presence of DMSO

The motivation for the research presented in this chapter is directly linked to section 4.2: if it is possible to switch the valency of negative tetravalent porphyrins by protonation of the core, it may be possible to switch the positive TAPP by deprotonation of the two R_2NH groups in the porphyrin (see Figure 5.36).

Literature on deprotonation of free base porphyrins reports that in aqueous medium R_2N^- is a stronger base than OH^- so that deprotonation does not take place upon NaOH addition (see section 2.2 [56-57]). The experiment shown in Figure 5.37 confirmed this reasoning in that there is the typical 4-band free base fingerprint spectrum for TAPP in

0.1 M NaOH. In combination with the observation that violet TAPP does not change its color upon addition of base, it can be concluded that TAPP cannot be protonated by sodium hydroxide in water.

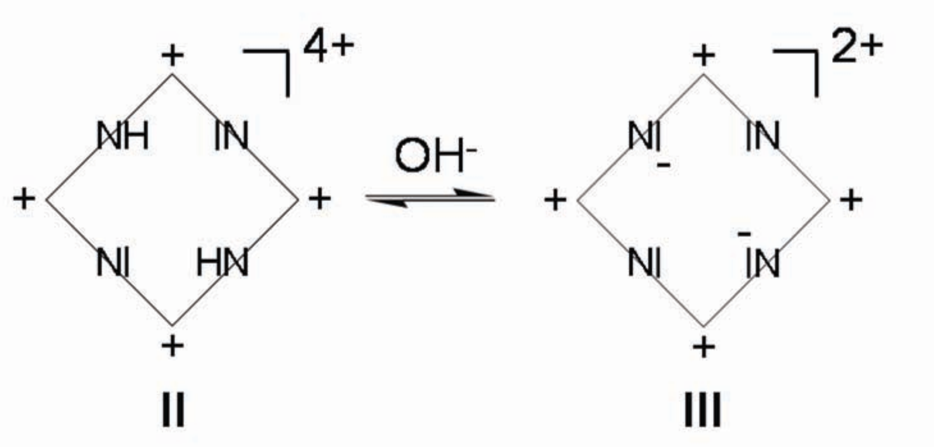

Figure 5.36: Schematic representation of the deprotonation of positively charged tetravalent porphyrin, scheme is part of Figure 2.9.

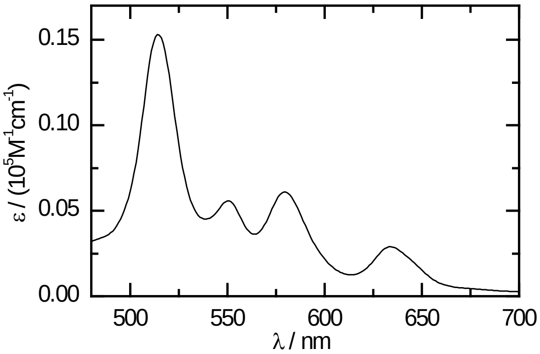

Figure 5.37: Absorption spectrum of TAPP c = 160 µM in 0.1 M NaOH in water.

However, inspired by literature where it is stated that aprotic DMSO can substantially increase the basicity of hydroxide ions due to the absence of hydroxide stabilization by hydrogen bonds, the solvent was exchanged to a 90/10 (weight based) DMSO/water mixture [57,171-174]. Both TAPP and PSS brush are well soluble in this solvent. This new system opens three new routes of experiments. First, the behavior of porphyrin-PSS aggregation in a solvent different from water can be compared to the aqueous case. Second, addition of NaOH to pure porphyrin TAPP in DMSO/water may potentially induce porphyrin self-aggregation and, last but not least, the behavior of brush-porphyrin aggregates may be influenced by NaOH in DMSO/water.

Figure 5.38 gives the UV-vis spectrum of the violet porphyrin TAPP in DMSO/H_2O

solution at neutral conditions. This is again the characteristic spectrum of the free base. Thus, TAPP is present in the non-aggregated and protonated form at the chosen concentration in DMSO/water. Due to the solvent exchange the Soret maximum is shifted from 412 nm to 418 nm.

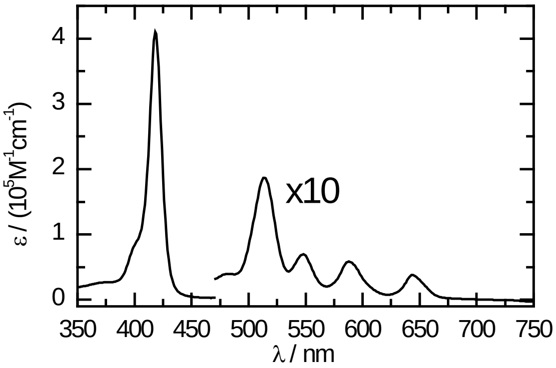

Figure 5.38: Absorption spectrum of TAPP c = 30 μM in DMSO/water at neutral conditions.

A first experiment to investigate brush-porphyrin complexation in the DMSO/water solvent mixture was to mix the components at charge stoichiometry (*l* = 1). Conducting this experiment, spontaneous percolation and precipitation of a red aggregate is observed, very similar to the behavior in pure water. Thus, obviously PSS brush and porphyrin TAPP form complexes in DMSO/water that precipitate at charge stoichiometry.

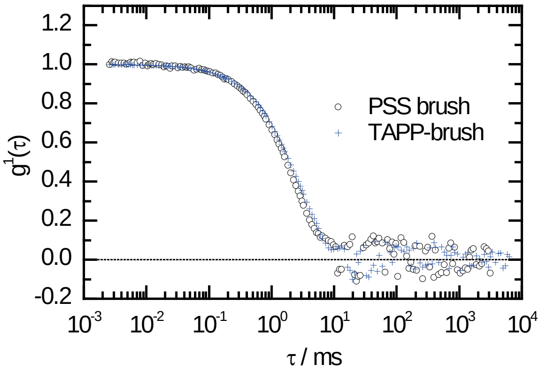

Figure 5.39: Electric field correlation function from DLS (IR laser, 90°) for PSS brush and TAPP-PSS brush, *l* = 0.4 in DMSO/water 90/10.

However, an experiment measuring the size of pure brush and brush-porphyrin samples at *l* = 0.4 resulted in only a slight size increase of the apparent hydrodynamic radius (IR laser, 90°) from R_h = 48.8 nm for the pure brush in DMSO/Water to R_h = 51.5 nm for the brush-TAPP sample (Figure 5.39).

An increase in scattering intensity from pure brush to brush-porphyrin by a factor of 8.1 was observed (relative light scattering intensities as multiples of solvent scattering: TAPP/1.23, brush/10.7, brush-TAPP/86.8). Thus, obviously no distinctive supramolecular assembly formation of brush molecules takes place at *l* = 0.4. The relative dielectric permittivity of DMSO/Water 90/10 is ε_r = 58.4 [175] and thus this solvent mixture is considerably less polar than pure water (ε_r = 78). This difference may be one reason for the different aggregation behavior. However, the increase of scattering intensity indicates that TAPP binds to the brush and this binding process can explain the precipitation of solid material at charge stoichiometry by full charge neutralization.

The binding of TAPP in DMSO/water can in addition be seen by spectral shifts that are induced by the binding process. Combining TAPP with excess PSS brush resulted in a color shift from violet (pure TAPP) to light-brown very similar to the observations that were made for pure aqueous solution. The spectrum of PSS-bound TAPP is given in Figure 5.40. As it can be seen, the TAPP spectrum is red-shifted and exhibits a reduction of intensity. Evidently, these results show that TAPP is binding to PSS brush and self-interacts on the polyelectrolyte.

Thus, for the case in neutral DMSO/water solution it can be concluded that at comparable charge ratio *l* brush-porphyrin complexes are formed but do not further assemble to larger supramolecular structures such as networks due to the different solvent if compared to the case in aqueous solution.

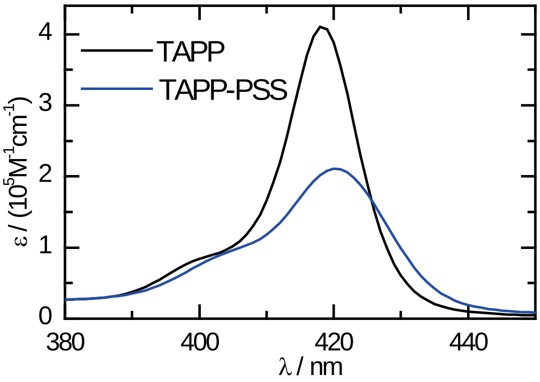

Figure 5.40: UV-vis spectrum of TAPP and TAPP-PSS brush complexes (*l* = 0.4) in DMSO/water 90/10.

In the next step, samples in DMSO/water with added sodium hydroxide were studied. Before discussing results for porphyrin and brush-porphyrin samples, the solubility of NaOH in DMSO has to be investigated. For DMSO with low water content a maximum solubility of NaOH is cited as c = 2.6 mM in [173]. Nevertheless, in order to get a first result if DMSO/water solvent may promote basicity of NaOH to such an extent that porphyrin TAPP becomes deprotonated a sample with 0.1 M NaOH content was prepared (arguably due to limited solubility the NaOH concentration will be lower than this nominal value). Albeit an observed turbidity due to the solubility issue, a strong color change from violet to green is observed. Figure 5.41 shows the color differences of TAPP samples at 0.1 M NaOH in aqueous solution as well as in the DMSO/water mixture and the quantitative spectral changes can be seen in the spectrum given in Figure 5.42.

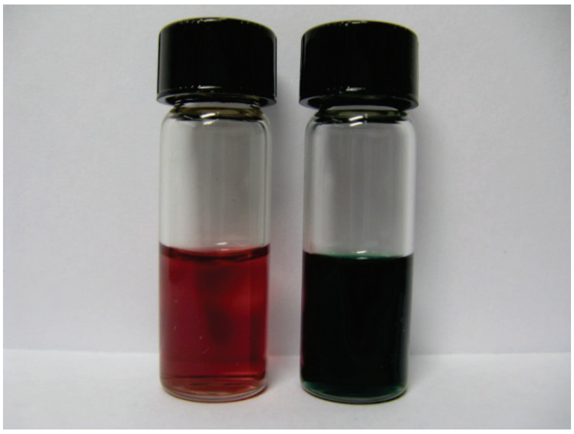

Figure 5.41: Photograph of TAPP samples; left (red): TAPP in 0.1 M NaOH in water (TAPP neutral in DMSO/H_2O shows identical color); right (green): TAPP in 0.1 M NaOH in DMSO/H_2O.

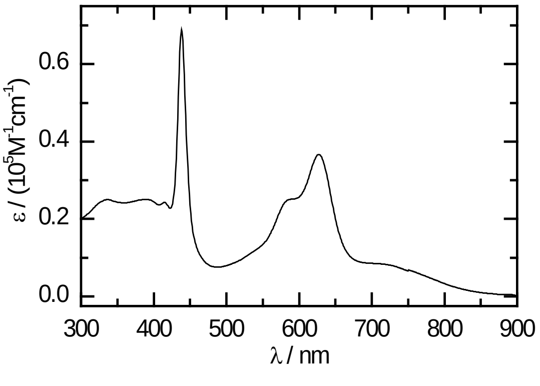

Figure 5.42: Absorption spectrum of TAPP c = 30 μM in 0.1 M NaOH in DMSO/H_2O.

Although the solution is not fully clear due to solubility issues of NaOH, the UV/vis spectrum gives valuable insights into the charge state of TAPP. The Soret peak is shifted to the red (from 418 nm to 438 nm) and in the Q-band region the spectrum transforms into a 2-band spectrum. This behavior as well as the color change to green is in analogy to the situation for TPPS porphyrin upon HCl addition (Figure 4.5). For both protonation and deprotonation a porphyrin molecule changes from D_{2h} to D_{4h} symmetry and thus similarities in spectra for this two routes are expected (see Figure 2.9). Thus, in conclusion, TAPP may be deprotonated by sodium hydroxide in DMSO. To the best knowledge of the author this has not been reported before.

The assembly of negatively charged porphyrin TPPS to nanorods in acidic conditions is explained in literature in part by its zwitterionic character and the valency reduction from -4 to -2. It is of interest to investigate whether deprotonation of TAPP in basic DMSO medium also may lead to porphyrin self-aggregation, since in principal a similar situation with TAPP being zwitterionic and of reduced valency is obtained. Figure 5.43 shows an image of the deprotonated TAPP sample after spin-coating on mica. Apparently, only rather flat and undefined particles on the surface are seen but no larger aggregates or nanorods (height of particles ~1.2 nm). Presumably, the observed coverage represents accumulations of unaggregated TAPP molecules (in addition large salt crystals were observed due to the sodium hydroxide; Figure 5.43 shows an image in between the crystals).

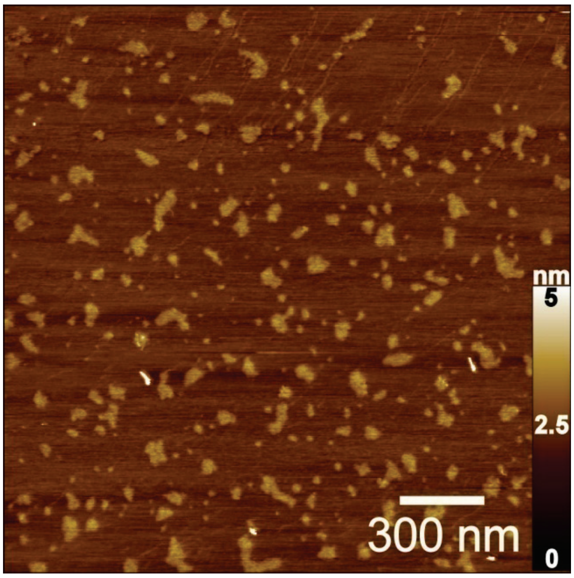

Figure 5.43: AFM height image of TAPP, c = 30 μM in DMSO/water at c(NaOH) = 0.1 M.

This result indicates that TAPP may not form self-aggregates at the chosen condition in contrast to an acidic TPPS sample where both AFM and light scattering reassured porphyrin self-aggregates that were described in literature before.

An infrared light scattering investigation of the system at c(NaOH) = 0.1 M is not feasible because of the turbidity of the sample and thus the system will be investigated at lower NaOH concentrations. It was found that at the chosen porphyrin concentration (30 μM) the lower threshold of NaOH concentration needed in DMSO/water to effectively deprotonate TAPP was between c(NaOH) = 0.5-5 mM. At 5 mM NaOH after time dependent spectral changes that will be discussed in a second step, eventually the same spectrum was obtained than in Figure 5.42 (see Figure 5.44; the sample is green).

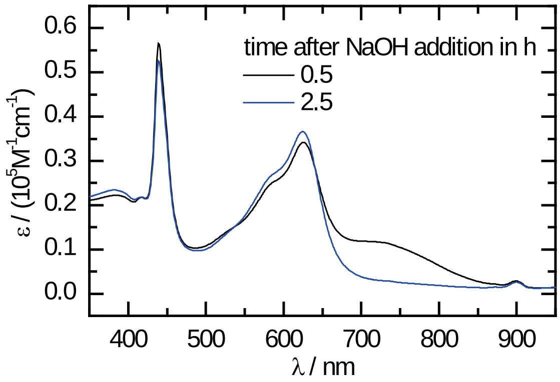

Figure 5.44: UV-vis spectrum of TAPP (30 μM) at c(NaOH) = 5 mM in DMSO/water.

A different result was obtained at c(NaOH) = 0.5 mM. Here the sample color spontaneously changed to green upon NaOH addition but then changed to blue after several hours. As can be seen from its absorption spectrum (Figure 5.45) the sample at first exhibits a red shifted Soret signal as it was also observed for higher NaOH content in the previous two spectra. However, the red shift is only observed to a partial extent at the original Soret signal is still present. In addition, with time the complete Soret signal shifts back to the free base porphyrin signal at 418 nm. Obviously, there is temporary deprotonation of TAPP but the NaOH concentration is too low to effectively maintain that state. Nevertheless, there is an additional striking feature observable in the spectrum: a very broad signal at high wavelengths (650-850 nm) that first shifts to higher wavelengths within hours and afterwards vanishes after one day. A similar but less pronounced time vanishing signal was already observed for c(NaOH) = 5 mM (Figure 5.44). Its appearance in the transition period of TAPP deprotonation indicated that this surprising signal is linked to the deprotonation mechanism. It would be interesting to further investigate this issue with methods that can better address the deprotonation mechanism (e.g. nuclear magnetic resonance (NMR) and in particular electron paramagnetic resonance (EPR)), however, that was not intended within the present scope of this thesis. Nevertheless, the UV-vis results allow to give a qualitative argument. Such very broad and long wavelength bands are usually associated with charge transfer (CT) mechanisms and thus this may be an indication that partially deprotonated TAPP porphyrin could have a radical anion character that will undergo CT complexes.

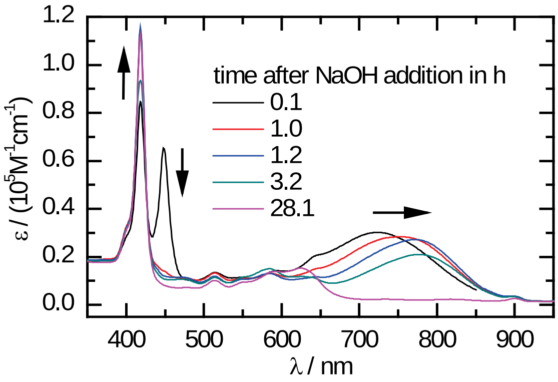

Figure 5.45: UV-vis spectra of TAPP at c(NaOH) = 0.5 mM in DMSO/water.

Besides the very interesting charge transfer effect, the experiment with 0.5 mM NaOH showed that this concentration is not sufficient to effectively deprotonate TAPP. In a next experimental step it was intended to investigate the TAPP sample with light scattering. Because of the solubility and thus turbidity issue described above for NaOH in DMSO, at first DMSO/water mixtures with different base content were measured. Pure DMSO/water (90/10) did show very low scattering intensity and a correlation function equivalent to the result for pure water. However, adding NaOH generally led to increasing scattering intensity and the build-up of a correlation function with amplitudes clearly larger than $g^2(\tau) = 1$. This is due to the bad solubility of the base in the medium that leads to aggregated NaOH particles and turbidity. This result was obtained for c(NaOH) = 100 mM, 5 mM but also for 0.5 mM. The effect for the lowest studied concentration contradicts the statement for NaOH solubility given by literature [173] but the discrepancy potentially results from different definitions of solubility (the sample with 0.5 mM NaOH is totally clear (unturbid) to the eye). Nevertheless, the conclusion from this result is that this system is not suitable to light scattering evaluation since such a low base concentration would be needed to obtain no aggregation effect of the base itself that the value would be too low to effectively deprotonate TAPP. However, in summary, UV-results show that TAPP can be deprotonated by sodium hydroxide in DMSO and the AFM investigation did not show any indication that TAPP is self-aggregating at these conditions.

CHAPTER 6

6 INFLUENCE OF POLYELECTROLYTE AND PORPHYRIN STRUCTURE ON PSS-PORPHYRIN COMPLEXATION

6.1 Influence of Polyelectrolyte Structure and Size: Linear PSS

In chapter 5 the interaction of porphyrin TAPP with a polystyrene sulfonate bottle brush was investigated. It was shown that TAPP cooperatively binds to the PSS brush and induces a build-up of polyelectrolyte brushes to nanoscale networks. In the present chapter these results will be compared to experiments where PSS brush is replaced by linear PSS polyelectrolyte. It will be investigated whether the experimental observations of chapter 5 are influenced by polyelectrolyte morphology while not changing the chemical nature of the polymer. In addition, differences between linear PSS polymers with different molecular weight will be addressed.

Spectroscopic Properties of Linear PSS-TAPP Aggregates

In this section UV-vis titrations with porphyrin TAPP and linear PSS polymers of different molecular weight and thus with different number of charged units per chain will be reported. As a control experiment Figure 6.1 shows a titration of TAPP where simple p-ethylbenzenesulfonate (sodium salt; “NaSS”) representing the repeat unit of PSS was added to the porphyrin.

Obviously, the spectrum of TAPP does not change significantly even at 50-fold excess of NaSS monomer. Concentration of NaSS here is with c = 0.36 mM still far below sodium chloride salt concentrations that induce porphyrin self-aggregation by charge shielding (see section 4.1). Apparently, NaSS also does not induce TAPP self-aggregation at the reported NaSS excess ratio of $1/l = 50$. This experiment proves that porphyrin aggregation on PSS templates, as reported in chapter 5 and in the present section, is enabled by the polyelectrolyte nature of PSS.

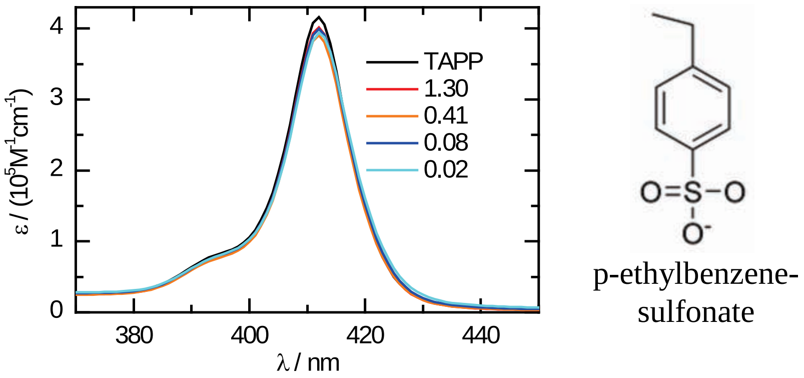

Figure 6.1: UV-vis titration of porphyrin TAPP (c = 3.4 μM) with p-ethylbenzene-sulfonate (NaSS); legend: charge ratio *l* = [TAPP]/[NaSS].

Table 6.1 gives an overview of polystyrene sulfonate samples used throughout the present thesis. As it can be seen, a wide range of degrees of polymerization is investigated. UV-vis titrations of TAPP with PSS8k and PSS43k are presented in Figure 6.2 and Figure 6.3. At first sight spectral shifts for the two linear PSS polymers are very similar to the observations with brush PSS in Figure 5.2. There is strong hypochromicity at monomer Soret wavelength and band splitting to H- and J-bands of higher and lower energy than the monomer signal. Also spectral shifts at the Q-band are comparable. Exciton splitting and band positions for PSS43k are identical to the results with PSS brush (Table 6.2). A plot of intensity at monomer band vs. relative PSS concentration (Figure 6.4) is very similar for PSS43k and PSS brush.

Table 6.1: Overview of PSS samples used in the present study.

polyelectrolyte	**M_w/g/mol**	**number of charges per molecule P_w**
NaSS monomer	206	1
PSS8k	8,600	42
PSS43k	43,300	210
PSS666k	666,000	3,230
PSS brush	7,810,000	36,300

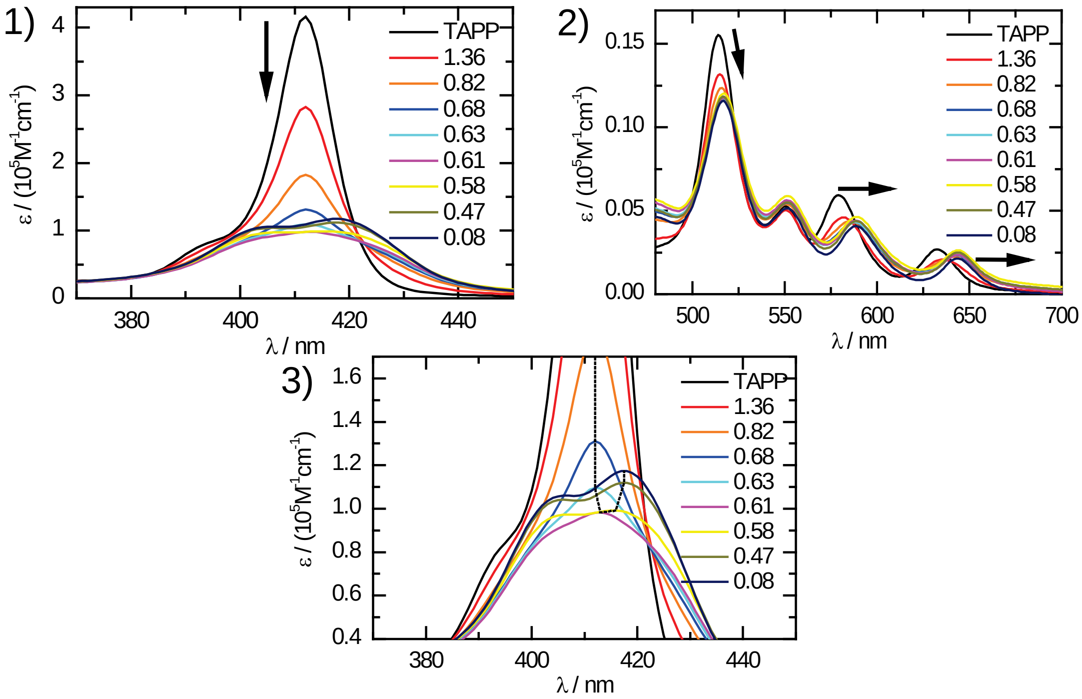

Figure 6.2: UV-vis titration of porphyrin TAPP (c = 3.8 μM) with linear PSS8k; (3): expansion of (1); legend: charge ratio *l* = [TAPP]/[PSS].

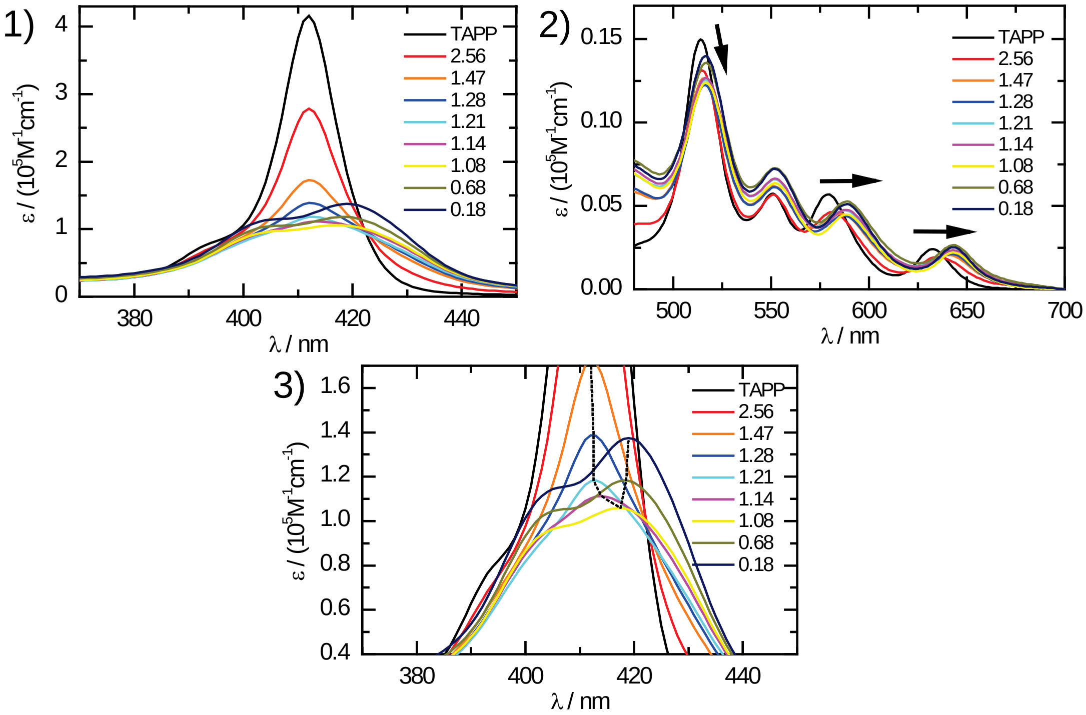

Figure 6.3: UV-vis titration of porphyrin TAPP (c = 2.9 μM) with linear PSS43k; (3): expansion of (1); legend: charge ratio *l* = [TAPP]/[PSS].

From the close similarity of spectral behavior between TAPP and PSS43k or PSS brush the following conclusions can be drawn: a) polymer chain length does not affect the local phenomenon of TAPP aggregation; at least above a threshold level of $P_w = 210$ and b) TAPP inter-dipole orientation is not affected by polyelectrolyte morphology (brush or linear).

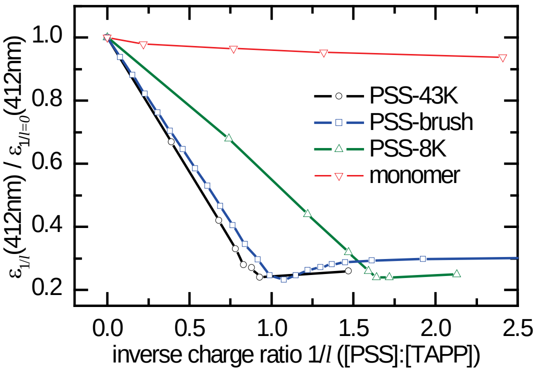

Figure 6.4: Normalized extinction coefficient at 412 nm for porphyrin TAPP plus linear PSS43k, PSS brush, linear PSS8k and the saturated monomer equivalent p-ethylbenzenesulfonate (NaSS).

Table 6.2: Positions of H- and J-band (wave numbers) of coupling TAPP on several PSS polymers; intensity ratio of J- to H-band; extent of hypochroism at monomer wavelength. All at minimum extinction coefficient at 412 nm.

polyelectrolyte	**$\tilde{\nu}_H$/cm^{-1}**	**$\tilde{\nu}_J$/cm^{-1}**	**$\Delta\tilde{\nu}$/cm^{-1}**	**$\varepsilon_J/\varepsilon_H$**	**$\varepsilon_M/\varepsilon_{M0}$**
PSS8k	24631	24096	534	1.02	0.24
PSS43k	24814	23981	833	1.11	0.25
PSS brush	24814	23981	833	1.07	0.23

The extent of splitting is smaller for PSS8k. Also, there is a difference for the charge ratio at maximum hypochroism as can be seen from Figure 6.4: whereas PSS43k and PSS brush both show minimum intensity at around $l = 1$, minimum intensity for PSS8k occurs at 1.6-fold excess of PSS. Evidently, more PSS8k is needed to achieve full self-aggregation of TAPP than for PSS43k and PSS brush. Thus, it can be concluded that there is an effect of PSS chain length on TAPP stacking that starts acting below a value of P_w which lies between $42 < P_w < 210$. Presumably, the relative high end group content of PSS8k if compared to PSS43k is negatively affecting its number of binding sites per monomer for cooperative TAPP binding. Above a threshold concentration end group effects are evidently insignificant.

Imaging of linear PSS-TAPP aggregates

As was shown by the UV-vis investigation discussed above, TAPP forms self-aggregates on linear PSS in a very similar way as on brush type PSS. It is of interest whether the TAPP binding also enables supramolecular structures as is the case for PSS brush. Therefore, potential aggregates are tried to be imaged with AFM. After spin-coating on bare mica both PSS666k and TAPP-PSS666k aggregate samples exhibited covered surfaces without distinctive structures shown. Presumably TAPP-PSS aggregates loose their structure upon deposition and drying on mica. Therefore, it was tried to image TAPP-PSS666k samples on an APTES-modified surface (see appendix B.2). Besides the charge inversion by the introduction of the amino-group containing silane, the surface also is much more hydrophobic as it can be seen by eye upon putting a droplet of water on the surface. After spin-coating a TAPP-PSS666k sample on the modified surface it was possible to image individual larger structures (Figure 6.5).

Apparently, the porphyrin links the linear polyelectrolyte molecules to relatively collapsed structures that have completely different morphology than the brush-porphyrin networks of chapter 5. As it is already expected from simple intuition, a difference in polyelectrolyte morphology will lead to different aggregates. Whereas the cylindrical brush molecules build up networks of brush cylinders, the mostly spherical linear PSS aggregates to loose structures that are composed of more or less spherical sub particles. Since the TAPP-PSS complexes were relatively problematic to image via AFM and thus it cannot be ruled out that surface interaction and deposition will lead to distortions, cryo-TEM was used to image their solution structure. In section 5.1.2 it was demonstrated that TEM contrast can be considerably increased upon replacing TAPP by its copper derivative CuTAPP. For the TAPP-brush investigations CuTAPP showed same aggregate structures with PSS brush than pure TAPP. Thus, here also linear PSS was combined with CuTAPP for cryo-TEM experiments. Results for PSS43k and PSS666k are given in Figure 6.6 and Figure 6.7.

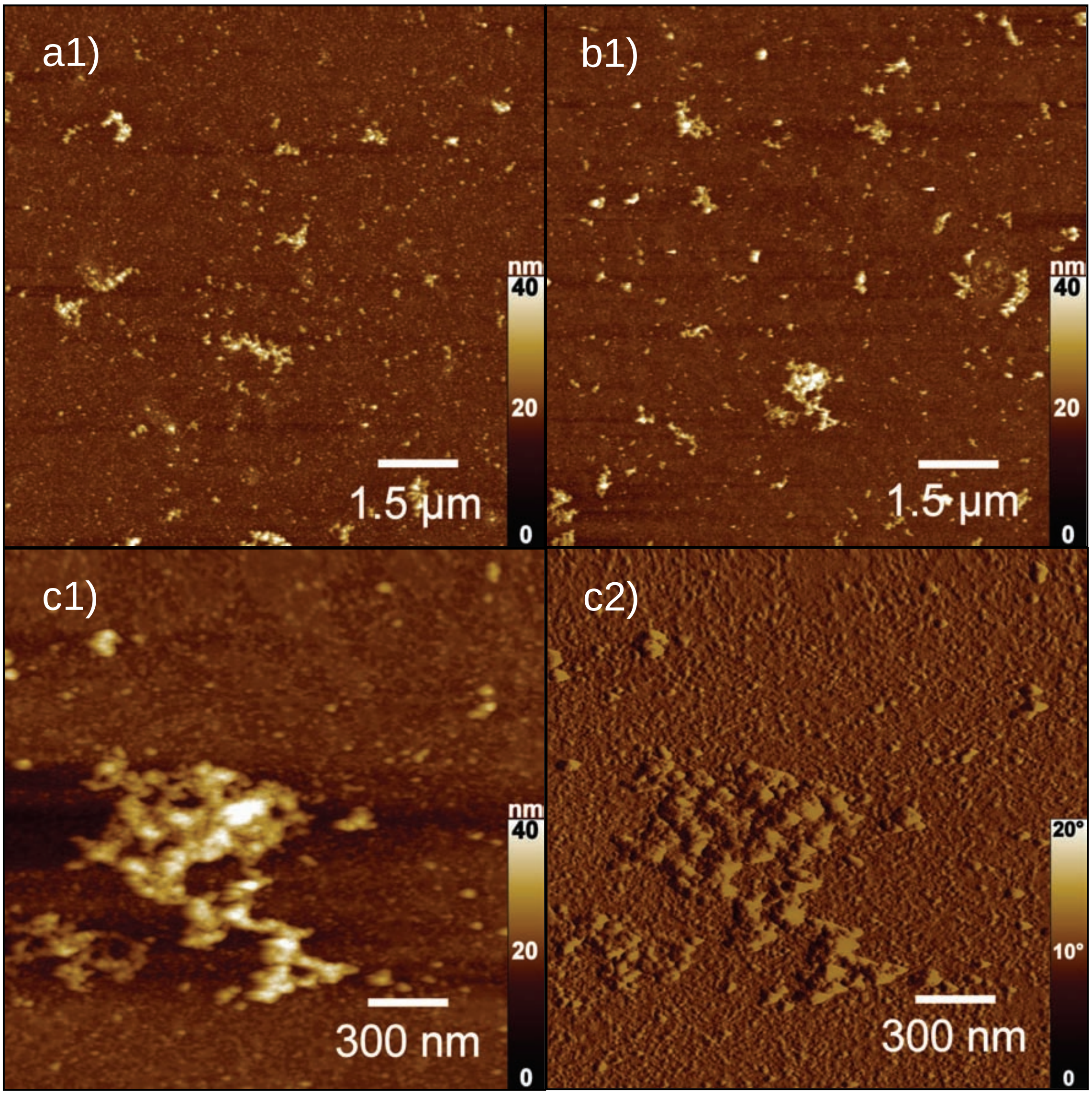

Figure 6.5: AFM images of linear PSS666k-TAPP aggregates, spin-coated on APTES-modified mica.

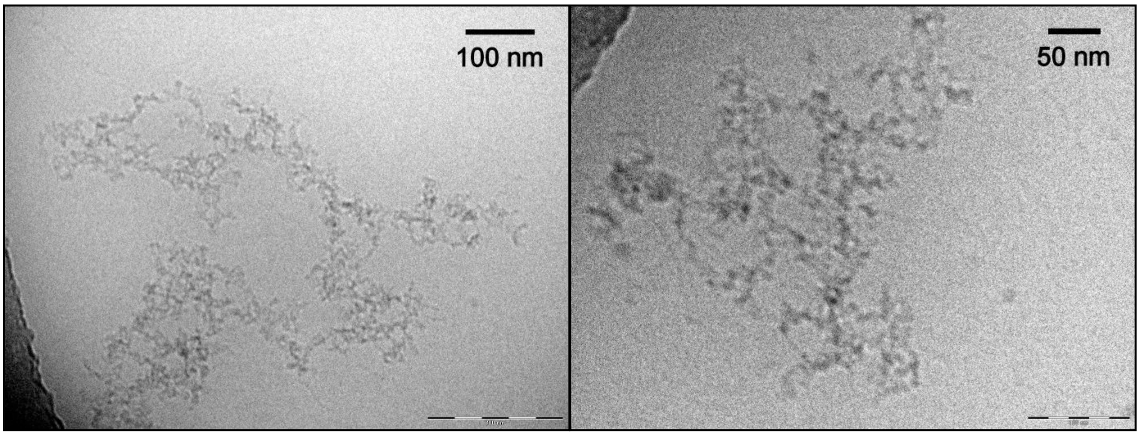

Figure 6.6: Cryo-TEM images of aggregates from linear NaPSS666k and CuTAPP.

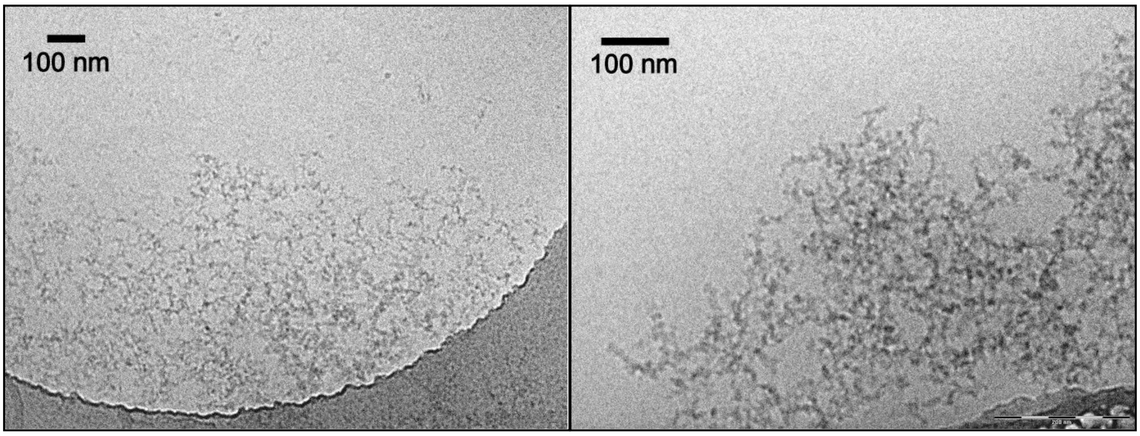

Figure 6.7: Cryo-TEM images of aggregates from linear NaPSS43k and CuTAPP.

The images closely resemble the AFM result in Figure 6.5 but have better resolution. Network-like structured assemblies of spherical sub particles can be seen. The structures seem to have fractal character. Very interestingly, there is no clear difference between the structure of aggregates involving PSS43k or PSS666k. In conclusion, structural character of PSS-TAPP aggregates is strongly related to the structure of PSS morphology and for linear PSS differences in molecular weight apparently do not affect aggregate morphology.

Light scattering investigation of linear PSS-TAPP aggregates

Light scattering behavior of linear PSS and PSS brush in salt-free water is described in appendix A and summarized in Table 6.3. The apparent hydrodynamic radii of PSS8K and PSS43K could not safely be measured even at highest laser intensity of the set up described in appendix B for the concentrations used here (c = 50 mg/L). However, due to the lower molecular weight that is specified by the producer of PSS8k and PSS43K the apparent R_h will be considerably lower.

Table 6.3 also summarizes a comparison of light scattering results at scattering angle $\theta = 90^o$ for TAPP-PSS aggregates at PSS excess ($l = 0.5$) with linear and brush type PSS. Combining porphyrin TAPP with all four PSS types resulted in significantly increased scattering intensities as well as higher apparent hydrodynamic radii. The results of Table 6.3 are obtained directly after sample preparation (20 min for handling) and thereafter were stable for at least several weeks. In that sense TAPP-PSS aggregates with linear PSS behave similarly to the complexes with brush PSS of chapter 5.

Table 6.3: Light scattering results at 90º with IR-laser; c(PSS) = 50 mg/L; charge ratio for samples containing TAPP: *l* = 0.5; apparent R_h from cumulant expansion; *: measured in 10 mM NaCl salt, see appendix A.2.

sample	**$R_{h,app}$(90º)/nm**	**I/I_{water}**	**$\mu_2/(\Gamma)^2$**
PSS8k	not measured	1.8	
PSS43k	not measured	1.6	
PSS666k	34.5*	7.2	0.14
PSS brush	36.0	38.4	0.18
PSS8k-TAPP	54.2	298	0.19
PSS43k-TAPP	47.6	385	0.21
PSS666k-TAPP	54.6	412	0.23
PSS brush-TAPP	55.6	571	0.27

If the different PSS samples are compared, hydrodynamic radii are rather similar and also scattering intensities are of comparable extent. Thus, although there are very significant differences in morphology and size between the studied polyelectrolytes, their overall aggregation behavior in the presence of porphyrin TAPP is comparable. In addition, all four polyelectrolytes exhibit macroscopic aggregation at PSS-TAPP charge stoichiometry (*l* = 1). It may be concluded that the size of polyelectrolyte-porphyrin aggregates is mainly controlled by absolute and relative concentrations of the two components as well as by their chemical nature (compare with chapter 3,were TAPP was replaced by nonaromatic $C6T^{4+}$) but not by the size of the polyelectrolyte unit.

6.2 Influence of Porphyrin Structure

The aim of this section is to investigate whether different porphyrin structures undergo different stacking behavior on PSS brush. All studied porphyrins have in common that they are positively charged with four charges per molecule. Self-aggregation of free base porphyrin TAPP on PSS brush was investigated in detail in chapter 5. In this section two metal derivatives of TAPP, CuTAPP and ZnTAPP, are studied (see Figure 6.8).

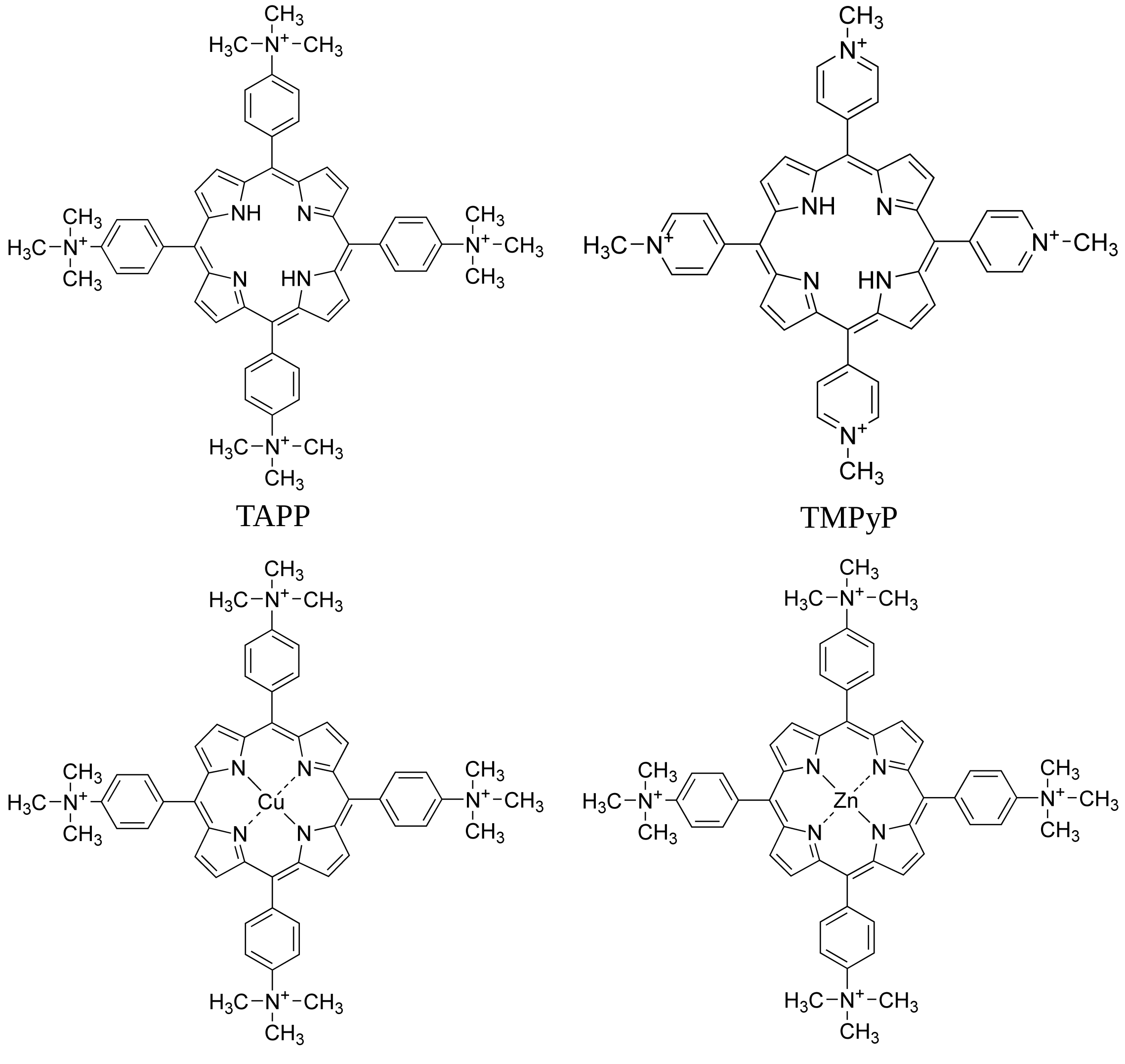

TAPP

TMPyP

CuTAPP

ZnTAPP

Figure 6.8: Molecular structures of studied porphyrins.

In literature it is reported that copper porphyrins generally show higher or similar self-aggregation tendency if compared to free porphyrins. Zn(II) porphyrins, however, are reported to aggregate less than their metal free counterparts [112,128-129]. It is reported that the reason for this observation is given by a stronger tendency of Zn(II) (electronic configuration: d^{10}) to bind axial ligands on top and below the porphyrin ring (see Figure 6.8) [41]. Thus, in order to bring two ZnTAPP porphyrins close to each other for face-to-face stacking, axial water molecules would have to be removed first. Also CuTAPP (Cu (II), d^9) may bind axial water ligands. However, it is well known that due to the so called Jahn-Teller distortion axial ligand binding is much looser for Cu (II). It will be investigated how theses differences in stacking tendency will affect the stacking geometry.

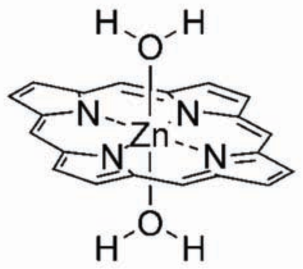

Figure 6.9: Scheme of ZnTAPP with axial water ligands.

In addition, a free base porphyrin TMPyP (Figure 6.9) was investigated. Here trimethylammonium groups are replaced by quaternized pyridinium units. The main difference of TMPyP if compared to TAPP is that here the charge centers are localized closer to the porphyrin central ring. Since like charge repulsion naturally influences porphyrin self-aggregation it is reasonable to assume that the position of theses charges can influence porphyrin stacking behavior.

Complexation of CuTAPP with PSS brush

The morphology of CuTAPP-PSS brush complexes was investigated in section 5.1.2 by cryo-TEM. It was shown that for CuTAPP finite-size brush-porphyrin networks were obtained that are of same structure than brush-porphyrin networks based on metal free TAPP. In addition, light scattering investigations revealed similar but slightly smaller network radii (see Table 6.6). Thus, on the relatively large length scale of several interconnecting brush-porphyrin cylinders there is no much difference visible in the aggregation of PSS brush with either TAPP or CuTAPP. Here the focus of study lies on a smaller length scale: with UV-vis spectroscopy the stacking geometry of porphyrin dyes on the polyelectrolyte brush is investigated.

In a first experiment polyelectrolyte PSS was added to CuTAPP in large excess (1/*l* = 8320). As in the equivalent experiment with TAPP in Figure 5.2, CuTAPP Soret band experiences a red shift (412 nm→ 417 nm) and slight hypochroism but band shape remains intact. Due to the large oversupply of PSS binding sites this red shifted spectrum clearly represents the signal for CuTAPP singly bound on the polyelectrolyte. Thus, CuTAPP as well as TAPP binds to the polyelectrolyte via its peripheral positive charges without significant perturbations to the porphyrin ring.

An UV-vis titration passing equimolar charge concentrations of PSS brush and CuTAPP is given in Figure 6.11. Here spectral shifts are obtained that are quite different to the results for porphyrin TAPP in chapter 5.

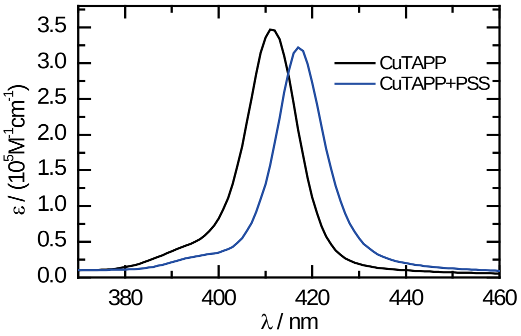

Figure 6.10: Soret band of CuTAPP at c = 3.7 μM, pure porphyrin in water in comparison to CuTAPP in large PSS excess (1/*l* = 8320).

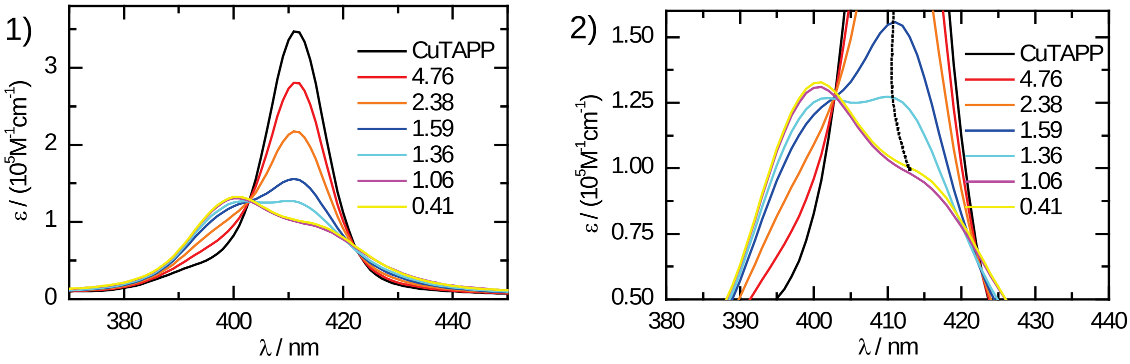

Figure 6.11: UV-vis titration of porphyrin CuTAPP (c = 0.89 μM) with PSS brush; (2): expansion of (1); legend: charge ratio *l* = [CuTAPP]/[PSS].

In the UV-vis titration two isosbestic points are clearly visible. The common intersection of signals at 422 nm is located at the same position as the isosbestic point found in the TAPP-PSS experiment. In addition, there is an isosbestic point at 403 nm. Considered as a whole, the spectral shifts in Figure 6.11 up to *l* = 1 can be described by the build-up of a new blue-shifted band at 401 nm at the expense of monomer signal at 412 nm. This increase of blue-shifted band intensity stops at charge stoichiometry (l = 1). Upon further PSS addition only minor weakening of the signal (compare with Figure 5.4) and no further shifts are detected. Thus, it is reasonable to assume that the spectrum at l = 1.06 does not contain contributions from single porphyrins but fully represents the spectrum of stacked CuTAPP. In that sense the shoulder band at 414 nm is interpreted as the J-signal of split Soret band. The remarkable difference to metal free TAPP is that the J-band is only slightly shifted from monomer position and, more obviously, that the intensity of H-band is much higher than the intensity of the J-signal. Thus, mutual stacking geometry of the copper porphyrin is presumably closer to the parallel type side-by-side dipole orientation given in Figure 5.6-1 (that will lead to a blue shifted H-band) than the oblique orientation of metal free TAPP (that is manifested in the experiment by band splitting into equal heights).

In terms of the effect of hypochroism, TAPP shows stronger weakening at monomer band than CuTAPP (see Table 6.4, Figure 6.14). In the experiment with TAPP addition of further PSS ($1/l > 1$) leads to raising band intensities. With CuTAPP, however, the spectrum of stacked porphyrin at l = 1 is not significantly affected by further PSS addition. Apparently, CuTAPP stacks are less affected by an oversupply of PSS binding sites. Possibly this difference is due to the stronger self-aggregation tendency of copper porphyrins if compared to metal free porphyrins as reported in literature [128].

In conclusion, the introduction of Cu(II) significantly affects porphyrin stacking geometry and strength while on a larger length scale (cryo-TEM, light scattering) only minor differences were observed in the morphology of complexes. The results for a non-stacking counterion in chapter 3 showed that there is no secondary aggregation of cylindrical brush-counterion complexes for this counterion. However, this second step in the hierarchical build-up was observed for brush-porphyrin networks. It is reasonable to assume that the general presence of porphyrin stacking strongly promotes brush-porphyrin network formation, however, differences in the geometry of stacked porphyrins have lower influence.

Table 6.4: Spectral signatures of porphyrins TAPP and CuTAPP self-stacked on PSS brush.

porphyrin	$\tilde{\nu}_M$/cm^{-1}	$\tilde{\nu}_H$/cm^{-1}	$\tilde{\nu}_J$/cm^{-1}	$\Delta\tilde{\nu}$/cm^{-1}	$\varepsilon_J/\varepsilon_H$	$\varepsilon_M/\varepsilon_{M0}$
TAPP	24272	24814	23981	833	1.07	0.23
CuTAPP	24272	24938	24155	783	0.74	0.29

Complexation of ZnTAPP and TMPyP with PSS brush

UV-vis titrations with porphyrins ZnTAPP and TMPyP are given in Figure 6.12 and Figure 6.13. Similarly to TAPP and CuTAPP these two porphyrins both show hypochroism upon PSS brush addition that is most intense at around *l* = 1. From the band shifts it is reasonable to conclude that both ZnTAPP and TMPyP self-interact on PSS brush. Isosbestic points at 429 nm for ZnTAPP and at 441 nm for TMPyP are visible.

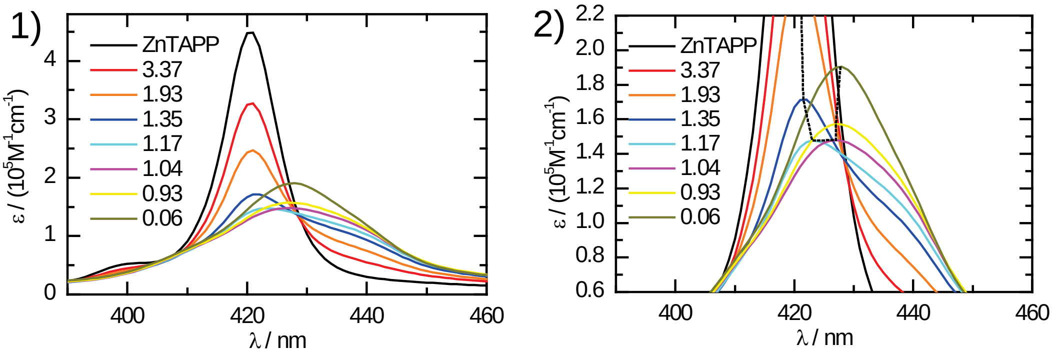

Figure 6.12: UV-vis titration of porphyrin ZnTAPP (c = 3.3 μM) with PSS brush; (2): expansion of (1); legend: charge ratio *l* = [ZnTAPP]/[PSS].

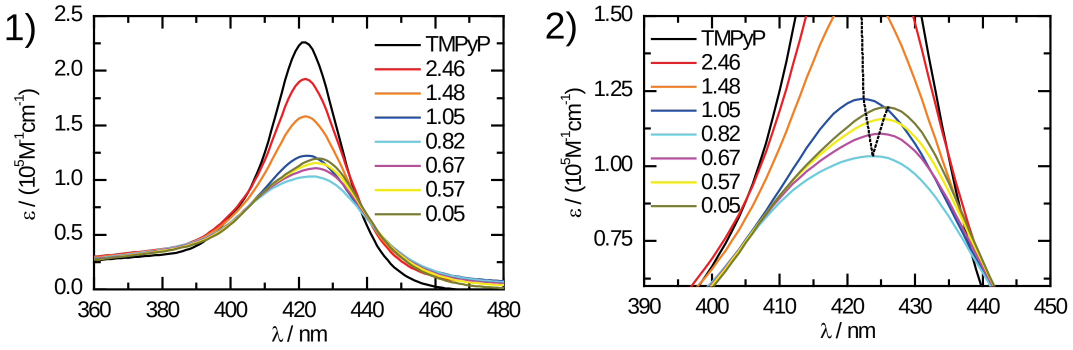

Figure 6.13: UV-vis titration of porphyrin TMPyP (c = 4.0 μM) with PSS brush; (2): expansion of (1); legend: charge ratio *l* = [TMPyP]/[PSS].

Extinction coefficients at the respective monomer bands for the four porphyrins studied here are compared in Figure 6.14. Several observations can be made: a) all porphyrins show minimal intensity of monomer band at around *l* = 1; b) all three porphyrins based on TAPP structure including its metal derivatives (TAPP, CuTAPP, ZnTAPP) show relatively similar values for the hypochromic effect at *l* = 1 (~75% intensity reduction), whereas TMPyP exhibits lower weakening of intensity (~55% intensity reduction); c) all porphyrins except CuTAPP show increasing absorption intensity upon further PSS addition for 1/*l* > 1, so for these three porphyrins additional PSS binding sites reduce porphyrin stacking strength.

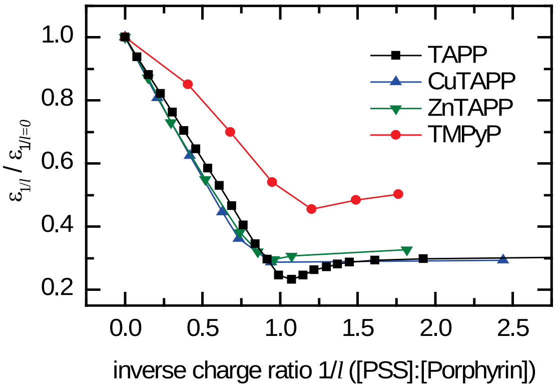

Figure 6.14: Normalized extinction coefficient at respective Soret maximum (according to Table A.4) for different porphyrins upon addition of PSS brush.

Band shapes in the UV-vis titrations of ZnTAPP and TMPyP are quite different to the results with TAPP and CuTAPP. Whereas the latter porphyrins clearly split into H- and J-bands upon self-stacking, this is not the case for ZnTAPP and TMPyP.

For ZnTAPP a red shift of monomer band from 421 nm to 428 nm is observed. In addition, the spectrum of stacked ZnTAPP is considerably broader than for single ZnTAPP. Within exciton formalism the red shifted signal can be assigned as J-band. Since no H-band is present, it may be argued that ZnTAPP stacking geometry is likely to be close to a head-to-tail orientation shown in Figure 5.6-2. This interpretation would also fit to the idea of ZnTAPP binding axial ligands (Figure 6.9). Given this constraint, a head-to-tail orientation would, from a sterical point of view, allow closer interaction between the porphyrins than for a side-by-side stacking. Since ZnTAPP curve in Figure 6.14 is very similar to TAPP and CuTAPP there is no sign that stacking of ZnTAPP would be strongly unfavored because of axial ligands. Thus, such ligands do not prevent porphyrin self-aggregation but rather change stacking geometry.

TMPyP also shows a monomer band that is red-shifted (from 422 nm to 426 nm) but which is for this porphyrin of similar width than for its single porphyrin spectrum. Like for ZnTAPP no further band or shoulder is visible and thus also here the shifted band is assigned as a J-band and more or less head-to-tail mutual dipole orientation is likely. If the curve progression in Figure 6.14 is compared with the other porphyrins, TMPyP shows significant lower hypochroism. Apparently, TMPyP has lower stacking tendency than TAPP in addition to the different stacking geometry. An explanation for less stacking could be given by the charged units in TMPyP, which are closer to the inner porphyrin ring and thus these charged units lead to increased self-repulsion of TMPyP. In addition, exciton splitting energy for TMPyP is much lower than for TAPP, CuTAPP and ZnTAPP (Table 6.4).

Table 6.5: Band positions and exciton splitting of UV-vis titrations. Due to the absence of H-band $\Delta\tilde{\nu}$ is given as double the difference between monomer and J-band.

porphyrin	$\tilde{\nu}_M$/cm^{-1}	$\tilde{\nu}_J$/cm^{-1}	$\Delta\tilde{\nu}$/cm^{-1}	$\varepsilon_M/\varepsilon_{M0}$
ZnTAPP	23753	23364	778	0.30
TMPyP	23697	23474	446	0.46

Table 6.6: Light scattering results for brush-porphyrin networks with different porphyrins; λ = 832.5 nm.

sample	$R_{h,app}$(90°)/nm	I/I_{water}	$\mu_2/(\Gamma)^2$
TAPP-brush	55.6	571	0.27
CuTAPP-brush	48.6	244	0.24
ZnTAPP-brush	80.5	339	0.25
TMPyP-brush	46.5	280	0.27

Thus, in the UV-vis results for TMPyP and ZnTAPP strong differences to TAPP indicate different porphyrin stacking behavior. On a larger length scale light scattering investigations for brush-porphyrin complexes with both porphyrins reveal the build-up of supramolecular structures (see Table 6.6). Whereas TMPyP leads to radii very similar to the CuTAPP case discussed above, ZnTAPP shows a significantly larger aggregate size. Thus, complex sizes with TAPP, CuTAPP and TMPyP are similar but different for ZnTAPP. This is surprising since ZnTAPP both shows similar stacking strength and geometry to one of the other porphyrins that show lower radii. To give an accurate explanation for this observation presumably further investigations would be needed.

CHAPTER 7

7 NETWORK FORMATION OF PVP BRUSHES WITH THE ANIONIC PORPHYRIN TPPS: PH-DEPENDENCE

The response of aqueous porphyrins to pH stimuli was described in section 2.2. It was pointed out that the two nitrogen bases within the porphyrin ring are easily protonated by addition of aqueous HCl. The net effect of protonating the porphyrin ring depends heavily on the sign of peripheral charges (Figure 2.9). Whereas tetravalent and positively charged porphyrins such as TAPP will experience a net charge increase from four to six upon protonation, the negatively charged counterpart TPPS will change from net charge four to two (Figure 7.8). This very difference gives the motivation for the research reported in this chapter.

Literature reports about the interaction of negatively charged porphyrins with polyelectrolytes are mainly focused on the mentioned porphyrin TPPS. Motivated by the previous findings of TPPS being able to form J-aggregates in acidic media (see section 4.2 and references therein) several groups investigated the J-aggregation of TPPS at polymeric templates [132,134,136-137,139,161,176-200]. Generally it was found that polyelectrolyte templates enhance J-aggregation of TPPS and e.g. it was observed that poly(lysine) enhances J-aggregation at much lower molar concentration compared to monomeric lysine (all at pH = 3) [187]. Besides TPPS association with poly(lysine) [136-137,181,187] several other polypeptides such as poly(glutamic acid) [134,136-137,180,188,201] and specially designed peptide sequences [179,190,196-197] were studied. In addition to polypeptides, also several studies about the association of TPPS with proteins, such as HSA (human serum albumin) and BSA (bovine serum albumin) that are positively charged at low pH were published [132,138,177-178,185-186,195,202]. The association of TPPS with other charged templates such as surfactants [182,184], cyclodextrins [203], PAMAM dendrimers [189], polysaccharides [192,200], PEG-b-PVP micelles [161,198-199] and other polyelectrolytes [176,191,204-205] were reported as well. However, none of the listed publications cover the topic of using TPPS as pH-dependent switch as counterion in electrostatically self-assembled nanoscopic systems; in the function as it is investigated in the present study.

Negatively charged PSS brushes assemble to network-like structures in the presence of tetravalent porphyrins of opposite charge (chapter 5). The implications of this statement were tested in several parts of the present dissertation. From section 3.2 it is evident that one prerequisite for network formation presumably is that the valency of the counterion added to PSS brush is higher than two. For the divalent counterions studied in chapter 3 intermolecular assemblies of PSS brushes were not observed.

In this context it is of interest to investigate a brush-porphyrin system where the porphyrin TPPS is added to positively charged brush. The idea is to first investigate TPPS in its neutral tetravalent state and later how its effect on the brush will change upon protonation and net charge reduction in acidic conditions. Positively charged poly(2-vinylpyridine) - PVP brushes were used as the brush entity in these investigations. 56% of the 2-vinylpyridine side chain monomers are quaternized with ethyl bromide. Figure 7.1 gives an AFM image of “PVP47”; the semiflexible brush character can easily be seen. Further description and characterization of PVP47 can be found in Appendix A.2.

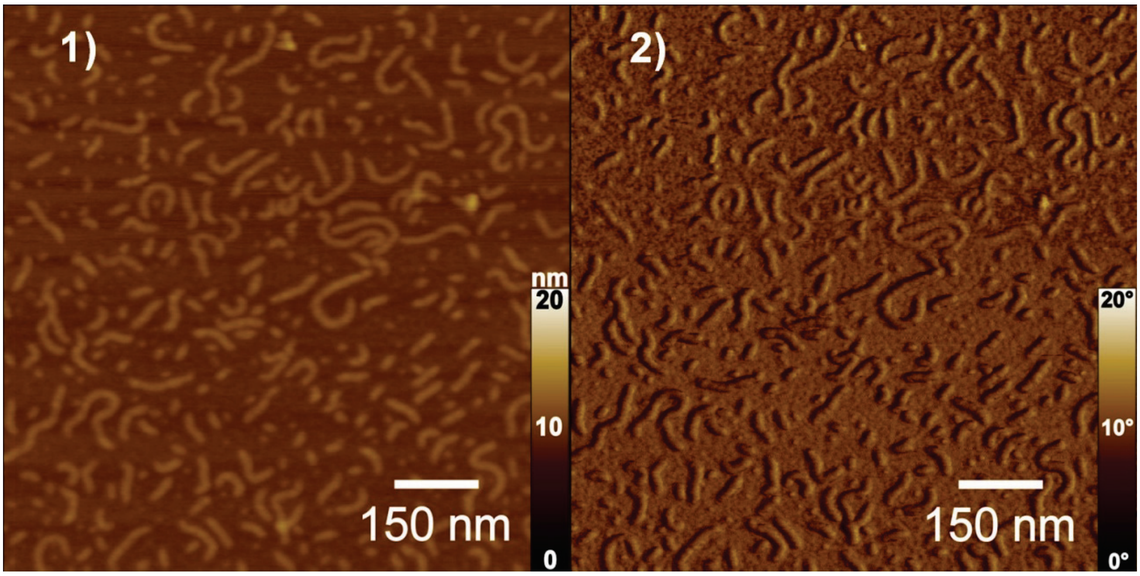

Figure 7.1: AFM height and phase images of PVP47, c = 0.072 g/L deposited on mica, 1): height, 2): phase image.

Cross-sectional profile analysis of AFM height images allows for height and width measurement of PVP brushes. Results are given in Table 7.1 (for a sample profile see Figure 7.6-2). Apparently, the brush molecules lie flat on the surface with higher width than height dimensions although they possess a circular cross-sectional profile in solution. This is due to brush-surface (hydrophilic mica surface) interaction and has already been observed and discussed for the PSS system in chapter 5.

Table 7.1: Measurements for height and width of PVP47 brushes as taken from sectional profiles extracted from Figure 7.1 data.

	height/nm	**width/nm**
PVP47	2.5 ± 0.3	15.6 ± 2.2

7.1 Complexation of PVP with TPPS at pH = 7

Spectroscopic properties of PVP-TPPS aggregates

The combination of PVP47 with TPPS in neutral salt-free water is studied in analogy to the investigations presented above for the complexation of PSS brush with TAPP. In order to compare the results that will be presented below to the experiments in chapter 5 the same absolute charge concentration for PVP was used: c = 0.24 mM (that is c = 0.072 g/L in PVP mass concentration).

Combining TPPS with PVP (c = 0.24 mM) at charge stoichiometry, that is $l = 1$, there is spontaneous precipitation of macroscopic aggregates. Obviously, tetravalent TPPS induces macroscopic aggregation by linking PVP brushes in a similar way as TAPP acts on PSS. The first observation by eye while adding violet TPPS to colorless PVP in excess PVP conditions is a color shift to light brown very similar to Figure 5.1. Apparently, self-interaction of porphyrin molecules occurs at the polyelectrolyte template. In order to further elucidate the spectral behavior of TPPS, an UV-vis titration of adding PVP to a solution with constant TPPS concentration is given in Figure 7.2.

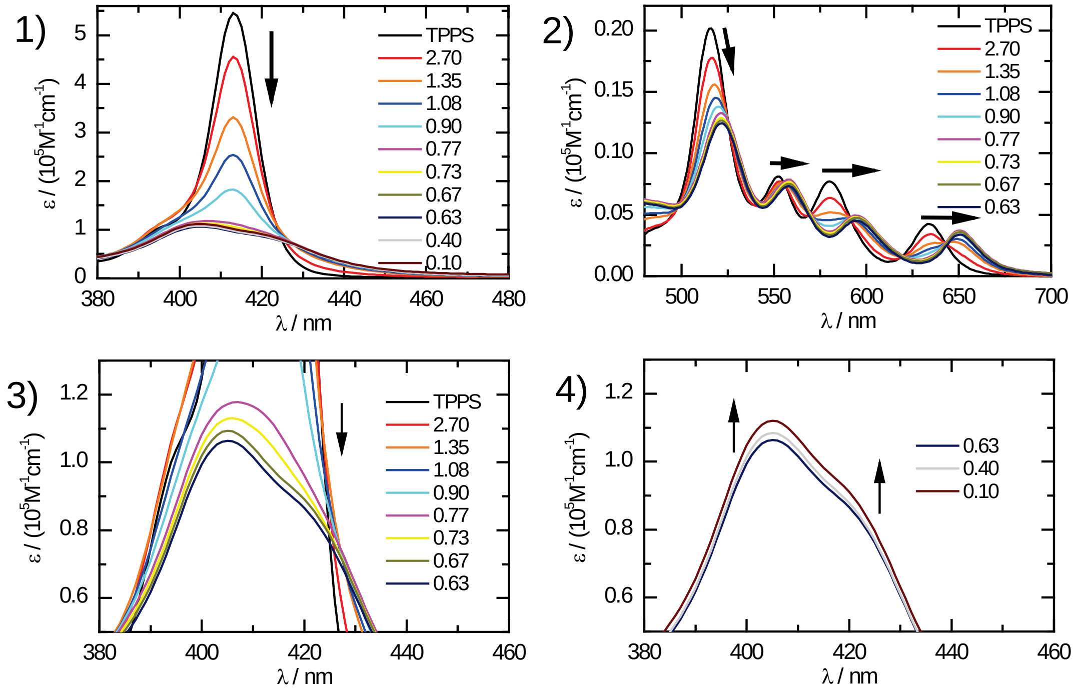

Figure 7.2: UV-vis titration of TPPS and PVP47, c(TPPS) = 3.8 µM; (3,4): enlargement of (1); legend: charge ratio *l* = [TPPS]/[PVP].

Upon polyelectrolyte addition the Soret signal at 413 nm exhibits a strong hypochromic effect of about 82% at a charge ratio *l* = 0.63 (1.6-fold excess of PVP). At this ratio the band splits into two signals at 405 nm and 421 nm. The Q-bands also exhibit hypochromicity as well as a red shift of 6 – 16 nm. Overall the spectral shifts are quite similar to literature investigations of TPPS association with poly(amidoamine) (PAMAM) dendrimers at pH = 7 [206]. Additionally, there is an isosbestic point at 427 nm and several isosbestic points in the Q-region. The presence of isosbestic points is an indication that there are two species present: a) the free porphyrin molecule and b) TPPS undergoing π-π interaction at the polyelectrolyte template. Qualitatively, the band shifts are similar to the shifts observed for PSS-TAPP (see Figure 5.4). The band splitting in the Soret band results in two bands at comparable wavelength values and the extent of exciton splitting is similar (see Table 7.2). However, whereas for TPPS-PVP the lower wavelength signal at 405 nm exhibits higher intensity than the red shifted signal at 421 nm, the TAPP-PSS system shows an opposite pattern: the 417 nm signal is higher in intensity than the blue shifted peak at 403 nm (intensity ratio: 1.25:1). It can be concluded that TPPS on PVP stacks with an oblique interdipole orientation as was the case for TAPP on PSS. However, the stacking geometry will be slightly different.

Table 7.2: Positions (wave number) of TPPS monomer and H- and J-bands of TPPS-PVP brush aggregate.

$\tilde{\nu}_{\mathrm{mon}}/\mathrm{cm}^{-1}$	$\tilde{\nu}_{\mathrm{H}}/\mathrm{cm}^{-1}$	$\tilde{\nu}_{\mathrm{J}}/\mathrm{cm}^{-1}$	$\Delta\tilde{\nu}/\mathrm{cm}^{-1}$
24272	24691	23753	938

As it is demonstrated in Figure 7.2-4 TPPS absorption intensity slightly increases after its minimum at *l* = 0.63 but band shape remains intact. In chapter 5 this parallel up-shift of the spectrum was explained by porphyrin-porphyrin stacks that do not significantly change their mutual orientation but show an overall reduction of coupling intensity due to the increasing amount of polyelectrolyte binding sites. Interestingly, the extent of weakening hypochromicity after passing its maximum value is much smaller for the TPPS-PVP case. For better illustration, extinction coefficients at Soret maximum are plotted vs. inverse charge ratio in Figure 7.3. Apparently, the level of intensity reduction at minimum absorption is similar for both porphyrin-brush systems. However, differences in Figure 7.3 are observable: minimum absorption for TPPS-PVP is obtained at 1.6-fold excess of PVP whereas for TAPP-PSS the minimum occurs at stoichiometric charge ratio. A value for minimum absorption apart from one (that was measured for TAPP-PSS) was observed for TAPP-PVS and for TAPP-aggrecan as well (cf. Figure 8.6) and thus is evidently dependent on the chemical structure of the polyelectrolyte. Another observable difference is that the extent of raising absorption after the observed dent is much higher for TAPP-PSS. Thus, TAPP-TAPP stacks on PSS are influenced by further polyelectrolyte addition whereas no strong effect is seen for TPPS on PVP.

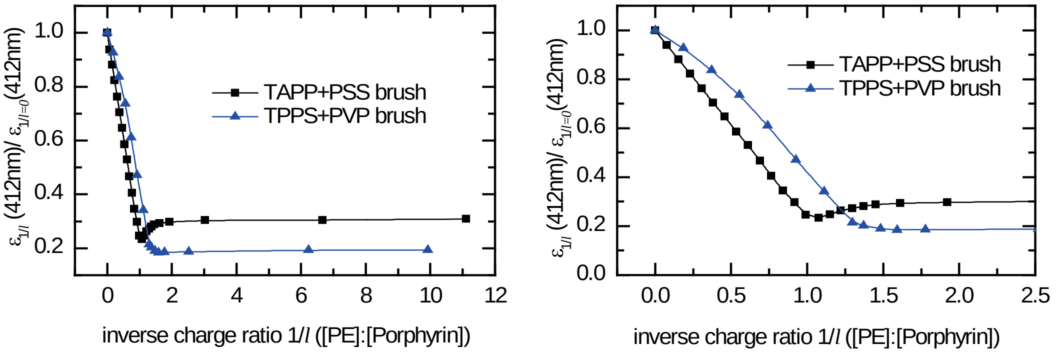

Figure 7.3: Normalized extinction coefficient at 412 nm vs. inverse charge ratio 1/*l* = [polyelectrolyte]/[porphyrin].

Imaging of PVP-TPPS aggregates

PVP-TPPS complexes (l = 0.5, well below the turbidity threshold) were spin-coated on mica and imaged with AFM in air (Figure 7.5). Brush-TPPS aggregates are observed. Images reveal the presence of intermolecular aggregates as well as free brush molecules. The aggregates exhibit a network structure and mainly consist of a brush entity that is higher on the surface than the single brush molecules. Both the network structure and the presence of two brush species are in full analogy to the results for the PSS-TAPP system (see Figure 5.15). These results provide the reasoning for a general expectation of network formation of brush-porphyrin aggregates mediated by peripheral charge as well as porphyrin core π - π interaction. In analogy to the scheme in Figure 5.18 for the hierarchical network formation of PSS brushes with counterion TAPP, an interpretation of the network build-up process is given for the PVP-TPPS case (Figure 7.4).

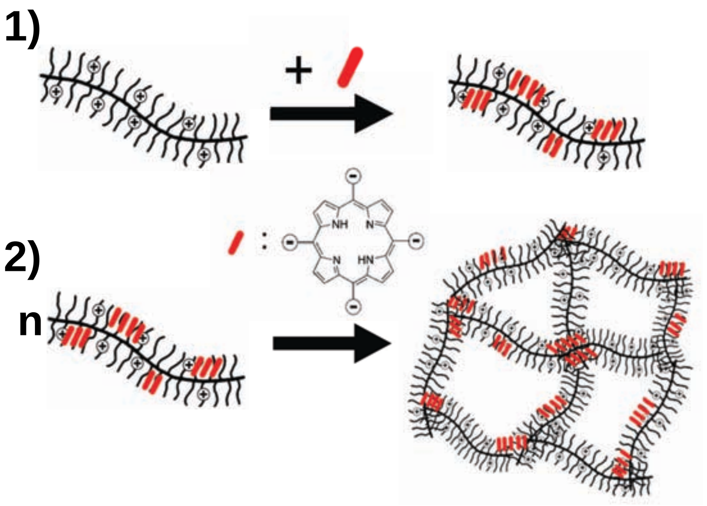

Figure 7.4: Schematic representation of network formation from PVP47 and TPPS. Drawing is not to scale: diameter brush: 10 nm, side-to-side distance in porphyrin: 2 nm.

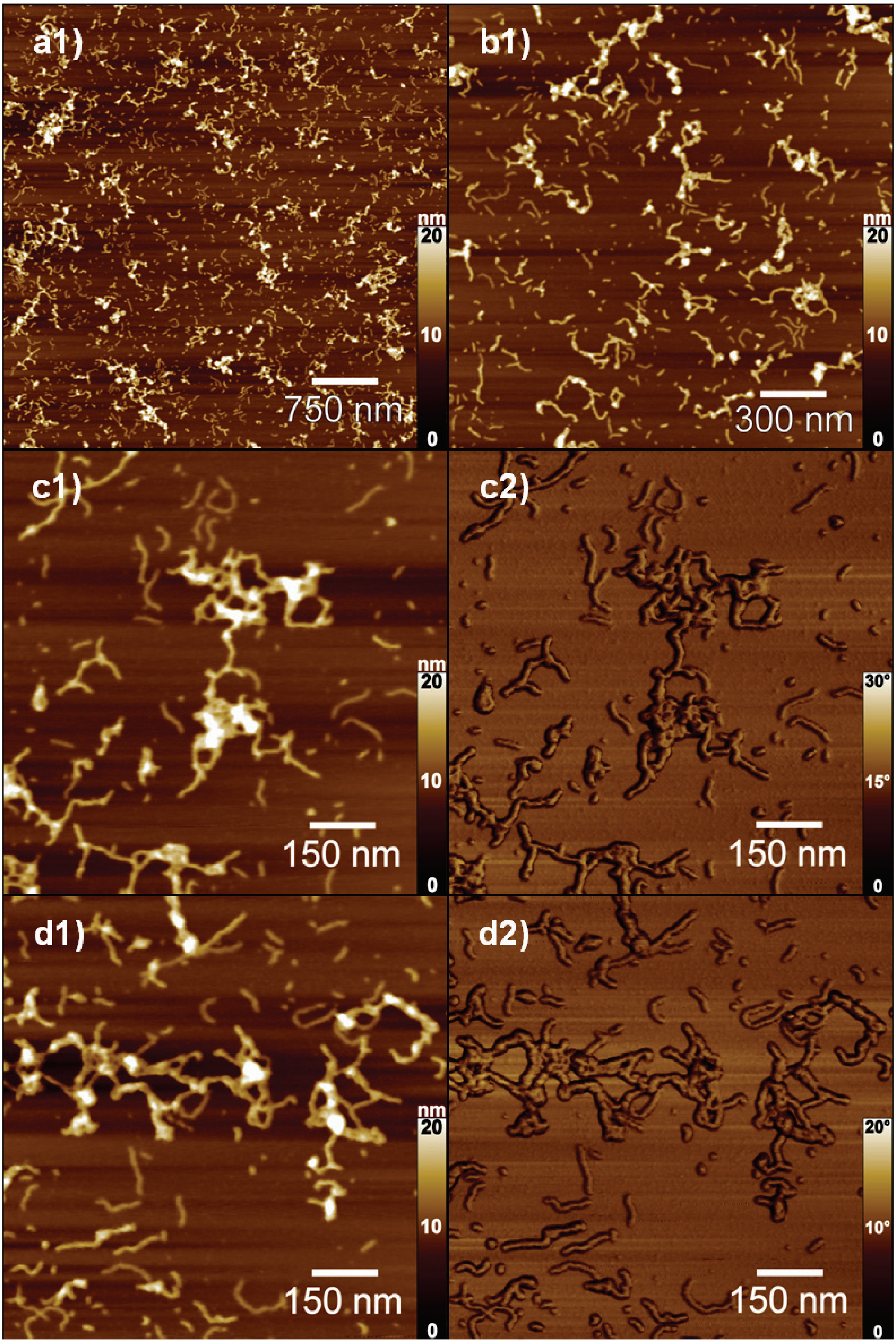

Figure 7.5: AFM height (1) and phase (2) images of PVP47-TPPS networks, *I* = 0.5, pH = 7.

Cross-sectional profiles and the extracted measurements for the two cylindrical species are given in Figure 7.6 and Table 7.3. The height difference in between the two types can be clearly extracted from the profile sections. Besides the difference in height, the higher species also shows higher lateral dimensions. Thus, the second species is both higher and wider.

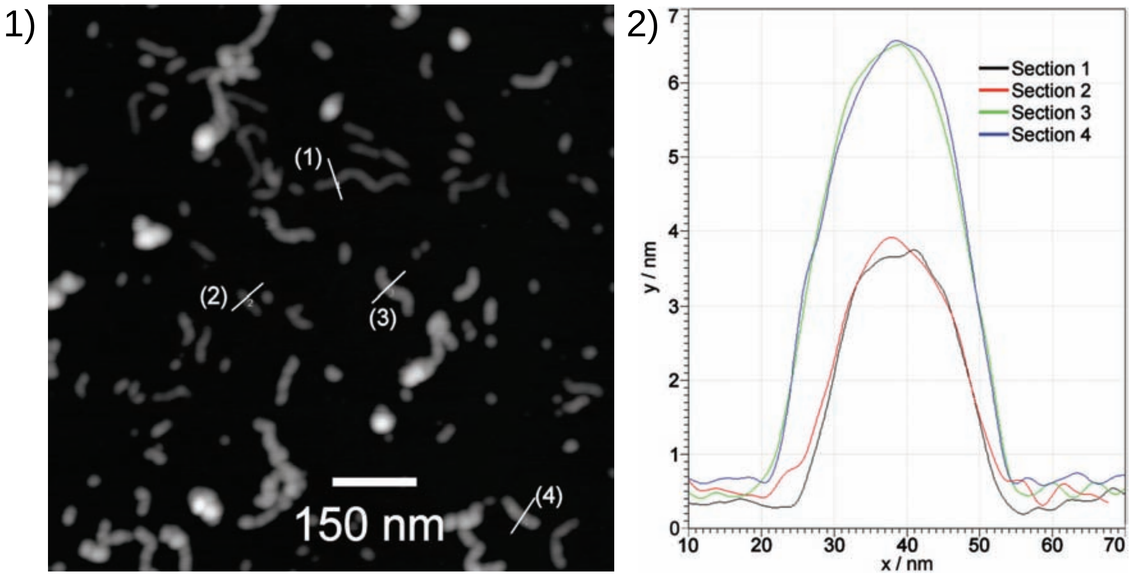

Figure 7.6: AFM height image of PVP47-TPPS complexes, *l* = 0.5 (1) and four sectional profiles (2).

Table 7.3: Measurements for heights and widths of brush species as taken from sectional profiles extracted from Figure 7.6 data.

brush species	height/nm	width/nm
“low”	3.6 ± 0.5	19.8 ± 1.5
“high”	6.2 ± 0.4	25.1 ± 2.2

From the observation that the networks mainly consist of the high brush species and the expectation that porphyrins are needed to link brush molecules, it can be concluded that this brush type actually represents brush-porphyrin complexes (a similar conclusion was drawn for the PSS-TAPP system above). Within this understanding it is reasonable to assume that the lower brush type represents free unloaded brush molecules that do not contribute to network formation due to the absence of porphyrin linker molecules.

In full analogy to the results and conclusions of chapter 5 these observations allow for the conclusion of networks built up in a hierarchical manner.

The non-uniform distribution of porphyrins on the brush can be explained by a cooperative binding mode of the porphyrins to the brush molecules as was already pointed out for the PSS-TAPP networks above. Additionally, higher spots on the networks can be seen (height ~20 nm). These spots can be explained by one or more brush layers of the three dimensional networks collapsed on top of each other on the dry surface. Another explanation would be the presence of porphyrin clusters as was also pointed out for the PSS-TAPP system before.

Size of PVP-TPPS aggregates

The characterization of PVP brushes with dynamic light scattering (red laser source) in salt-free solution is described in appendix A.2. PVP-TPPS aggregates were analyzed using an IR laser (because of the absorption of visible light by porphyrin TPPS) at angle 90°. PVP exhibits an apparent hydrodynamic radius of $R_h = 34.8$ nm using the red laser at $\theta_{red} = 65°$ (at this angle the scattering vector q is approximately the same as at $\theta_{IR} = 90°$ for the IR laser). Using the IR setup at $\theta_{IR} = 90°$ a very similar hydrodynamic radius of $R_h = 35.5$ is obtained, thus demonstrating again the applicability of using the IR setup here.

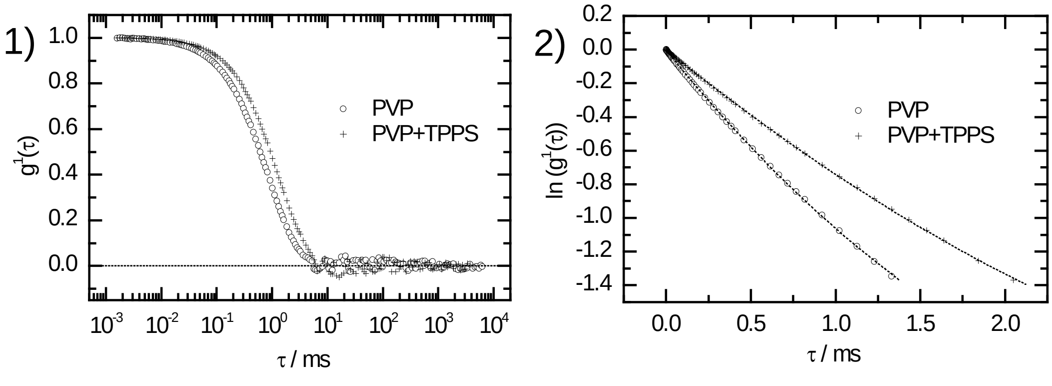

Figure 7.7: Dynamic light scattering results for pure PVP and PVP-TPPS (*l* = 0.5) aggregates at 90° (IR laser); 1) electric field autocorrelation function; 2) second order cumulant evaluation of 1.

Combining PVP47 brush with TPPS porphyrin at polyelectrolyte excess results in correlation functions significantly shifted towards higher relaxation times and thus higher hydrodynamic radii (see Figure 7.7 and Table 7.4). Additionally, a ten-fold increase in scattering intensity due to the aggregation process is observed. A strong influence of mixing procedure on the resulting aggregate size is expected from the detailed experiments presented for the mixing of PSS brushes with TAPP in chapter 5. Therefore, the very same preparation procedure that yielded well reproducible aggregate sizes for the PSS-TAPP system was employed here. That is filtrated TPPS porphyrin solution was added drop wise to a vigorously stirred PVP solution into a dust-free light scattering cell (for details of procedure see appendix B.2). Here applying this procedure reproducible values for the hydrodynamic radius of aggregates are obtained as well.

Table 7.4: Apparent R_h at 90° as measured with IR-DLS, evaluation with second order cumulant evaluation, c(PVP) = 0.072 g/L.

	$R_{h,app}$/nm	$\mu_2/(\Gamma)^2$	I/I_{water}
PVP47	35.5	0.24	23.5
PVP47 + TPPS l = 0.5	51.9	0.23	232

The aggregate size was monitored over time. The radius given in Table 7.4 is measured directly after sample preparation (≈ 15 minutes time lag because of handling issues) and is stable for at least two weeks (not tested for longer times).

In summary, this section has shown that in neutral solution tetravalent TPPS induces network formation of PVP brushes in a very similar way as TAPP-PSS brush complexes assemble to networks. Spectral shifts and AFM images are comparable. Also the apparent hydrodynamic radii of networks by light scattering are very similar: for TAPP-PSS the result for complexes with two-fold polyelectrolyte excess (l = 0.5) is $R_h(90^o)$ = 55.6 (Table 6.6) and for TPPS-PVP $R_h(90^o)$ = 51.9 (Table 7.4). These observations suggest that the formation of self-assembled networks from cylindrical brushes and oppositely charged porphyrins is a general and versatile concept that may be applied to generate novel self-assembled materials.

7.2 Complexation of PVP with TPPS at pH < 4

The target of this section is to evaluate the interaction of TPPS with PVP at pH < 4. TPPS in its unprotonated free porphyrin state at pH > 4 has four negative charges. Upon protonation of its inner nitrogen atoms the molecule exhibits a reduction of charge from four to two (see Figure 7.8). As was pointed out in the introduction to this chapter, it was investigated how this charge switch will change the complexation behavior of TPPS to PVP brush. The idea is that potentially tetravalent TPPS is able to assemble PVP to networks as shown in section 7.1 but TPPS in its divalent state at pH < 4 is not. Thus, by adjusting the pH it may be potentially possible to switch networks “on” and “off”.

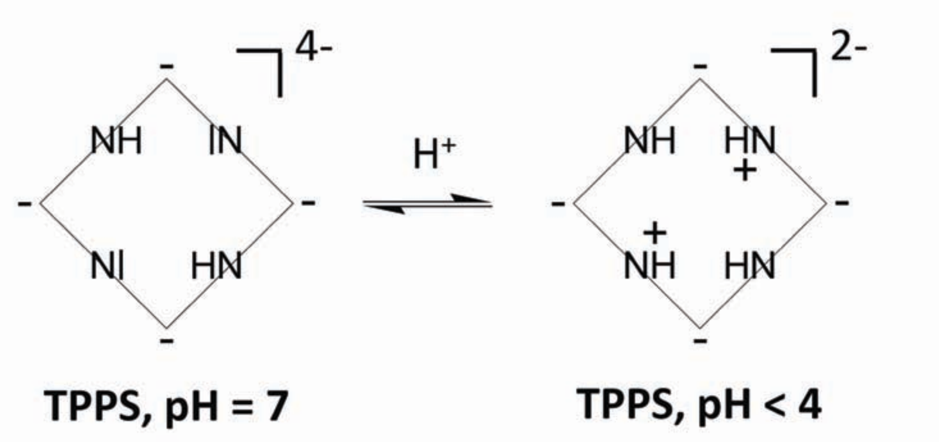

Figure 7.8: Schematic representation of the protonation of negatively charged tetravalent porphyrin (e.g. TPPS), scheme is part of Figure 2.9.

In section 4.2 for pure TPPS solutions three major pH regimes were identified as summarized in Table 7.5. The present section focuses on the two lower regimes where TPPS is protonated in pure solution.

In addition to the effect of pH on TPPS it should be noted that the partially quaternized PVP47 brush may be protonated as well at pH < 4 (pK_a ~ 5 for PV2P [207-208]) and thus the percentage of charged side chain units may reach 100%. The combination of both protonation effects on TPPS and PVP results in a reduction of the charge ratio l (eq. 3.1) since the charge concentration of counterion decreases and the charge concentration of polyelectrolyte increases upon protonation of the respective component. Thus, at pH < 4 an effective charge ratio l_{eff} may be introduced. In order to avoid confusion with samples that are switched between the different protonation states and charge ratios, all samples in this section are labeled with the charge ratio l of a neutral solution if not stated otherwise. Charge ratios used in this section for neutral solutions are $l = 1$, $l = 0.75$ and $l = 0.5$. For pH < 4 these ratios translate to effective charge ratios in acidic conditions of $l_{eff} = 0.28$, $l_{eff} = 0.21$ and $l_{eff} = 0.14$ if full protonation of both components is assumed. As will be shown below for several samples at ($3 \leq \text{pH} < 4$) TPPS is evidently not protonated. Here the charge ratio is solely reduced by PVP protonation. Assuming full protonation of unquaternized PVP segments gives corresponding ratios of $l_{eff} = 0.56$, $l_{eff} = 0.42$ and $l_{eff} = 0.28$. For other samples at ($1.5 < \text{pH} \leq 2.5$) TPPS is partially protonated (see below) and thus here the effective charge ratios will be in between the values for the two described cases.

From the results for the size of PSS brush - TAPP networks in section 5 it is generally expected that a reduction of charge ratio will result in a lower network radius (see Figure 5.26). Thus, from this point of view a reversible reduction of charge ratio of switching pH may lead to a reversible change of network size. However, the background of the investigations within this section is the expectation that TPPS as divalent counterion in acidic conditions may not be able to build-up brush-porphyrin networks at all. Thus, if this hypothesis is correct a switch to protonated components would not result in networks of lower size but in a disconnection of all network joints. This will be addressed by light scattering and AFM investigations below.

From section 5.1.5 it is clear that the preparation protocol of samples can be crucial for their properties. Thus, besides the separate investigation of the two pH regimes described in section 4.2 with pH < 4 (Table 7.5), it also will be investigated in the present section whether results are affected by the pH at mixing the stock solutions and not only by the later pH in the measurement. Thus, it will be differentiated between samples that are prepared at pH = 7 and then adjusted to either ($3 \leq \text{pH} < 4$) or ($1.5 < \text{pH} \leq 2$) with samples that are directly prepared at the respective pH.

Generally, it was shown in both the experiments of sections 4.2 and 7.2 that samples in the respective pH regimes showed equal results irrespective of pH differences within the regimes (e.g. pH = 3.0 and pH = 3.7). Thus, differentiations present in this section are no matter of concern.

Table 7.5: Overview of protonation and aggregation state of TPPS as concluded from section 4.2.

	protonation state	**net negative charge**	**monomer/aggregate**
pH = 7	unprotonated	four	monomer
(3 ≤ pH < 4)	protonated	two	monomer
(1.5 < pH ≤ 2.5)	protonated	two	monomer + J-aggregate

Spectroscopic properties of PVP-TPPS aggregates at pH < 4

The spectroscopic behavior of pure TPPS in acidic conditions was described in section 4.2. Whereas at pH = 7 TPPS is violet and shows a 4-band Q-spectrum, it is green at pH < 4 with a 2-band Q-spectrum characteristic for a protonated porphyrin species. Additionally, it was already pointed out that at even lower pH (e.g. pH = 2) J-aggregates are formed in TPPS solutions. Thus, there are two regimes of investigation as was shown in Table 7.5.

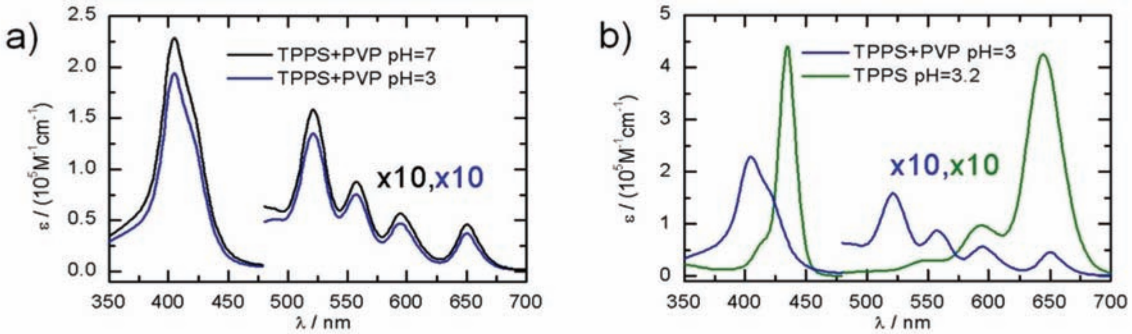

Figure 7.9: UV-vis spectra of PVP-TPPS complexes at pH = 7 and pH = 3 (a) and comparison to pure TPPS spectrum at pH = 3.2 (b).

First the case a) at (3 ≤ pH < 4) is discussed. Figure 7.9-a gives the UV-vis spectrum of TPPS-PVP (*l* = 0.5) complexes that were prepared at pH = 7 and were tuned to pH = 3 by subsequent addition of HCl. Apparently, the spectrum does not shift to the protonated porphyrin two-band Q-spectrum as it would be expected for pure TPPS at pH = 3 (see Figure 7.9-b). The band shape of Soret signal does not change albeit some weakening of intensity is observed throughout the spectrum. Thus, qualitatively the same spectrum at pH = 3 and in neutral condition is observed. Given this observation, it can safely be concluded that TPPS is not protonated here. The porphyrin remains bound to PVP in a similar electronic state and surrounding as at pH = 7 basically unaffected by the additional protons.

In the introduction to this section it was pointed out that potentially the pH at mixing of stock solutions may be important. Thus, in addition an experiment was conducted where each of the TPPS and PVP stock solutions were adjusted to the pH range (3 ≤ pH < 4) and thereafter combined. The result is given in Figure 7.10: there is virtually no difference visible in the UV-vis spectrum as compared to the first preparation route. Also the color of the sample remains same as in pH = 7 (light-brown). Thus, TPPS at (3 ≤ pH < 4) is bound as unprotonated tetravalent porphyrin to PVP no matter if the molecule was at the tetravalent or divalent state at the time of bringing to contact with PVP.

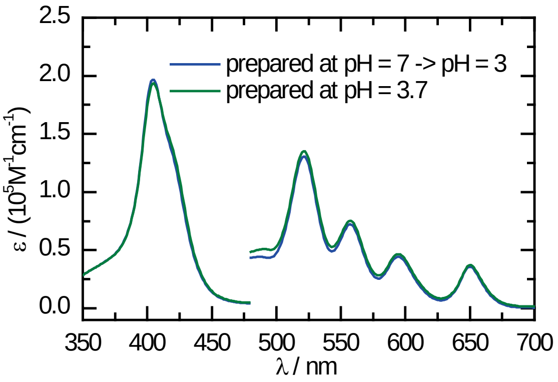

Figure 7.10: UV-vis spectra of PVP-TPPS complexes with different preparation procedures in the range of pH = 3-4. Blue: prepared at pH = 7 and adjusted to pH = 3, same sample as in Figure 7.9. Green: prepared at pH = 3.7.

If the porphyrin TPPS remains bound to the polyelectrolyte in an unprotonated state at (3 ≤ pH < 4), it is consequently of interest to evaluate the situation at pH regime (b) (that is at (1.5 < pH ≤ 2.5)) where J-aggregates may be present. Potentially here TPPS may be divalent in the presence of PVP.

If the pH of a PVP-TPPS sample is lowered to (1.5 < pH ≤ 2.5) a shift of sample color towards green is noticeable. Figure 7.11-a shows the spectral changes that occur if further HCl is added to the TPPS-PVP sample at pH = 3. Table 7.6 gives an overview of band positions of the porphyrin species discussed here.

Apparently, further addition of HCl has a pronounced effect on the spectrum. There is a build-up of a new signal at 488 nm. This peak is very close to the J-aggregate signal that was reported of before for TPPS in (1.5 < pH ≤ 2.5) (see Figure 7.11-b1). The signal is slightly (3 nm) shifted to smaller wavelengths, and is broader and less symmetric compared to the TPPS J-aggregate signal for pure TPPS in pH = 2. Still, the presence of this signal here is a strong indication that TPPS J-aggregates are formed. The deviation in peak shape and position may be explained by slightly different TPPS stacking geometry. For example the broader line shape indicates that there is less electronic communication in the aggregates. The observation of a broadening of the J-aggregate Soret signal compared to template free TPPS aggregation has also been reported in literature e.g. for the interaction of TPPS at low pH with poly(lysine), PEG-b-PVP micelles and PAMAM dendrimers [187,198,206] supporting the conclusion of template-directed TPPS assembly. However, at the chosen conditions no particular enhancement of TPPS J-aggregation tendency could be observed in the present study (see Figure 7.11-b1) as it e.g. was observed for the three mentioned literature studies [187,198,206].

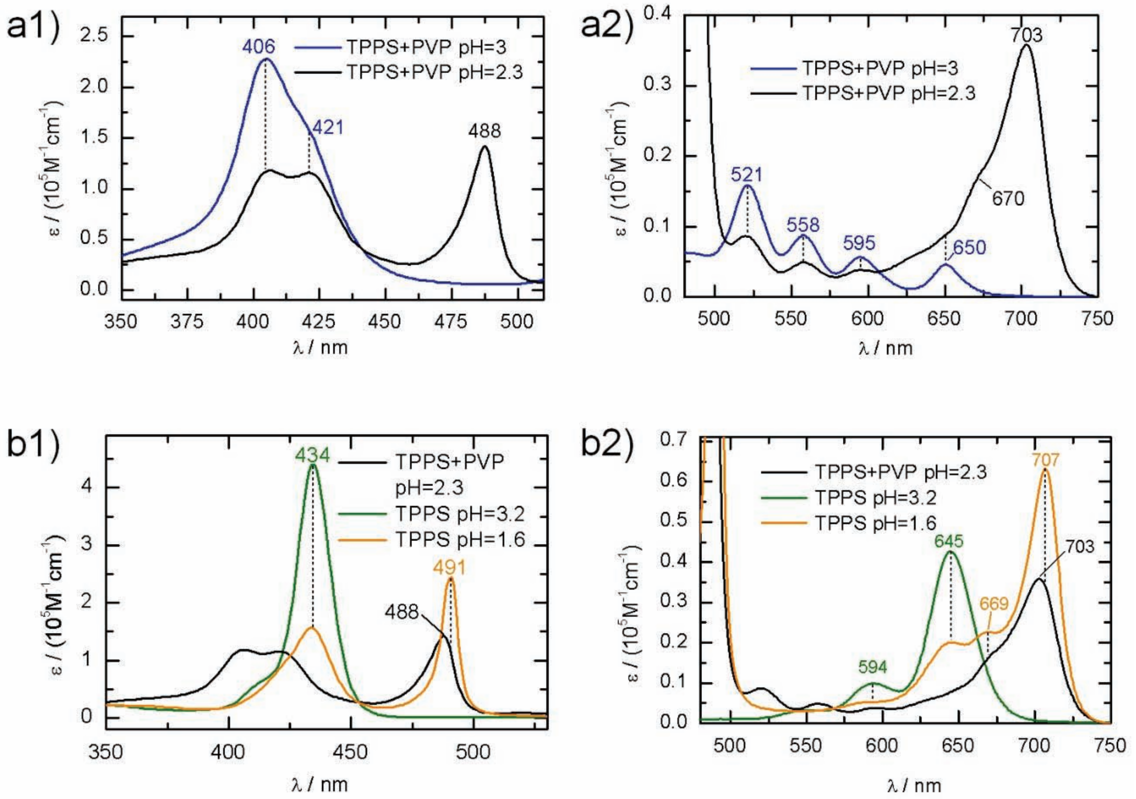

Figure 7.11: Spectral behavior of PVP-TPPS complexes at pH = 2.3. The PVP-TPPS aggregates were first prepared at pH = 7 and then adjusted to pH = 2.3: a) PVP+TPPS *l* = 0.5, pH = 2.3 in comparison to PVP-TPPS at pH = 3; b) PVP+TPPS *l* = 0.5 at pH = 2.3 in comparison to pure TPPS at pH = 3.2 and pure TPPS at pH = 1.6.

There is also considerable spectral change for the Soret signal with a strong hypochromicity. The two signals do not shift in location but the intensity ratio changes. For a better estimation of the effects the evolution of the spectrum upon subsequent HCl addition is presented in Figure 7.12.

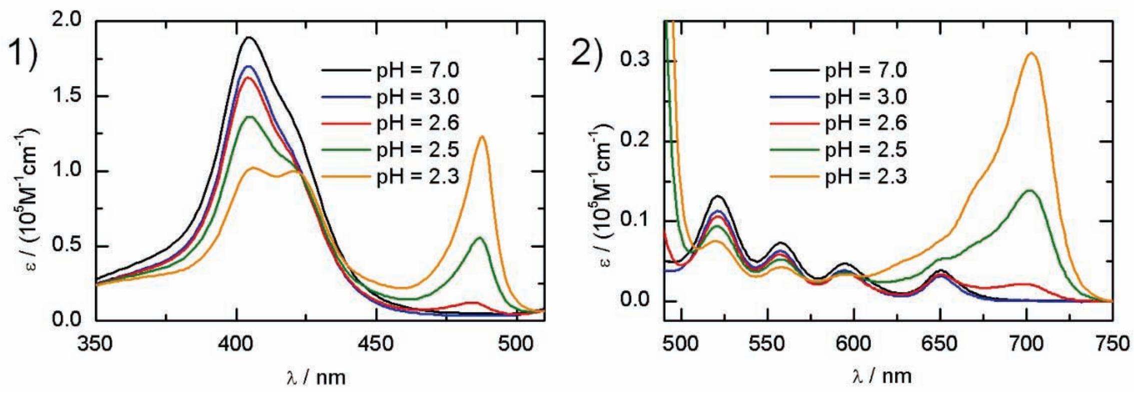

Figure 7.12: PVP+TPPS *l* = 0.5 prepared at pH = 7, subsequent addition of HCl.

As was already reported before and reproduced in Figure 7.11-b1, TPPS in the Soret region exhibits strong hypochromicity upon partial transformation from protonated porphyrin to J-aggregate. This simply can be explained by the fact that a fraction of TPPS that was previously bound as tetravalent molecule to PVP now forms J-aggregates that solely exhibit the 491 nm signal in the Soret region.

In Figure 7.11-b1 the TPPS-PVP sample at pH = 2.3 does not show any signal at the peak position of single protonated TPPS (m-PH_4; overview of short form nomenclature in Table 7.6) at 434 nm. This indicates that there is no such species present. The TPPS bound to PVP in neutral pH (PH_2-PVP) directly transforms to J-aggregates. This reasoning is additionally supported by the lack of an arising signal at 645 nm in the Q-band spectrum that would be indicative for m-PH_4.

A further observation in the Q-band region is the evolution of a long wavelength signal at around 700 nm, which is characteristic for J-aggregates. However, the signal in comparison to the signal of J-aggregates from pure TPPS is shifted towards a lower wavelength by 4 nm and very similarly to the 488 nm signal is considerably broadened.

Surely the question arising here is whether the J-aggregates are built up from porphyrins in solution not bound to the polyelectrolyte after leaving their previous binding sites or if the TPPS forms J-aggregates in or on the polyelectrolyte template itself. At first sight it is difficult to draw a safe conclusion about this question from the present UV-vis experiment and eventually further investigation is needed. However, the broadening and blue shift of the two J-aggregate signals indicate that the J-aggregate formation is affected by the presence of the polyelectrolyte.

Table 7.6: Band positions of TPPS and PVP-TPPS complexes at different pH. PH_2: free base porphyrin, PH_4: protonated porphyrin, m-PH_x: monomeric porphyrin, J-PH_x: J-aggregate of porphyrin, PH_2-PVP: unprotonated TPPS bound to PVP, s: shoulder.

	B-bands: λ/nm single porphyrin	**Q-bands: λ/nm single porphyrin**	**J-bands: λ/nm J-aggregate**
TPPS, pH = 7 PH_2	413, (s 393)	516, 552, 580, 634	-
TPPS, = 3.2 PH_4	434, (s 410)	594, 645	-
TPPS, pH = 1.6 m-PH_4 + J-PH_4	434	593, 645	491, 669, 707
TPPS+PVP, pH = 7 PH_2-PVP	405, 421	522, 558, 595, 650	-
TPPS+PVP – pH = 3 PH_2-PVP	405, 420	521, 558, 595, 650	-
TPPS+PVP – pH = 2.3 PH_2-PVP + J-PH_4	406, 421	520, 558, 595 (s648)	488, (s 670), 703

Also in the pH regime (1.5 < pH ≤ 2.5) it may be of interest to investigate an experiment where the stock solutions are freshly adjusted (10 min for handling) to pH = 2 prior mixing. In contrast to the situation at pH = 3 where the order of pH adjustment did not affect results, here a complication may occur: if the pure TPPS stock solution is adjusted to pH = 2, J-aggregates may form in a time dependent fashion. Thus, the history of the stock solution can influence the results after mixing.

Figure 7.13 shows UV-vis results for TPPS-PVP prepared at pH = 2, that is where stock solutions were adjusted to pH = 2 prior to mixing. Interestingly, the J-aggregate signals at 488 nm, 669 nm and 703 nm are very similar to the sample that was mixed at pH = 7 and thereafter adjusted to pH = 2.3. Thus, also here J-aggregates are formed that have a different spectral signature than in pure TPPS solution: evidently there is an effect of PVP on the J-aggregates. This effect which was already described above for the sample mixed at pH = 7 is evidently very similar if either J-aggregates are formed from TPPS molecules that previously were bound to PVP brush or from TPPS molecules that were present within free J-aggregates before.

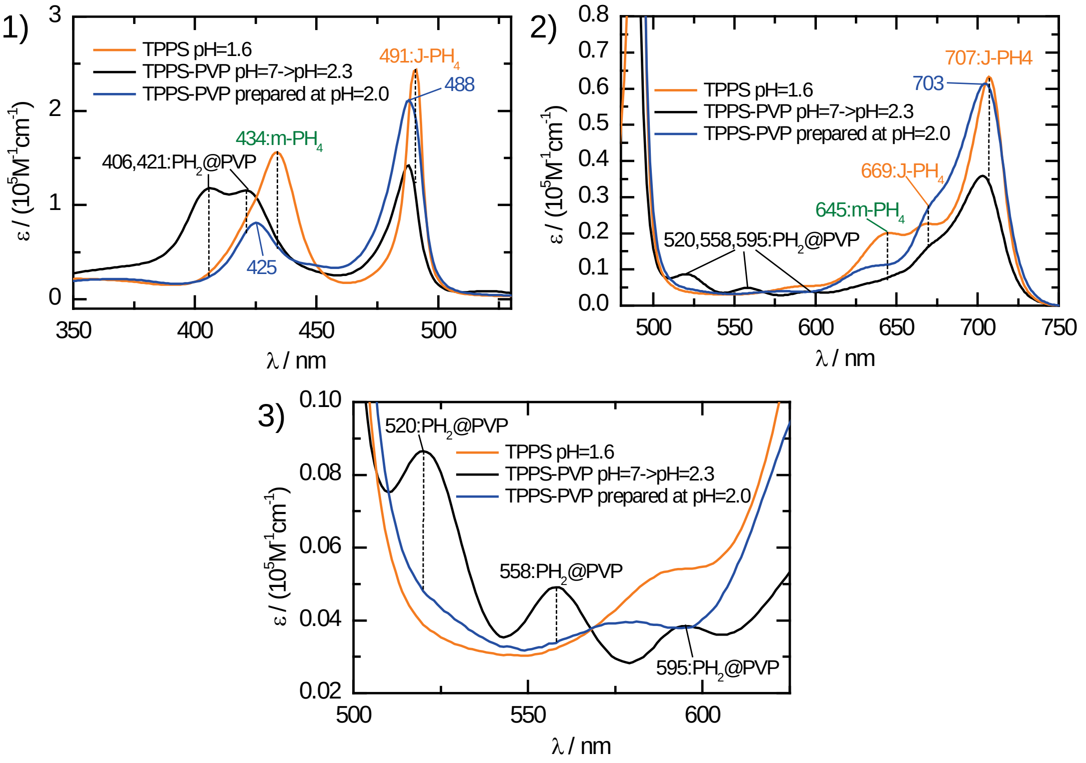

Figure 7.13: Comparison of spectra of TPPS-PVP complexes prepared at pH = 2.0 with two samples from Figure 7.11: pure TPPS at pH = 1.6 and TPPS-PVP complexes prepared at pH = 7 and then adjusted to pH = 2.3. (3) Magnification of part of (2).

Another interesting observation in Figure 7.13 can be made for the signals apart from J-aggregate bands: in the Soret region only one band is visible at 425 nm that lies in between the red shifted band of PVP-bound TPPS (PH_2-PVP: 421 nm) and the Soret band of free protonated TPPS (434 nm). In addition, the Q-bands of PVP-bound TPPS (PH_2-PVP) are not present for this sample. Evidently, the species PH_2-PVP is not present here. A comparison with the spectrum of pure TPPS at pH = 1.6 indicates that the species present in the blue TPPS-PVP spectrum at pH = 2 may be a monomeric and protonated form of TPPS that shows a blue-shifted Soret (434 nm → 425 nm) signal potentially due to binding to PVP and thus shows no Q-band signals at 520-560 nm.

Summarizing the results from the UV-vis investigation of PVP-TPPS at $pH < 4$ the first important result is that at ($3 \leq pH < 4$) TPPS is in the tetravalent state if PVP is present. This result is independent on the procedure of either adjusting pH to ($3 \leq pH < 4$) before or after mixing. Evidently, the pK_a of TPPS is reduced by the polyelectrolyte. It also has been reported in literature that polyelectrolytes may reduce the pK_a of binding pH-sensitive counterions [157,161,184,189]. In the presence of polyelectrolytes for TPPS a pK_a of about 2.5 is reported [161,189]. Thus, the present observations are in line with the mentioned literature reports.

In turn this result means that it is very unlikely that e.g. at $pH = 3$ one of the goals of this section of switching networks “on” and “off” may be accomplished, since TPPS in effect is not switched to divalent state at $pH = 3$ if PVP is present. The same conclusion will be drawn below from light scattering results and thus it was not attempted to image samples with AFM at $pH = 3$ but rather at $pH = 2$ as will be shown in the next paragraphs. For the goal of switching between networks and disconnected networks this result is quite unfortunate: switching from $pH = 7$ to $pH = 3$ would be advantageous in that sense that lower ion build-up would occur if the switching is repeated several times.

For the samples at ($1.5 < pH \leq 2.5$) the first important result is that there are TPPS J-aggregates present for either adjusting from $pH = 7$ to $pH = 2$ or preparation at $pH = 2$. That means the samples actually contain divalent TPPS molecules since J-aggregates are built up from that species. In addition, there are indications of divalent TPPS that is not within J-aggregates for the preparation method at $pH = 2$. Thus, in that sense samples at $pH = 2$ fulfill the prerequisite of divalency for the intended switching experiments. Independent from this goal it is interesting to note that eventually the spectral signature of J-aggregates at $pH = 2$ is influenced by the presence of PVP and thus J-aggregate formation is apparently controlled by the polyelectrolyte template.

Imaging of PVP-TPPS aggregates at pH < 4

Following the investigations of UV-vis spectra discussed above, in this section results are presented for AFM imaging investigation of TPPS-PVP samples at pH = 2. As before, both experiments will be discussed: mixing of stock solutions at pH = 7 and thereafter adjusting to pH = 2 as well as direct preparation at pH = 2.

If TPPS and PVP are combined at charge stoichiometry (l = 1) in neutral solution (porphyrin state: PH_2^{4-}) spontaneous precipitation occurs due to complete charge neutralization as was reported above. At pH = 2 in pure porphyrin solution it is expected that TPPS is present as divalent protonated porphyrin (PH_4^{2-}). If the same experiment at same molecular TPPS to PVP ratio is reproduced at pH = 2, the charge ratio theoretically reduces to l_{eff} = 0.28 due to the lower TPPS valency and PVP protonation if full protonation for both species is assumed (see above; from the spectroscopy results it is evident that TPPS is only partially protonated and thus the effective charge ratio is in between l_{eff} = 0.28 and l_{eff} = 0.56). In order to test if the real charge ratio reduction indeed affects aggregation, a simple experiment was conducted: both TPPS and PVP were freshly adjusted to pH = 2 and combined at the charge ratio l_{eff} = 0.28 (using charge number 2 for TPPS and assuming full PVP protonation). A clear green solution with same color as pure TPPS in pH = 2 is observed that remains clear for at least a week. This observation supports the idea of a possible network size manipulation by the pH switch. If the very same sample is afterwards adjusted to pH = 7, spontaneous precipitation of TPPS-PVP aggregates occurs. However, from this experiment it is unclear whether the effect is due to the divalent state of TPPS at pH = 2 that possibly is not able to interconnect brushes to networks or simply due to the reduction of the charge ratio. Further investigations by AFM and light scattering that deal with this question are presented below.

Very interestingly, a different behavior at pH = 2 was observed if the TPPS was not freshly prepared at pH = 2 but rather was allowed to stand overnight before PVP addition. In this experiment TPPS-PVP aggregates spontaneously precipitate at pH = 2 at the same molecular ratio as given above. Obviously, the time dependent evolution of TPPS J-aggregates affects aggregation and/or the extent of charge neutralization here. A possible explanation for this effect will be given below.

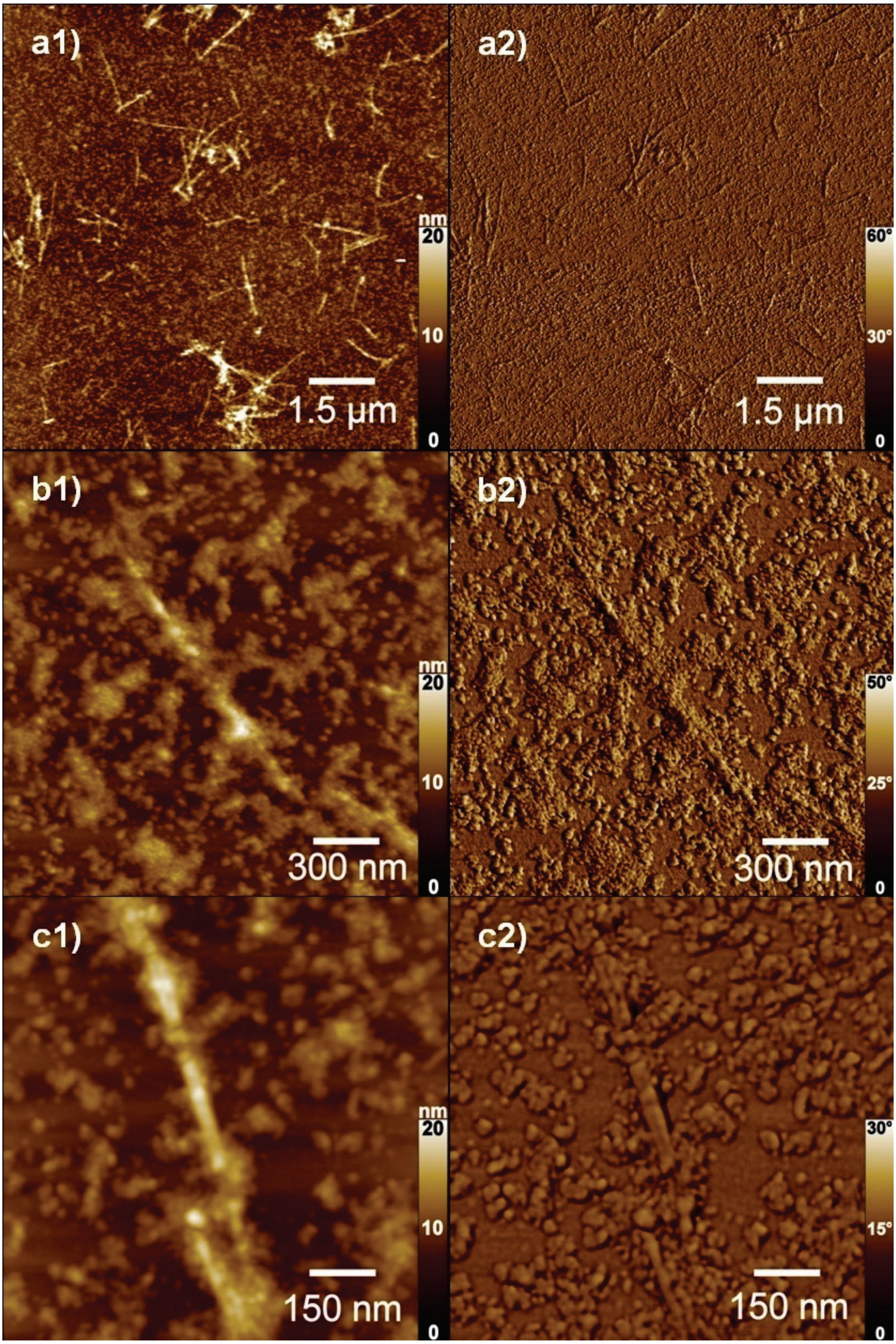

Figure 7.14: AFM 1) height and 2) phase images of PVP47+TPPS prepared at pH = 2, *l* = 1.

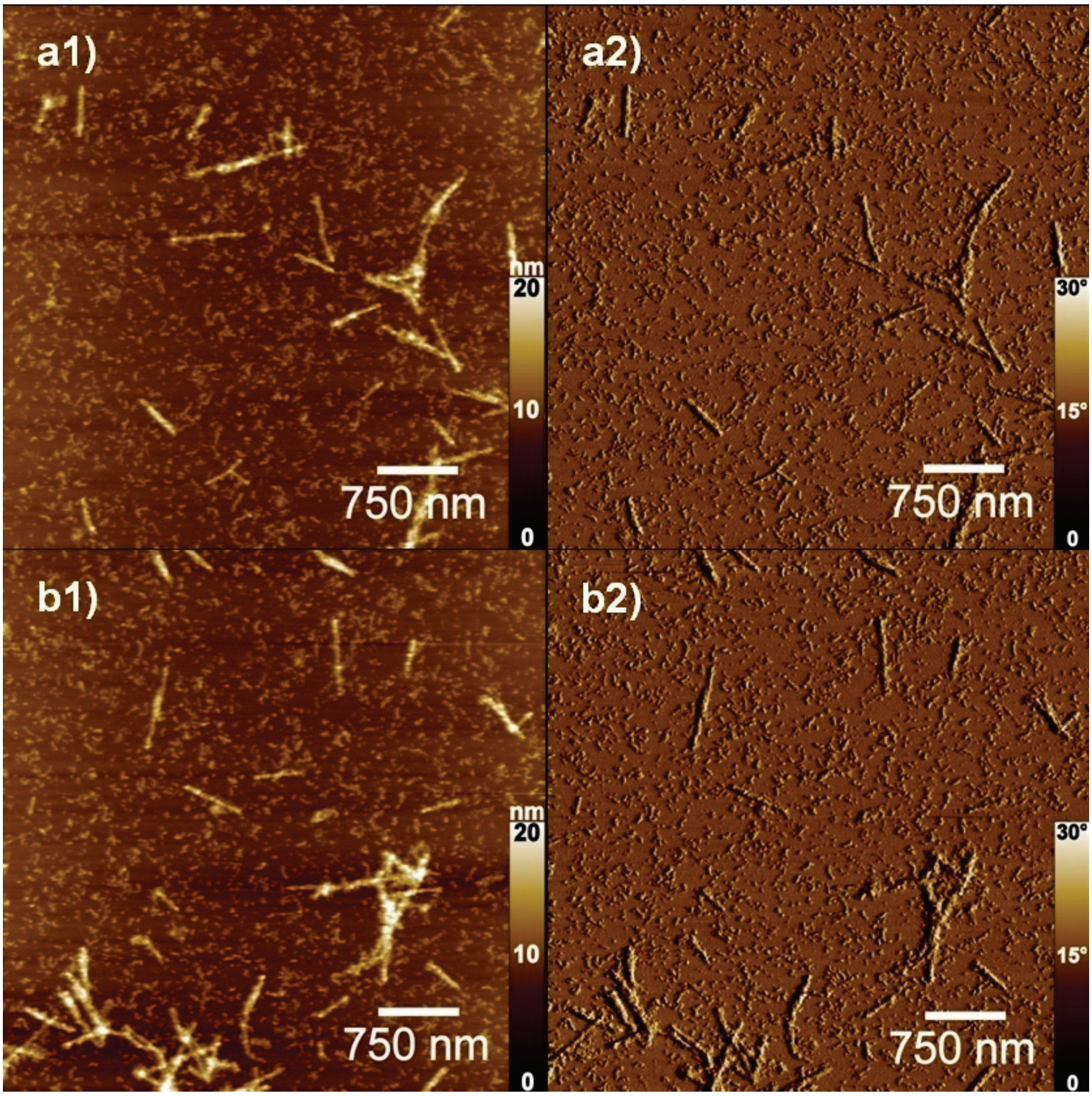

Figure 7.15: AFM 1) height and 2) phase images of PVP47+TPPS prepared at pH = 2, *l* = 0.75.

AFM images of the clear TPPS-PVP sample at *l* = 1 from freshly prepared stock solutions of pH = 2 are given in Figure 7.14. Evidently, rod-like TPPS J-aggregates can be observed in the images besides a relatively large amount of additional material that could consist of either TPPS porphyrin, added HCl or a combination thereof. Due to the surface coverage single brush molecules cannot be observed. The J-aggregates apparently show shorter contour lengths as compared to TPPS nanorods from pure TPPS solutions (see Figure 4.9). This observation corresponds well to the difference of spectra between “free” TPPS J-aggregates and J-aggregates in the presence of PVP that were discussed in the UV-vis section above. There significant broadening of J-aggregate bands was observed. Since the width of aggregate bands generally gets broader if the extent of electronic communication between aggregated dyes is reduced, this spectral change corresponds well to the fact that smaller J-aggregates are seen in the AFM images.

An additional observation in Figure 7.14 is that the rods seem to have a tendency to accumulate or aggregate that was not observed for the pure TPPS case. If the relative TPPS concentration is lowered to ratio l = 0.75 as in Figure 7.15, single brush molecules can be observed besides rod-like J-aggregates that are present here as well. Again the TPPS rods are noticeably shorter than for the pure porphyrin case and show a tendency for inter-rod attraction. At both TPPS to PVP ratios for these samples prepared at pH = 2 no aggregation of PVP brushes to networks is observed.

Evaluating the current experiment, it has to be taken into account that the TPPS solution is adjusted to pH = 2 prior addition of PVP. Even though the time between bringing TPPS to pH = 2 and adding PVP was kept below 10 minutes, still free evolution of TPPS nanorods will have taken place before PVP addition. Thus, it is uncertain if this initial time period will have influenced the later morphology of TPPS rods. When PVP brush is added to pre-developed TPPS nanorods the oppositely charged brushes potentially interconnect several rods to the aggregates present in Figure 7.15. This explanation for the observed aggregate formation is supported by the above described precipitation of aggregates if the TPPS was allowed to age overnight at pH = 2. Here the larger number and size of already grown nanorods may lead to aggregates that are not colloidally stabilized and thus precipitate. It is unclear whether the growth of nanorods is terminated by PVP addition or if the growth continues in the new environment. But clearly the brush presence inhibits growth (potentially due to PVP nanorod binding) resulting in overall shorter rod lengths than would be expected without brush addition.

A clearer experiment to test how TPPS J-aggregates evolve in the presence of PVP brushes is to first prepare TPPS-PVP complexes at pH = 7 and subsequently add HCl to lower the pH to about 2. In this procedure TPPS J-aggregates evolve in the presence of PVP as was shown by the UV-vis results above. The resulting images are given in Figure 7.16. Also in this experiment two different issues need to be discussed. Continuing the discussion about J-aggregate formation with polyelectrolytes, the formation of nanorods will be considered. But first it has to be noted that no brush-porphyrin networks can be observed for the present sample that was prepared by addition of HCl to the brush-porphyrin networks. Thus, in addition to the previous observation that such networks are not formed at low pH, it can be concluded that networks assembled in neutral pH become disconnected by HCl addition.

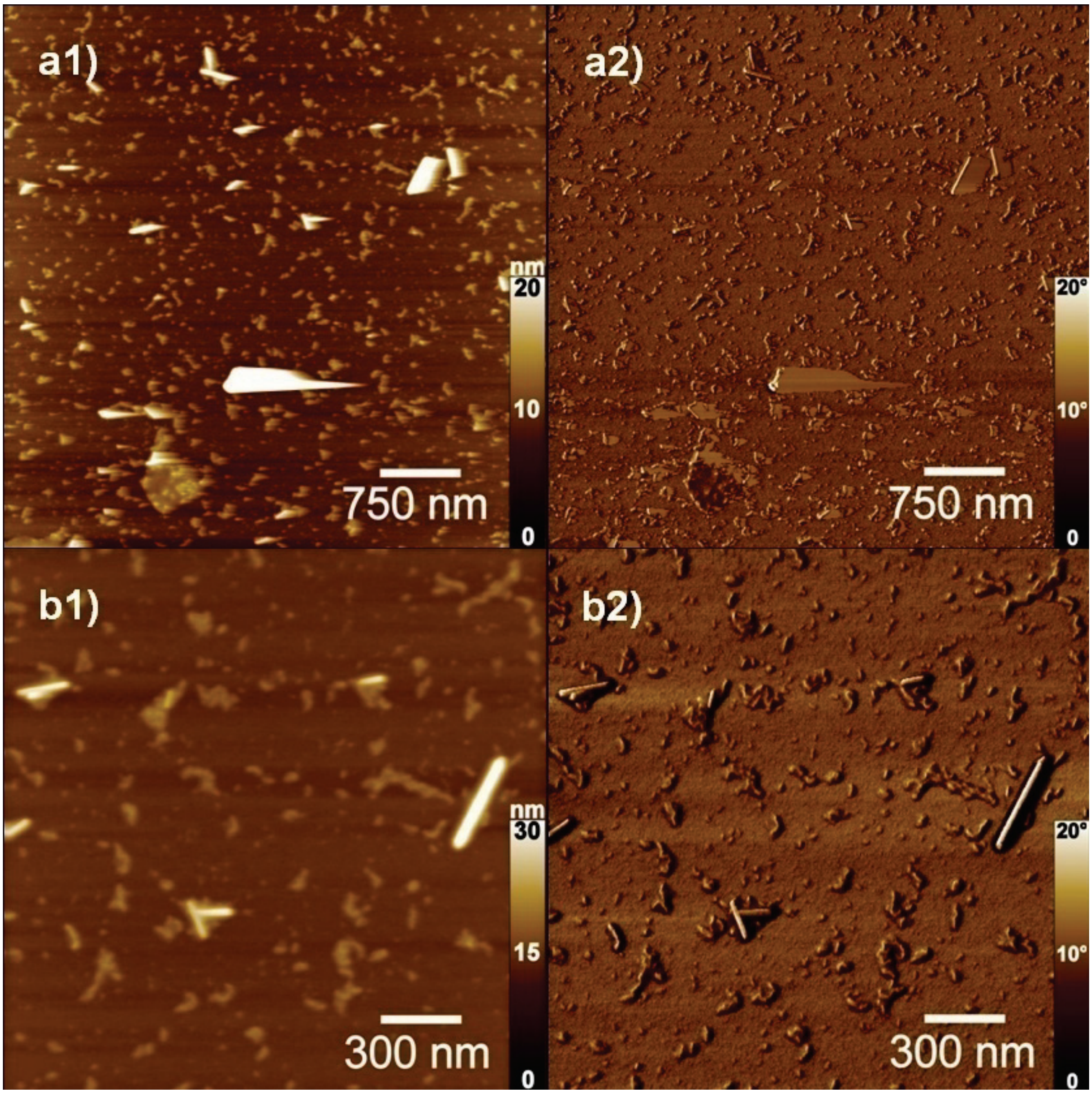

Figure 7.16: AFM 1) height and 2) phase images of PVP47+TPPS prepared at pH = 7, *l* = 0.5 (see Figure 7.5) and subsequently adjusted to pH = 1.6 by addition of HCl.

Coming back to the question of how TPPS nanorods evolve in a solution where PVP brush molecules are present, the effect of PVP brushes on J-aggregate formation can clearly be seen in Figure 7.16 by the observation that the nanorods are considerably shorter than in the absence of PVP (as in Figure 4.9). Throughout the sample surface no cylinders longer than the ones in Figure 7.16 are observed. From absorption spectra discussed above it was concluded that the TPPS molecules bound to PVP at pH = 2 will partially transfer to J-aggregates (j-PH_4) without the formation of free protonated TPPS (m-PH_4). From the spectra it could not be safely concluded if J-aggregates are formed within brush templates (potentially only oligomeric stacks) or if the porphyrins leave the brush and thereafter build up J-aggregate cylinders that, however, are to some extent affected by PVP as was seen in the spectra. The experiment of Figure 7.16 corresponds to the spectrum in Figure 7.13. Since J-aggregate TPPS cylinders can be seen in Figure 7.16, the J-aggregate signals in the spectrum clearly correspond to TPPS cylinders outside the brush templates. Thus, it can be concluded that a fraction of TPPS molecules leaves the PVP binding sites to build up TPPS nanorods. Whether these porphyrin rods are still connected to brush molecules or if they are free in solution cannot safely be concluded from the AFM images. However, as was already discussed, the TPPS nanorod formation is influenced by PVP and leads to shorter rod lengths.

Summarizing the AFM results for PVP-TPPS complexes at pH = 2, the first important result is that for both preparation routes, mixing in pH = 7 and adjusting to pH = 2 as well as preparation directly at pH = 2, no brush-porphyrin networks are observed. Evidently, no networks are formed at pH = 2 and networks present at pH = 7 get disconnected upon HCl addition. The question whether this effect is due to the TPPS valency switch or to the screening effect of newly introduced ions will be addressed below. An additional topic that was covered in the AFM investigations at pH = 2 was the morphology of J-aggregates in comparison to J-aggregates in pure TPPS solution (for comparison see Figure 4.9). Generally, TPPS J-aggregates are of smaller length in the presence of PVP and if PVP is added to preformed TPPS J-aggregates the nanorods tend to aggregate.

The experiment of Figure 7.16 shows that PVP-TPPS networks may be disassembled by HCl addition but the experiment does not give a certain answer to the question if the disassembly is due to the valence “switch” of TPPS from -4 to -2 at pH = 2 and its assembly to J-aggregates or if its a screening effect by the additional ions. An answer to this question may be given by another experiment where a sample at pH = 2 is adjusted to pH = 7 by addition of NaOH. If the crucial parameter for network assembly and disassembly is the valency state of TPPS, networks should be able to be reassembled by

NaOH addition. If it would be a salt effect, networks should not be formed by NaOH addition since the addition will increase ion concentration.

Figure 7.17 gives the AFM image of a TPPS-PVP sample at pH = 9 that was prepared from the sample in Figure 7.15 (pH = 2) by addition of NaOH.

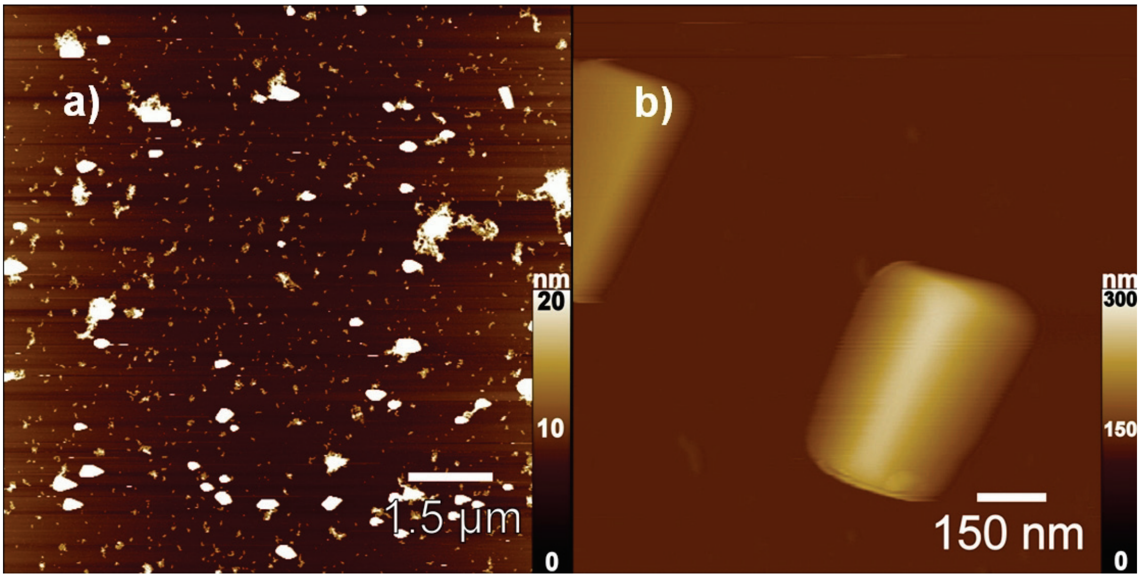

Figure 7.17: AFM height images of PVP47+TPPS prepared at pH = 2, *l* = 0.75 added NaOH to pH = 9, right: NaCl salt crystals.

At first sight the image on the left reveals the presence of rectangular crystals with heights larger than 100 nm. Figure 7.15-b shows a high resolution image of such a rectangular crystal. These crystals are from sodium chloride that is formed in the neutralization process. Due to the relatively high crystals, imaging of the rather low height (~10 nm) brush particles is somehow hindered since the tip probe easily becomes blunt when imaging the rough surface. However, if the tip is carefully approached to the surface using a rather small scan area, parts of the surface may be imaged in between the salt crystals (see Figure 7.18). Still, the tip is negatively affected by the salt crystals and due to its bluntness the resolution is quite poor, but still brush-porphyrin networks can clearly be seen. The networks seem to be of similar morphology as the PVP-TPPS and PSS-TAPP networks discussed above. Thus, it seems to be possible to “switch on” TPPS-PVP networks by adjusting the pH from acid to neutral due to the change of TPPS valency from -2 to -4. In the next part of this section the “switching” behavior will be further investigated by light scattering.

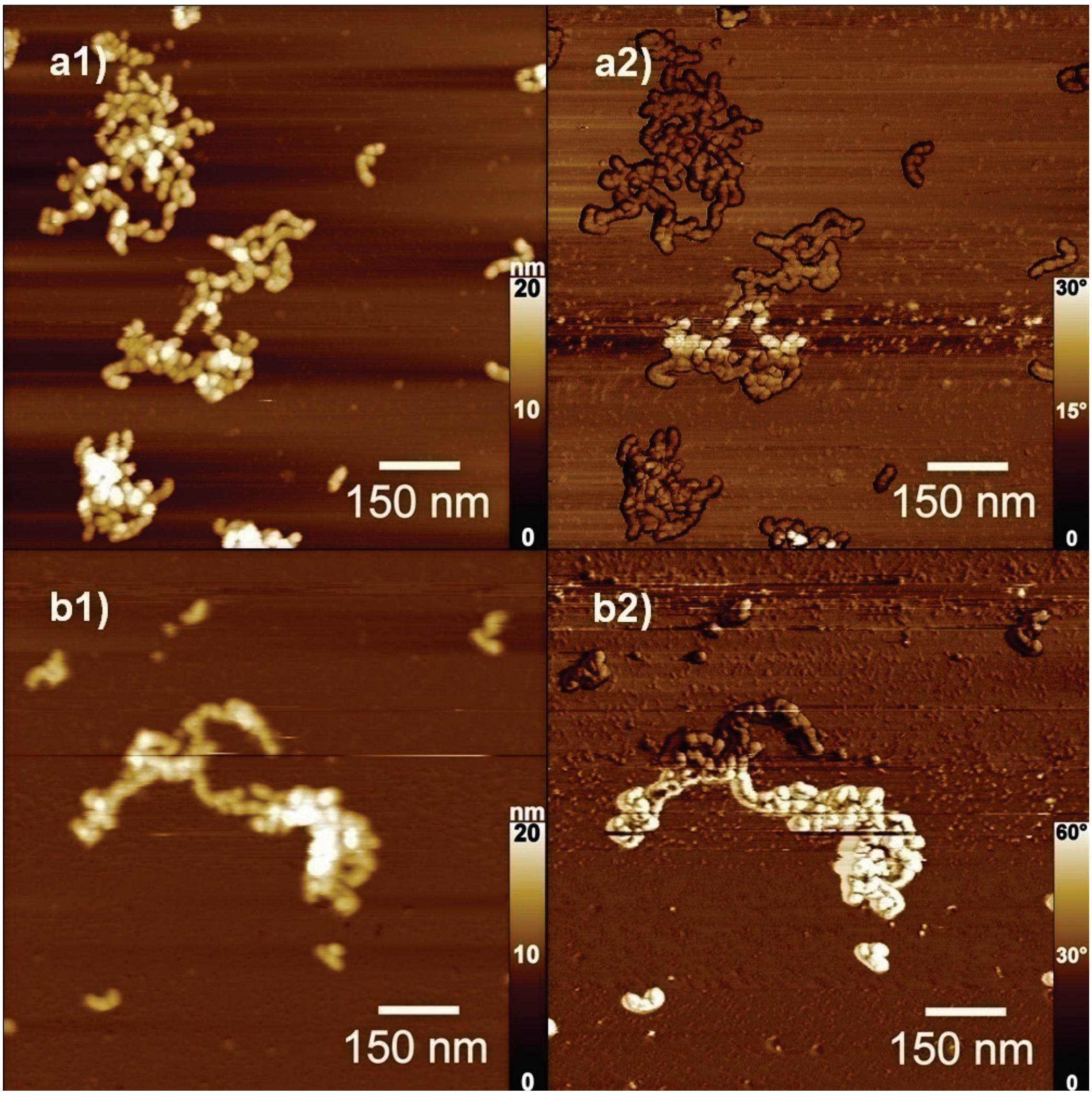

Figure 7.18: AFM 1) height and 2) phase images of PVP47+TPPS prepared at pH = 2, *I* = 0.75 added NaOH to pH = 9 (same sample as in Figure 7.17 – "in between" salt crystals, pure resolution due to tip defects induced by NaCl crystals.

Size of PVP-TPPS aggregates at pH < 4

In this section the size changes of PVP-TPPS aggregates as investigated by light scattering on changing the solution pH will be presented. For a better comparison of PVP-TPPS radii with pure brush size Table 7.7 lists radii and intensities of PVP brush at different pH values.

It has been reported in section 7.1 that in neutral solution the addition of TPPS porphyrin to PVP leads to a distinct increase in hydrodynamic radius due to brush-porphyrin network formation. The network size in salt-free neutral solution is observed to be time stable. Additionally, it has been reported that after adjusting the pH of the solution to pH = 2 no networks could be imaged with AFM due to a switch of network morphology to single brushes and TPPS J-aggregates. This switch should also be visible by light scattering in a size change. It should be kept in mind that changing pH from 7 to 2 does not simply induce a structural shift from networks to single brushes but that additional J-aggregates are built up and it has been reported in section 4.2 that TPPS nanorods may have a significant contribution to the scattering intensity.

Table 7.7: Infrared light scattering results for PVP brush at different pH values (θ = 90°).

PVP47	**$R_{h,app}$/nm**	**$\mu_2/(\Gamma)^2$**	**I/I_{water}**
pH = 7	35.5	0.24	23.5
pH = 3.9	32.3	0.19	25.8
pH = 1.8	29.3	0.17	25.1

In order to avoid complications by TPPS nanorod contribution to light scattering intensity, at first the scattering behavior at the regime ($3 \leq pH < 4$) will be discussed. Directly (~15 min due to handling issues) after adding HCl to a TPPS-PVP network solution at pH = 7 (l = 0.5) resulting in a pH of 3.9 same intensity and size was measured as in Table 7.4. Apparently the switch in pH does not have an instantaneous effect on aggregate size. This observation has to be evaluated keeping the UV-vis results of Figure 7.9 in mind. The spectrum shows that TPPS at pH = 3 stays bound to PVP and is not protonated and thus this conclusion can explain why the networks at first do not disassemble. In addition to the possible protonation effect of the pH change to TPPS the added Cl^- ions may also induce a salt effect due to their screening potential. The concentration of added Cl^- ions here is $c(Cl^-)$ = 0.5 mM and thus is already larger than the porphyrin and polyelectrolyte charge concentration of 0.12 mM and 0.24 mM, respectively.

If the scattering behavior of the described sample with pH = 3.9 is monitored over time, a slow decrease in scattering intensity and radius is observed (see Figure 7.19) that is nearly complete after 35 hours. The hydrodynamic radius reduces from R_h = 50.9 nm to R_h = 30.2 nm over that time. Apparently, the PVP-TPPS networks get disconnected by HCl addition since the size after 35 h is close to brush size at this pH (see Table 7.7).

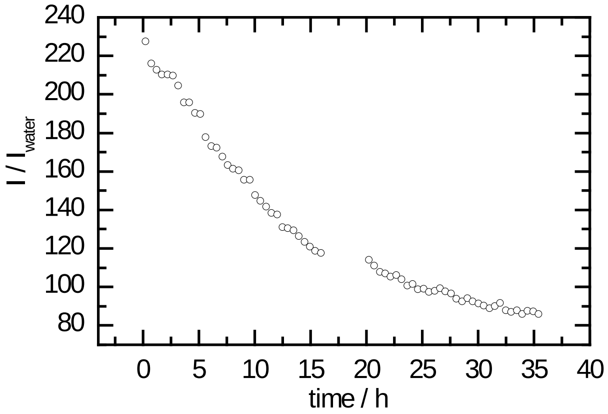

Figure 7.19: Time dependent decrease of PVP-TPPS aggregate light scattering intensity at 90º (displayed as multiple of pure water scattering) after addition of HCl to pH = 3.9 at time = 0.

The shape of intensity decrease appears to be similar to the decay function that was measured for disassembly to PSS brush-TAPP networks after sodium chloride addition in chapter 5 (Figure 5.32). This observation together with the fact that TPPS does not show the UV-vis spectrum of protonated porphyrin indicates that the size reduction most likely is due to the salt effect of added ions (the spectrum of the sample in Figure 7.19 remains same after network disintegration and is identical with Figure 7.9).

An additional experiment has been conducted where TPPS and PVP were adjusted to pH = 3.9 prior to mixing and thereafter the stock solutions were combined. Thus, here TPPS is mixed in the protonated state (m-PH_4^{2-}) with PVP. It was shown above that the obtained UV-vis spectrum of the PVP-TPPS complexes is identical with the other preparation route. Thus, TPPS binds to PVP and thereafter has the same electronic state as if it was bound in neutral solution (PH_2^{4-}) to PVP. If this sample is investigated with light scattering shortly after combining the stock solutions (~15 min after mixing) a size of R_h = 45.0 and intensity of I/I_{water} = 150.0 is measured. These values are in between the situation for pure brush molecules and PVP-TPPS networks. It can be concluded that a network build-up takes place even in pH = 3.9 that corresponds to TPPS switching to tetravalent state by binding to PVP. However, the network size and scattering intensity are not stable but rather continuously decrease over time. After about 30 hours a plateau is reached and there is no further reduction of radius. Resulting radius and intensity are comparable to the previous experiment where single PVP-TPPS complexes were prepared from HCl addition to PVP-TPPS networks at pH = 7 (Table 7.8).

Table 7.8: IR-DLS results at 90° for two PVP-TPPS samples at pH = 3.9 after disassembly of PVP-TPPS networks.

PVP-TPPS	**$R_{h,app}$/nm**	**$\mu_2/(\Gamma)^2$**	**I/I_{water}**
pH = 7 to pH = 3.9	30.2	0.201	85.3
prepared at pH = 3.9	31.1	0.225	70.3

This phenomenon of network build-up and subsequent disassembly resembles closely the observation of PSS brush-TAPP networks that are assembled in salt containing aqueous solution and after ~1 day disassembled again to brush size (see [82]). The conclusion of the present network decomposition being induced by electrostatic screening of added ion is thus supported by the present observation.

A further experimental step to investigate the present system is to add NaOH to adjust the pH of the disassembled networks back to pH = 7 in order to test whether networks are built up again. If the previously described network disintegration is solely due to the ion screening effect it is expected that no new aggregation is observed. This is actually what is observed by light scattering: adding NaOH to both samples of Table 7.8 up to a pH = 7 results in no significant change in hydrodynamic radius as well as in scattering intensity.

Summarizing the findings for the PVP-TPPS system at pH = 3.9 it has to be concluded that “switching” between PVP-TPPS networks and PVP-TPPS single brush complexes is not possible at this pH. The reason thereof is given by the fact that TPPS is in fact divalent in polyelectrolyte free solution at pH = 3.9 but changes to tetravalent state upon binding to PVP. Thus, the idea of switching TPPS from a tetravalent to divalent counterion is inherently prohibited by the system at this pH. In the next paragraphs it will be discussed if this situation potentially changes if the pH is lowered further.

Another important conclusion of the present investigation is that using pH adjustment to switch TPPS valency state has the drawback that for the switching effect to take place, ions have to be introduced to the system that may shield the secondary network build-up and thus will affect the network stability even if the desired switch would be possible.

In order to shine further light on the quite complex aggregation behavior of TPPS-PVP at $pH < 7$ the situation at $(1.5 < pH \leq 2.5)$ where TPPS J-aggregates are present shall be discussed. Spectral evidence has shown that TPPS J-aggregates consist of divalent TPPS molecules and thus the previously stated thought experiment of "switching" TPPS from PH_2^{4-} to PH_4^{2-} (in contrast to the case at $pH = 3.9$) happens here in the presence of PVP. In addition, AFM investigation revealed that J-aggregates are formed at $(1.5 < pH \leq 2.5)$ (if PVP is present) that are shorter than free TPPS J-aggregates. It may thus be possible to disassemble TPPS-PVP networks by "extracting" and protonating TPPS molecules from PVP-TPPS complexes that then build up J-aggregate nanorods. Within this idea it then should be possible to reassemble the networks by "releasing" and deprotonating TPPS that was previously present within J-aggregates. Indeed, AFM investigations (see above) show the disconnection and reassembly of PVP-TPPS networks when changing to pH ~ 2 and back to neutral. However, in the further discussion it has to be kept in mind that the spectral investigation has proven that no full transformation of porphyrins bound to PVP to J-aggregates containing protonated (PH_4^{2-}) TPPS is observed. In fact, Figure 7.11 shows that at $pH = 1.6$ TPPS J-aggregates coexist with PVP-bound and tetravalent TPPS.

Using the same approach as for the $pH = 3.9$ case before, at first a PVP-TPPS sample will be discussed that was prepared at $pH = 7$, showed stable networks there and afterwards was adjusted to $pH = 1.6$. As in the previous case, the addition of HCl leads to a marked decrease in hydrodynamic radius from $R_h = 50.9$ nm to now $R_h = 29.3$ nm (Table 7.9). Surprisingly, this value is very close to the hydrodynamic radius of pure PVP brush at this pH (Table 7.7). This is surprising because the presence of J-aggregates has been proven by both UV-vis and AFM investigation and thus these aggregates should contribute to sample scattering.

Figure 7.20 shows the correlation function of this sample together with a CONTIN size distribution analysis. The main decay here exhibits only one signal independent on the regularization strength applied to the fit. It is thus not possible to decompose the scattering signal to the contribution of PVP-TAPP single brush complexes and TPPS J-aggregates. Since the scattering intensity is higher by a factor of about 1.6 comparing PVP-TPPS scattering at pH = 1.6 with the case at pH = 3.9, a contribution of J-aggregates is presumably detected here. However, due to the reduced size of J-aggregates in comparison to their PVP free counterparts apparently their size range is similar to the size of PVP-TAPP complexes here and thus cannot be separated from PVP-TPPS scattering.

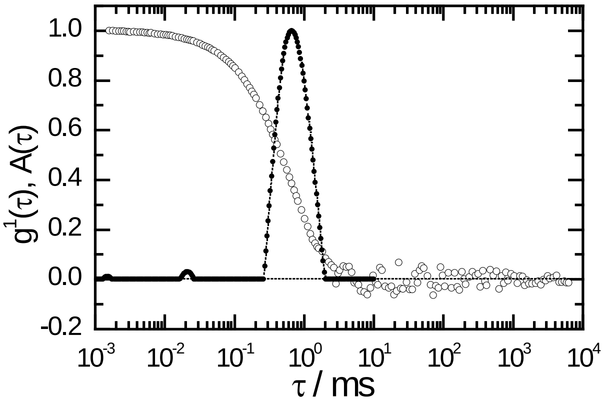

Figure 7.20: CONTIN evaluation of PVP-TPPS correlation function at pH = 1.6.

Although the light scattering behavior of PVP-TPPS complexes at pH = 1.6 is up to now quite similar to the case of pH = 3.9, there is a significant difference in the time dependency. Whereas the network disassembly for pH = 3.9 takes place over more than 30 hours, the size and intensity reduction from network to single brush was measured here directly after HCl addition (~20 min for handling).

One explanation for an enhanced speed of network disconnection can be the higher salt concentration. However, the results of salt addition experiments presented above, where the processes always take multiple hours, indicate that a simultaneous switch induced by the screening effect of added salt is rather unlikely.

UV-vis and AFM investigations of the system at pH ~ 2 show that J-aggregates are instantaneously formed after reduction of pH (10-20 min for handling). It is assumed that TPPS molecules in the J-aggregate rods cannot contribute to brush-porphyrin network stability due to their divalent state. Thus, this fast formation of TPPS aggregates from porphyrins that leave their previous PVP binding sites presumably serves as a better explanation for the observed fast network disconnection.

Again the next experimental step for investigating TPPS-PVP behavior a pH = 1.6 is to add NaOH up to neutral pH in order to find out if networks are “switched on”. The process of network formation in this experiment has been successfully shown by AFM investigation (see Figure 7.18). Light scattering results for the sample after adjustment back to pH = 7 is given in Table 7.9.

Table 7.9: IR-DLS results at 90° a PVP-TPPS samples at pH = 1.6 after disassembly of PVP-TPPS networks and after adjusting the pH back to pH = 7.

PVP-TPPS	**$R_{h,app}$/nm**	**$\mu_2/(\Gamma)^2$**	**I/I_{water}**
pH = 7 to pH = 1.6	29.3	0.16	134.4
pH = 1.6 to pH = 7	27.0	0.23	70.1

In contrast to the results from AFM imaging, the hydrodynamic radius in the light scattering experiment does not increase upon neutralization as it would be expected for a network build-up. Also after several days the radius does not increase. Regarding the scattering intensity, a decrease is taking place upon NaOH addition (see Table 7.9) resulting in an intensity very similar to the single brush PVP-TPPS complexes at pH = 3.9 (Table 7.8). The decrease in intensity may be well explained by the disassembly of TPPS nanorods that is taking place upon NaOH addition and thus this scattering contribution will be removed. In contrast, network formation should result in a rising intensity as described above for several systems. It is reasonable to assume from the findings of the PVP-TPPS experiments at pH = 3.9 that the salt affect of the introduced ions is taking an important role here. Lowering the pH of such a sample to the regime where J-aggregates are formed and back to neutral will result in the formation of about 20 mM sodium chloride in the neutralization process. Considering that the charge concentration of PVP polyelectrolyte is only c = 0.24 mM here, this salt concentration may strongly shield secondary PVP-TPPS brush interaction. This shielding was observed for the PSS-TAPP system at same polyelectrolyte charge concentration and a salt concentration of c(NaCl) = 10 mM in chapter 5. However, processes described above for networks disconnected by salt addition were repeatedly quite slow. Thus, even though the salt concentration is high, a similar behavior as in pH = 3.9 where networks formed first but then disconnected due to salt with time may be expected apart from the light scattering results.

As reported above, AFM and light scattering show oppositional results. Whereas in AFM networks can be detected directly after sample preparation, there is no light scattering contribution measurable from these aggregates. In principal, it may be possible that large networks are formed that are not detected by light scattering at scattering angle θ_{IR} = 90º. This is the case if the networks have such a pronounced dependency of scattering intensity on angle that there is virtually no contribution at θ_{IR} = 90º. Then the measured scattering signal at 90º may correspond to single brush-porphyrin complexes that are coexistent with some large networks. In order to support this idea, further investigations with a setup enabling measurements at smaller angles may be helpful. Nevertheless, AFM imaging clearly shows the formation of networks directly after sample preparation. Whether the networks are stable or disconnect in salt solution with time as was the case for pH = 3.9 also may be tested by small angle light scattering investigations.

Summarizing section 7.2 about PVP-TPPS complexation at low pH, it again has to be differentiated between the two pH regimes of ($3 \leq pH < 4$) and ($1.5 < pH \leq 2.5$):

For ($3 \leq pH < 4$) no J-aggregation of TPPS has been detected for pure TPPS solutions as well as in the presence of PVP brushes. Whereas TPPS at ($3 \leq pH < 4$) in polyelectrolyte free solution is in the protonated and divalent state (section 4.2), it remains unprotonated in the presence of PVP due to a reduction of TPPS pK_a. Although TPPS is unprotonated and thus tetravalent, in light scattering only initially network formation could be detected and within 1-2 days the networks were fully disconnected. This result is explained by the screening effect of ions introduced for the reduction of pH. Apparently, the ionic strength of sample solutions at ($3 \leq pH < 4$) effectively induces disconnection of brush-porphyrin networks. Such a time-dependent network disconnection effect by the screening potential of added salt is described for PSS brush-TAPP networks in chapter 5 as well. If the conclusion is correct, this result would effectively prohibit the switching of networks “on” and “off” by pH variation since the pH is not low enough to effectively induce TPPS protonation but the concentration of added salt is apparently already sufficient to induce network disconnection by charge screening.

For ($1.5 < pH \leq 2.5$) J-aggregation of TPPS molecules was detected in the absence and presence of PVP47. Evidently, the polyelectrolyte has an influence on TPPS nanorod formation. Whereas in pure TPPS solution porphyrin rods show persistence lengths in the multi-micrometer scale, much shorter rod-like aggregates were found in the presence of PVP47 (rod length significantly smaller than 1 μm). The effect of PVP on J-aggregates is also visible in spectroscopy: the J-aggregate signal is considerably broadened and slightly blue-shifted.

In addition to TPPS J-aggregates generally a second form of TPPS is detected by spectroscopy. Whereas in pure TPPS solution this second species is a protonated and thus divalent free TPPS molecule, this is not the case for samples containing polyelectrolytes. Here J-aggregates coexist with unprotonated and thus tetravalent TPPS molecules that are bound to the polyelectrolyte. Thus, also in this pH regime TPPS is not fully protonated. This result, in analogy to the conclusion above, may be counterproductive for switching brush-porphyrin aggregates. Nevertheless, at least a part of TPPS is in the divalent state at this pH regime. AFM investigations show that at ($1.5 < pH \leq 2.5$) no brush-porphyrin networks are present. If compared to ($3 \leq pH < 4$) the size reduction from networks to single brush-porphyrin complexes and TPPS nanorods is much faster. It was concluded above that the disconnection mechanisms are thus different for the two pH regimes: At ($3 \leq pH < 4$) screening by salt ions leads to a slow opening of connections between brush-shape PVP-TPPS complexes. At ($1.5 < pH \leq 2.5$), however, the fast assembly of TPPS nanorods that leave PVP binding sites induces a fast network disconnection process. Even within this conclusion the added salt may still affect brush-porphyrin aggregates in the long run in that sense that it potentially prohibits the reformation of networks if the pH is adjusted back to neutral (as observed at ($3 \leq pH < 4$)). Added ion concentration at ($1.5 < pH \leq 2.5$) is naturally even higher than for ($3 \leq pH < 4$). In order to test whether the postulated switch of networks by J-aggregate formation and disformation is also effective in the reformation of networks, the sample at ($1.5 < pH \leq 2.5$) is adjusted back to pH = 7. Here TPPS is surely back in its protonated state but the added ion concentration is even larger.

AFM investigation has shown that indeed brush-porphyrin networks are reassembled due to the pH switch by disformation of TPPS nanorods and adjustment of the previously divalent fraction of porphyrins back to the tetravalent state. Thus, this result indicates that switching networks “off” and “on” is possible. However, the structural stability of the newly formed networks at relatively high salt concentration that inherently builds up by pH manipulation is doubtful.

In an overall conclusion to chapter 7 it was shown that a system of PVP brushes and porphyrin TPPS assembles to networks similarly as it was observed for PSS brushes and porphyrin TAPP. Thus, brush-porphyrin network formation provides a versatile access to novel self-assembled systems. At low pH it could be shown that TPPS J-aggregates are formed. The growth and thus final size of porphyrin nanorods is affected by PVP polyelectrolyte brushes. Thus, the addition of PVP may provide a promising tool to control the size of porphyrin nanorods that have potential applications as molecular antennae or photoconductive material. Moreover, it was shown that PVP-TPPS networks can be switched by pH manipulation to a limited extent. Responsive systems are of large interest in the field of self-assembled materials and thus further investigations should address the potential of pH switchable polyelectrolyte-porphyrin systems that use the concept suggested in the present study.

CHAPTER 8

8 COMPLEXATION OF AGGRECAN WITH TAPP

Molecules with bottle brush morphology similar to the synthetic brush molecules investigated above can be found in nature as well. An intriguing example is the proteoglycan aggrecan that is found in the cartilage tissue of joints in vertebrate animals (including humans) [209-211]. There, together with collagen, aggrecan serves as a major structural component of articular cartilage. The main function of aggrecan is to build up large osmotic pressures whenever the joint needs to withstand compressional forces. A scheme of the aggrecan molecule is given in Figure 8.1.

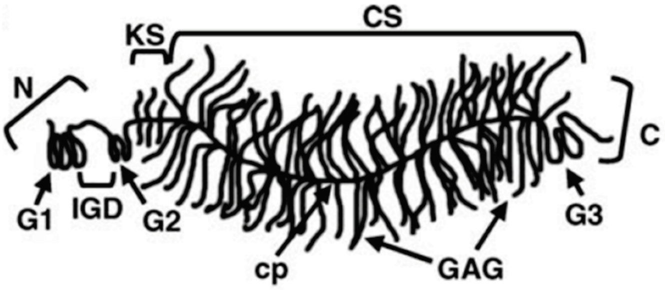

Figure 8.1: Structure of aggrecan: N: amine-terminal of core protein; G1, G2, G3: globular domains; IGD: interglobular domain between G1 and G2; cp: core protein; KS: keratan sulfate region; CS: chondroitin sulfate brush region: GAG: glycosaminoglycan chains; C: carboxyl-terminal of cp; text and figure from [212].

As it is illustrated, the molecule consists of a protein backbone that mainly carries glycosaminoglycan (GAG) side chains and on the ends folds to globular head groups that allow for attaching to another biomolecule: hyaluronic acid (see below). The proteoglycan has a rather high molecular weight of 1×10^6 g/mol < M_w < 3×10^6 g/mol [213]. Imaging investigations of aggrecan molecules in the literature report a contour length of about 400-500 nm and a width of the GAG domain of 60-100 nm (see Figure 8.2) [212,214-215]. The large variation of size dimensions results from aggrecan size differences across species, type of tissue and even age and health of the animal. In addition, aggrecan molecules in contrast to e.g. DNA are biomolecules with a considerable degree of polydispersity.

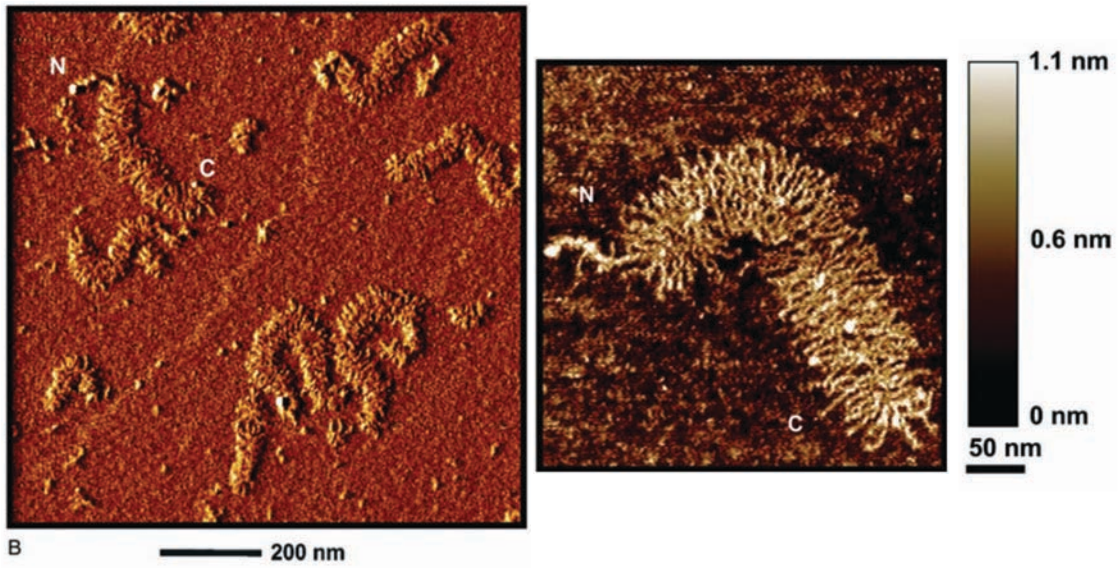

Figure 8.2: Literature high resolution AFM images of aggrecan molecules as reported in [212].

Aggrecan consists of charged carbohydrate side chain groups (GAG) for about 90% of its mass [211]. Besides a negligible keratan sulfate part, the carbohydrate groups in the side chains mainly represent chondroitin sulfate groups with 20-60 disaccharide monomers per chain. The structure of chondroitin sulfate is given in Figure 8.3. Chondroitin sulfate (CS) is a polysaccharide that carries one negatively charged unit per sugar ring and in that sense aggrecan is a highly charged and branched polyelectrolyte; similar to PSS brush discussed in earlier chapters. The molecular weight of a CS disaccharide monomer is 503.34 g/mol. Assuming that about 90% of aggrecan mass consists of CS a total number of charges in an aggrecan molecule of 3.500 to 10.500 can be calculated (using the range of molecular weight given above).

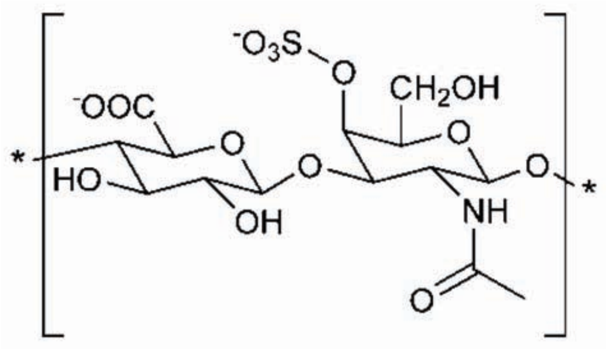

Figure 8.3: Molecular structure of chondroitin sulfate (CS), the main component of aggrecan.

In articular cartilage aggrecan assembles to large supramolecular structures (thus the name "aggrecan") with negatively charged hyaluronic acid via its globular protein domain (via G1 in Figure 8.1). This aggregation process presumably is needed to mechanically fix the aggrecans in the joints [211]. However, in the present investigation only the monomeric aggrecan form will be investigated (left part in Figure 8.4).

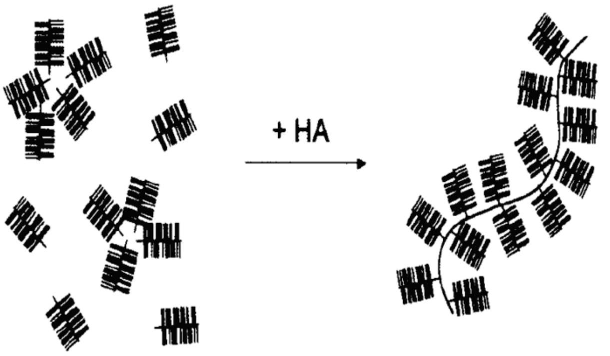

Figure 8.4: Assembly of aggrecan molecules with hyaluronic added (HA); from [213].

Within the present investigations aggrecan was combined with porphyrin TAPP in experiments similar to those for PSS brush-TAPP described in chapter 5. It is of interest here whether brush-porphyrin networks found for the PSS brush-TAPP system as well as for the PVP brush-TPPS system can also be obtained for the biological brush aggrecan.

Spectroscopic properties of aggrecan-TAPP aggregates

Upon combining colorless aggrecan and violet TAPP the color immediately shifts to light-brown. The colors observed are very similar to the colors seen for TAPP-PSS (see Figure 5.1). For a quantitative evaluation an UV-vis titration with addition of aggrecan to TAPP was conducted (Figure 8.5). The observed band shifts for $l > 0.5$ are quite similar to the titration of TAPP with PVS in Figure 5.13. Here like in the PVS case the H-band (402 nm) has higher intensity than the J-band (414 nm) with a ratio of 1.19:1. Minimum intensity at monomer band (412 nm) is observed for $l = 0.56$ (~1.75-fold excess of aggrecan charges). However, splitting energy is lower for TAPP-aggrecan than for TAPP-PSS and TAPP-PVS (Table 8.1). In a plot of extinction coefficient at 412 nm vs. the concentration of polyelectrolyte, clear differences between the three polymers are observed. The extent of hypochroism for PSS and aggrecan is similar (reduction to about 25% absorption of monomer), but minimum intensity occurs at different charge ratios for all three polymers. In addition, spectral behavior after minimum absorption at *l* = 0.56 upon further aggrecan addition is different than for the other polyelectrolytes (Figure 8.5-3): for increasing aggrecan concentration the relative ratio of H-band to J-band is reversed. Apparently, addition of further aggrecan changes inter-dye orientation to a larger extent than PSS and PVS do.

In conclusion, TAPP cooperatively binds to all three polyelectrolytes and stacks in oblique relative geometries as can be seen by the fact that all spectra show split Soret bands. However, the stacking geometry varies across the experiments. Interestingly, strongest exciton coupling for PSS is seen at equimolar charge ratios whereas an excess of either PVS or aggrecan was needed for strongest porphyrin coupling (Figure 8.6).

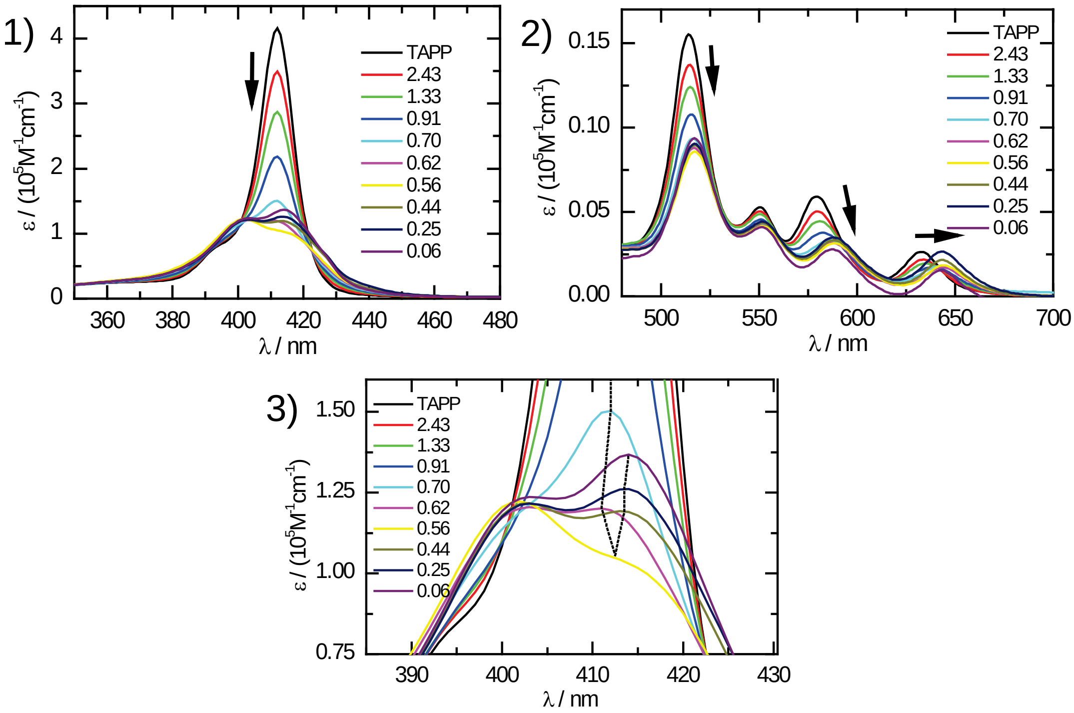

Figure 8.5: UV-vis titration of porphyrin TAPP (c = 3.9 μM) with aggrecan; (3): expansion of (2); legend: charge ratio *l* = [TAPP]/[CS].

Table 8.1: Positions (wave number) of TAPP monomer and H- and J-bands of TAPP-PVS aggregate.

$\tilde{\nu}_{mon}$/cm^{-1}	$\tilde{\nu}_{H}$/cm^{-1}	$\tilde{\nu}_{J}$/cm^{-1}	$\Delta\tilde{\nu}$/cm^{-1}
24272	24876	24155	721

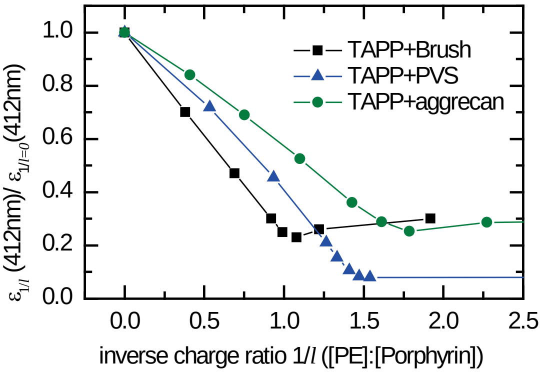

Figure 8.6: Normalized extinction coefficient at Soret maximum (412 nm) for TAPP upon addition of PSS brush, PVS and aggrecan.

Light scattering of aggrecan-TAPP aggregates

In this section aggregation behavior of TAPP-aggrecan aggregates will be investigated at the same polyelectrolyte concentration as in chapter 5. If TAPP is combined with aggrecan at sub-stoichiometric charge ratio l = 0.76 a solid red material spontaneously flocculates. The same observation is generally made for samples with $l \geq$ 0.76. This is in close analogy to PSS-TAPP samples where precipitation is observed for $l \geq$ 0.7. However, as in the already discussed brush case, non-turbid samples below l = 0.76 (aggrecan excess) are obtained. From the UV-vis results it is clear that TAPP binds to aggrecan and undergoes self-stacking. Presumably, aggrecan-porphyrin complexes below the flocculation limit are stabilized in solution by the remaining and not neutralized charges.

Correlation functions of pure aggrecan at different salt concentrations are given in Figure 8.7. All decay functions are quite broad and thus represent a summation of many exponential functions probably due to polydispersity of the sample. In addition, tailing effects at relaxation rates shortly before the function crosses zero indicate the presence of large aggregates. Evidently, the correlation function gets steeper and left-shifted upon salt addition. However, the shoulder at long relaxation rates remains even in salt conditions with ten-fold salt excess (charge concentration of aggrecan is 0.25 mM). Thus, it is assumed that these observations cannot simply be explained by polyelectrolyte effects but rather represent the constitution of the aggrecan sample. For a relative evaluation of light scattering behavior of aggrecan and aggrecan-TAPP complexes all correlation functions in this section are fitted by a third order cumulant expansion which is necessary due to the broadness of observed decay functions. The evaluation of correlation functions in Figure 8.7 gives an apparent hydrodynamic radius $R_h(90°, l = 632.8\ nm) = 59.1$ nm in salt-free solution that reduces slightly to $R_h = 51.5$ nm at equimolar salt concentrations (0.3 mM NaCl). Further reduction of the radius to $R_h = 42.1$ nm is observed for ten-fold salt excess. It should be noted that this rather strong dependence of aggrecan size on salt concentration does not apply to PSS brush size as it is discussed in appendix B.

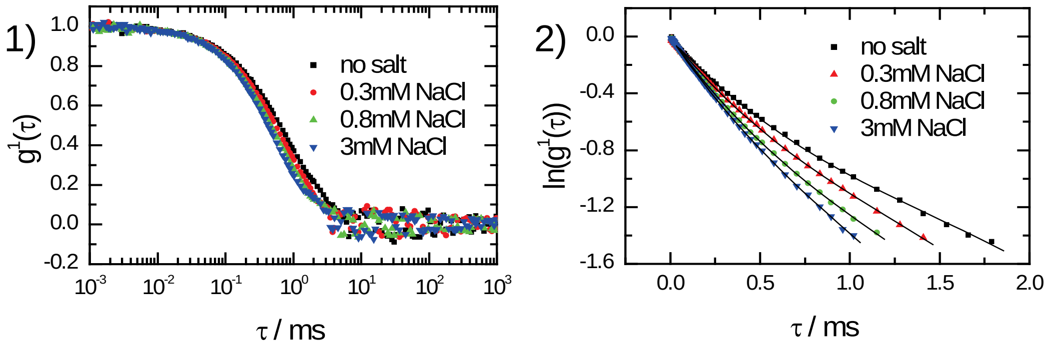

Figure 8.7: Light scattering results for aggrecan at different salt concentrations. (1): field correlation functions; (2): third order cumulant expansion of (1); red-laser, θ = 90°.

Light scattering results for aggrecan upon addition of porphyrin TAPP are given in Figure 8.8 and Figure 8.9. Addition of TAPP up to $l = 0.67$ results in a size reduction from $R_h(90°, \lambda = 831.5\ nm) = 56.3$ nm to $R_h = 31.0$ nm. As discussed above the size reduction due to screening effects of simple salt is much smaller at 0.3 mM NaCl (equivalent to $l = 1$). In addition, the sample with TAPP $l = 0.67$ exhibits a scattering intensity that is about 50-fold higher than aggrecan scattering in salt-free water whereas the control experiment with NaCl does not show changes of scattering intensity upon salt addition. Thus, it is concluded that TAPP binds to aggrecan and induces the rise in intensity. Apparently, TAPP here due to intramolecular binding induces a contraction of aggrecan size that is similar to the observations for the PSS brush – $C6T^{4+}$ system of chapter 3. It is very interesting to observe the described effect with porphyrin TAPP since for PSS brush as well as for linear PSS supramolecular TAPP-polyelectrolyte complexes with higher radii than the starting material were obtained.

Upon further addition of TAPP to $l = 0.73$ the hydrodynamic radius of aggrecan-TAPP complexes increases significantly to values much larger than the aggrecan starting position and a strong increase of scattering intensity is observed. As mentioned above, even further addition of TAPP (*l* = 0.76) results in spontaneous precipitation of a red aggregate material. This behavior of aggregate size correlates well with the observations for PSS brush and nonaromatic C6T^{4+} in chapter 3.

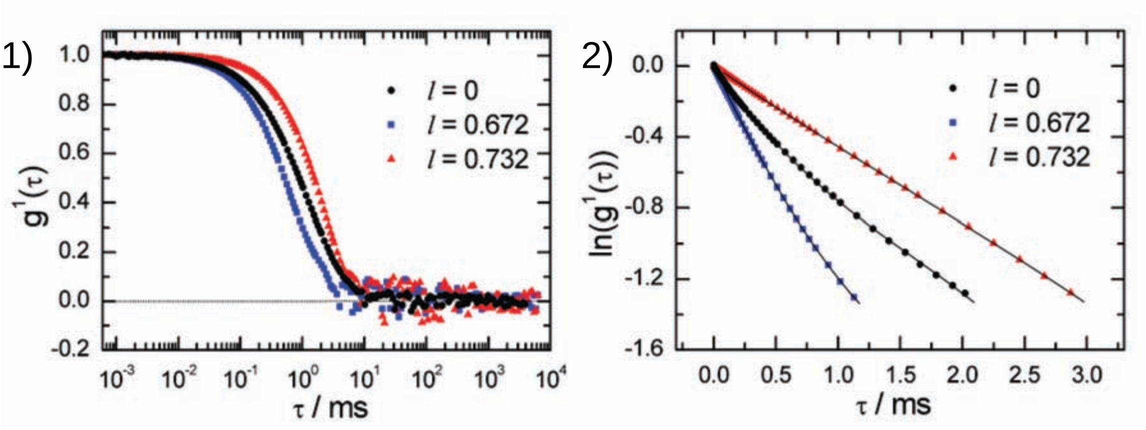

Figure 8.8: Light scattering results for aggrecan and aggrecan-TAPP aggregates in salt-free aqueous solution; *l* in legend is the charge ratio [TAPP]/[aggrecan]. (1): field correlation functions; (2): third order cumulant expansion.

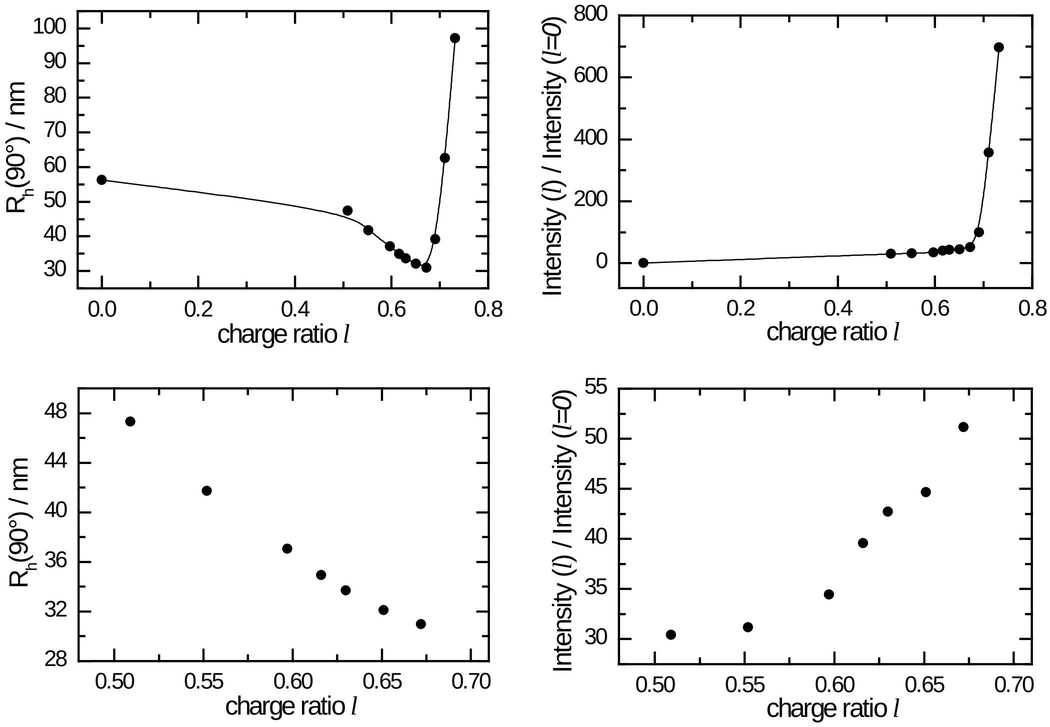

Figure 8.9: Light scattering results for aggrecan-TAPP aggregates. Left: hydrodynamic radius from third order cumulant expansion. Right: normalized intensity. Below: expansions of upper part; IR-laser 90°.

The sharp transition from single aggrecan-TAPP complexes to precipitation of supramolecular aggregates indicates that the observed rise in size and scattering intensity may be due to simple desolubilization of aggrecan-TAPP complexes (due to charge neutralization) rather than intermolecular binding of several aggrecan molecules by TAPP.

If the observations are summed up, aggrecan which mainly consists of polysaccharides shows a similar TAPP complexation behavior than PSS brush with $C6T^{4+}$: there is no tendency of the complexes to form assemblies with multiple polyelectrolyte molecules. In contrast to this, for PSS with TAPP as well as for PVP with TPPS it was found that polyelectrolyte molecules assemble to supramolecular structures even at relatively low porphyrin concentrations.

Imaging of aggrecan-TAPP aggregates

In the introduction to this chapter AFM images of aggrecan molecule from literature were already shown. With the setup described in the appendix the level of resolution given in Figure 8.2 cannot be achieved but the cylindrical shape of aggrecan molecules have been confirmed in Figure 8.10. In addition, polydispersity visible in light scattering is also seen in AFM.

AFM images of aggrecan-TAPP complexes at $l = 0.73$ are given in Figure 8.11. Evidently, separated cylindrical structures were detected that have a different appearance than pure aggrecan. Also the height of the aggrecan-TAPP sample is higher than that of pure aggrecan (Table 8.2). Thus, it is concluded that the objects imaged in Figure 8.11 represent aggrecan-porphyrin aggregates. It is clearly visible that only single complexes of size similar to pure aggrecan are obtained and no further secondary assembly of the cylindrical complexes can be seen. This observation supports the results of light scattering that showed the absence of inter-aggrecan aggregates.

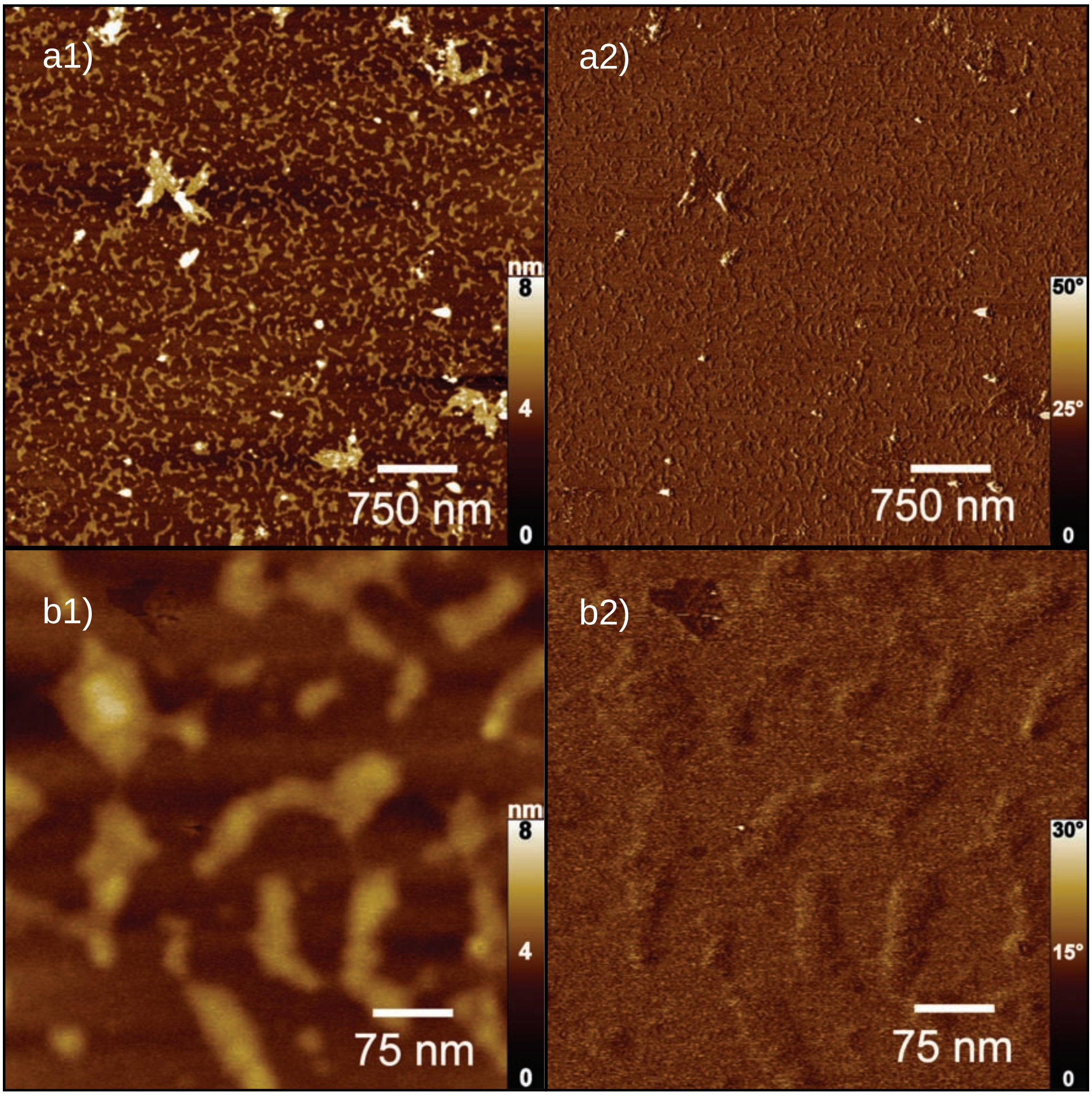

Figure 8.10: AFM (1) height and (2) phase images of aggrecan, prepared by spin-coating.

Table 8.2: Height on surface as measured by sectional profile analysis of AFM images in Figure 8.10 and Figure 8.11.

sample	**height/nm**
aggrecan	2.0 ± 0.3
aggrecan+TAPP *l* = 0.73	2.5 ± 0.6

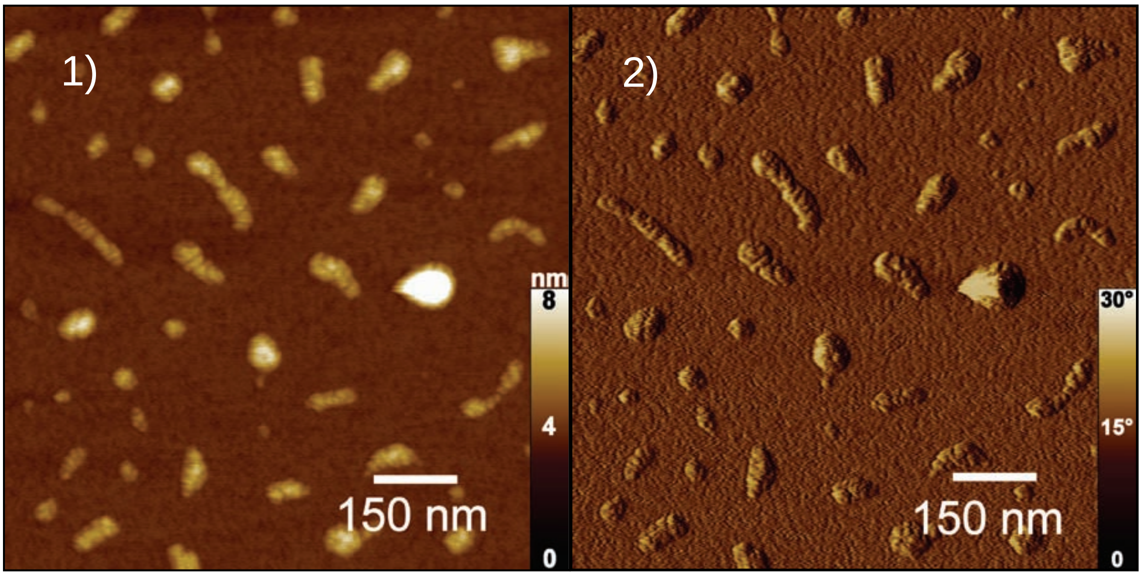

Figure 8.11: AFM (1) height and (2) phase images of aggrecan-TAPP aggregates at *l* = 0.73.

Summarizing this chapter, it was shown that porphyrin TAPP interacts with the biological brush molecule aggrecan. Similarly to the observations for synthetic PSS brush and linear PSS, TAPP is stacking on aggrecan via π-π self-interaction. However, in contrast to the case with PSS, TAPP is not able to interconnect aggrecan molecules to supramolecular structures but rather reduces the hydrodynamic size of aggrecan in solution. This behavior is similar to the observations for the nonaromatic counterion $C6T^{4+}$ in chapter 3 where the counterion also induced a size reduction. For $C6T^{4+}$ this was explained by the absence of inter-counterion interaction if compared to TAPP. This argumentation is not valid here. Aggrecan is in contrast to PSS a polysaccharide that does not contain aromatic units. Potentially this chemical difference may be one reason for the different behavior in supramolecular structure formation. However, further investigations would be needed to finally explain the different observations.

CHAPTER 9

9 SUMMARY & CONCLUSION

In this work the self-assembly of different structural counterions with polyelectrolytes was studied in salt-free aqueous solution. Various polyelectrolytes of synthetic and biological origin having different molecular weight and architecture were investigated. The counterions of study were varied in their number of charges and their structure. Within this investigations several findings were made that by contributing to the common knowledge about self-organizational processes of charged entities in solution may potentially help to "construct" new materials with the bottom-up method. Parameters were indentified that by the interplay of different interactions control the final structure and size of an assembly from charged objects. The approach of this work was in contrast to many investigations in the literature to study the build-up of supramolecular structures in solution instead of analyzing precipitated complexes that were often in the focus of literature studies. The main focal point was on cylindrical polyelectrolyte brushes. These molecules are interesting potential building units for self-assembled systems due to their inherent cylindrical shape and their high charge density. It was shown that synthetic polyelectrolyte brushes from poly(styrene sulfonate) and poly(2-vinylpyridine) can assemble into nano-networks with selected counterions. A combination of charge attraction with inter-counterion π-π interaction is crucial for network formation. Thus, networks were only obtained for multivalent counterions that in addition to their potential for charge-charge attraction can self-interact with further counterions by π-π interaction with their aromatic system. In particular, the tetravalent and water-soluble porphyrin molecules TAPP and TPPS were able to induce brush-network formation. Investigations with the quaternized tetramine $C6T^{4+}$ have shown that in the absence of either multivalency or aromaticity of counterions no supramolecular structures of brush molecules can be observed.

Using aromatic and tetravalent porphyrin counterions, it was shown that brush-porphyrin networks exhibit two hierarchical levels. On a smaller length scale porphyrins may connect to brush molecules resulting in single, cylindrical brush-porphyrin complexes. Due to the dye character of porphyrins it was possible to investigate porphyrin-porphyrin interaction on the brush templates in detail. On the secondary level of hierarchy these pre-assembled cylindrical brush-porphyrin complexes connect to larger supramolecular structures. By salt addition it clearly was shown that the attraction between brush-porphyrin cylinders is mediated by charge-charge interactions and the secondary aggregation can be suppressed with salt. A detailed study of the influence of both polyelectrolyte and counterion structure was presented. Interestingly, it was shown that linear polyelectrolytes of same chemical structure as the previously described poly(styrene sulfonate) brush molecules also assemble to supramolecular structures with tetravalent porphyrins. However, the assembled structures do not show network structure. Another important result is that both the geometry of inter-porphyrin interaction as well as the overall supramolecular size were mainly governed by the chemical structure of the polyelectrolyte and much less by its molecular weight or architecture.

Several investigations about the possibility of switching networks “on” and “off” were conducted and it was shown that in principal (but with limitations) brush-porphyrin networks may be disconnected and rebuild by switching their valency from four to two and back to four. Since brush-porphyrin network formation was observed for two independent synthetic brush-porphyrin systems it was also tried whether charged polymer brushes sourced from nature may build up networks as well. Aggrecan, a biological brush molecule with charged polysaccharide side groups that is extractable from cartilage tissue was chosen as suitable model system. However, no supramolecular network formation with porphyrins was observed for the biological and nonaromatic polysaccharide brush. Potentially, this difference results from the different chemical structure. If generally aromatic polyelectrolytes are needed to observe network formation would be an interesting topic for future investigations.

In summary, the presented results give valuable insights into parameters that control charged self-assembled systems in aqueous solution such as shape, size and chemical structure of the building units. Self-assembled networks from semi-flexible objects such as found in this thesis may find potential applications as materials with interesting and switchable mechanical properties. Systems containing stacked porphyrins are used in medical and optical applications such as photodynamic therapy and light harvesting. The presented results for porphyrin stacks controlled by different synthetic and biological polyelectrolytes may help to support the development of such applications.

APPENDIX A

A MATERIALS

A.1 NaPSS Brush

Cylindrical brush molecules with side and main chain both consisting of polystyrene subunits were synthesized via the macromonomer approach [58,60,65,69,216-217] by Adrian Strack within the scope of his dissertation [218]. At first a polystyrene macromonomer was prepared by anionic polymerization of styrene and subsequent end-functionalization with 1,1-Diphenylethylene and p-vinylbenzyl chloride (Figure A.1).

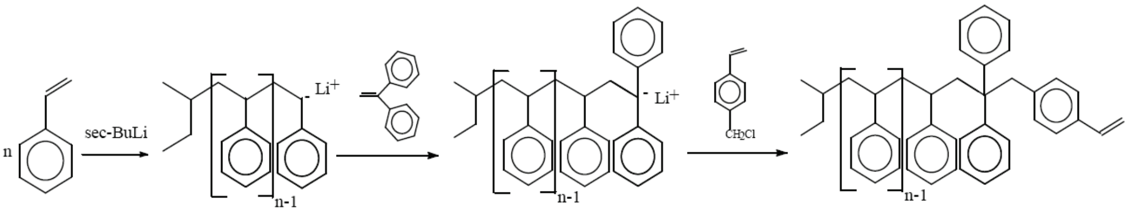

Figure A.1: Preparation route of polystyrene macromomers by anionic polymerization and subsequent endfunctionalization; from [218].

Investigation by MALDI-TOF and GPC yielded M_w = 4452 g/mol and M_w/M_n = 1.06 for the polystyrene macromonomer [218] and thus each macromonomer consists in average of 39.3 (n_w = 39.3 in Figure A.1) styrene subunits (M = 104.15 g/mol) plus the end groups (M = 354.53 g/mol) that contain three benzene rings as well. The macromonomer was homopolymerized by free radical polymerization in benzene using AIBN as thermal initiator (see [218]) yielding a polystyrene brush with $M_w = 2.13 \times 10^6$ g/mol and M_w/M_n = 3.02. In order to obtain lower polydispersities, the polystyrene brush was fractionated by continuous polymer fractionation (CPF) [218-219]. For the present study a high molecular mass fraction with $M_w = 4.12 \times 10^6$ g/mol and M_w/M_n = 1.51 [218,220] was chosen that has a weight-average degree of polymerization (of macromonomers in the main chain) of P_w = 925. Sabine Duschner carried out the sulfonation of the polystyrene brush in her dissertation [220]. The polystyrene brush was sulfonated with sulfuric acid/acetic anhydride in 1,2-dichloroethane at 50 °C [65,221]. The precipitated product was isolated as the sodium salt by dissolution in aqueous NaOH (without prior drying) and subsequent removal of excess dichloroethane by evaporation and purification via ultra filtration, resulting in a NaPSS brush with 100% sulfonation according to elemental analysis [220]. The molecular weight of the sulfonated PSS brush molecule was determined by light scattering in 10 mM aqueous sodium chloride solution as $M_w = 7.81 \times 10^6$ g/mol [82]. Thus, the increase of molecular weight due to sulfonation can be used to evaluate the degree of sulfonation in addition to elemental analysis. A virtual macromonomer mass for NaPSS brush can be calculated as $M_w = 8439$ g/mol by the ratio of NaPSS brush molecular weight to its degree of macromonomer polymerization (P_w). Assuming that the 3 benzene rings of the macromonomer end groups that now are present in the inner core of the brush are not sulfonated, this virtual macromonomer weight gives a degree of sulfonation for the styrene side chain repeat units ($n_w = 39.3$ per side chain) of 99.8% and thus each side chain of the polymacromonomer has a weight-average number of $n_{w,charged} = 39.2$ charged groups and thus the brush molecule exhibits in total $N_{w,charged} = n_{w,charged} \times P_w =$ 36,300 potential negative charge centers.

Light Scattering

The concentration of NaPSS brush for light scattering investigations within the present thesis is chosen to be c = 50 mg/L (that is 240 μM in charged groups concentration), if not stated otherwise. It was shown that at this concentration light scattering results for the PSS brush molecule are comparable to the values after extrapolation to zero concentration and thus can be used as a reasonable approximation instead of actually conducting a concentration extrapolation (see [82]). In 10 mM salt (NaCl) conditions extracted radii ($c_{NaPSS} = 50$ mg/L) are $R_g = 59.5$ and $R_h = 36.4$ with $\rho = R_g/R_h = 1.54$.

In several investigations of the present thesis it is necessary to study PSS brushes in salt-free conditions. Therefore, it is useful to evaluate PSS light scattering behavior in the absence of salt, especially since it is well known that polyelectrolytes may be difficult to analyze at these conditions (see section 2.3). A first indication of a polyelectrolyte effect that negatively influences size determination of the sample would be the presence of a second mode (“slow mode”) in the autocorrelation function from dynamic light scattering. Figure A.2 shows the autocorrelation functions at 90° of PSS brush in 10 mM salt condition as well as in pure water. Apparently, both samples exhibit only one decay process and the correlation functions are nearly identical. Furthermore, no second step in the decay function was found for any of the investigated angles (30-150°).

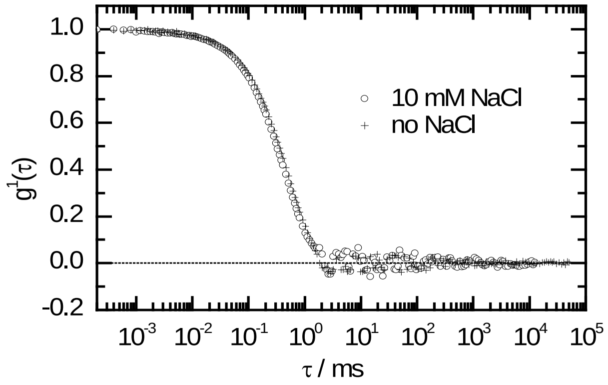

Figure A.2: Field correlation function of PSS brush at 90° (λ = 632.8 nm) with and without added salt.

The angular dependence of light scattering results for the salt and no-salt case is given in Figure A.3. Clearly at both ionic strengths linear fitting of the angle dependent data gives well-defined results for extracted radii. This result further indicates that the PSS brush may be safely analyzed in salt-free conditions.

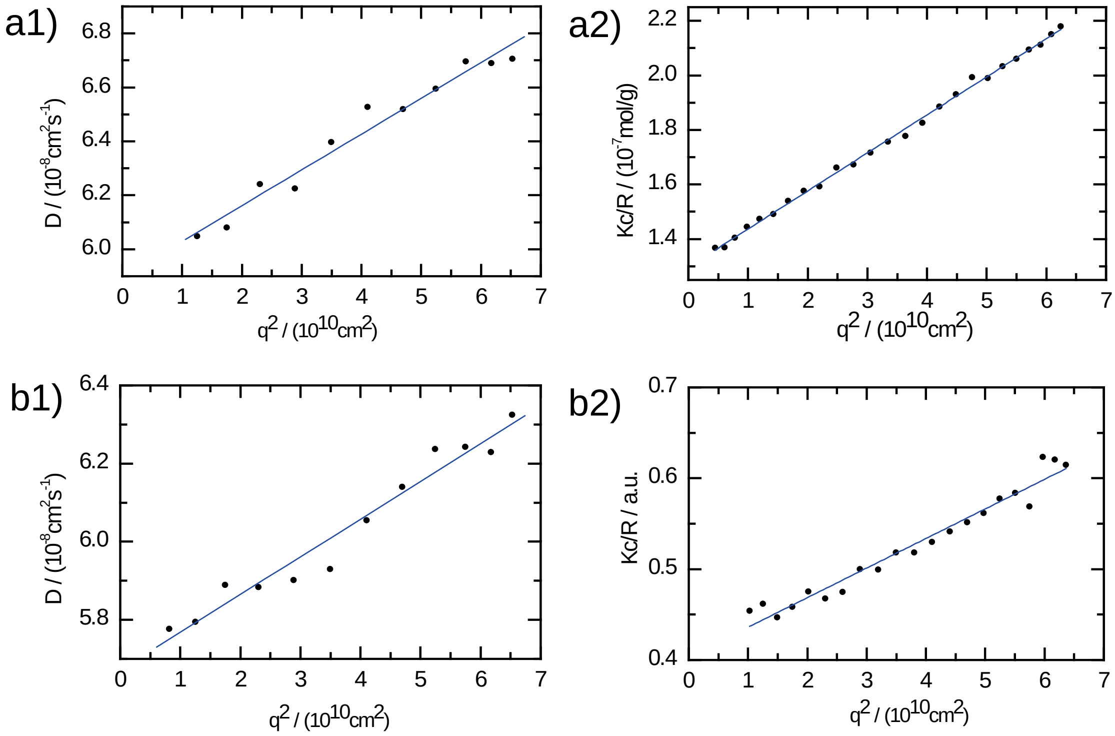

Figure A.3: Angular extrapolation of dynamic (1) and static (2) light scattering data from PSS brush in (a) 10 mM NaCl and (b) without added salt; dn/dc = 0.168 ml/g in 10 mM NaCl [82]; dn/dc not measured for sample without added salt.

The extrapolation of the angular data yields apparent radii of PSS brush in salt-free water of R_g = 50.0 and R_h = 36.4.

Although up to now there is no indication for a polyelectrolyte effect present for PSS brush in salt-free water, it also should be noted that since a slow mode is under certain conditions difficult to detect it is possible that the accelerated fast mode is observed even though a slow mode is not (see section 2.3). In order to eliminate this possibility a reasonable test would be to investigate the dependency of the apparent diffusion coefficient of PSS on the salt concentration. If the observed mode at zero salt concentration would indeed represent an accelerated non self-diffusive fast mode, its speed should slow done and thus its diffusion coefficient should fall upon salt addition (see Figure 2.3). The result of this experiment for PSS brush in Figure A.4 indicates a slightly positive slope for the apparent diffusion coefficient vs. salt concentration. From this observation it safely can be concluded that at the investigated concentration (c_{NaPSS} = 50 mg/L; c_{NaSS} = 240 µM) the measured diffusion coefficient is not affected by potential polyelectrolyte effects and thus represents self-diffusion of the sample molecules.

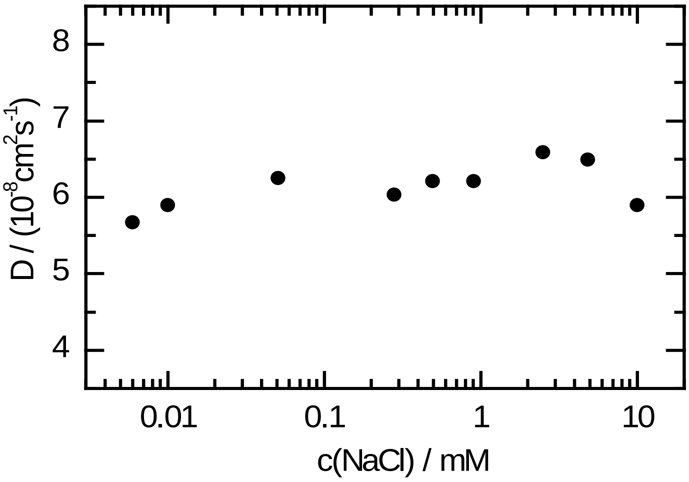

Figure A.4: Dependence of diffusion coefficient D of NaPSS brush on salt concentration.

Therefore, radii calculated from the apparent diffusion coefficient here are a safe measure of size for the investigated samples. From the experiment it is unclear whether the suppression of polyelectrolyte effect here is in addition to the low concentration also affected by the polyelectrolyte brush structure. It has been reported that cylindrical polyelectrolyte brushes exhibit a lower effective charge density when compared to their linear counterparts and thus show the transition to monomodal correlation functions at higher concentrations than linear polyelectrolytes [65,222-223]. It will be shown in appendix A.2 that linear NaPSS behaves different than its branched counterpart keeping all other conditions same.

Imaging of PSS Brush

NaPSS brush molecules have been imaged by AFM in air after deposition of the molecules on freshly cleaved mica. As pointed out in appendix B.2, deposition in principal can follow two routes: a) drying or b) immobilization through interaction forces out of solution. Mica is negatively charged due to surface OH groups. Therefore, it is no surprise that after incubating a PSS brush solution on top of a mica surface and subsequent rinsing with water only a bare mica surface was obtained by AFM imaging. Obviously, immobilization of the PSS brush molecules does not take place using this sample preparation way because of the lacking attractive interaction between negative brush and equally charged surface.

However, there is a facile way for modifying mica yielding in a positively charged surface by treatment with 3-aminopropyltriethoxysilane (APTES) (see appendix B.2). Figure A.5 gives the AFM result for PSS brushes deposited on APTES modified mica. Here again a brush solution was in contact with the surface for some minutes and subsequently rinsed off. Obviously charge-charge attraction of the negative brush with the positive surface was sufficient to immobilize PSS brush molecules.

In order to measure AFM images of the sample in a state closer to the situation in solution, AFM can be conducted in liquid solution instead of in air. That is substrate and probe both are submerged in the respective solvent [224-225]. Apparently drying effects of the sample to be imaged can be mostly ruled out by imaging in liquid. However, perturbations that occur due to substrate-sample interaction cannot be eliminated by this measurement technique.

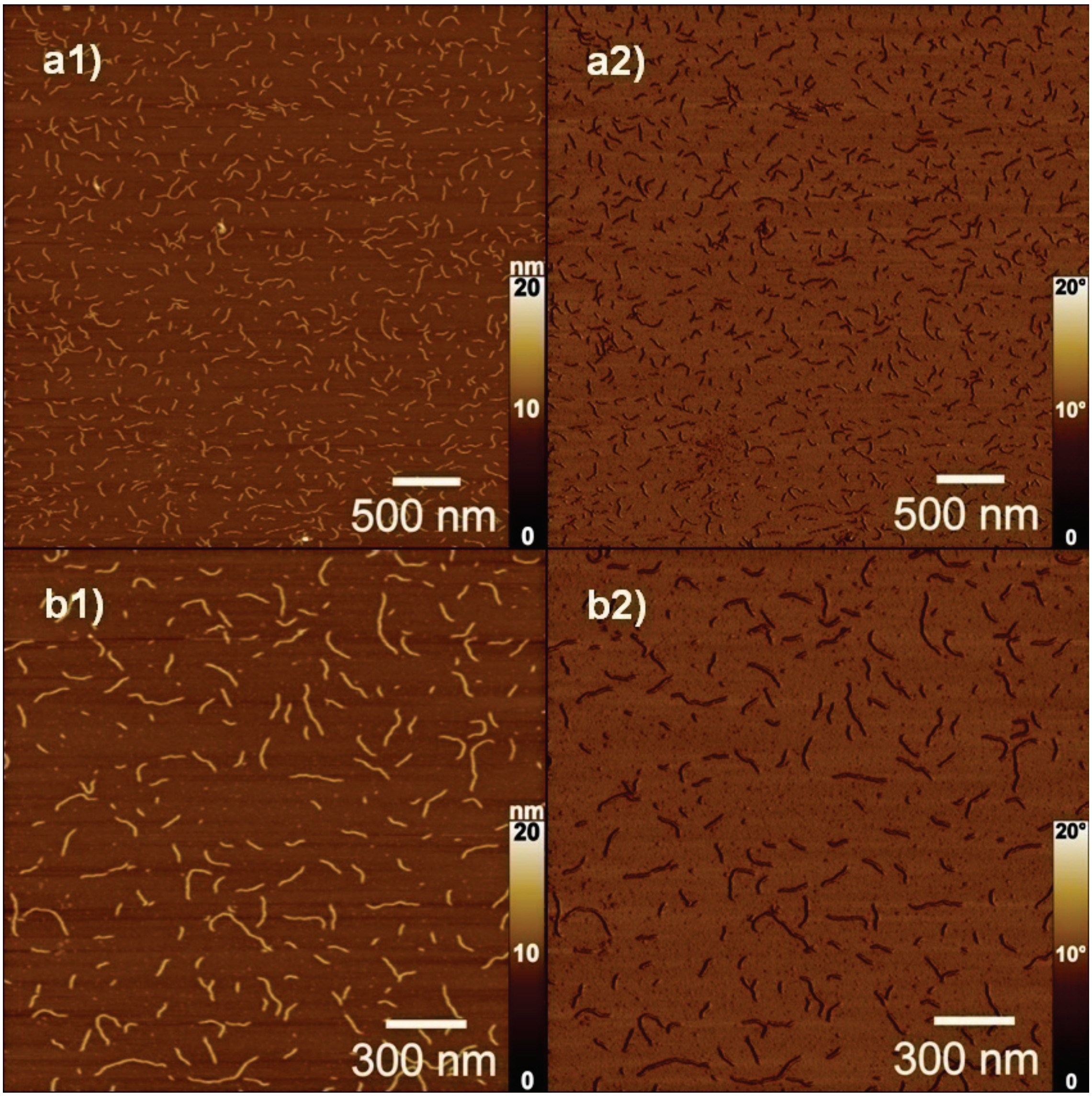

Figure A.5: AFM height (1) and phase (2) images of NaPSS brush after deposition and subsequent rinsing with ample water on an APTES (1% aqueous solution) modified mica surface.

Since it was shown in Figure A.5 that PSS brushes can be immobilized out of aqueous solution by an APTES-modified mica surface, it was tried to image the brush molecules directly in water. As it is shown in Figure A.6, PSS brushes could be imaged in water. Compared to brush molecules on the same substrate in air the resolution appears to be slightly poorer because of the tip probe moving brush molecules to a higher degree. Apparently shape and modification of brush molecules is very similar in water and in air so that it safely can be concluded that drying does not have large impact on brush structure.

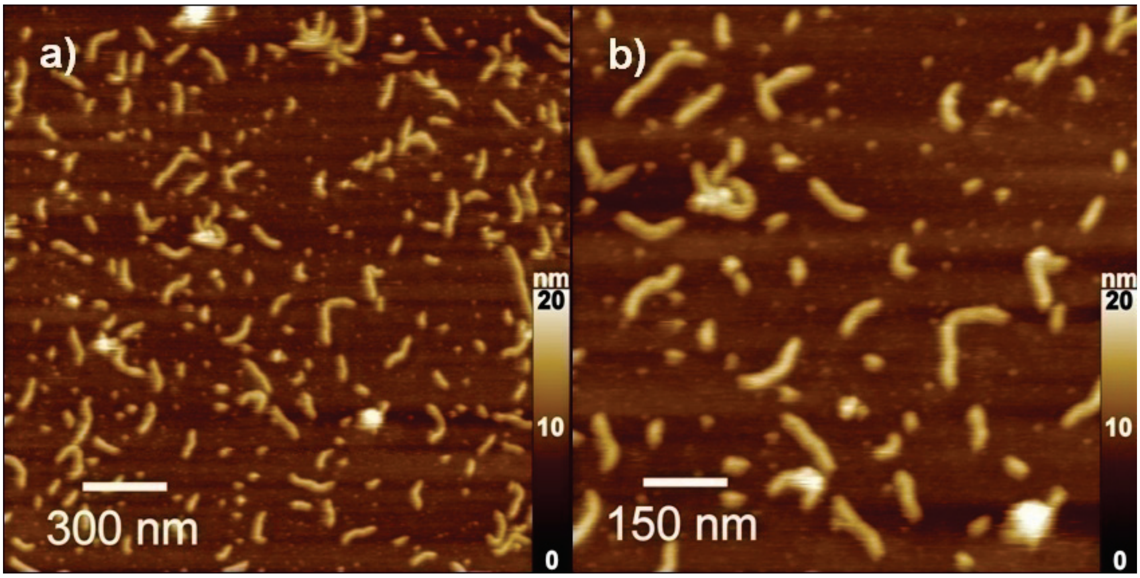

Figure A.6: AFM height images measured in water of NaPSS brush immobilized on an APTES (1% aqueous solution) modified mica surface.

As will be described in a later part of this section, the successful immobilization of brush-porphyrin aggregates on either bare or APTES-modified mica was not accomplishable to a satisfying degree. Due to charge neutralization the aggregates possess a charge density smaller than the charged building units and therefore show lower attraction to either one of the two surface types. It is because of this observation why it is more reasonable to apply a drying preparation route here where charge-charge (or other) attraction is not essential for successful sample deposition.

Figure A.7 gives the AFM image for PSS brushes where a droplet of brush solution was placed on bare mica and the solvent was allowed to evaporate at room temperature. Evidently, the drying process leads to film formation of brush molecules. The cylindrical molecules pack closely but mostly do not overlap due to charge repulsion. It is reasonable that such films can be formed in the drying process because drying will lead to a local increase of brush concentration.

In order to achieve a deposition with separated brush molecules on the surface that more closely represents the non-aggregated state in solution, a different preparation technique was used. The samples were prepared by spin-coating a droplet of the solution on mica. This preparation route allows for a surface coverage with uniformly distributed and separated brush molecules (see Figure A.8) and therefore was used as the more favorable preparation mode for the drying processes.

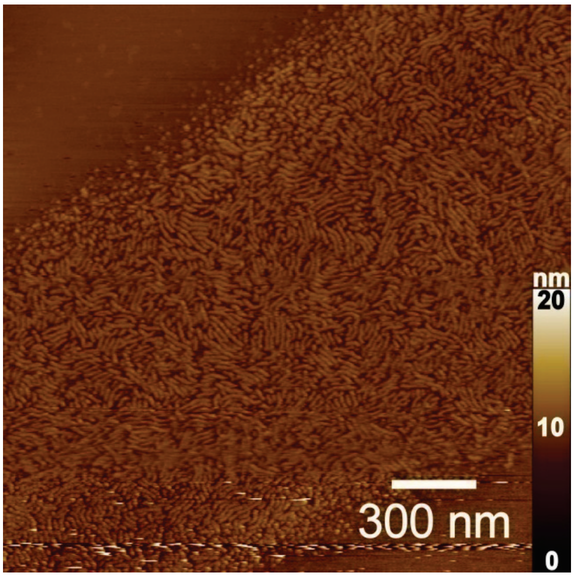

Figure A.7: AFM height image of PSS brush drop casted on mica.

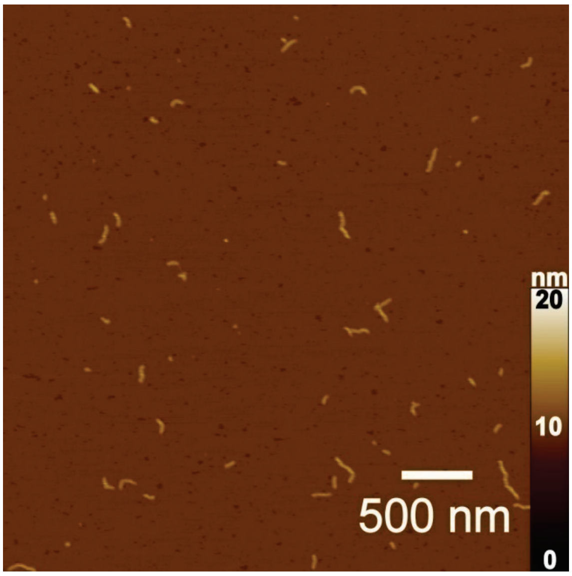

Figure A.8: AFM height image of PSS brush, spin-coated on mica.

Cross-sectional profile analysis of AFM height images allows for height and width measurement of PSS brushes. Results for brush molecules on bare mica are given in Table A.1. Evidently, the brush molecules lie flat on the surface with higher width than height dimensions although they possess a circular cross-sectional profile in solution as it was shown by cryo-TEM investigations in chapter 5. This is due to brush-surface (hydrophilic mica surface) interaction. The brush width as reported in Table A.1 is given as the full width at half maximum of the sectional profile allowing for a more reliable relative determination of brush diameter (see appendix B.2). It has to be taken into account that the full width at half maximum determined by this method is systematically lower than the brush diameter at surface (diameter at surface for PSS brush: d ~26 nm).

Table A.1: Measurements for height and width of NaPSS brushes on bare mica in air as taken from sectional profiles.

	height/nm	**width/nm**
NaPSS-brush	4.1 ± 0.2	18.4 ± 1.1

A.2 Linear NaPSS

NaPSS polyelectrolyte samples of linear structure (in contrast to the brush morphology described before) were obtained from PSS Polymer Standards Service GmbH (Mainz, Germany). Samples of different molecular weight were used that all have a rather narrow molecular weight distribution ($M_w/M_n < 1.2$ as guaranteed by the producer). The molecular weights chosen were M_w = 8,600 g/mol, M_w = 43,300 g/mol and M_w = 666,000 g/mol. The two PSS samples with 43k and 666k molecular weight were dialyzed for one week against salt-free water using a membrane with molecular weight cut-off of 10,000 g/mol and replacing the water each day. The dialyzed solutions (c_{NaPSS} = 2 g/L) were filtrated through Millex-GS syringe filters and the white polymer was reisolated thereafter by freeze drying.

Light Scattering

At the concentration regime used throughout the present dissertation the two lower molecular weight PSS species (8k and 43k) do not show scattering intensity significantly higher than the intensity of pure water. On the contrary, for the high molecular weight NaPSS (666k) a detailed light scattering analysis is feasible at the chosen concentration (for pure polyelectrolyte samples and the experiments described in chapter 6 the same standard concentration of c = 50 mg/L was used).

Both for the sample in salt as well as in salt-free conditions an autocorrelation function with one main decay process was obtained (Figure A.9). Nevertheless, differences in the slope of the correlation function indicate a significant effect of salt concentration on light scattering behavior in contrast to the case in Figure A.2. This indication is clearly supported by the differences between the experiments in salt and no-salt conditions if plotted versus angle (Figure A.10). In 10 mM sodium chloride extracted radii are given by R_g = 73.1 nm and R_h = 37.9 nm (please note the similarity of hydrodynamic radius between PSS666k and PSS brush).

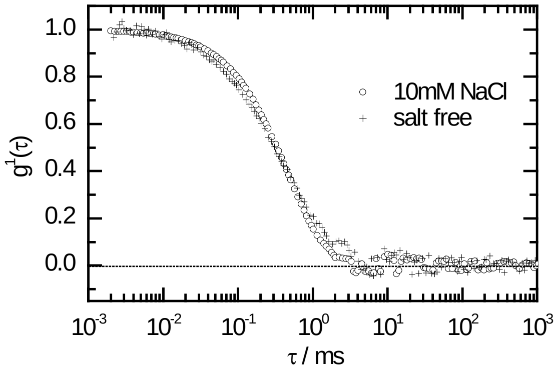

Figure A.9: Autocorrelation functions for PSS666k, c = 0.05g/L in salt-free water and in 10 mM NaCl, θ = 90°, λ = 632.8 nm.

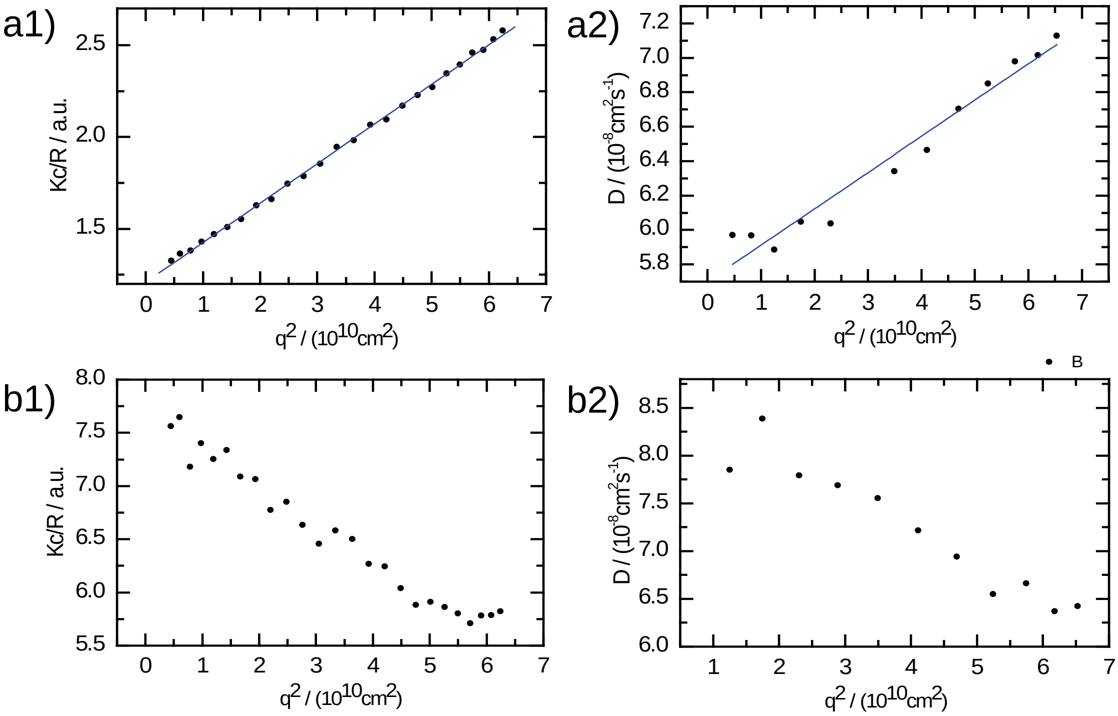

Figure A.10: Angular extrapolation of static (1) and dynamic (2) light scattering data from PSS 666k in (a) 10 mM NaCl and (b) without added salt.

However, in salt-free water no radii can be extracted since negative slopes both for inverse scattering intensity and diffusion coefficient versus the square of scattering vector are measured. Such negative slope observations can often be explained by intermolecular interactions in the sample and thus this is a sign that here some sort of polyelectrolyte effect is taking place. So, determination of hydrodynamic radii in salt-free and pure linear PSS solution is not feasible here. Still, as already discussed in appendix A.2 many samples investigated within the present text have to be measured in salt-free conditions. Fortunately the experiments described for the PSS666k – TAPP system in chapter 6 have revealed that the angle dependent behavior turns to a positive slope upon complexation. Presumably charge neutralization of PSS by porphyrin complexation reduces the observed polyelectrolyte effect.

A.3 PVP47 Brush

"PVP47" - quaternized poly(2-vinylpyridine) brushes were kindly provided by the groups of M. Maskos and M. Schmidt [170]. The brush molecules have been synthesized via the macromonomer approach by Tim Stephan within the scope of his dissertation [226-227]. They have a molecular mass of $M_w = 3.3 \times 10^6$ g/mol and consist of a methyl methacrylate main chain with P_w ~450 and PVP side chains having 47 monomers. 56% of the 2-vinylpyridine side chain monomers are quaternized with ethyl bromide. Thus, total number (weight average) of charged units per PVP47 brush is about 11,000. For the calculation of charged monomer concentration from PVP mass concentration in neutral solution a molecular weight per quaternized 2-vinylpyridine group of M = 302.8 g/mol can be introduced (see [227]). The pK_a of poly(2-vinylpyridine) is pK_a ~ 5 [207-208]. Thus, in the experiments at pH < 4 described in section 7.2 the unquaternized part of PVP47 is presumably protonated. Assuming full protonation of the unquaternized part results in a molecular weight per charged group of M = 170.3 g/mol.

Atomic Force Microscopy

An AFM image of the semi-flexible brush polymers is given in Figure 7.1. Since PVP is used for samples in chapter 7 where high acidic conditions (e.g. pH = 1.6) are needed it is of interest to check its stability in these conditions. Figure A.11 gives the

AFM image of PVP brushes at pH = 1.6 after several days at this pH.

If compared to Figure 7.1, it is evident that PVP47 is stable under acidic conditions. Dimensions of the brush molecules are very similar for the two experiments. However, there is a marked difference in the distribution of brush molecules on the surface. Apparently due to the presence of additional ions (HCl was added to lower the pH, nominal c(Cl^-) = 20 mM) the brush-brush repulsions are partially screened and the brush molecules can therefore be aligned in a much denser packing on the surface. It should be noted that both samples have been treated equally by spin-coating the sample on freshly cleaved mica so that preparational influences can be ruled out.

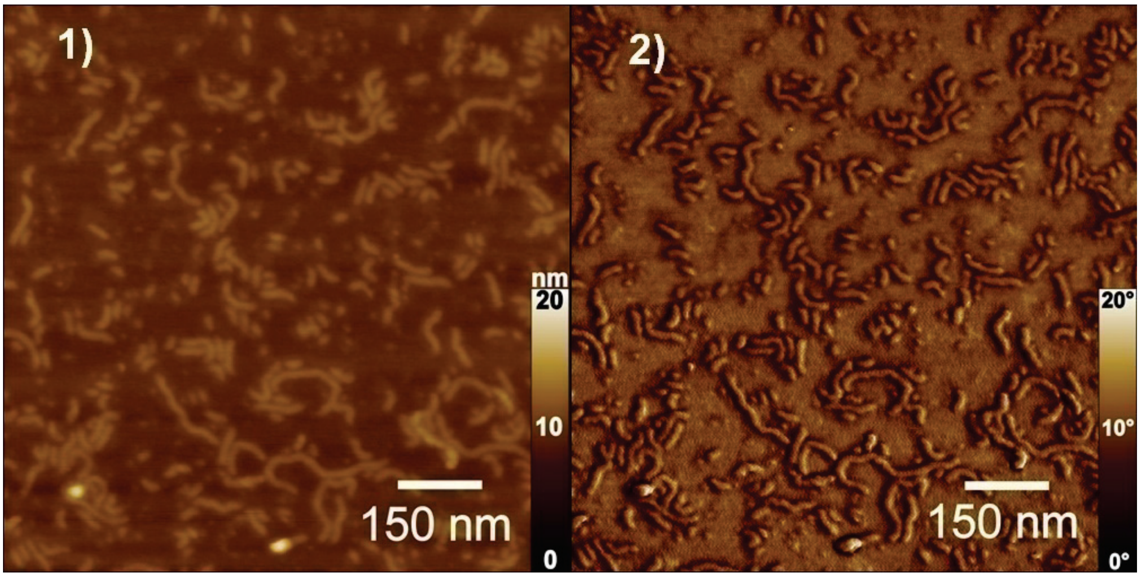

Figure A.11: AFM height and phase images of PVP47, c(PVP) = 0.07 g/L; 0.24 mM deposited on mica, 1): height, 2): phase image, pH = 1.6.

Light Scattering

Complexation experiments of PVP with TPPS (chapter 7) are carried out in salt-free water since salt addition strongly influences their interaction pattern and prohibits the formation of stable PVP-TPPS networks. However, the light scattering characterization of polyelectrolytes in salt-free conditions can be problematic due to long-range inter-polyelectrolyte attraction (see Appendix A.1). PVP47 has been characterized with static and dynamic light scattering in 5 mM sodium phosphate buffer (pH = 7) by D. Störkle and M. Schmidt (Table A.2) [227]. At these salt conditions straight lines for angle dependent scattering data are reported that were similar to the results in Figure A.14 (see below).

Table A.2: Light scattering results for PVP47 in 5 mM sodium phosphate buffer (pH = 7) as reported in [227], extrapolation for q = 0 and c = 0 if not stated otherwise.

R_g/nm	**R_h/nm**	**R_h/nm c = 0.0764 g/L**
45.8	33.1	30.9

Within this dissertation PVP47 has been characterized by light scattering at two conditions that are equivalent to the conditions in the experiments of chapter 7. These are a) salt-free water at pH ~7 and b) water with addition of HCl with c(HCl) ~15 - 20 mM and pH ~1.6 - 2.0 (without addition of further salt).

The results for the measurements in salt-free water have to be discussed in context with findings for the scattering behavior of linear quaternized poly(2-vinylpyridine) in salt-free aqueous solution by Förster et al. [40] that were already described in chapter 2. Förster reported that depending on several factors, especially salt and polyelectrolyte concentration, the correlation functions that are measured for PVP either show only one decay or an additional second “slow” mode. An example for a decay function where the slow mode is present is given in Figure 2.2. In addition to the presence of the slow mode, it was also reported that the corresponding “fast” mode shows an elevated diffusion coefficient in comparison to the self-diffusion coefficient as present under high salt conditions (see Figure 2.3).

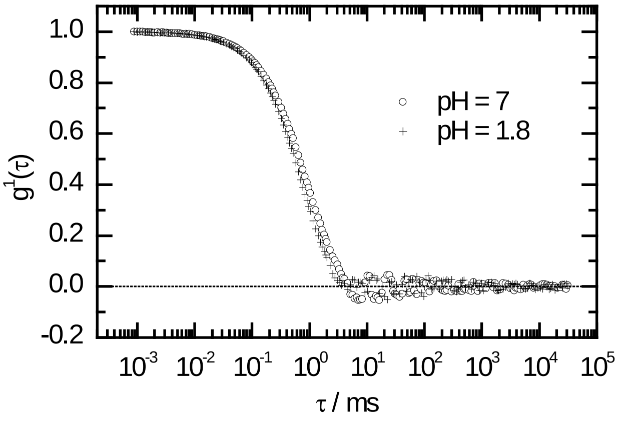

Figure A.12: Autocorrelation functions for PVP47, c = 0.072 g/L in salt-free water (pH = 7) and after addition of HCl to c(HCl) = 16 mM (pH = 1.8), θ = 60°, λ = 632.8 nm.

Figure A.12 gives the correlation function for PVP47 in “salt-free” conditions at pH

= 7. Apparently, a single decay function can be measured besides a small tail at high relaxation times (close to the spot where the function crosses zero) that may be attributed to a small number of aggregates present. However, this slight step is not always present and can be seen for salt-free samples as well as for samples with added salt.

The absence of a second mode for polyelectrolyte samples is generally explained by either the presence of sufficient added salt that suppresses inter-polyelectrolyte attraction or by a rather low polyelectrolyte concentration so that the polymer chains are isolated simply by dilution. Here in principal salt impurities in the sample may contribute to the effect but it is more likely that the rather low concentration of PVP has the stronger impact. As discussed in appendix A.1 there is an additional contribution to slow mode suppression that can be explained by the brush structure of PVP here: it has been reported that cylindrical polyelectrolyte brushes exhibit a lower effective charge density when compared to their linear counterparts and thus show the transition to monomodal correlation functions at higher concentrations than linear polyelectrolytes [65,222-223].

The angle dependency of diffusion coefficients extracted from PVP47 correlation functions without salt (all functions exhibit only one mode as in Figure A.12) is given in Figure A.13-1. Evidently, there is no linear trend. The calculated radii vary between R_h = 34.0 nm and R_h = 35.4 nm, and for further evaluation the arithmetic average is taken. Also the Zimm representation of static light scattering data (Figure A.9-2) does not show a linear correlation.

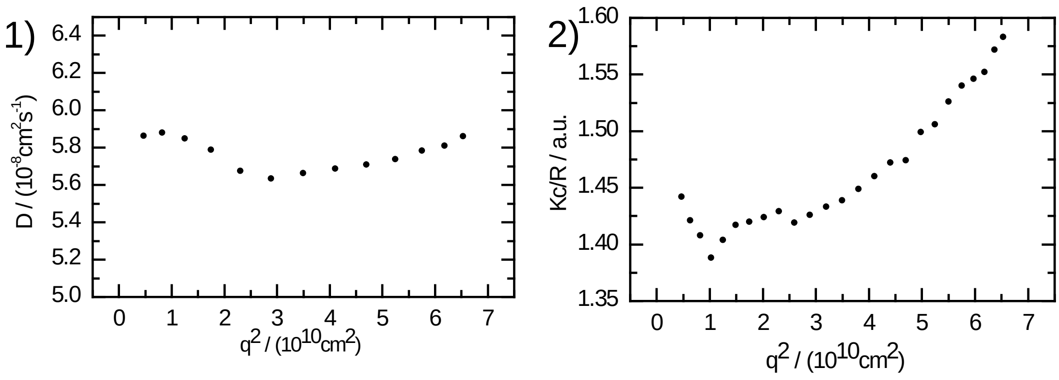

Figure A.13: Angle dependent dynamic (1) and static (2) light scattering results for PVP47, c = 0.072 g/L in salt-free water, pH = 7, λ = 632.8 nm.

These results shall be compared with the situation in added salt conditions as given in Figure A.14. Here unambiguous results with clear linearity similar to the findings in [227] are obtained.

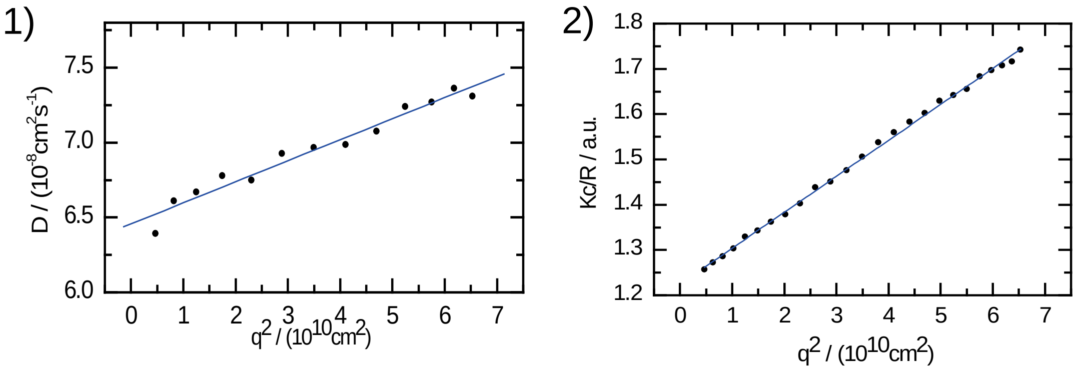

Figure A.14: Angle dependent dynamic (1) and static (2) light scattering results for PVP47, c = 0.072 g/L after addition of HCl to sample from Figure A.13 up to c(HCl) = 16 mM, pH = 1.8, λ = 632.8 nm.

The extracted radii as given in Table A.3 are very close to the values for PVP47 in sodium phosphate buffer as presented above.

Table A.3: Light scattering results for PVP47, c = 0.0764 g/L.

	R_g/nm	**R_h/nm**
pH = 7 no salt	-	34.6
pH = 1.8 16 mM HCl	44.1	30.9

Comparing these result to the findings for PVP47 in salt-free conditions, it can be concluded that although PVP47 at the chosen concentration in salt-free water exhibits only one decay function in dynamic light scattering, there are apparently polyelectrolyte effects present at these conditions. This is in clear contrast to the results for NaPSS brush (see appendix A.1) where at the same polyelectrolyte charge concentration c = 0.24 mM no polyelectrolyte effect is observed.

Therefore, these effects have to be considered when evaluating results for PVP scattering in salt-free water that are presented in chapter 7 since here salt-free conditions are desired for the complexation experiments. Although angle dependency here is somehow ambiguous and the extracted diffusion coefficient might contain contributions besides self-diffusional mechanisms, the extracted apparent hydrodynamic radius is still a quite good approximation to the “real” value in salt conditions. For the relative effects that are observed in chapter 7 and for the much larger size change as observed there, this precision should suffice.

A.4 C6T^{4+} Counterion

The tetravalent counterion′ 4,4 -(hexane-1,6-diyl)bis(1-ethyl-1,4-diazoniabicyclo [2.2.2]octane) (C6T^{4+}, Figure 3.3) was synthesized by Hakan Yildiz: a mixture of 1,4-diazabicyclo(2.2.2)octane (DABCO) in DMF/MeOH and 1,6-dibromohexane or ethyl bromide was stirred at 100 °C for 96 h. The product was precipitated in acetone. The white precipitate was filtered, dissolved in MilliQ water, and extracted with ether multiple times. The solution was freeze-dried and the product was obtained as white powder [53].

A.5 *p*-Phenylene bis(trimethylammonium tosylate)

p-Phenylene bis(trimethylammonium tosylate) was synthesized by stepwise methylation of *N*,*N*,*N′*,*N′*-tetramethyl-*p*-phenylenediamine with 6-fold excess of methyl *p*-toluenesulfonate at 60 °C for several hours first in nitromethane giving 60% monomethylated product and 40% dication as verified by ^{1}H NMR. In a second step the precipitate was redissolved in water (some ethanol was added to enhance solubility of methylating agent), and the reaction was carried out under otherwise identical conditions yielding a 96% divalent product. Twofold careful recrystallization from an ethanol/water mixture yielded 100% of the desired product.

A.6 Further Materials

meso-Tetrakis(4-(trimethylammonium)phenyl)porphyrin copper(II) tetrachloride (CuTAPP) was prepared from TAPP according to literature [84]. *meso*-Tetrakis(4-(trimethyl-ammonium)phenyl)-porphyrin zinc(II) tetratosylate (ZnTAPP) was bought from TriPorTech GmbH, Germany and used as received. *meso*-Tetrakis(4-sulfonatophenyl)-porphyrin (TPPS) was bought from Fluka and used as received. All other chemicals including the porphyrins *meso*-tetrakis(4-(trimethylammonium)-

phenyl)porphyrin tetratosylate (TAPP), *meso*-tetrakis(4-*N*-methylpyridinium)porphyrin tetratosylate (TMPyP) and as well as aggrecan from bovine articular cartilage were bought from Sigma-Aldrich and used as received, if not stated otherwise. All porphyrin concentrations were calibrated from literature extinction coefficients at Soret maximum (Table A.4).

Table A.4: Literature extinction coefficients at Soret maximum for the porphyrins used in this study.

	Soret maximum λ/nm	**ε/(10^5 M^{-1} cm^{-1})**	**reference**
TAPP	412	4.16	[84]
CuTAPP	412	3.46	[84]
ZnTAPP	419	4.48	[85]
TMPyP	424	2.26	[85]
TPPS	412	5.33	[88]

APPENDIX B

B METHODS

B.1 Light Scattering

Measurement Conditions

Light scattering measurements were carried out either with a red or infrared laser source dependent on the light absorption properties of the respective sample. Light scattering measurements were carried out at 20°C using an ALV 5000 correlator with 320 channels (ALV Langen, Germany) at scattering angles of 30°-150° with the red and 50°-110° with the infrared laser. The red He-Ne laser (JDS Uniphase) has a wavelength of λ = 632.8 nm and 22 mW output power. For light absorbing samples containing porphyrins, an IR laser diode (Schäfter + Kirchhoff laser diode with single mode fiber and gauss profile) with a wavelength of λ = 831.5 nm and 80 mW output power was used. The scattered intensity was divided by a beam splitter (approximately 55:45), each portion of which was detected by an avalanche diode. The two signals were cross-correlated in order to eliminate nonrandom electronic noise.

Well-defined polystyrene standards in toluene gave the same hydrodynamic radii (extrapolated to zero angle) from both laser sources and the same agreement was obtained for PSS brush samples that was used as an internal standard in the present text (e.g. R_h from angular extrapolation of the same NaPSS brush sample: R_h = 36.4 nm for red laser and R_h = 36.0 nm for IR laser).

A setup was installed allowing for subsequent use of red and infrared laser for the same sample (Figure B.1). This method enables an easier handling of IR measurements in that sense that before IR use the sample can be aligned and viewed using the visible red laser. Given the difference in wavelength one angle θ of the light scattering setup represents different scattering vectors for the two laser sources.

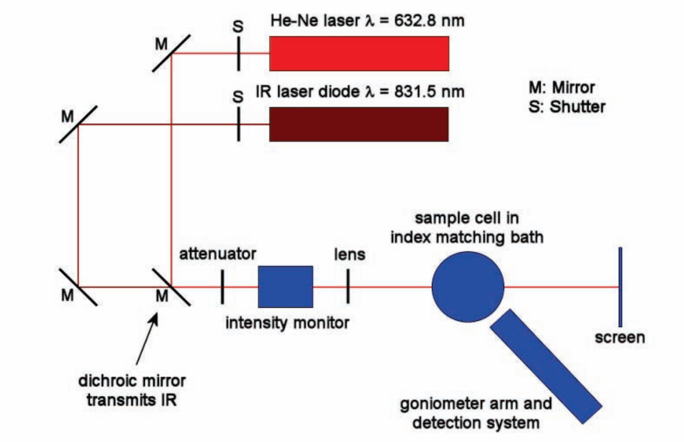

Figure B.1: Setup of light scattering system combining an infrared and red laser source.

For direct comparison of infrared light scattering with data from red light scattering the convenient fact was used that scattering vector q for IR laser at $\theta_{IR} = 90°$ can be very well approximated by q for the red laser at $\theta_{red} = 65°$. Thus, throughout the present text this connection will be frequently used.

Sample Preparation

Prior to measurements, samples were filtrated several times through syringe filters into Hellma quartz cuvettes with 2 cm internal diameter that were previously rinsed with freshly distilled acetone in a special glass apparatus (“acetone fountain”) to a dust-free state. The choice of filter material was dependent on the solvent to be filtrated and size characteristics of the particles. 5 μm pore sized filters did not yield sufficiently dust reduced samples. For aqueous solutions Millipore Millex-GS mixed cellulose esters membrane filters with 0.22 μm pore size were successfully used for dust particle removal. For solutions containing HCl or NaOH in water Millex-LG filters with pore size of 0.2 μm and hydrophilic PTFE as filter material was used. The same filter unit was used for samples in DMSO and in solvent mixtures of DMSO and water. For nonpolar organic solvents like toluene Millex-FG with pore size 0.2 μm and hydrophobic PTFE filter material was used.

Since self-assembled aggregates reported of throughout this text are larger or of a comparable size to the filter pore size, the stock solutions of the to be self-assembled building units were separately filtered prior mixing.

The mixing was conducted in the light scattering cell in the dust reduced environment of a flow box. As it is reported in chapter 5 the mixing protocol is crucial for the size of aggregates and therefore was precisely controlled. If not stated otherwise in the text, the following standard procedure of preparation was followed: in order to obtain a maximized homogeneous distribution the previously filtrated sample solution was vigorously stirred at the time of further addition of stock solution. To further ensure a good distribution the added freshly filtrated solution was added drop wise (time interval ~3-4s) directly out of the syringe filter. For stirring a magnetic bar (15 × 1.5 mm) was used that was cleaned in an acetone fountain to be dust-free and then transferred to the measurement cell. Due to its low height the bar could simply stay in the cell during measurement. The scattering behavior of pure water was basically the same either for samples containing a pre-cleaned stirring bar or not. Additionally light scattering results for PSS brush molecules were compared with and without a stirrer present and it was confirmed that same results for radii and intensity are obtained. It can be concluded that the stirring bar after adequate treatment does not bring in an amount of dust that will influence the light scattering measurement of the present samples.

Data Analysis

Measurement and data analysis procedure were as established: the time autocorrelation function of the scattered intensity was measured (homodyne mode) and converted into the scattered electric field autocorrelation function via Siegert relation (eq. 2.9). The electric field autocorrelation function was analyzed by second-order cumulant analysis (eq. 2.13). The apparent diffusion coefficient was calculated from the inverse relaxation time and extrapolated to zero scattering vector square (for angle dependent measurements). The hydrodynamic radius was obtained via the Stokes-Einstein relation from the diffusion coefficient.

Table B.1: Constants and values for light scattering data analysis at 20°C [228-231].

	water	**DMSO/water 90/10**	**toluene**
$n_{632.8\ \mathrm{nm}}$	1.3321	1.4649	1.4937
$n_{831.5\ \mathrm{nm}}$	1.3277	(same value used as for red light)	1.4855
η/mPas	1.002	2.70	0.59

Since an infrared laser was partly used in the presented experiments the wavelength dependency of refractive index in the respective solvent medium was taken into account. Table B.1 summarizes constants and values used for the evaluation of light scattering data.

B.2 Atomic Force Microscopy

Measurement Conditions

A commercial MultiMode microscope operated in tapping mode with a Nanoscope IIIa controller and 12 × 12 μm E-scanner from Veeco Instruments, Santa Barbara, CA was used. For imaging in air an Olympus cantilever OMCL-AC160TS with a spring constant of 42 N/m and a nominal tip radius < 10 nm was used after cleaning in argon plasma. Imaging in water requests for a softer Si cantilever and thus Olympus OMCL-AC240TN-W2 with spring constant of 2 N/m and a nominal tip radius < 10 nm was used again after cleaning in argon plasma.

Sample Preparation: General Remarks

For imaging objects on a surface by AFM several types of surfaces generally are used. Throughout the present dissertation mica, a sheet silicate mineral, was used that provides easily accessible very smooth surfaces by freshly cleaving the mineral sheets. Additionally mica is hydrophilic and due to OH groups at the surface actually is negatively charged in aqueous media. Due to this property it is an adequate candidate to immobilize charged polymers on its surface.

There are several different procedures to deposit a sample for AFM investigation on the surface. It should be differentiated between two main classes: in one class of procedures a solution of the sample will be put on the surface by evaporating the liquid of the solution leaving the sample but also everything else in the solution on the surface. In the other case a sample solution will be put on the surface and will stay there to incubate for some time during that a desired sample surface interaction take place that leads to an immobilization of the sample in solution. After some time the solution can be rinsed off by ample solvent and the sample will be dried. This second technique is very useful to get rid of material in the sample solution that is not supposed to be covering the surface like added salt. The immobilization of particles by interaction forces is the only procedure for imaging in liquid solution. Naturally, such an immobilization for polyelectrolyte samples as investigated within the present thesis will make use of charge interactions.

However, such an immobilization is not always feasible depending on sample properties, e.g. if the sample to be investigated is only lowly charged. This is the case for the brush-porphyrin networks reported of in chapter 5. Whereas pure PSS brush molecules may be immobilized by a positively charged surface and afterwards clearly be imaged (see chapter 5), the PSS-TAPP networks can only be fixed to the surface to a certain extent and hardly be imaged since the tip probe will easily move the loosely fixed particles. For such samples a procedure out of the "drying class" as described above is much more practicable.

In this class two techniques can be differentiated. A droplet of the sample solution can be put on the surface and the solvent will simply evaporate with time ("drop-casting"). This drying procedure, however, may lead to enhanced local concentration of sample particles due to the drying process and in fact leads to film formation of PSS brush molecules as reported in chapter 5. In order to achieve a more homogeneous and thus more natural distribution of the sample particles on the surface (closer to the situation in solution), the sample may be deposited on the surface by "spin-coating". Here a droplet of the sample solution will be added to the surface and the surface will be rotated with high speed (e.g. 3000 rpm) to simultaneously distribute the particles on the surface and on the same time evaporate the solvent.

Sample Preparation: Details

If not otherwise stated the AFM results presented throughout the present dissertation are taken from samples that have been prepared by spin-coating a 15 μL droplet of sample solution on freshly cleaved mica at 3000 rpm for 120s and measured in air.

For samples that are prepared with the "incubate-rinse-and-dry" technique a droplet of ~60 - 100 μL (depending on size and hydrophilicity of surface in order to ensure a full coverage of the surface throughout incubation time) was incubated for 5 minutes on the surface and afterwards was rinsed with ample water and then dried in air before imaging. For certain investigations it is necessary to immobilize negatively charged molecules (e.g. PSS brush) on the surface. Therefore, the negatively charged mica substrate was modified with 3-aminopropyltriethoxysilane (APTES) that in contact with the mica surface will be covalently bound to the surface and leaves amino groups that can be positively charged at the surface according to literature [53,232]. Here a droplet of ~100 μL APTES solution (chosen APTES concentration is dependent on required density of APTES modification c = 0.01 - 1% (v/v)) in water was incubated for 10 minutes on mica and afterwards extensively rinsed off with ample water and dried in air.

For the AFM images in water reported in chapter 5 a special AFM cell for liquids was used. Both the substrate and the probe were submerged in a droplet of water and afterwards combined. After focusing the detection laser system on the cantilever, the tip was lowered carefully toward the substrate. Before measurement the system was left for equilibration for at least 2 hours in order to avoid drift because of solvent movement.

Data Analysis

For samples that exhibit cylindrical brush structure as measured by AFM sectional profiles perpendicular to the brush main axis were extracted by the SPM data analysis software “Gwyddion”. The height of the brush is extracted from the sectional profiles as vertical distance from profile maximum to the absolute minimum surrounding the brush cross-section. In order to allow for a more reliable determination and better comparability in between samples, the width of the brush was taken as the full width at half maximum of the spectral profile throughout the present dissertation. It has to be taken into account that the width determined by this method is systematically lower than the brush diameter at surface.

B.3 Cryo-Transmission Electron Microscopy

Cryo-TEM images were recorded on a FEI Tecnai 12 at an acceleration voltage of 120 kV. Quantifoil copper grids with 2 μm holes were used for sample preparation. All samples were vitrified without any external staining from room temperature in liquid ethane using a FEI Vitrobot.

B.4 Small-Angle Neutron Scattering

Samples for SANS were prepared in D_2O with a polymer concentration of 1 g/L (4.8 mM) and transferred into optical quality quartz cells with 2 mm path length. SANS studies were performed at the FRM II, Munich, Germany, and at Institute Laue

Langevin (ILL), Grenoble, France. Data shown result from the KWS 1 instrument of the Jülich Center for Neutron Science at FRM II using three configurations with the neutron wavelengths λ and sample-detector distances d of λ = 0.45 nm/d = 1.6 m, λ = 0.45 nm/d = 7.6 m, and λ = 1.2 nm/d = 7.6 m. A total scattering vector range of 0.034 nm^{-1} < q < 3.0 nm^{-1} was covered. Data were corrected for empty quartz cell scattering, electronic background, and detector uniformity and converted to an absolute scale using secondary standards. The data were further corrected by subtracting the contributions from solvent scattering and incoherent background. All measurements and data treatment have been performed according to common procedures. Experimental errors of I(q) data are within 1% for q < 0.6 nm^{-1}, below 10% for q < 1 nm^{-1}, and increase up to 50% for highest q data. Cross-section radii of gyration were determined from cross-section Guinier analysis [36]:

$$qI(q) = I_0 e^{-\left(\frac{q^2 R_{g,c}}{2}\right)} \tag{B.1}$$

Data were further analyzed according to the cylindrical geometry applying the Fourier transformation for cylindrical particles where the cross-section distribution function $P_c(r)$ is calculated via

$$qI(q) = 2\pi \int_{r=0}^{\infty} P_c(r) J_0(qr) dr \tag{B.2}$$

with $J_0(x)$ being the zero-order Bessel function, r the radial distance, and q the scattering vector magnitude [165-168]. The indirect transformation method is applied in order to minimize termination effects. The program ITP, indirect transformation for the calculation of $P(r)$, by Glatter was used which includes smoothing of the primary data by a weighted least-squares procedure (estimation of the optimum stabilization parameter based on a stability plot), desmearing, and transforming into real space simultaneously. The actual calculations dealing with the experimental scattering curves accounted for the measured beam profile and the wavelength distribution of the experimental setup.

B.5 UV-vis Spectroscopy

Spectra were recorded in Hellma optical quartz cells (path length 1 cm) with Lambda 25 from Perkin-Elmer.

LIST OF ABBREVIATIONS

$\mu_{1,2}$	second and third cumulant
$A_{2,3}$	second and third virial coefficient of osmotic pressure
AFM	atomic force microscopy
APTES	3-aminopropyltriethoxysilane
B	signal-to-noise ratio
c	concentration
c_p	charge concentration of polyelectrolyte
c_s	charge concentration of salt or counterion
CS	chondroitin sulfate
CuTAPP	*meso*-tetrakis(4-(trimethyl-ammonium)phenyl)-porphyrin copper(II)
$C6T^{4+}$	4,4′-(hexane-1,6-diyl)bis(1-ethyl-1,4-diazoniabicyclo [2.2.2]octane
D	diffusion coefficient
DABCO	1,4-Diazabicyclo[2.2.2]octane
DLS	dynamic light scattering
DMSO	dimethyl sulfoxide
ε	light extinction coefficient
ε_r	relative dielectric permittivity
Γ	first cumulant, relaxation rate
GAG	glycosaminoglycan
$g_1(\tau)$	electric field time autocorrelation function
$g_2(\tau)$	intensity time autocorrelation function
η	viscosity
I(q), I	scattering intensity
IR	infrared
l	charge ratio at pH = 7
l_{eff}	effective charge ratio, $l_{eff} \neq l$ at pH < 7 for certain conditions
λ	wavelength
m	mass
M	molecular weight
M	molar concentration in mol/l

M_n	number average of molecular weight
M_w	weight average of molecular weight
n	refractive index
NaPSS	sodium poly(styrene sulfonate)
NaSS	p-ethylbenzenesulfonate sodium salt
$\tilde{\nu}$	wave number
P(q)	form factor
Π	osmotic pressure
PH_2	free base porphyrin
PH_4	protonated porphyrin
m-PH_x	monomeric porphyrin
J-PH_x	J-aggregate of porphyrin
PH2-PVP	unprotonated porphyrin bound to PVP.
PSS	poly(styrene sulfonate)
PSS8k	poly(styrene sulfonate), M_w = 8,000 g/mol
PSS43k	poly(styrene sulfonate), M_w = 43,000 g/mol
PSS666k	poly(styrene sulfonate), M_w = 666,000 g/mol
PVP	poly(2-vinylpyridine)
PVS	polyvinyl sulfuric acid potassium salt
P_w	degree of polymerization, weight average
θ	scattering angle
q	scattering vector
$P_c(r)$	cross-sectional pair distance distribution function
R(q)	Rayleigh ratio
R	ideal gas constant
ρ	characteristic ratio (= R_g/R_h)
R_g	radius of gyration
$R_{g,c}$	cross-sectional radius of gyration
R_h	hydrodynamic radius
S(q)	structure factor
$S_{inter}(q)$	intermolecular structure factor
SANS	small angle neutron scattering

SLS	static light scattering
t	time
τ	relaxation time
T	temperature
TAPP	*meso*-tetrakis(4-(trimethyl-ammonium)phenyl)-porphyrin
TEM	transmission electron microscopy
TMPyP	*meso*-tetrakis(4-*N*-methylpyridinium)porphyrin
TPP	tetraphenylporphyrin
TPPS	*meso*-tetrakis(4-sulfonatophenyl)porphyrin
ZnTAPP	*meso*-tetrakis(4-(trimethyl-ammonium)phenyl)-porphyrin zinc(II)

BIBLIOGRAPHY

[1] Pelesko, J. A. *Self Assembly: The Science of Things That Put Themselves Together;* Taylor & Francis Group: Boca Raton, 2007.

[2] Lehn, J. M. *Supramolecular chemistry : concepts and perspectives;* Wiley-VCH: Weinheim, 1995.

[3] Sijbesma, R. P.; Beijer, F. H.; Brunsveld, L.; Folmer, B. J. B.; Hirschberg, J. H. K. K.; Lange, R. F. M.; Lowe, J. K. L.; Meijer, E. W. *Science* **1997,** *278,* 1601-1604.

[4] Schmuck, C.; Wienand, W. *Angew. Chem., Int. Ed.* **2001,** *40,* 4363-4369.

[5] Schlaad, H.; Krasia, T.; Antonietti, M. *J. Am. Chem. Soc.* **2004,** *126,* 11307-11310.

[6] Kaiser, T. E.; Wang, H.; Stepanenko, V.; Würthner, F. *Angew. Chem., Int. Ed.* **2007,** *46,* 5541-5544.

[7] Lehn, J. M. *Angew. Chem., Int. Ed.* **1988,** *27,* 89-112.

[8] Antonietti, M.; Conrad, J.; Thünemann, A. *Macromolecules* **1994,** *27,* 6007-6011.

[9] Rädler, J. O.; Koltover, I.; Salditt, T.; Safinya, C. R. *Science* **1997,** *275,* 810-814.

[10] Koltover, I.; Salditt, T.; Rädler, J. O.; Safinya, C. R. *Science* **1998,** *281,* 78-81.

[11] Thünemann, A. F.; Beyermann, J. *Macromolecules* **2000,** *33,* 6878-6885.

[12] Ikeda, Y.; Beer, M.; Schmidt, M.; Huber, K. *Macromolecules* **1998,** *31,* 728-733.

[13] Peng, S. F.; Wu, C. *Macromolecules* **1999,** *32,* 585-589.

[14] Schweins, R.; Huber, K. *Eur. Phys. J. E* **2001,** *5,* 117-126.

[15] Schweins, R.; Lindner, P.; Huber, K. *Macromolecules* **2003,** *36,* 9564-9573.

[16] Schweins, R.; Goerigk, G.; Huber, K. *Eur. Phys. J. E* **2006,** *21,* 99-110.

[17] Goerigk, G.; Huber, K.; Schweins, R. *J. Chem. Phys.* **2007,** *127,* 154908.

[18] Lin, W.; Zhou, Y. S.; Zhao, Y.; Zhu, Q. S.; Wu, C. *Macromolecules* **2002,** *35,* 7407-7413.

[19] Gröhn, F.; Klein, K.; Brand, S. *Chem. Eur. J.* **2008,** *14,* 6866-6869.

[20] Willerich, I.; Gröhn, F. *Chem. Eur. J.* **2008,** *14,* 9112-9116.

[21] Gröhn, F. *Macromol. Chem. Phys.* **2008,** *209,* 2295-2301.

[22] Li, Y.; Yildiz, U. H.; Mullen, K.; Grohn, F. *Biomacromolecules* **2009,** *10,* 530-

540.

[23] Ruthard, C.; Maskos, M.; Kolb, U.; Gröhn, F. *Macromolecules* **2009,** *42,* 830-840.

[24] Willerich, I.; Ritter, H.; Gröhn, F. *J. Phys. Chem. B* **2009,** *113,* 3339-3354.

[25] Yildiz, U. H.; Koynov, K.; Gröhn, F. *Macromol. Chem. Phys.* **2009,** *210,* 1678-1690.

[26] Gröhn, F.; Klein, K.; Koynov, K. *Macrom. Rap. Comm.* **2010,** *31,* 75-80.

[27] Reinhold, F.; Kolb, U.; Lieberwirth, I.; Gröhn, F. *Langmuir* **2009,** *25,* 1345-1351.

[28] Wasielewski, M. R. *Chem. Rev.* **1992,** *92,* 435-461.

[29] Lin, V. S. Y.; Dimagno, S. G.; Therien, M. J. *Science* **1994,** *264,* 1105-1111.

[30] Gust, D.; Moore, T. A.; Moore, A. L. *Acc. Chem. Res.* **2001,** *34,* 40-48.

[31] Guldi, D. M. *Chem. Soc. Rev.* **2002,** *31,* 22-36.

[32] Bonnett, R. *Chem. Soc. Rev.* **1995,** *24,* 19-33.

[33] Dougherty, T. J.; Gomer, C. J.; Henderson, B. W.; Jori, G.; Kessel, D.; Korbelik, M.; Moan, J.; Peng, Q. *J. Natl. Cancer Inst.* **1998,** *90,* 889-905.

[34] Sternberg, E. D.; Dolphin, D.; Brückner, C. *Tetrahedron* **1998,** *54,* 4151-4202.

[35] Kratochvil, P. *Classical Light Scattering from Polymer Solutions;* Elsevier Science: New York, 1987.

[36] *Neutrons, X-rays, and Light: Scattering Methods Applied to Soft Condensed Matter;* Elsevier: Amsterdam, 2002.

[37] Brown, W., *Dynamic Light Scattering, The Method and Some Applications*. Clarendon Press: Oxford, 1993.

[38] Berne, J. B.; Pecora, R. *Dynamic Light Scattering with Applications to Chemistry, Biology and Physics;* Wiley Interscience: New York, 1976.

[39] Förster, S.; Schmidt, M. *Adv. Polym. Sci.* **1995,** *120,* 51-133.

[40] Förster, S.; Schmidt, M.; Antonietti, M. *Polymer* **1990,** *31,* 781-792.

[41] Gouterman, M. In *The Porpyrins - Physical Chemistry, Part A;* Dolphin, D.; Ed.; Academic Press: New York, 1978; Vol. 3, pp 1-165.

[42] Milgron, L. R. *The Colours of Life;* Oxford University Press: Oxford, 1997.

[43] Gouterman, M. *J. Mol. Spectrosc.* **1961,** *6,* 138-163.

[44] Pasternack, R. F.; Centuro, G. C.; Boyd, P.; Hinds, L. D.; Huber, P. R.; Francesc.L; Fasella, P.; Engasser, G.; Gibbs, E. *J. Am. Chem. Soc.* **1972,** *94,*

4511-4517.

[45] Ohno, O.; Kaizu, Y.; Kobayashi, H. *J. Chem. Phys.* **1993,** *99,* 4128-4139.

[46] Akins, D. L.; Zhu, H. R.; Guo, C. *J. Phys. Chem.* **1996,** *100,* 5420-5425.

[47] Kano, K.; Takei, M.; Hashimoto, S. *J. Phys. Chem.* **1990,** *94,* 2181-2187.

[48] Kano, K.; Minamizono, H.; Kitae, T.; Negi, S. *J. Phys. Chem. A* **1997,** *101,* 6118-6124.

[49] Helmich, F.; Lee, C. C.; Nieuwenhuizen, M. M. L.; Gielen, J. C.; Christianen, P. C. M.; Larsen, A.; Fytas, G.; Leclere, P. E. L. G.; Schenning, A. P. H. J.; Meijer, E. W. *Angew. Chem. Int. Ed.* **2010,** *49,* 3939-3942.

[50] Gibbs, E. J.; Tinoco, I.; Maestre, M. F.; Ellinas, P. A.; Pasternack, R. F. *Biochem. Biophys. Res. Commun.* **1988,** *157,* 350-358.

[51] Bloomfield, V. A. *Biopolymers* **1991,** *31,* 1471-1481.

[52] Bloomfield, V. A. *Biopolymers* **1997,** *44,* 269-282.

[53] Li, Y.; Yildiz, U. H.; Müllen, K.; Gröhn, F. *Biomacromolecules* **2009,** *10,* 530-540.

[54] Pasternack, R. F.; Schaefer, K. F.; Hambright, P. *Inorg. Chem.* **1994,** *33,* 2062-2065.

[55] Schwab, A. D.; Smith, D. E.; Rich, C. S.; Young, E. R.; Smith, W. F.; de Paula, J. C. *J. Phys. Chem. B* **2003,** *107,* 11339-11345.

[56] McEwen, W. K. *J. Am. Chem. Soc.* **1936,** *58,* 1124-1129.

[57] Clarke, J. A.; Dawson, P. J.; Grigg, R.; Rocheste.Ch. *J. Chem. Soc. Perkin Trans.* **1973**, 414-416.

[58] Wintermantel, M.; Schmidt, M.; Tsukahara, Y.; Kajiwara, K.; Kohjiya, S. *Macromol. Rapid Commun.* **1994,** *15,* 279-284.

[59] Wintermantel, M.; Gerle, M.; Fischer, K.; Schmidt, M.; Wataoka, I.; Urakawa, H.; Kajiwara, K.; Tsukahara, Y. *Macromolecules* **1996,** *29,* 978-983.

[60] Dziezok, P.; Sheiko, S. S.; Fischer, K.; Schmidt, M.; Möller, M. *Angew. Chem., Int. Ed.* **1997,** *36,* 2812-2815.

[61] Gerle, M.; Fischer, K.; Roos, S.; Müller, A. H. E.; Schmidt, M.; Sheiko, S. S.; Prokhorova, S.; Möller, M. *Macromolecules* **1999,** *32,* 2629-2637.

[62] Schlüter, A. D.; Rabe, J. P. *Angew. Chem., Int. Ed.* **2000,** *39,* 864-883

[63] Cheng, G. L.; Boker, A.; Zhang, M. F.; Krausch, G.; Müller, A. H. E. *Macromolecules* **2001,** *34,* 6883-6888.

[64] Pyun, J.; Kowalewski, T.; Matyjaszewski, K. *Macromol. Rapid Commun.* **2003,** *24,* 1043-1059.

[65] Rühe, J.; Ballauff, M.; Biesalski, M.; Dziezok, P.; Gröhn, F.; Johannsmann, D.; Houbenov, N.; Hugenberg, N.; Konradi, R.; Minko, S.; Motornov, M.; Netz, R. R.; Schmidt, M.; Seidel, C.; Stamm, M.; Stephan, T.; Usov, D.; Zhang, H. N. *Adv. Polym. Sci.* **2004,** *165,* 79-150.

[66] Lienkamp, K.; Ruthard, C.; Lieser, G.; Berger, R.; Gröhn, F.; Wegner, G. *Macromol. Chem. Phys.* **2006,** *207,* 2050-2065.

[67] Lienkamp, K.; Noe, L.; Breniaux, M. H.; Lieberwirth, I.; Gröhn, F.; Wegner, G. *Macromolecules* **2007,** *40,* 2486-2502.

[68] Sheiko, S. S.; Sumerlin, B. S.; Matyjaszewski, K. *Prog. Polym. Sci.* **2008,** *33,* 759-785.

[69] Zhang, B.; Gröhn, F.; Pedersen, J. S.; Fischer, K.; Schmidt, M. *Macromolecules* **2006,** *39,* 8440-8450.

[70] Gunari, N.; Cong, Y.; Zhang, B.; Fischer, K.; Janshoff, A.; Schmidt, M. *Macromol. Rapid Comm.* **2008,** *29,* 821-825.

[71] Cong, Y.; Gunari, N.; Zhang, B.; Janshoff, A.; Schmidt, M. *Langmuir* **2009,** *25,* 6392-6397.

[72] Li, C. M.; Gunari, N.; Fischer, K.; Janshoff, A.; Schmidt, M. *Angew. Chem. Int. Ed.* **2004,** *43,* 1101-1104.

[73] Sheiko, S. S.; Prokhorova, S. A.; Beers, K. L.; Matyjaszewski, K.; Potemkin, I. I.; Khokhlov, A. R.; Moller, M. *Macromolecules* **2001,** *34,* 8354-8360.

[74] Gallyamov, M. O.; Tartsch, B.; Khokhlov, A. R.; Sheiko, S. S.; Börner, H. G.; Matyjaszewski, K.; Möller, M. *Chem. Eur. J.* **2004,** *10,* 4599-4605.

[75] Stephan, T.; Muth, S.; Schmidt, M. *Macromolecules* **2002,** *35,* 9857-9860.

[76] Mei, Y.; Ballauff, M. *Eur. Phys. J. E* **2005,** *16,* 341-349.

[77] Pincus, P. *Macromolecules* **1991,** *24,* 2912-2919.

[78] Borisov, O. V.; Birshtein, T. M.; Zhulina, E. B. *J. Phys. II* **1991,** *1,* 521-526.

[79] Dubreuil, F.; Guenoun, P. *Eur. Phys. J. E* **2001,** *5,* 59-64.

[80] Xu, Y. Y.; Bolisetty, S.; Drechsler, M.; Fang, B.; Yuan, J. Y.; Ballauff, M.; Muller, A. H. E. *Polymer* **2008,** *49,* 3957-3964.

[81] Xu, Y. Y.; Bolisetty, S.; Drechsler, M.; Fang, B.; Yuan, J. Y.; Harnau, L.; Ballauff, M.; Müller, A. H. E. *Soft Matter* **2009,** *5,* 379-384.

[82] Ruthard, C. Diploma thesis, University of Mainz, 2007.

[83] Hunter, C. A.; Sanders, J. K. M. *J. Am. Chem. Soc.* **1990,** *112,* 5525-5534.

[84] Bütje, K.; Nakamoto, K. *Inorg. Chim. Acta* **1990,** *167,* 97-108.

[85] Kalyanasundaram, K. *J. Chem. Soc., Faraday Trans. 2* **1983,** *79,* 1365-1374.

[86] Dixon, D. W.; Steullet, V. *J. Inorg. Biochem.* **1998,** *69,* 25-32.

[87] Huang, C. Z.; Li, Y. F.; Luo, H. Q.; Huan, X. H.; Liu, S. P. *Anal. Lett.* **1998,** *31,* 1149-1171.

[88] Fleischer, E. B.; Palmer, J. M.; Srivasta, T. S.; Chatterjee, A. *J. Am. Chem. Soc.* **1971,** *93,* 3162-3167.

[89] Pasternack, R. F. *Ann. Ny. Acad. Sci.* **1973,** *206,* 614-630.

[90] Akins, D. L.; Zhu, H. R.; Guo, C. *J. Phys. Chem.* **1994,** *98,* 3612-3618.

[91] Ribo, J. M.; Crusats, J.; Farrera, J. A.; Valero, M. L. *J. Chem. Soc. Chem. Commun.* **1994**, 681-682.

[92] Collings, P. J.; Gibbs, E. J.; Starr, T. E.; Vafek, O.; Yee, C.; Pomerance, L. A.; Pasternack, R. F. *J. Phys. Chem. B* **1999,** *103,* 8474-8481.

[93] Micali, N.; Mallamace, F.; Romeo, A.; Purrello, R.; Scolaro, L. M. *J. Phys. Chem. B* **2000,** *104,* 5897-5904.

[94] Lauceri, R.; De Napoli, M.; Mammana, A.; Nardis, S.; Romeo, A.; Purrello, R. *Synthetic Met.* **2004,** *147,* 49-55.

[95] Micali, N.; Villari, V.; Castriciano, M. A.; Romeo, A.; Scolaro, L. M. *J. Phys. Chem. B* **2006,** *110,* 8289-8295.

[96] Wang, Z. C.; Medforth, C. J.; Shelnutt, J. A. *J. Am. Chem. Soc.* **2004,** *126,* 15954-15955.

[97] Rotomskis, R.; Augulis, R.; Snitka, V.; Valiokas, R.; Liedberg, B. *J. Phys. Chem. B* **2004,** *108,* 2833-2838.

[98] Kitahama, Y.; Kimura, Y.; Takazawa, K. *Langmuir* **2006,** *22,* 7600-7604.

[99] Friesen, B. A.; Nishida, K. R. A.; McHale, J. L.; Mazur, U. *J. Phys. Chem. C* **2009,** *113,* 1709-1718.

[100] Schwab, A. D.; Smith, D. E.; Bond-Watts, B.; Johnston, D. E.; Hone, J.; Johnson, A. T.; de Paula, J. C.; Smith, W. F. *Nano Lett.* **2004,** *4,* 1261-1265.

[101] Ribo, J. M.; Crusats, J.; Sagues, F.; Claret, J.; Rubires, R. *Science* **2001,** *292,* 2063-2066.

[102] Escudero, C.; Crusats, J.; Diez-Perez, I.; El-Hachemi, Z.; Ribo, J. M. *Angew.*

Chem. Int. Ed. **2006,** *45,* 8032-8035.

[103] Aggarwal, L. P. F.; Borissevitch, I. E. *Spectrochim. Acta, Part A* **2006,** *63,* 227-233.

[104] Fiel, R. J.; Howard, J. C.; Mark, E. H.; Dattagupta, N. *Nucleic Acids Res.* **1979,** *6,* 3093-3118.

[105] Fiel, R. J.; Munson, B. R. *Nucleic Acids Res.* **1980,** *8,* 2835-2842.

[106] Pasternack, R. F.; Gibbs, E. J.; Villafranca, J. J. *Biochemistry* **1983,** *22,* 2406-2414.

[107] Pasternack, R. F.; Gibbs, E. J.; Villafranca, J. J. *Biochemistry* **1983,** *22,* 5409-5417.

[108] Pasternack, R. F.; Antebi, A.; Ehrlich, B.; Sidney, D.; Gibbs, E. J.; Bassner, S. L.; Depoy, L. M. *J. Mol. Catal.* **1984,** *23,* 235-242.

[109] Pasternack, R. F.; Gibbs, E. J.; Gaudemer, A.; Antebi, A.; Bassner, S.; Depoy, L.; Turner, D. H.; Williams, A.; Laplace, F.; Lansard, M. H.; Merienne, C.; Perreefauvet, M. *J. Am. Chem. Soc.* **1985,** *107,* 8179-8186.

[110] Pasternack, R. F.; Giannetto, A.; Pagano, P.; Gibbs, E. J. *J. Am. Chem. Soc.* **1991,** *113,* 7799-7800.

[111] Pasternack, R. F.; Bustamante, C.; Collings, P. J.; Giannetto, A.; Gibbs, E. J. *J. Am. Chem. Soc.* **1993,** *115,* 5393-5399.

[112] Pasternack, R. F.; Gurrieri, S.; Lauceri, R.; Purrello, R. *Inorg. Chim. Acta* **1996,** *246,* 7-12.

[113] Huang, C. Z.; Li, K. A.; Tong, S. Y. *Anal. Chem.* **1996,** *68,* 2259-2263.

[114] Bustamante, C.; Gurrieri, S.; Pasternack, R. F.; Purrello, R.; Rizzarelli, E. *Biopolymers* **1994,** *34,* 1099-1104.

[115] Sirish, M.; Schneider, H. J. *Chem. Commun.* **1999**, 907-908.

[116] Pasternack, R. F.; Ewen, S.; Rao, A.; Meyer, A. S.; Freedman, M. A.; Collings, P. J.; Frey, S. L.; Ranen, M. C.; de Paula, J. C. *Inorg. Chem. Acta* **2001,** *317,* 59-71.

[117] Scolaro, L. M.; Romeo, A.; Pasternack, R. F. *J. Am. Chem. Soc.* **2004,** *126,* 7178-7179.

[118] Takatoh, C.; Matsumoto, T.; Kawai, T.; Saitoh, T.; Takeda, K. *Chem. Lett.* **2006,** *35,* 88-89.

[119] Jin, B.; Ahn, J. E.; Ko, J. H.; Wang, W.; Han, S. W.; Kim, S. K. *J. Phys. Chem. B* **2008,** *112,* 15875-15882.

[120] Wei, C. Y.; Wang, L. H.; Jia, G. Q.; Zhou, J.; Han, G. Y.; Li, C. *Biophys. Chem.* **2009,** *143,* 79-84.

[121] Wei, C. Y.; Wang, J. H.; Zhang, M. Y. *Biophys. Chem.* **2010,** *148,* 51-55.

[122] Strickland, J. A.; Marzilli, L. G.; Wilson, W. D. *Biopolymers* **1990,** *29,* 1307-1323.

[123] Sehlstedt, U.; Kim, S. K.; Carter, P.; Goodisman, J.; Vollano, J. F.; Norden, B.; Dabrowiak, J. C. *Biochemistry* **1994,** *33,* 417-426.

[124] Anantha, N. V.; Azam, M.; Sheardy, R. D. *Biochemistry* **1998,** *37,* 2709-2714.

[125] Ren, J. S.; Chaires, J. B. *Biochemistry* **1999,** *38,* 16067-16075.

[126] Lubitz, I.; Borovok, N.; Kotlyar, A. *Biochemistry* **2007,** *46,* 12925-12929.

[127] Kim, J. O.; Lee, Y. A.; Yun, B. H.; Han, S. W.; Kwag, S. T.; Kim, S. K. *Biophys. J.* **2004,** *86,* 1012-1017.

[128] White, W. I. In *The Porpyrins - Physical Chemistry, Part C;* Dolphin, D.; Ed.; Academic Press: New York, 1978; Vol. 3, pp 303-339.

[129] Pasternack, R. F.; Francesconi, L.; Raff, D.; Spiro, E. *Inorg. Chem.* **1973,** *12,* 2606-2611.

[130] Pancoska, P.; Urbanova, M.; Bednarova, L.; Vacek, K.; Paschenko, V. Z.; Vasiliev, S.; Malon, P.; Kral, M. *Chem. Phys.* **1990,** *147,* 401-413.

[131] Pasternack, R. F.; Gibbs, E. *J. Inorg. Org. Polym.* **1993,** *3,* 77-88.

[132] Borissevitch, I. E.; Tominaga, T. T.; Imasato, H.; Tabak, M. *J. Lumin.* **1996,** *69,* 65-76.

[133] Borissevitch, I. E.; Tominaga, T. T.; Imasato, H.; Tabak, M. *Anal. Chim. Acta* **1997,** *343,* 281-286.

[134] Bellacchio, E.; Lauceri, R.; Gurrieri, S.; Scolaro, L. M.; Romeo, A.; Purrello, R. *J. Am. Chem. Soc.* **1998,** *120,* 12353-12354.

[135] Purrello, R.; Raudino, A.; Scolaro, L. M.; Loisi, A.; Bellacchio, E.; Lauceri, R. *J. Phys. Chem. B* **2000,** *104,* 10900-10908.

[136] Urbanova, M.; Setnicka, V.; Kral, V.; Volka, K. *Biopolymers* **2001,** *60,* 307-316.

[137] Ikeda, S.; Nezu, T.; Ebert, G. *Biopolymers* **1991,** *31,* 1257-1263.

[138] Andrade, S. M.; Costa, S. M. B. *Chem. Eur. J.* **2006,** *12,* 1046-1057.

[139] Castriciano, M. A.; Romeo, A.; Angelini, N.; Micali, N.; Longo, A.; Mazzaglia, A.; Scolaro, L. M. *Macromolecules* **2006,** *39,* 5489-5496.

[140] Wang, X. P.; Pan, J. H.; Li, W. H.; Zhang, Y. *Talanta* **2001,** *54,* 805-810.

[141] Mosinger, J.; Slavetinska, L.; Lang, K.; Coufal, P.; Kubat, P. *Org. Biomol. Chem.* **2009,** *7,* 3797-3804.

[142] Paulo, P. M. R.; Costa, S. M. B. *J. Phys. Chem. B* **2005,** *109,* 13928-13940.

[143] Bindig, U.; Endisch, C.; Fuhrhop, J. H.; Komatsu, T.; Tsuchida, E.; Siggel, U. *J. Colloid Interf. Sci.* **1998,** *199,* 123-130.

[144] Schwarz, G.; Klose, S.; Balthasar, W. *Eur. J. Biochem.* **1970,** *12,* 454-460.

[145] Horn, D. *Prog. Colloid Polym. Sci.* **1978,** *65,* 251-264.

[146] Bradley, D. F.; Wolf, M. K. *Proc. Natl. Acad. Sci. U. S. A.* **1959,** *45,* 944-952.

[147] Moreno-Villoslada, I.; Jofre, M.; Miranda, V.; Chandia, P.; Gonzalez, R.; Hess, S.; Rivas, B. L.; Elvira, C.; San Roman, J.; Shibue, T.; Nishide, H. *Polymer* **2006,** *47,* 6496-6500.

[148] Moreno-Villoslada, I.; Torres, C.; Gonzalez, F.; Shibue, T.; Nishide, H. *Macromol. Chem. Phys.* **2009,** *210,* 1167-1175.

[149] Kasha, M.; Rawls, H. R.; Ashraf El-Bayoumi, M. *Pure Appl. Chem.* **1965,** *11,* 371-392.

[150] Kasha, M.; McRae, E. G. In Augenstein, L.; Mason, R.; Rosenberg, B.; Eds.; Academic Press: New York, 1964; pp 23-42.

[151] Kasha, M. *Rad. Res.* **1963,** *20,* 55-71.

[152] Ribo, J. M.; Bofill, J. M.; Crusats, J.; Rubires, R. *Chem. Eur. J.* **2001,** *7,* 2733-2737.

[153] Selensky, R.; Holten, D.; Windsor, M. W.; Paine, J. B.; Dolphin, D.; Gouterman, M.; Thomas, J. C. *Chem. Phys.* **1981,** *60,* 33-46.

[154] Zimmermann, J.; Siggel, U.; Fuhrhop, J. H.; Röder, B. *J. Phys. Chem. B* **2003,** *107,* 6019-6021.

[155] Monahan, A. R.; Blossey, D. F. *J. Phys. Chem.* **1970,** *74,* 4014-4021.

[156] Moreno-Villoslada, I.; Gonzalez, R.; Hess, S.; Rivas, B. L.; Shibue, T.; Nishide, H. *J. Phys. Chem. B* **2006,** *110,* 21576-21581.

[157] Moreno-Villoslada, I.; Jofre, M.; Miranda, V.; Gonzalez, R.; Sotelo, T.; Hess, S.; Rivas, B. L. *J. Phys. Chem. B* **2006,** *110,* 11809-11812.

[158] Moreno-Villoslada, I.; Gonzalez, F.; Rivera, L.; Hess, S.; Rivas, B. L.; Shibue, T.; Nishide, H. *J. Phys. Chem. B* **2007,** *111,* 6146-6150.

[159] Moreno-Villoslada, I.; Torres, C.; Gonzalez, F.; Soto, M.; Nishide, H. *J. Phys. Chem. B* **2008,** *112,* 11244-11249.

[160] Moreno-Villoslada, I.; Gonzalez, F.; Arias, L.; Villatoro, J. M.; Ugarte, R.; Hess, S.; Nishide, H. *Dyes Pigm.* **2009,** *82,* 401-408.

[161] Moreno-Villoslada, I.; Murakami, T.; Nishide, H. *Biomacromolecules* **2009,** *10,* 3341-3342.

[162] Moreno-Villoslada, I.; Torres-Gallegos, C.; Araya-Hermosilla, R.; Nishide, H. *J. Phys. Chem. B* **2010,** *114,* 4151-4158.

[163] Sayar, M.; Stupp, S. I. *Phys. Rev. E* **2005,** *72,* Art. No. 011803.

[164] Duschner, S.; Gröhn, F.; Maskos, M. *Polymer* **2006,** *47,* 7391-7396.

[165] Glatter, O. *Acta Phys. Austriaca* **1977,** *47,* 83-102.

[166] Glatter, O. *J. Appl. Crystallogr.* **1980,** *13,* 577-584.

[167] Gröhn, F.; Bauer, B. J.; Amis, E. J. *Macromolecules* **2001,** *34,* 6701-6707.

[168] Glatter, O. *J. Appl. Crystallogr.* **1977,** *10,* 415-421.

[169] Thünemann, A. F.; Müller, M.; Dautzenberg, H.; Joanny, J. F. O.; Löwen, H. *Adv. Polym. Sci.* **2004,** *166,* 113-171.

[170] Störkle, D.; Duschner, S.; Heimann, N.; Maskos, M.; Schmidt, M. *Macromolecules* **2007,** *40,* 7998-8006.

[171] Rochester, C. H. *Quarterly Reviews* **1966,** *20,* 511.

[172] Bowden, K. *Chem. Rev.* **1966,** *66,* 119.

[173] Trofimov, B. A.; Vasiltsov, A. M.; Amosova, S. V. *Bulletin of the Academy of Sciences of the Ussr Division of Chemical Science* **1986,** *35,* 682-686.

[174] Sheinin, V. B.; Andrianov, V. G.; Berezin, B. D. *Zhurnal Organicheskoi Khimii* **1984,** *20,* 2224-2230.

[175] Kaatze, U.; Pottel, R.; Schäfer, M. *J. Phys. Chem.* **1989,** *93,* 5623-5627.

[176] Ioki, M.; Igarashi, S.; Yotsuyanagi, T. *Anal. Sci.* **1995,** *11,* 123-125.

[177] Borissevitch, I. E.; Tominaga, T. T.; Imasato, H.; Tabak, M. *Biophysical Journal* **1996,** *70,* Wp330-Wp330.

[178] Borissevitch, I. E.; Tominaga, T. T.; Imasato, H.; Tabak, M. *Analytica Chimica Acta* **1997,** *343,* 281-286.

[179] Venkatesh, B.; Jayakumar, R.; Pandian, R. P.; Manoharan, P. T. *Biochem. Bioph. Res. Co.* **1996,** *223,* 390-396.

[180] Aoudia, M.; Rodgers, M. A. J. *J. Am. Chem. Soc.* **1997,** *119,* 12859-12868.

[181] Purrello, R.; Bellacchio, E.; Gurrieri, S.; Lauceri, R.; Raudino, A.; Scolaro, L. M.; Santoro, A. M. *J. Phys. Chem. B* **1998,** *102,* 8852-8857.

[182] Maiti, N. C.; Mazumdar, S.; Periasamy, N. *J Porphyr. Phthalocya.* **1998,** *2,* 369-376.

[183] Maiti, N. C.; Mazumdar, S.; Periasamy, N. *J. Phys. Chem. B* **1998,** *102,* 1528-1538.

[184] Gandini, S. C. M.; Yushmanov, V. E.; Borissevitch, I. E.; Tabak, M. *Langmuir* **1999,** *15,* 6233-6243.

[185] Andrade, S. M.; Costa, S. M. B. *J. Fluoresc.* **2002,** *12,* 77-82.

[186] Huang, C. Z.; Liu, Y.; Wang, Y. H.; Guo, H. P. *Anal. Biochem.* **2003,** *321,* 236-243.

[187] Koti, A. S. R.; Periasamy, N. *Chem. Mater.* **2003,** *15,* 369-371.

[188] Aoudia, M.; Rodgers, M. A. J. *Langmuir* **2005,** *21,* 10355-10361.

[189] Kubat, P.; Lang, K.; Janda, P.; Anzenbacher, P. *Langmuir* **2005,** *21,* 9714-9720.

[190] Kovaric, B. C.; Kokona, B.; Schwab, A. D.; Twomey, M. A.; de Paula, J. C.; Fairman, R. *J. Am. Chem. Soc.* **2006,** *128,* 4166-4167.

[191] Sadasivan, S.; Kohler, K.; Sukhorukov, G. B. *Adv. Funct. Mater.* **2006,** *16,* 2083-2088.

[192] Synytsya, A.; Synytsya, A.; Blafkova, P.; Volka, K.; Kral, V. *Spectrochim. Acta, Part A* **2007,** *66,* 225-235.

[193] Valanciunaite, J.; Bagdonas, S.; Streckyte, G.; Rotomskis, R. *Photoch. Photobio. Sci.* **2006,** *5,* 381-388.

[194] Egawa, Y.; Hayashida, R.; Anzai, J. I. *Langmuir* **2007,** *23,* 13146-13150.

[195] Tian, F.; Johnson, E. M.; Zamarripa, M.; Sansone, S.; Brancaleon, L. *Biomacromolecules* **2007,** *8,* 3767-3778.

[196] Kokona, B.; Kim, A. M.; Roden, R. C.; Daniels, J. P.; Pepe-Mooney, B. J.; Kovaric, B. C.; de Paula, J. C.; Johnson, K. A.; Fairman, R. *Biomacromolecules* **2009,** *10,* 1454-1459.

[197] Kuciauskas, D.; Caputo, G. A. *J. Phys. Chem. B* **2009,** *113,* 14439-14447.

[198] Zhao, L. Z.; Ma, R. J.; Li, J. B.; Li, Y.; An, Y. L.; Shi, L. Q. *Biomacromolecules* **2008,** *9,* 2601-2608.

[199] Zhao, L. Z.; Ma, R. J.; Li, J. B.; Li, Y.; An, Y. L.; Shi, L. Q. *Biomacromolecules* **2009,** *10,* 3343-3344.

[200] Synytsya, A.; Synytsya, A.; Blafkova, P.; Ederova, J.; Spevacek, J.; Slepicka, P.; Kral, V.; Volka, K. *Biomacromolecules* **2009,** *10,* 1067-1076.

[201] Aoudia, M.; Guliaev, A. B.; Leontis, N. B.; Rodgers, M. A. J. *Biophys. Chem.* **2000,** *83,* 121-140.

[202] Valanciunaite, J.; Bagdonas, S.; Streckyte, G.; Rotomskis, R. *Photochem. & Photobiol. Sci.* **2006,** *5,* 381-388.

[203] Mosinger, J.; Deumie, M.; Lang, K.; Kubat, P.; Wagnerova, D. M. *J. Photoch. Photobio. A* **2000,** *130,* 13-20.

[204] Onouchi, H.; Miyagawa, T.; Morino, K.; Yashima, E. *Angew. Chem. Int. Ed.* **2006,** *45,* 2381-2384.

[205] De Luca, G.; Romeo, A.; Villari, V.; Micali, N.; Foltran, I.; Foresti, E.; Lesci, I. G.; Roveri, N.; Zuccheri, T.; Scolaro, L. M. *J. Am. Chem. Soc.* **2009,** *131,* 6920-+.

[206] Paulo, P. M. R.; Costa, S. M. B. *Photoch. Photobio. Sci.* **2003,** *2,* 597-604.

[207] Gohy, J. F.; Mores, S.; Varshney, S. K.; Zhang, J. X.; Jerome, R. *E-Polymers* **2002**.

[208] Sidorov, S. N.; Bronstein, L. M.; Kabachii, Y. A.; Valetsky, P. M.; Soo, P. L.; Maysinger, D.; Eisenberg, A. *Langmuir* **2004,** *20,* 3543-3550.

[209] Watanabe, H.; Yamada, Y.; Kimata, K. *J. Biochem.* **1998,** *124,* 687-693.

[210] Knudson, C. B.; Knudson, W. *Seminars in Cell & Developmental Biology* **2001,** *12,* 69-78.

[211] Kiani, C.; Chen, L.; Wu, Y. J.; Yee, A. J.; Yang, B. B. *Cell Res.* **2002,** *12,* 19-32.

[212] Ng, L.; Grodzinsky, A. J.; Patwari, P.; Sandy, J.; Plaas, A.; Ortiz, C. *J. Struct. Biol.* **2003,** *143,* 242-257.

[213] Horkay, F.; Basser, P. J.; Hecht, A. M.; Geissler, E. *J. Chem. Phys.* **2008,** *128,* -.

[214] Rosenberg, L.; Hellmann, W.; Kleinsch, A. K. *J. Biol. Chem.* **1970,** *245,* 4123-4130.

[215] Rosenberg, L.; Hellmann, W.; Kleinschmidt, A. K. *J. Biol. Chem.* **1975,** *250,* 1877-1883.

[216] Tsukahara, Y.; Mizuno, K.; Segawa, A.; Yamashita, Y. *Macromolecules* **1989,** *22,* 1546-1552.

[217] Tsukahara, Y.; Tsutsumi, K.; Yamashita, Y.; Shimada, S. *Macromolecules* **1990,** *23,* 5201-5208.

[218] Strack, A. PhD thesis, University of Mainz, 2000.

[219] Hugenberg, N.; Loske, S.; Müller, A. H. E.; Schärtl, W.; Schmidt, M.; Simon, P.

F. W.; Strack, A.; Wolf, B. A. *J. Non-Cryst. Solids* **2002,** *307,* 765-771.

[220] Duschner, S. PhD thesis, University of Mainz, 2007.

[221] Gröhn, F.; Antonietti, M. *Macromolecules* **2000,** *33,* 5938-5949.

[222] Dziezok, P. PhD thesis, University of Mainz, 1999.

[223] Hugenberg, N. PhD thesis, University of Mainz, 2000.

[224] Drake, B.; Prater, C. B.; Weisenhorn, A. L.; Gould, S. A. C.; Albrecht, T. R.; Quate, C. F.; Cannell, D. S.; Hansma, H. G.; Hansma, P. K. *Science* **1989,** *243,* 1586-1589.

[225] Putman, C. A. J.; Vanderwerf, K. O.; Degrooth, B. G.; Vanhulst, N. F.; Greve, J. *Appl. Phys. Lett.* **1994,** *64,* 2454-2456.

[226] Stephan, T. PhD thesis, University of Mainz, 2002.

[227] Störkle, D. PhD thesis, University of Mainz, 2007.

[228] In *CRC Handbook of Chemistry and Physics;* Lide, D. R.; Ed.; Vol. 90th Edition - Internet Version 2010.

[229] Debenham, M.; Dew, G. D. *J. Phys. E: Sci. Instrum.* **1981,** *14,* 544-545.

[230] Rheims, J.; Köser, J.; Wriedt, T. *Meas. Sci. Technol.* **1997,** *8,* 601-605.

[231] Lebel, R. G.; Goring, D. A. I. *J. Chem. Eng. Data* **1962,** *7,* 100-101.

[232] Liu, Z.; Li, Z.; Zhou, H.; Wei, G.; Song, Y.; Wang, L. *J. Microsc.* **2005,** *218,* 233-239.

ACKNOWLEDGMENTS